



University of
Nottingham

UK | CHINA | MALAYSIA

**Numerical-laboratory modelling
of waves interacting with dams
and rigid/flexible plates**

Tommaso Attili

Thesis submitted to the University of Nottingham

for the degree of Doctor of Philosophy

September 2023

This page was intentionally left blank.

Abstract

Fluid-Structure Interaction (FSI) is relevant for a range of mechanical processes, including wave impacts on offshore and coastal structures, wind-excited vibrations of tall buildings, fluttering of bridges and blood flows in arteries. Within the FSI phenomenon, Wave-Structure Interaction (WSI) involves wave impacts on dams, flood protection barriers, wave energy converters, seawalls, breakwaters, oil and gas platforms and offshore wind turbines. These structures are often challenged by extreme waves, e.g. tsunamis generated by landslides, rockfalls and iceberg calving, potentially leading to structural damage under exceptional conditions. For structures undergoing non-negligible deformations, referred to as Wave-Flexible Structure Interaction (WFSI) herein, the physical processes are even more complex. Unfortunately, accurate predictions of the wave effects, e.g. forces, on rigid and flexible structures are still challenging and laboratory models often involve scale effects.

This thesis explored a range of WSI phenomena based on the numerical model `solids4foam`, along with small-scale laboratory experiments. Two-Dimensional (2D) and Three-Dimensional (3D) tsunamis impacting dams were investigated first. The numerical wave loading agreed with predictions based on an existing approach and new empirical equations for wave run-ups and overtoppings of dams were proposed. The dynamic pressures were also investigated and correlated with new semi-theoretical equations. New insight into the 3D effects, including the dam curvature and asymmetrical wave impacts, were provided for selected cases. The combination of both these effects resulted in up to 32% larger run-ups compared to the 2D predictions.

2D wave impacts on offshore and onshore plates of different stiffnesses were then

modelled, along with selected 3D tests. The plate stiffness had a negligible effect on the upwave forces for the majority of these tests. However, the offshore flexible plates resulted in up to 40% smaller total forces, compared to the rigid ones, due to increased downwave water depths following the plate deformations. For the onshore tests, the time series of the wave loading were characterised by two force peaks, according to previous studies. The second force peaks were up to 3.3 times larger than the first peaks. New semi-theoretical equations were proposed to predict the onshore wave forces and run-ups of a plate, as a function of the offshore wave energy.

Finally, a systematic investigation of the scaling approaches and scale effects for wave impacts on rigid and flexible plates was conducted based on numerical modelling supported by small-scale laboratory tests. The WFSI governing parameters were derived and successfully validated based on the numerical results. A number of simulations, involving non-breaking and breaking wave impacts, were then conducted for the prototypes and up to 40 times smaller models. These were scaled according to the scaling approaches (i) precise Froude (fluid and plate properties scaled), (ii) traditional Froude-Cauchy (fluid properties unscaled, plate properties scaled), (iii) traditional Froude (fluid and plate properties unscaled) and (iv) a new WFSI approach (partial conservation of the WFSI governing parameters). No scale effects were observed for (i). Non-breaking waves were correctly scaled by (ii), however, up to 132% scale effects were observed in the breaking wave pressures due to the unscaled fluid properties. Further, the plate displacements were up to 98% underestimated by (iii). The new approach (iv) successfully predicted non-breaking wave impacts, with less than 4.3% deviations for the maximum wave forces and plate displacements.

In conclusion, the findings of this PhD thesis are intended at enhancing the physical understanding of WSI to support the design and laboratory modelling of a range of offshore and onshore structures. Future studies should address a number of further aspects, such as the 3D effects on tsunami impacts and the role of the air compressibility on WFSI. Also, the WFSI governing parameters and the new scaling approach should be further validated using numerical and laboratory experiments.

Acknowledgements

Foremost, I would like to thank my principal supervisor, Dr. Valentin Heller, for his endless support and encouragement. My gratitude goes also to my second supervisor, Dr. Panagiotis Psimoulis, for his support and to my external supervisor, Dr. Savvas Triantafyllou, for his helpful guidance and suggestions. I would like to thank my internal examiner, Dr. Fangying Zhang, for her valuable advice and feedback. Dr. Tao Liu is acknowledged for helpful discussions during the first 2 years of this study. Additionally, I would like to thank Prof. Ling Qian from the Manchester Metropolitan University for acting as my external examiner and for reviewing this PhD thesis.

A special gratitude goes to the University of Nottingham for financially supporting this PhD study and for providing access to the HPC cluster Augusta. I want to thank the Environmental Fluid Mechanics and Geoprocesses Research Group and particularly the head of the group, Dr. Barbara Turnbull, for her valuable support.

I would like to thank Dr. Frederic Evers from ETH Zurich for providing the experimental data of Kobel et al. (2017) and the photos in Fig. 3.4. I also would like to thank Dr. Ricardo Correia and Dr. Sándor Erdódy from the Optics and Photonics Group for providing the fibre optic sensors used in the laboratory tests. Dr. Walid Tizani from the Centre for Structural Engineering & Informatics is acknowledged for lending the interrogator for the laboratory tests. In addition, a particular thanks goes to Mr. Sam Cook and Mr. Alistair Palmer for supporting the experimental design and for helping with the measurement equipment for the laboratory experiments.

Finally, I want to express my deepest gratitude to my family and friends for their precious help and support which made me achieve this milestone.

This page was intentionally left blank.

Author's declaration

I certify that this thesis is submitted by integrating published works. Statements from each co-author are included below to certify my contribution to the joint journal articles. This is followed by a list of lead-author conference proceedings and presentations at which my PhD work was presented. I declare that, where necessary, I have obtained permission to use my own published work for which the copyright is held by another party.

Lead-author journal articles:

Attili, T., Heller, V., Triantafyllou, S., 2021. A numerical investigation of tsunamis impacting dams. *Coastal Engineering* 169, 103942.

Statement from lead author: I confirm that the numerical simulations, the data processing and the data analysis were performed solely by the lead author. The first draft of the article was also written by the lead author, including the preparation of all figures and tables. However, both co-authors reviewed and edited the original draft and contributed to the revisions of the article.

Statement of contribution from Dr. Valentin Heller: I confirm that the statements of the lead author are correct. My contribution was limited to administrative tasks, supervision meetings, defining the concept of the work and to review drafts and revised versions of the article.

Statement of contribution from Dr. Savvas Triantafyllou: I confirm that the statements of the lead author are correct. My contribution was limited to administrative tasks, supervision meetings and to review drafts and revised versions of the

article.

Attili, T., Heller, V., Triantafyllou, S., 2023. Wave impact on rigid and flexible plates. *Coastal Engineering* 182, 104302.

Statement from lead author: I confirm that the numerical simulations, the data collection, the data processing and the data analysis were performed solely by the lead author. The lead author designed most aspects of the laboratory experiments and contributed to define the concept of the article with the help of both co-authors. The first draft of the article was also written by the lead author, including the preparation of all figures and tables. However, both co-authors reviewed and edited the original draft and contributed to the revisions of the article.

Statement of contribution from Dr. Valentin Heller: I confirm that the statements of the lead author are correct. My contribution was limited to administrative tasks, supervision meetings, supporting the design of the laboratory experiments, help to define the concept of the work and to review drafts and revised versions of the article.

Statement of contribution from Dr. Savvas Triantafyllou: I confirm that the statements of the lead author are correct. My contribution was limited to administrative tasks, supervision meetings, help to define the concept of the work and to review drafts and revised versions of the article.

Attili, T., Heller, V., Triantafyllou, S., 2023. Scaling approaches and scale effects in wave-flexible structure interaction. *Journal of Fluids and Structures* (in press).

Statement from lead author: I confirm that the numerical simulations, the data collection, the data processing and the data analysis were performed solely by the lead author. The lead author designed most aspects of the laboratory experiments and contributed to define the concept of the article with the help of both co-authors. The first draft of the article was also written by the lead author, including the preparation of all figures and tables. However, both co-authors reviewed and edited the original

draft and contributed to the revisions of the article.

Statement of contribution from Dr. Valentin Heller: I confirm that the statements of the lead author are correct. My contribution was limited to administrative tasks, supervision meetings, supporting the design of the laboratory experiments, help to define the concept of the work and to review drafts and revised versions of the article.

Statement of contribution from Dr. Savvas Triantafyllou: I confirm that the statements of the lead author are correct. My contribution was limited to administrative tasks, supervision meetings, help to define the concept of the work and to review drafts and revised versions of the article.

Lead-author conference contributions:

Attili, T., Heller, V., Triantafyllou, S., 2020. Numerical modelling of impulse wave forces on dams. *In: Proceedings of the 1st IAHR Young Professionals Congress online*, 186 – 187.

Attili, T., Heller, V., Triantafyllou, S., 2022. Numerical investigation of impulse waves impacting on dams. *In: 39th International Association for Hydro-Environmental Engineering and Research World Congress*, 2222 – 2229.

Attili, T., Heller, V., Triantafyllou, S., 2022. Numerical investigation of waves interacting with rigid and flexible plates. *In: 39th International Association for Hydro-Environmental Engineering and Research World Congress*, 4438 – 4447.

Conference presentations:

“Modelling of Wave-Flexible Structure Interaction (WFSI)”. *Engineering Research Showcase 2020 (Pitch Perfect PhD, 1 minute presentation)*, The University of Nottingham, UK, May 2020.

“Numerical modelling of impulse wave forces on dams”. *1st IAHR Young Professionals Congress, online*, November 2020.

“A numerical study of tsunamis impacting dams”. *Young Coastal Scientists and Engineers Conference, online*, March 2021.

“A numerical investigation of waves interacting with rigid and flexible structures”. *Engineering Research Showcase 2021 (Poster), The University of Nottingham, UK*, May 2021. Outcome: Winner Best Poster - Research Quality.

“A numerical investigation of waves interacting with rigid and flexible structures”. *HPC Conference 2021, The University of Nottingham, UK*, September 2021.

“Simulations of solitary waves impacting onshore plates”. *Young Coastal Scientists and Engineers Conference, Bournemouth University, UK*, April 2022.

“Numerical-experimental modelling of wave-structure interaction”. *Engineering Research Showcase 2022 (Three Minute Thesis, presentation), The University of Nottingham, UK*, April 2022.

“Numerical investigation of waves interacting with rigid and flexible plates”. *39th IAHR World Congress, Granada, Spain*, June 2022.

“Numerical modelling of waves impacting rigid and flexible structures”. *SIAM GS23 conference, Bergen, Norway*, June 2023.

Table of Contents

Abstract	I
Acknowledgements	III
Author's declaration	V
List of Figures	XV
List of Tables	XXVII
1 Introduction	1
1.1 Background and motivation	1
1.2 Aims and objectives	5
1.3 Thesis outline	6
2 Literature review	9
2.1 Overview	9
2.2 Theoretical background	9
2.2.1 Wave theories	9
2.2.2 Analytical models for wave loading on a rigid plate	12
2.3 Previous work	15
2.3.1 Laboratory findings	15
2.3.1.1 Rigid walls	15
2.3.1.2 Flexible walls	20
2.3.2 Numerical findings	23
2.3.2.1 Mesh-based models	24

2.3.2.2	Coupled mesh-based and mesh-free models	26
2.3.2.3	Mesh-free models	27
2.4	Model-prototype similarity	31
2.4.1	Introduction	31
2.4.2	Froude similarity	33
2.4.3	Cauchy similarity	33
2.4.4	Scale effects	34
2.5	Summary and research gaps	37
3	A numerical investigation of tsunamis impacting dams	39
3.1	Introduction	41
3.1.1	Background	41
3.1.2	Previous work	42
3.1.3	Aims and structure	45
3.2	Methodology	46
3.2.1	Governing equations of fluid	46
3.2.2	Numerical set-up and test programme	48
3.2.2.1	3D simulations	49
3.3	Results	51
3.3.1	Validation of the numerical toolbox	51
3.3.1.1	Comparison with experiments and an analytical solution	51
3.3.1.2	Comparison with numerical solutions	52
3.3.1.3	Validation for overtopping waves with laboratory experiments	53
3.3.2	No overtopping	54
3.3.2.1	Run-up	55
3.3.2.2	Force and bending moment	56
3.3.2.3	Dynamic pressure	57

3.3.3	Overtopping waves	61
3.3.3.1	Force and bending moment	61
3.3.3.2	Overtopping	63
3.4	Discussion of results	65
3.4.1	Validation of the available prediction method and limitations	65
3.4.2	Run-up height	65
3.4.3	Overtopping	67
3.4.4	3D simulations to investigate 3D effects	69
3.4.4.1	Symmetrical wave impact angle	69
3.4.4.2	Asymmetrical wave impact	71
3.5	Conclusions	74
Appendix 3.A	Overtopping wave forces at dams	76
Appendix 3.B	Convergence tests	76
3.B.1	Convergence of the main tests	76
3.B.2	Convergence of the validation tests	77
Appendix 3.C	Overtopping waves: dynamic pressure	78
4	Wave impact on rigid and flexible plates	81
4.1	Introduction	83
4.1.1	Background	83
4.1.2	Previous work	84
4.1.2.1	Laboratory studies	84
4.1.2.2	Numerical modelling	86
4.1.3	Aims and structure	87
4.2	Numerical model	88
4.2.1	Governing equations and coupling method	88
4.2.2	Numerical set-up and test programme	91
4.2.3	3D simulations	93
4.3	Physical model	94

4.4	Results	95
4.4.1	Offshore	95
4.4.1.1	Validation of solids4foam with new laboratory exper- iments	95
4.4.1.2	A numerical representative test	99
4.4.1.3	Numerical run-up and force	101
4.4.1.4	Numerical plate response	103
4.4.1.5	Numerical 3D tests	105
4.4.2	Onshore	106
4.4.2.1	Validation of solids4foam with an available laboratory experiment	106
4.4.2.2	A numerical representative test	108
4.4.2.3	Numerical force	109
4.4.2.4	Numerical plate response	110
4.5	Discussion of results	111
4.5.1	Offshore	111
4.5.1.1	Force	111
4.5.2	Onshore	112
4.5.2.1	Transformation into overland flow	112
4.5.2.2	Run-up height	115
4.6	Conclusions	116
Appendix 4.A	Convergence tests	119
Appendix 4.B	An application of the Euler-Bernoulli beam theory for off- shore plates	120
Appendix 4.C	Correlations of the onshore plate response	124
5	Scaling approaches and scale effects in wave-flexible structure in- teraction	127
5.1	Introduction	129

5.1.1	Background	129
5.1.2	Aims and structure	132
5.2	Methodology	133
5.2.1	Numerical model	133
5.2.1.1	Governing equations and coupling technique	133
5.2.1.2	Numerical set-up and test programme	135
5.2.1.3	Numerical simulation of breaking waves impacting plates	136
5.2.2	Governing parameters in WFSI	136
5.2.3	Scaling approaches	137
5.3	Results	139
5.3.1	Validation of the governing parameters	139
5.3.2	Non-breaking wave impacts	141
5.3.3	Breaking wave impacts	144
5.4	Discussion of results	147
5.4.1	Governing parameters	147
5.4.2	Scale effects in non-breaking waves	148
5.4.3	Scale effects in breaking waves	150
5.4.4	Upscaling of the laboratory tests	153
5.5	Conclusions	154
	Appendix 5.A Convergence tests	157
	Appendix 5.B Physical model	157
	5.B.1 Laboratory set-up	157
	5.B.2 Laboratory results	159
	Appendix 5.C Supplementary tables	161
6	Conclusions and outlook	163
6.1	Conclusions	163
6.2	Outlook	166

Notation	169
Subscripts	175
Abbreviations	177
Appendix A Supplementary laboratory data	179
Appendix B Breaking wave impact on a deformable truncated vertical wall (CCP-WSI comparative study 1)	185
B.1 Laboratory set-up and test programme	186
B.2 Numerical simulations	187
B.3 Numerical results	189
References	193

List of Figures

1.1	Fluid-structure interaction failures: (a) Tacoma Narrows Bridge during fluttering in 1940 (Irvine, 2009), (b) collapse of the Ferrybridge cooling towers in 1965 (Shellard, 1967) and (c) Sines breakwater after collapsing in 1978 (Baird et al., 1980).	2
1.2	Examples of wave-structure interaction: (a) a hydro-power dam (Wikipedia, 2023), (b) wave impact on a vertical seawall (Allsop et al., 2008), (c) prototype of the OBREC wave energy converter (Contestabile et al., 2017) and (d) the MOSE mobile gate (Mose, 2023).	3
1.3	Scale effects in breaking wave impact on a rigid wall: snapshots of the wave impact at different geometrical scales (after Bredmose et al., 2015).	4
2.1	Water surface elevation with main parameters and orbit of a surface particle for (a) linear, (b) 2nd order Stokes, (c) cnoidal and (d) solitary wave theories.	11
2.2	Analytical wave pressure on a vertical wall: (a) from the theory of Sainflou (1928) and (b) the solution of Tadjbakhsh and Keller (1960) with $\varepsilon_p = 0.11$ and $\omega_0 = 0.75$	14
2.3	Sketches with the main parameters for (a) wave run-up and overtopping of a dam and (b) solitary wave transformation to overland flow.	18

2.4	Side view of the experimental set-up from Mallayachari and Sundar (1995).	19
2.5	Dam break wave: (a) side view of the tank with elastic gate experiment from Antoci et al. (2007) and (b) overview of the experiments of Liao et al. (2015).	21
2.6	Side view of the experimental set-up with location of the measurement systems in the study of Linton et al. (2013).	22
2.7	Comparison between experimental and numerical results of a dam break wave impacting a flexible plate (Liao et al., 2015). The colour function ϕ_m denotes the water, air and solid phases.	25
2.8	Validation of the numerical model of Rao et al. (2017) with a dam break laboratory experiment (Antoci et al., 2007).	27
2.9	Comparison between the experiment of Antoci et al. (2007) and numerical results of Zhang et al. (2019b), showing the pressure p and stress σ_s fields.	27
2.10	Dam break wave with an elastic gate: comparison between laboratory measurements and numerical observations of Antoci et al. (2007). . .	28
2.11	Numerical-laboratory modellings of wave impacts on a rigid onshore wall (Didier et al., 2014).	29
2.12	Dam break wave impacting a flexible obstacle: comparison between laboratory experiments (Liao et al., 2015) and simulations of Sun et al. (2019).	30
2.13	Dam break wave impacting a flexible obstacle: comparison of the horizontal plate displacement d_x between laboratory (Liao et al., 2015) and numerical (Liao et al., 2015; Sun et al., 2019; O'Connor and Rogers, 2021) experiments.	30

2.14	Upscaling approaches to remove scale effect in wave impact pressures: (a) p_{max}/p_0 versus Ba from Cuomo et al. (2010b) and (b) pressure scaling curves based on Bagnold-Mitsuyasu and the Froude scaling laws (after Bredmose et al., 2015).	36
3.1	Numerical set-ups: (a) 2D tests, (b, c) lateral and (d, e) top views of the 3D tests with (b, d) showing the gravity and (c, e) the arch dam.	50
3.2	Comparison of the numerical pressure $p_d/(\rho_w g H)$ versus z/h with laboratory measurements (Mallayachari and Sundar, 1995) and analytical p_{lin} and p_{nonlin} (Tadjbakhsh and Keller, 1960) for (a) $H = 0.023$ m and $T = 0.950$ s and (b) $H = 0.048$ m and $T = 0.873$ s (after Attili et al., 2020).	51
3.3	Comparison of the time series of the dimensionless forces $F/(\rho_w g h^2)$ at the dam with that of Cooker et al. (1997) for $a/h = 0.1, 0.2, 0.3, 0.4,$ and 0.5	52
3.4	Comparison between laboratory (Kobel et al., 2017) and numerical snapshot series of a solitary wave impact on a vertical dam with overtoppings with $a/h = 0.30$. The units of the x and z axes are m.	54
3.5	Snapshot series of a solitary wave impact on a dam without overtopping with $a/h = 0.31$ with (a, c, e) pressure contours in MPa and (b, d, f) mean velocity $\bar{u} = \sqrt{\bar{u}_x^2 + \bar{u}_z^2}$ contours.	55
3.6	(a) Relative run-up height R/h and (b) $(R/h)(\beta/90^\circ)^{1/3}$ with Eq. (3.13) ($R^2 = 0.94$) versus the relative wave amplitude a/h	56
3.7	Comparison of the horizontal dimensionless (a) force F_H/F_h and (b) moment M_H/M_h at the dam versus a/h with predictions from Evers et al. (2019) and data of Ramsden (1996).	57

3.8	Distribution of the pressure response factor at the wall K_{pw} with z/h for $\beta = 90^\circ$ and Eq. (3.17) for $a/h = 0.10$ ($R^2 = 1.00$), 0.16 ($R^2 = 1.00$), 0.17 ($R^2 = 1.00$), and 0.42 ($R^2 = 1.00$) and $A = 3.47, 5.79, 4.45,$ and $1.28,$ respectively.	59
3.9	Coefficient A versus the relative wave amplitude a/h and (a) Eq. (3.18) for Stokes and cnoidal waves ($R^2 = 0.59$) and (b) Eq. (3.19) for solitary waves ($R^2 = 0.72$).	59
3.10	Comparison of the total $p/(\rho_w gh)$ and dynamic pressure $p_d/(\rho_w gh)$ with predictions from Evers et al. (2019) (Eq. 3.3) and Eq. (3.16) for cnoidal waves with $a/h = 0.10$ and (a) $\beta = 90$ and (b) 60° and solitary waves with $a/h = 0.20$ and (c) $\beta = 90$ and (d) 60°	60
3.11	Snapshot series of a solitary wave impact on a dam with overtopping with $a/h = 0.28$ with (a, c, e) pressure contours in MPa and (b, d, f) mean velocity \bar{u} contours.	61
3.12	Overtopping waves: relative reduced horizontal force $F_{H,red}/F_h$ versus (a) a/h and (b) f/h , moment $M_{H,red}/M_h$ versus (c) a/h and (d) f/h , and comparison of the predicted (Evers et al., 2019) and numerical (e) $F_{H,red}/F_h$ and (f) $M_{H,red}/M_h$ at the dam.	62
3.13	Relative overtopping (a) volume \mathcal{V}/h^2 and (b) maximum depth d_0/h versus a/h and correlations of (c) \mathcal{V}/h^2 with Eq. (3.23) ($R^2 = 0.99$) and (d) d_0/h with Eq. (3.24) ($R^2 = 0.96$).	64
3.14	Predicted relative run-up heights R_{pred}/h (a) based on Eq. (3.13) versus the experimental R_{exp}/h of Street and Camfield (1967), Maxworthy (1976), and Müller (1995) with $\beta = 90^\circ$ and (b) based on Hall and Watts (1953), Müller (1995), Evers and Boes (2019), and Eq. (3.13) (Table 3.4) versus the numerical R_{num}/h of the present study.	67

3.15	Comparison of the predicted and numerical relative overtopping (a) volume \mathcal{V}/h^2 and (b) maximum depth d_0/h with encircled data predicted by Kobel et al. (2017) for $a \leq f$	68
3.16	Maximum relative run-up height R_{max}/h versus y/h for the gravity dam and R/h versus y/h for the arch dam at $t = 6.8$ s, with $a/h = 0.3$ and $\gamma = 0^\circ$	70
3.17	Symmetrical wave impact ($\gamma = 0^\circ$): dimensionless force F_H/F_h versus the relative dam width y/h at the (a) gravity and (b) arch dam and pressure $p/(\rho_wgh)$ versus y/h and z/h during the maximum force at the (c) gravity and (d) arch dam.	70
3.18	Snapshot series with surface elevation contours in m of a solitary wave impact on the gravity dam with $a/h = 0.3$ and $\gamma = 30^\circ$ at $t =$ (a) 0.0, (b) 1.0, (c) 2.0, and (d) 3.0 s.	72
3.19	Snapshot series of a solitary wave impact on the (a, b, c) gravity and (d, e, f) arch dams with $a/h = 0.3$ and $\gamma = 30^\circ$ at $t = 2, 3,$ and 4 s.	72
3.20	Asymmetrical wave impact ($\gamma = 30^\circ$): dimensionless force F_H/F_h versus the relative dam width y/h at the (a) gravity and (b) arch dam and pressure $p/(\rho_wgh)$ versus y/h and z/h during the maximum force at the (c) gravity and (d) arch dam.	73
3.B.1	Convergence tests of the relative force $F/(\rho_wgh^2/2)$ with the mesh size $\Delta x = \Delta z$ for the (a) main and (b) validation tests.	77
3.B.2	Numerical set-up with a detail of the mesh.	78
3.C.1	Total pressure p and dynamic pressure p_d at the dam in two overtopping tests with $a/h = 0.21$ and $\beta = 90^\circ$ with (a) $f/h = 0.389$ and (b) $f/h = 0.042$ and pressure response factor at the wall K_{pw} versus z/h for $f/h = 0.042$ for some representative (c) cnoidal and (d) solitary wave overtopping tests for $\beta = 90^\circ$	79
4.1	Side views of the numerical set-ups: (a) offshore and (b) onshore.	91

4.2	3D simulations: (a) lateral view and (b) section AA of the 3D numerical set-up with the hull of a FPSO unit.	93
4.3	Experimental set-up: (a) side view of the wave flume and plate, (b) frontal view of the plate (dimensions in m) and (c) overview of the flume with the instrumentation.	94
4.4	Comparison of the experimental and numerical water surface elevations η/h at all 3 WGs for experiment 1 (a, c, e) and 2 (b, d, f) of Table 4.3.	97
4.5	Comparison of the experimental and numerical pressures $p/(\rho_w g h)$ at (a) PPT1 ($nRMSE = 0.097$) and 2 ($nRMSE = 0.085$), (c) 3 ($nRMSE = 0.041$) and 6 ($nRMSE = 0.078$) and (e) force $F_{3D}/(\rho_w g h^3)$ for experiment 1 and $p/(\rho_w g h)$ at (b) PPT1 ($nRMSE = 0.108$) and 2 ($nRMSE = 0.115$), (d) 3 ($nRMSE = 0.094$) and 6 ($nRMSE = 0.102$) and (f) $F_{3D}/(\rho_w g h^3)$ for experiment 2 of Table 4.3.	98
4.6	Comparison of the experimental and numerical strains ε_{zz} at SGb and SGc for experiment 2 of Table 4.3.	99
4.7	Snapshot series of a 2D linear wave impacting a plate with $a/h = 0.038$, $T(g/h)^{1/2} = 3.54$, $s = 2.00$ m and $E = 1.00$ GPa showing the mean velocity $\bar{u} = \sqrt{\bar{u}_x^2 + \bar{u}_z^2}$, pressure contours (MPa) and horizontal displacement d_x	100
4.8	Offshore tests: time series of the relative (a) total $F_H/(\rho_w g h^2)$ and upstream $F_{H,u}/(\rho_w g h^2)$ forces and (b) horizontal displacement d_x/l at the top end of the offshore plates (Fig. 4.1a) with $E = 1$ and 1000 GPa and $\beta = 90^\circ$ for a linear wave with $a/h = 0.038$ and $T(g/h)^{1/2} = 3.54$	101

4.9	Offshore tests: (a) relative run-up height R/h versus a/h , (b) predicted R_{pred}/h with Miche (1951) for the linear and Müller (1995) for the solitary wave tests (Table 4.4) versus the numerical R_{num}/h , (c) upwave $F_{H,u}/(\rho_w g h^2)$ and (d) total $F_H/(\rho_w g h^2)$ forces versus a/h for the different plates shown in Table 4.1.	102
4.10	Plate response for offshore tests: (a) relative maximum displacement $d_{x,max}/l$ versus a/h , (b) relative maximum vertical stress component $\sigma_{zz,max}/(\rho_s g l)$ versus a/h for the solitary wave tests and (c, d) comparison between $d_{x,max,num}/l$ and (c) $d_{x,max,pred}/l$ ($R^2 = -0.42$) and (d) $d_{x,max,pred}/(2l)$ ($R^2 = 0.94$).	104
4.11	3D simulations of offshore tests: (a) relative forces $F_{H,3D}/(\rho_w g h^3)$ and $F_{H,u,3D}/(\rho_w g h^3)$ versus $t(g/h)^{1/2}$, (b) relative pressures $p_u/(\rho_w g h)$ and $p_d/(\rho_w g h)$ along z/h at $y = 7.5$ m, (c) relative displacements d_x/l and (d) relative stresses $\sigma_{zz}/(\rho_s g l)$ at the inner fibre along z/h at $y = 7.5$ m during the maximum force for $E = 2 \cdot 10^2$ and $2 \cdot 10^4$ GPa.	105
4.12	Validation of solids4foam with an experiment of Kimmoun et al. (2009): (a) experimental set-up, (b) comparison between the laboratory and numerical snapshots at $t = 0.03$ s and (c) horizontal plate displacement d_x at $z = 0.35$ m (after Attili et al., 2022b).	107
4.13	Snapshot series of a 2D solitary wave impacting an onshore plate with $a/h = 0.40$, $s = 0.15$ m and $E = 1.00$ GPa showing the mean velocity $\bar{u} = \sqrt{\bar{u}_x^2 + \bar{u}_z^2}$, pressure contours (kPa) and horizontal displacement d_x	108
4.14	Plate forces at the 5 plates shown in Table 4.2 for onshore tests: relative force $F_H/(\rho_w g h^2)$ versus t with (a) $a/h = 0.40$ and (b) $a/h = 0.75$ and (c, d) $F_H/(\rho_w g h^2)$ versus (c) a/h and (d) z_f/h	109

4.15	Plate response for the 5 plates (Table 4.2) in the onshore tests: (a) dimensionless horizontal displacement d_x/l and (b) vertical stress component $\sigma_{zz}/(\rho_s gl)$ along z/h at $t(g/h)^{1/2} = 2.64$ with $a/h = 0.4$ and maximum (c) $d_{x,max}/l$ and (d) $\sigma_{zz,max}/(\rho_s gl)$ versus a/h	111
4.16	Comparison of the predicted $F_{H,u,pred}/(\rho_w gh^2)$ (Evers et al., 2019) and numerical $F_{H,u,num}/(\rho_w gh^2)$ for the linear and solitary (encircled) wave tests.	112
4.17	Sketch with the main parameters of a solitary wave and its transformation to overland flow.	113
4.18	Overland flow: (a) comparison of the predicted (Cross, 1967) and numerical $F_I/(\rho_w gh^2)$ ($R^2 = 0.93$) at plate R, (b) energy of the overland flow $E_{of}/[\rho_w g(h + z_f + a)^2]$ with Eq. (4.16) ($R^2 = 0.98$) for plate R, (c) $F_I/[\rho_w g(h + z_f + a)^2]$ with Eq. (4.17) ($R^2 = 0.90$) versus the wave energy $E_w/[\rho_w g(h + z_f + a)^3]$ and (d) $F_{II}/[\rho_w g(h + z_f + a + l)^2]$ versus $E_w/[\rho_w g(h + z_f + a)^3]$ with Eq. (4.18) ($R^2 = 0.96$) for all 5 plates in Table 4.2.	115
4.19	Dimensionless run-up $R/(h + z_f)$ versus the dimensionless wave amplitude $a/(h + z_f)$ with Eq. (4.19) ($R^2 = 0.75$).	116
4.A.1	Convergence tests: semi-logarithmic diagramme for the relative (a, c) force $F_{H,u}/(\rho_w gh^2)$ and (b, d) horizontal displacement d_x/l with the number of cells and mesh size $\Delta x = \Delta z$ for an (a, b) offshore and (c, d) onshore test.	119
4.B.1	Sketch with the main parameters and pressure distribution of a wave impact on offshore plates.	121

4.B.2	Comparison of the predicted and numerical (a) d_x/l ($nRMSE = 0.27$) and $\sigma_{zz}/(\rho_s gl)$ ($nRMSE = 0.22$) for a linear wave test with $a/h = 0.027$, $T(g/h)^{1/2} = 4.13$, $E = 1$ GPa and $\beta = 90^\circ$, (b) d_x/l ($nRMSE = 0.10$) and $\sigma_{zz}/(\rho_s gl)$ ($nRMSE = 0.09$) for a linear wave test with $a/h = 0.046$, $T(g/h)^{1/2} = 3.84$, $E = 1$ GPa and $\beta = 90^\circ$, (c) d_x/l ($nRMSE = 0.14$) and $\sigma_{zz}/(\rho_s gl)$ ($nRMSE = 0.10$) for a solitary wave test with $a/h = 0.073$, $E = 1$ GPa and $\beta = 90^\circ$ and (d) d_x/l ($nRMSE = 0.04$) and $\sigma_{zz}/(\rho_s gl)$ ($nRMSE = 0.17$) for a solitary wave test with $a/h = 0.062$, $E = 30$ GPa and $\beta = 60^\circ$	124
4.C.1	Plate response in the onshore tests: maximum relative (a) displacement $d_{x,max}Es^3/(\rho_s gl^5)$ with Eq. (4.C.1) ($R^2 = 0.93$) and (b) stress $\sigma_{zz,max}s^2/(El^2)$ with Eq. (4.C.2) ($R^2 = 0.93$) for plates RS and (c) $d_{x,max}Es^3/(\rho_s gl^5)$ with Eq. (4.C.3) ($R^2 = 0.95$) and (d) $\sigma_{zz,max}s^2/(El^2)$ with Eq. (4.C.4) ($R^2 = 0.96$) for plates TF versus the dimensionless wave energy $E_w/[\rho_w g(h + z_f + a)^3]$	125
5.1	Side view of the prototype numerical set-ups for the (a) non-breaking wave and (b) breaking wave tests.	135
5.2	Validation of the dimensionless governing parameters: dimensionless time histories of the (a) water surface elevations η/h at $x = 0$ m, (b) forces $F_H/(\rho_w gh^2)$ and (c) displacements d_x/l for the tests of Table 5.5.	141
5.3	Scale series for a regular wave test with $H/h = 0.13$ and $T(g/h)^{1/2} = 4.45$: dimensionless $F_H/(\rho_w gh^2)$ and d_x/l versus $t(g/h)^{1/2}$ for the prototype ($\lambda = 1$) and scaled models according to (a, b) PFr, (c, d) TFr _E , (e, f) TFr and (g, h) GP approaches.	142

5.4	Scale series for a regular wave test with $H/h = 0.13$ and $T(g/h)^{1/2} = 8.90$: dimensionless $F_H/(\rho_w g h^2)$ and d_x/l versus $t(g/h)^{1/2}$ for the prototype ($\lambda = 1$) and scaled models according to (a, b) PFr, (c, d) TFr _E , (e, f) TFr and (g, h) GP approaches.	143
5.5	Scale series for a solitary wave test with $a/h = 0.13$: dimensionless $F_H/(\rho_w g h^2)$ and d_x/l versus $t(g/h)^{1/2}$ for the prototype ($\lambda = 1$) and scaled models according to (a, b) PFr, (c, d) TFr _E , (e, f) TFr and (g, h) GP approaches.	144
5.6	Breaking wave impacts for the prototype ($\lambda = 1$) and scaled after TFr _E : time histories of the dimensionless (a) forces $F_H/(\rho_w g h^2)$ and (b) displacements d_x/l , with details of (c) $F_H/(\rho_w g h^2)$ and (d) d_x/l , and (e) pressure $p/(\rho_w g h)$ distribution at the plate at $t(g/h)^{1/2} = 27.7$.	145
5.7	Snapshots of breaking wave impact on the flexible plate at $t(g/h)^{1/2} = 27.7$ of the prototype ($\lambda = 1$) and TFr _E scaled models showing only minor scale effects.	146
5.8	Regular wave test with $H/h = 0.13$ and $T(g/h)^{1/2} = 8.90$: prototype and TFr _E scaled (a) $p/(\rho_w g h)$ versus z/h and (b) $\sigma_{zz}/(\rho_s g l)$ along the inner fibre (upwave) of the plate at the instant during $F_{H,max}$	149
5.9	Upscaling of d_x under TFr with Eq. (5.13) to remove scale effects: comparison of the numerical $\frac{d_{x,P}}{l_P}$ and predictions based on Eq. (5.13).	149
5.10	Scale effects in wave breaking impacts: (-) prediction based on the Froude scaling laws and data of numerical relative impact pressures $p_{max,P}/p_{max,M}$ versus $\frac{Re_P}{Re_M} \frac{We_P}{We_M} \frac{Ma_P}{Ma_M}$	151
5.11	Comparison of the numerical p_{max}/p_0 with the predictions based on the Bagnold-Mitsuyasu and the Froude scaling laws (after Bredmose et al., 2015).	153
5.A.1	Convergence tests for a solitary non-breaking wave test with $a/h = 0.13$: semi-logarithmic diagramme for the relative (a) force $F_H/(\rho_w g h^2)$ and (b) horizontal displacement d_x/l with the mesh size $\Delta x = \Delta z$	157

5.B.1	Laboratory set-up: (a) schematic side view of the wave flume and plate, (b) frontal view of the plate with location of the measurement systems and (c) picture of the wave flume with some of the instrumentation (Attili et al., 2023b).	158
5.B.2	Laboratory experiments: (a) maximum relative forces $F_{3D,H}/(\rho_w g h^3)$ versus a/h for all tests of Table 5.B.1, (b) $F_{3D,H}/(\rho_w g h^3)$ with Eq. (5.B.1) (coefficient of determination $R^2 = 0.98$) and the data points of the non-breaking wave prototype ($\lambda = 1$) numerical tests (Table 5.2), (c) maximum ε_{zz} at SGb versus a/h for the flexible plate ($E = 3.30$ GPa) tests and (d) ε_{zz} at SGb with Eq. (5.B.2) ($R^2 = 0.98$).	160
A.1	Laboratory set-up: (a) movable angled ramp and stainless steel plate, (b) acrylic plate with $\beta = 60^\circ$, (c) detail view of the acrylic plate with SGa, b and d and (d) laboratory wave flume with the wave gauges and the stainless steel plate.	180
A.2	Laboratory tests 6 and 32: dimensionless time series of (a) η/h at WG2, (b) $p/(\rho_w g h)$ at PPT1 and 3, (c) $F_{3D}/(\rho_w g h^3)$ and (d) ε_{zz} at SGb.	182
A.3	Laboratory tests 21 and 47: dimensionless time series of (a) η/h at WG2, (b) $p/(\rho_w g h)$ at PPT1 and 3, (c) $F_{3D}/(\rho_w g h^3)$ and (d) ε_{zz} at SGb.	182
A.4	Laboratory tests 11 and 37: dimensionless time series of (a) η/h at WG2, (b) $p/(\rho_w g h)$ at PPT1 and 3, (c) $F_{3D}/(\rho_w g h^3)$ and (d) ε_{zz} at SGb.	183
A.5	Laboratory tests 26 and 52: dimensionless time series of (a) η/h at WG2, (b) $p/(\rho_w g h)$ at PPT1 and 3, (c) $F_{3D}/(\rho_w g h^3)$ and (d) ε_{zz} at SGb.	183

B.1	Laboratory set-up of the CCP-WSI (2021) comparative study 1: (a) photograph of the experimental flume and wall and (b) sketch of the wall and spring system (all measurements are in mm).	187
B.2	Side view of the numerical set-up for the (CCP-WSI, 2021) comparative study 1.	188
B.3	Time series of the laboratory and numerical water surface elevations η/h at several wave gauges for test 1 of Table B.1.	189
B.4	Time series of the numerical water surface elevations η/h at several wave gauges for the 3 tests of Table B.1.	190
B.5	Time series of the numerical results (a) $F_{3D}/(\rho_w g h^2)$ and (b) d_x/l for the 3 tests in Table B.1 of CCP-WSI (2021).	191

List of Tables

2.1	Prediction equations and limitations for the relative run-up height R/h in previous studies.	16
2.2	Overview of numerical models for WSI.	31
2.3	Scaling laws for relevant parameters under Froude-Cauchy similarity, with the 3 units length [L], mass [M] and time [T].	34
3.1	The test programme for the 2D tests. Values marked with * were observed at $x = -hcot\beta$ in simulations conducted without the dam and are slightly different, due to bottom friction, from the round values used at the input.	48
3.2	Overview of the main parameters in the comparison with experiments of Kobel et al. (2017).	53
3.3	Main parameters of some subaerial landslide-tsunami events.	65
3.4	Predictions and limitations of the run-up height R in the present and other studies.	66
3.5	Summary of the most suitable equations to predict landslide-tsunami run-ups and overtoppings.	68
4.1	Test programme for the 2D numerical tests.	92
4.2	Classification of the 5 plates used in the onshore tests.	93
4.3	Main parameters in the validation with 2 laboratory experiments. Values marked with * were observed at WG1 in tests conducted without the plate.	96

4.4	Run-up height R prediction equations of Miche (1951) and Müller (1995).	102
4.B.1	Boundary conditions at the 4 significant points for the offshore plate of Fig. 4.B.1.	122
4.B.2	Values for the constants in Eqs. (4.B.4), (4.B.5) and (4.B.6).	123
5.1	Relevant scaling studies for various WSI phenomena.	132
5.2	Test programme for the prototype numerical tests.	136
5.3	Dimensionless governing parameters in 2D WFSI.	137
5.4	Scaling laws for all WFSI relevant parameters under different scaling approaches.	137
5.5	Test programme to validate the WFSI dimensionless parameters. . .	140
5.6	Dimensionless governing parameters in 3D WFSI.	148
5.7	Comparison of the upscaled relative breaking wave impact pressures $p_{P,max}/p_0$ based on the approach of Cuomo et al. (2010b) with the numerical results of the present study, where $p_0 = 101.325$ kPa and $\Delta\lambda_p$ is the deviation between $\lambda_{p,pred}$ and $\lambda_{p,num}$	152
5.8	Upscaled laboratory test parameters of the rigid and flexible plate under the TFr $_E$ and GP approaches, with $\lambda = 40$	154
5.B.1	Test programme for the laboratory tests.	159
5.C.1	Natural plate period $T_s = [2\pi l^2/1.875^2]\sqrt{12\rho_s/(Es^2)}$ (Gibson, 2007) and dimensionless plate period $T_s(g/h)^{1/2}$ for the non-breaking wave tests of Table 5.2 under the scaling approaches shown in Table 5.4. .	161
5.C.2	Scale effects $\Delta F_{H,max}$ and $\Delta d_{x,max}$ for the maximum force and displacement, respectively, for the non-breaking wave tests of Table 5.2 under the scaling approaches shown in Table 5.4.	161
5.C.3	Ranges of Re, We, Ma, Ca and WFSI dimensionless parameters investigated in the non-breaking wave impact tests for different scaling approaches.	161

A.1	Accuracy and locations of the instruments used in the laboratory tests.	179
A.2	Overview of main investigated parameters for the 52 laboratory tests. R stands for a 3 mm thick stainless steel plate (Young's modulus $E = 200$ GPa) and F for a 4 mm thick acrylic plate ($E = 3.3$ GPa). Values marked with * were observed at WG1 in tests conducted without the plate.	181
B.1	Test programme for the CCP-WSI (2021) laboratory tests.	186
B.2	Wave gauge locations along the flume: distance (m) from the wave maker.	187
B.3	Properties of the numerical block used to model the CCP-WSI (2021) laboratory tests.	188

This page was intentionally left blank.

Chapter 1

Introduction

1.1 Background and motivation

Fluid-Structure Interaction (FSI) is crucial for a range of mechanical processes in engineering, science and nature. Among these, the most common FSI phenomena include wave impacts on offshore and coastal structures, wind-excited vibrations of tall buildings, fluttering and buffeting of bridges and blood flows in arteries and artificial heart valves (Jain et al., 1996; Yang et al., 2004; Sotiropoulos and Borazjani, 2009; He and Kashiwagi, 2012; Didier et al., 2014; Hu et al., 2023). These structures experience stresses and deformations under the fluid forces, leading to a mutual interplay between the fluid and structure domains. This may have significant effects, resulting in damage of the structure and severe modifications of the flow under extreme conditions.

FSI resulted in disastrous failures in the past, hence the need to fully understand its underlying mechanisms and quantify their effect on structures. On November 7th, 1940, the Tacoma Bridge collapsed during extraordinary wind conditions. Wind speeds of up to 68 km/h were observed, inducing torsional vibration modes of the bridge (Fig. 1.1a). The two halves of the bridge oscillated out of phase with one another, resulting in the failure of the structure (Irvine, 2009). Large wind speeds have also caused the collapse of the 3 Ferrybridge cooling towers on November 1st,

1965 (Fig. 1.1b, Shellard, 1967). One more relevant example is the failure of the Sines breakwater during a storm on February 26th, 1978 (Fig. 1.1c). Wave amplitudes of up to 10 m have been estimated to have impacted the breakwater, with even larger values in front of the structure due to wave refraction. Several aspects have been identified to cause the failure of the breakwater, including an inadequate design, extreme waves and the removal of the dolos due to wave action (Baird et al., 1980).

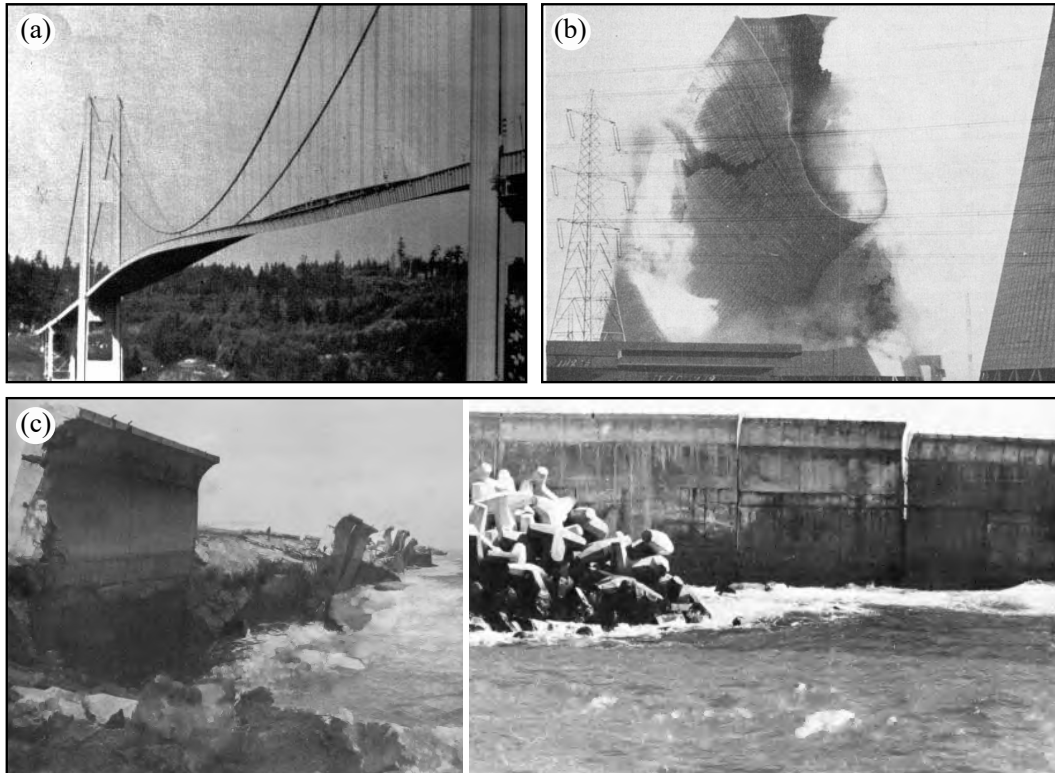


Figure 1.1. Fluid-structure interaction failures: (a) Tacoma Narrows Bridge during fluttering in 1940 (Irvine, 2009), (b) collapse of the Ferrybridge cooling towers in 1965 (Shellard, 1967) and (c) Sines breakwater after collapsing in 1978 (Baird et al., 1980).

The present thesis focuses on Wave-Structure Interaction (WSI), a category of FSI phenomena. WSI is relevant for numerous offshore and onshore applications, including hydro-power dams, flood protection barriers, wave energy converters, sea-walls, breakwaters, oil and gas platforms and offshore wind turbines (Fig. 1.2). These structures are often endangered by extreme waves, such as tsunamis generated by landslides, rockfalls and iceberg calving. For instance, the Vajont landslide on Oc-

tober 9th, 1963, is one of the most catastrophic events ever recorded. The tsunami, generated by the landslide impacting into the reservoir, overtopped the dam crest and destroyed the downstream villages, resulting in approximately 2000 fatalities (Panizzo et al., 2005b). More recently, WSI was responsible for the collapse of an offshore platform during the 2002 hurricane in the Gulf of Mexico (Moan, 2018) and the Dawlish seawall breach on February 5th, 2014 (Dawson et al., 2016).

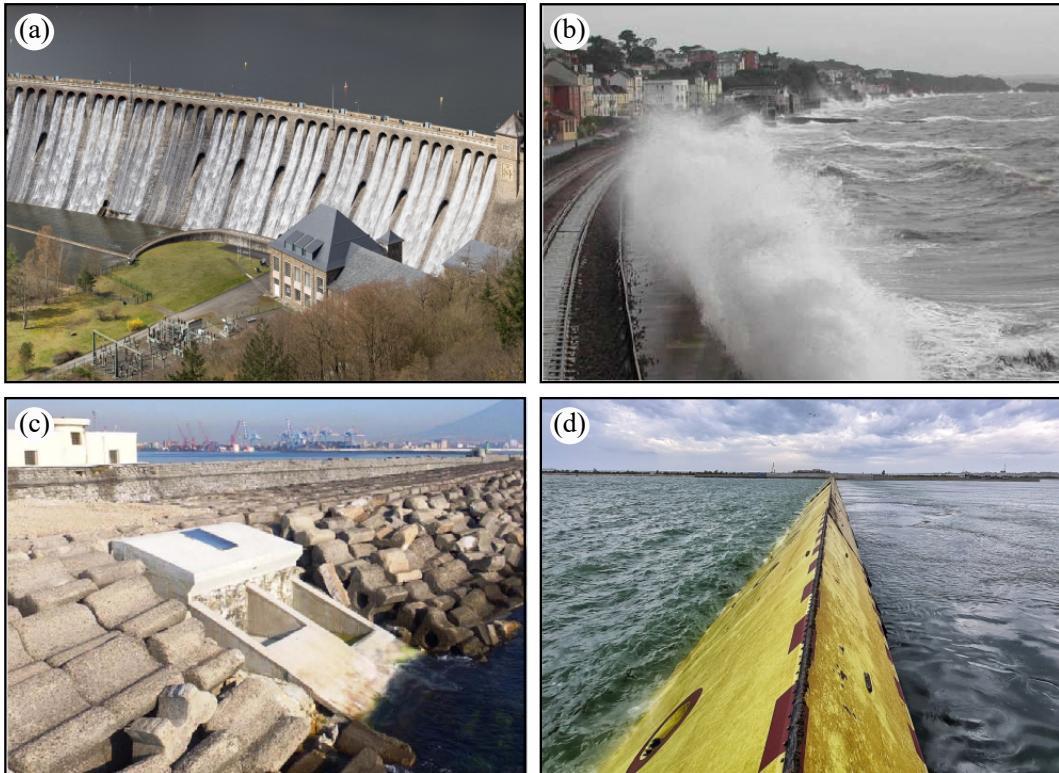


Figure 1.2. Examples of wave-structure interaction: (a) a hydro-power dam (Wikipedia, 2023), (b) wave impact on a vertical seawall (Allsop et al., 2008), (c) prototype of the OBREC wave energy converter (Contestabile et al., 2017) and (d) the MOSE mobile gate (Mose, 2023).

Unfortunately, the available prediction approaches for the tsunami forces and effects, e.g. run-ups and overtoppings, are still associated with large uncertainties (Ramsden, 1996; Heller et al., 2009; Evers et al., 2019), requiring further investigations. Furthermore, Three-Dimensional (3D) effects on the tsunami forces and run-ups are commonly neglected due to a lack of knowledge (Heller et al., 2009). These include the dam curvatures, asymmetrical wave impact angles and/or complex

reservoir geometries, potentially enhancing forces and run-ups (Müller, 1995).

For flexible structures undergoing significant deformations, referred to as Wave-Flexible Structure Interaction (WFSI) herein, the physical processes are even more complex. These concern deformable wave energy converters, e.g. the Anaconda (Chaplin et al., 2012), or slender structures such as wood coastal houses or offshore platforms. Previous studies revealed that the mechanical properties of the structure, e.g. the Young’s modulus, have an effect on the WFSI pressures and forces (He and Kashiwagi, 2012; Linton et al., 2013; Mai et al., 2020; Krautwald et al., 2022; Hu et al., 2023). However, current findings are inconclusive, such that an accurate understanding of the plate flexibility effect on wave loading is required.

Given the challenge to accurately model WFSI phenomena, laboratory tests are often used for research, to validate numerical models and to support design solutions. Smaller laboratory models are designed by downscaling all the relevant parameters according to appropriate scaling laws. However, they are typically characterised by scale effects, potentially leading to erroneous experimental results. For free-surface flows, scale effects commonly arise when ordinary water and air are used in the laboratory models. Scale effects can manifest themselves in various ways; for instance, they result in different void fractions (Catucci et al., 2021; 2023) and/or non-identical pressures in air-water flows (Fig. 1.3, Bredmose et al., 2015).

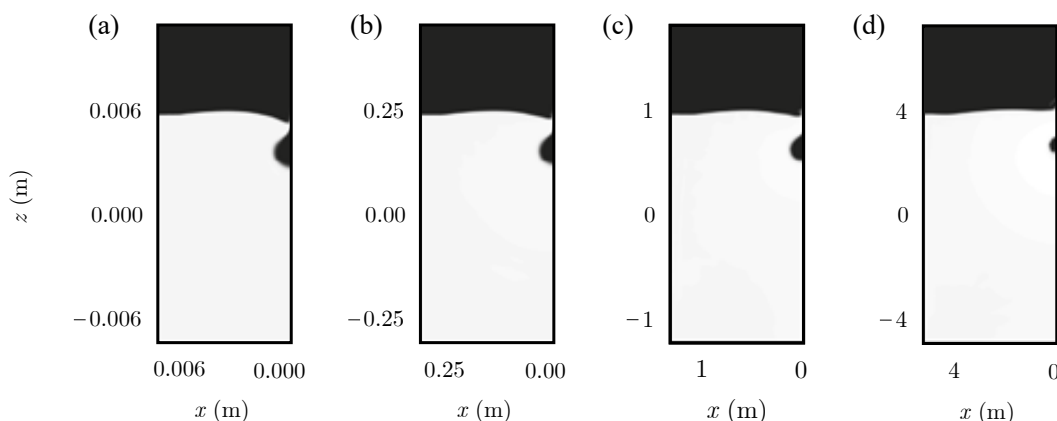


Figure 1.3. Scale effects in breaking wave impact on a rigid wall: snapshots of the wave impact at different geometrical scales (after Bredmose et al., 2015).

While scale effects have been largely investigated in free-surface flows interacting with rigid walls (Cuomo et al., 2010b; Blenkinsopp and Chaplin, 2011; Bredmose et al., 2015; Seiffert et al., 2015; Catucci et al., 2021; 2023), potential deformations of the structures have not been taken into account. In WFSI, the structural properties must also be appropriately scaled (Hughes, 1993; Chakrabarti, 2005; Heller, 2011; Krautwald et al., 2022; Abrahamsen et al., 2023), however, it might be challenging to find a material with the desired properties for the laboratory tests. Conversely, the incorrect scaling of the structural properties can lead to inaccurate predictions of the prototype behaviour, as was the case for the Sines breakwater, whose failure was partially due to an underdesign informed by misleading results from laboratory experiments (Fig. 1.1a).

Therefore, an improved understanding and further investigation of WSI, including both rigid and flexible structures, are necessary to support the design and assessment of offshore and onshore structures. For these reasons, the present thesis presents a systematic investigation of WSI based on numerical and laboratory modelling. This includes an extensive investigation of wave impacts on rigid and flexible structures, relying on both Two-Dimensional (2D) and 3D experiments. Furthermore, a systematic analysis of scale effects for wave impacts on rigid and flexible plates is provided.

1.2 Aims and objectives

The present thesis is aimed at systematically investigating WSI to enhance the physical understanding, support the design and assist laboratory investigations of offshore and onshore structures. These aims will be achieved with the following objectives:

- Design a laboratory set-up to investigate wave impacts on plates in the wave flume of the Department of Civil Engineering at the University of Nottingham.
- Perform laboratory experiments for a range of incident waves impacting rigid and flexible plates of various inclinations.

- Validate the numerical model `solid4foam` for WSI with analytical and other numerical results along with new and available laboratory experiments.
- Provide new physical insight into tsunamis impacting steep dams based on 2D and 3D numerical simulations.
- Expand the validation conditions of existing approaches and provide new empirical equations to predict tsunami forces, run-ups and overtoppings on dams.
- Formulate and validate a set of dimensionless governing parameters for WFSI.
- Provide new physical insight into regular and solitary waves impacting offshore and onshore plates of different stiffnesses.
- Formulate a new scaling approach for WFSI.
- Quantify and understand scale effects in WSI under different scaling approaches.

1.3 Thesis outline

The present thesis is comprised of 6 chapters; the current introduction, a literature review (Chapter 2), 3 chapters containing journal articles (Chapters 3, 4 and 5) and the conclusions (Chapter 6). The remainder of this thesis is organised as follows.

In Chapter 2 a comprehensive review of WSI is presented. This includes the theoretical background along with previous WSI numerical and experimental investigations. Studies of waves interacting with rigid and flexible structures are addressed with a main focus on the latter. The main aspects about the scaling of WSI phenomena are also included. These concern model-prototype similarity, traditional scaling laws and scale effects in WSI.

Chapter 3 is comprised of a published article (Attili et al., 2021), focusing on tsunami impacts on dams. After the validation of the numerical model, this chapter offers a detailed numerical investigation of a range of waves impacting dams of different inclinations. The 2D tsunami effects on the dam are discussed along with the 3D effects for some selected cases.

Chapter 4 covers a systematic investigation of wave impacts on rigid and flexible plates, consisting of a published article (Attili et al., 2023b). Further validation of the numerical model with available and new laboratory tests is included in this chapter. A comprehensive analysis of waves impacting offshore and onshore plates of different stiffnesses is then presented based on numerical modelling.

Scaling approaches and scale effects in WSI are then explored and discussed in Chapter 5. This chapter is comprised of an article currently under review for publication (Attili et al., 2023a). Several scaling laws along with a new scaling approach are investigated based on numerical modelling supported by small-scale laboratory experiments.

Finally, the main conclusions of the present thesis and potential directions for future work are discussed in Chapter 6. The appendices include supplementary data for the laboratory tests (Appendix A) and the numerical investigation of wave impact on a flexible wall conducted for the CCP-WSI (2021) comparative study 1 (Appendix B).

Given the structure of this thesis, there is some repetition between the chapters, concerning parts of the literature review and the description of the numerical and physical models. Although background information and previous studies are included in Chapters 3, 4 and 5, Chapter 2 is required to offer a more complete and extensive overview of the literature review. The nomenclature and reference list are provided at the end of this thesis.

This page was intentionally left blank.

Chapter 2

Literature review

2.1 Overview

This chapter presents a full review of analytical, laboratory and numerical Wave-Structure Interaction (WSI) studies. Given the structure of this thesis, further literature reviews are also included in Chapters 3, 4 and 5, however, these are more concise and include only selected studies. In Section 2.2, theoretical insight into wave theories and the analytical models for wave pressures and forces on vertical and rigid walls are presented. The most relevant laboratory and numerical WSI studies are then addressed in Section 2.3. Basic concepts of experimental modelling and scale effects are then presented in Section 2.4. Finally, the WSI review is summarised in Section 2.5 and the main research gaps are highlighted.

2.2 Theoretical background

2.2.1 Wave theories

Surface waves are deformations of the free water surface propagating across a water body. These may be generated by several causes, including the wind action on the water surface, the passage of a boat, an earthquake or a landslide. Based on the water depth h relative to the wave length L , they are classified into shallow, intermediate and deep-water waves. Shallow-water waves are typically observed near the shore,

where $h < L/20$. Deep-water waves occur in the open sea where $h > L/2$, such that the wave motion affects the top layers of the water body only. For $L/20 \leq h \leq L/2$, intermediate-water waves are observed.

Based on the water surface profiles, several mathematical theories have been developed. Cartesian coordinates (x, y, z) are used in the present study, with the origin at the still water level (Fig. 2.1). The x -axis is parallel to the wave propagation and positive in the wave propagation direction and the z -axis is defined positive upwards.

Airy (1845) derived the 2D wave profile of periodic waves, known as regular waves. For relatively small wave heights H ($H/h < 0.03$) and steepnesses ($H/L < 0.006$), these are commonly referred to as linear waves. The wave profile is described by a sinusoidal curve (Fig. 2.1a) with the water surface elevation

$$\eta(x, t) = \frac{H}{2} \cos(kx - \omega t). \quad (2.1)$$

In Eq. (2.1) t is the time, $k = 2\pi/L$ the wave number, $\omega = 2\pi/T$ the wave angular frequency, with the wave period T , and $a = H/2$ in Fig. 2.1a is the wave amplitude. For this wave type, the particle orbits at the surface are circular, with the centre at $z = 0$ and no mass transport is observed. The sinusoidal wave celerity is given by

$$c = \sqrt{\frac{gL}{2\pi} \tanh\left(\frac{2\pi h}{L}\right)}. \quad (2.2)$$

Fig. 2.1b shows the wave profile of a 2nd order Stokes wave. Stokes wave profiles are typically expressed by a power series of H . The linear term is identical to the linear wave (Eq. 2.1) and the higher order terms are expressed in function of H , L and T . According to Dean and Dalrymple (1991), 2nd order Stokes waves are described as

$$\eta(x, t) = \frac{H}{2} \cos(kx - \omega t) + \frac{H^2 k}{16} \frac{\cosh(kh)}{\sinh^3(kh)} [2 + \cosh(2kh)] \cos(2kx - 2\omega t). \quad (2.3)$$

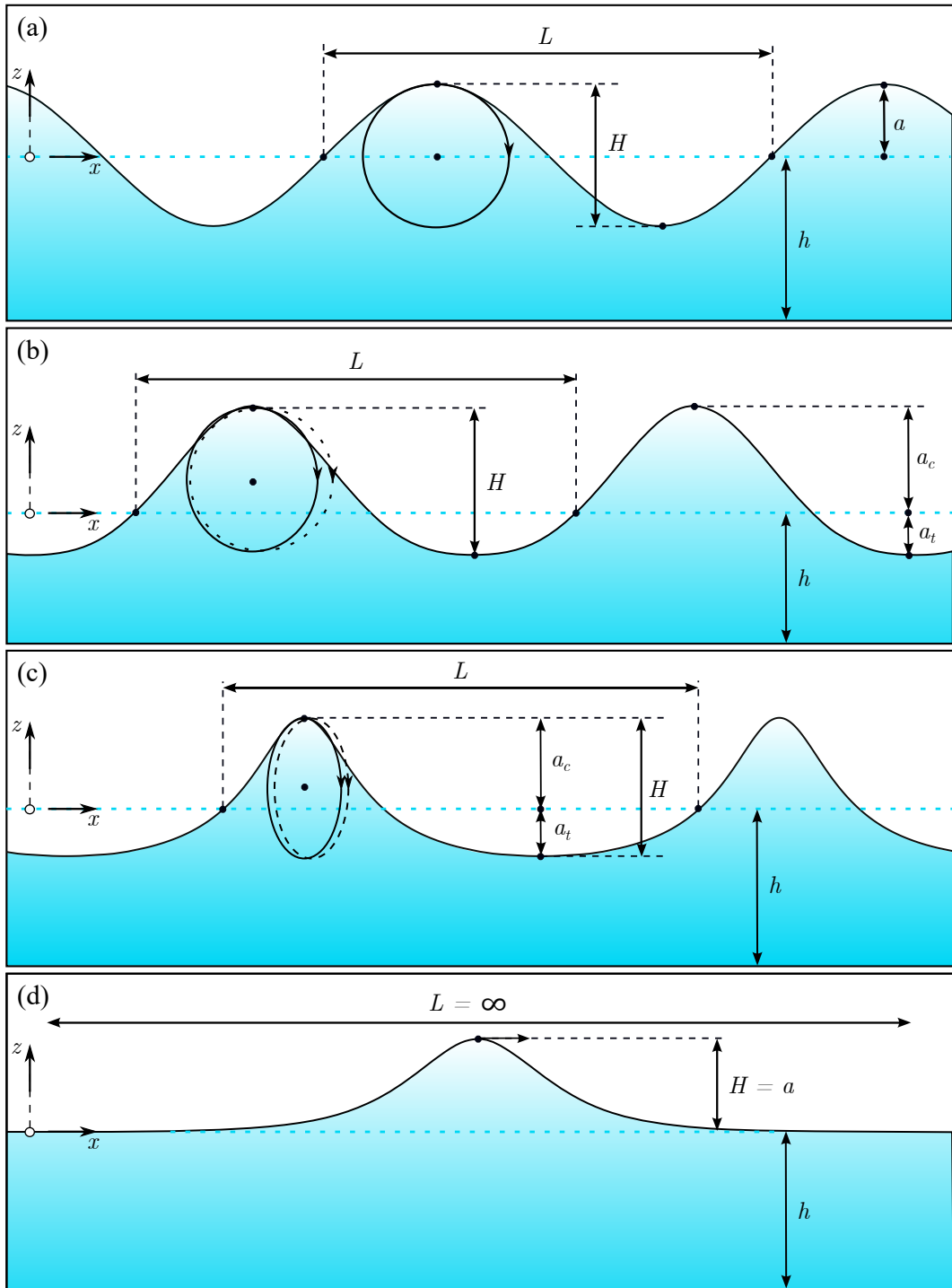


Figure 2.1. Water surface elevation with main parameters and orbit of a surface particle for (a) linear, (b) 2nd order Stokes, (c) cnoidal and (d) solitary wave theories.

Cnoidal waves (Fig. 2.1c) are typically used to model extreme waves, e.g. tsunamis. They are characterised by sharper crests (subscript c) a_c and flatter troughs (subscript t) a_t compared to linear waves, being strongly nonlinear. According to Dingemans (1997), η is expressed as

$$\eta(x, t) = a_t + H \operatorname{cn}^2 \left(2K_e(m) \frac{x - ct}{L} |m| \right), \quad (2.4)$$

with the elliptic function cn and the complete elliptic integral of the first kind $K_e(m)$. These functions depend on the elliptic parameter m , which determines the shape of the cnoidal wave.

Finally, Fig. 2.1d shows a solitary wave profile. Solitary waves do not have troughs and are purely translatory, involving significant fluid mass transport. The wave profile can be expressed as (Boussinesq, 1871)

$$\eta(x, t) = a \operatorname{sech}^2 \left(\sqrt{\frac{3a}{4h^3}} (x - ct) \right). \quad (2.5)$$

The solitary wave celerity c (Laitone, 1960) and L (Lo et al., 2013) are commonly approximated as

$$c = \sqrt{g(h + a)}, \quad (2.6)$$

$$L = \frac{2\pi h}{\sqrt{0.75 \frac{a}{h}}}. \quad (2.7)$$

2.2.2 Analytical models for wave loading on a rigid plate

Analytical models (Sainflou, 1928; Tadjbakhsh and Keller, 1960) have been derived to describe the wave pressures on vertical and rigid walls. These were expressed in terms of the wave pressure exceeding the hydrostatic rate (Dean and Dalrymple, 1991)

$$p_d(z) = \begin{cases} p(z) & \text{for } 0 < z \leq \eta \\ p(z) + \rho_w g z & \text{for } -h \leq z \leq 0 \end{cases} \quad (2.8)$$

with the pressure p , the water (subscript w) density ρ_w and the gravitational acceleration g . Sainflou (1928) developed a mathematical formulation of $p_d(z)$ due to nonlinear waves impacting a rigid wall. This model was based on the trochoidal wave theory (Gerstner, 1802), assuming a complete wave reflection from the wall. At the

maximum wave elevation $z = H + r_0$, $p_d(z) = 0$ (Fig. 2.2a), with the elevation of the orbit centre after a full reflection

$$r_0 = \frac{\pi H^2}{L} \coth(2\pi h/L). \quad (2.9)$$

For reducing z , $p_d(z)$ linearly increases up to the maximum value

$$p_{d,2} = \frac{(\rho_w g h + p_{d,1})(r_0 + H)}{H + r_0} + h \quad (2.10)$$

at $z = 0$, with the pressure at the sea bed ($z = -h$) $p_{d,1}$. For $z < 0$, $p_d(z)$ decreases with increasing depth reaching

$$p_{d,1} = \frac{\rho_w g H}{\cosh(2\pi h/L)} \quad (2.11)$$

at $z = -h$.

Tadjbakhsh and Keller (1960) proposed a theoretical solution for $\eta(x, t)$ and $p_d(z)$ for gravity wave impacts on a rigid wall. This model was derived under the assumptions of inviscid and incompressible fluid and periodical waves, both in time and horizontal direction, with a finite h . The dimensionless $\eta(x, t)$ due to the incident and reflected waves was expressed as

$$\begin{aligned} \varepsilon_p k \eta = & \left[\varepsilon_p + \frac{\varepsilon_p^3}{256} (9\omega_0^{-8} + 6\omega_0^{-4} - 15 + 8\omega_0^4) \right] \cos(kx) + \\ & + \frac{1}{8} \varepsilon_p^2 (\omega_0^{-2} + 3\omega_0^{-6}) \cos(2kx) + \\ & + \frac{3}{256} \varepsilon_p^3 (9\omega_0^{-12} + 6\omega_0^{-8} + 30\omega_0^{-4} - 16 + \omega_0^4 + 2\omega_0^8) \cos(3kx), \end{aligned} \quad (2.12)$$

with $\varepsilon_p = kH$ and $\omega_0 = \sqrt{\tanh kh}$.

Based on Bernoulli's equation, the distribution of $p_d(z)$ at the wall was derived as

$$\begin{aligned} \frac{k}{\rho_w g} p_d = & \left[\varepsilon_p + \frac{\varepsilon_p^3}{256} (9\omega_0^{-8} - 234\omega_0^{-4} + 81 - 8\omega_0^4) \right] \frac{\cosh(kz + kh)}{\cosh kh} - \\ & \varepsilon_p^2 \left[\frac{1}{2}\omega_0^2 + \frac{3}{8}(\omega_0^2 - \omega_0^{-6}) \right] \frac{\cosh 2(kz + kh)}{\cosh 2kh} + \quad (2.13) \\ & \frac{\varepsilon_p^3}{256} (1 + 3\omega_0^4) (27\omega_0^{-12} - 63\omega_0^{-8} + 39\omega_0^{-4} - 5 + 2\omega_0^4) \frac{\cosh 3(kz + kh)}{\cosh 3kh}. \end{aligned}$$

Fig. 2.2b shows $p_d(z)$ for $\varepsilon_p = 0.11$ and $\omega_0 = 0.75$. The solution $p_{linear} = \varepsilon_p[\cosh(kz + kh)]/\cosh kh$ takes only the linear term of Eq. (2.13) into account while $p_{nonlinear}$ was computed with Eq. (2.13). This model has been extended up to the 4th order by Goda (1967).

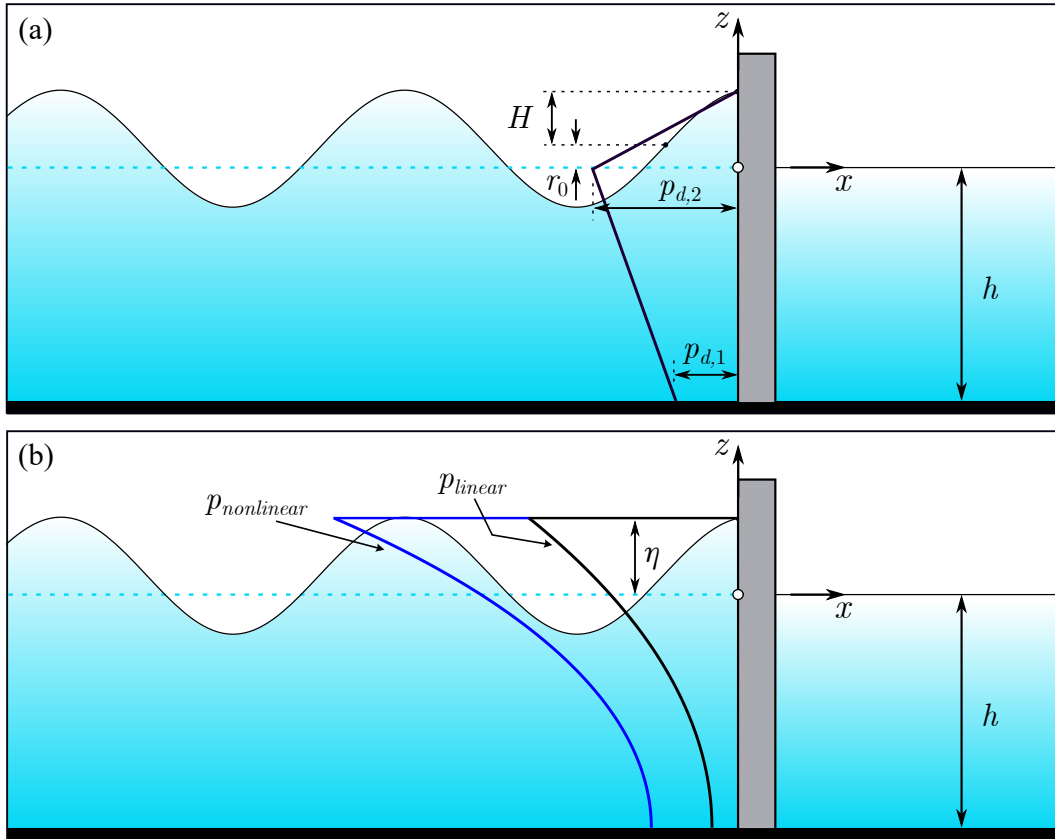


Figure 2.2. Analytical wave pressure on a vertical wall: (a) from the theory of Sainflou (1928) and (b) the solution of Tadjbakhsh and Keller (1960) with $\varepsilon_p = 0.11$ and $\omega_0 = 0.75$.

While the models of Sainflou (1928) and Tadjbakhsh and Keller (1960) were developed for unexceptional events, e.g. wind waves, Cross (1967) considered more

extreme waves, such as tsunamis transforming into surges. The impact force due to a surge was expressed as (Cross, 1967)

$$F_I = \frac{1}{2}\rho_w g h_s^2 + C_f \rho_w h_s \bar{u}_s^2, \quad (2.14)$$

with the shore (subscript s) water depth h_s , the depth-averaged shore velocity \bar{u}_s and the coefficient related to the inclination of the free water surface C_f . Eq. (2.14) was derived by imposing the conservation of momentum, where the terms $\frac{1}{2}\rho_w g h_s^2$ and $\rho_w h_s \bar{u}_s^2$ take the hydrostatic and dynamic forces into account. Cross (1967) suggested to evaluate C_f as

$$C_f = (\tan \theta)^{1.2} + 1, \quad (2.15)$$

where $\theta = dh/dx$ is the inclination of the free water surface. For a uniform flow, where the free water surface is parallel to the shore, $C_f = 1$. From the comparison with experimental measurements, it was found that $C_f = 1$ can be used for $\theta \leq 15^\circ$. Instead, for a sharper water surface C_f should be evaluated with Eq. (2.15) (Cross, 1967).

2.3 Previous work

2.3.1 Laboratory findings

The most relevant WSI laboratory investigations are presented in this section. The majority of these studies have been conducted to validate and calibrate numerical models. Laboratory investigations involving rigid walls will be presented first (Section 2.3.1.1). These include only a few relevant studies as Wave-Flexible Structure Interaction (WFSI) is the main interest of the present study. Laboratory experiments with flexible plates are then presented in Section 2.3.1.2.

2.3.1.1 Rigid walls

Several studies have been undertaken to investigate wave impacts on rigid walls. These focused on the wave run-ups, overtoppings, pressures and forces, being funda-

mental parameters for the design of dams and other coastal and offshore structures. Only a few of these studies have been performed in a wave basin (3D), with the majority conducted in a wave flume (2D). Pertinent research about wave run-ups and overtoppings is covered first, followed by the studies of wave pressures and forces.

Hall and Watts (1953), Street and Camfield (1967) and Maxworthy (1976) conducted experiments of solitary wave run-up on a wall within the investigated ranges of a/h and wall inclination β shown in Table 2.1 (Fig. 2.3a). The measured run-up heights R were approximated by Hall and Watts (1953) as a function of a, h and β only. However, this prediction equation cannot be used for vertical walls ($\beta = 90^\circ$) as the tangent of 90° is undefined. No prediction equations have been suggested by Street and Camfield (1967) and Maxworthy (1976).

Müller (1995) conducted more than 700 experiments to investigate the run-up of solitary waves on dams, both in 2D and 3D. This study offered a valid prediction approach, based on a wide range of the investigated parameters (a/h and β , Table 2.1). Additionally, asymmetrical wave impact angles and non-rectangular reservoir sections have been qualitatively explored based on 3D experiments.

Table 2.1. Prediction equations and limitations for the relative run-up height R/h in previous studies.

Reference	R/h	Limitations
Hall and Watts (1953)	$3.05 \tan(\beta)^{-0.13} \left(\frac{a}{h}\right)^{1.15 \tan(\beta)^{0.02}}$	$0.050 \leq a/h \leq 0.564$, $10^\circ \leq \beta \leq 45^\circ$
Street and Camfield (1967)	No empirical equation available	$0.100 \leq a/h \leq 0.645$, $\beta = 90^\circ$
Maxworthy (1976)	No empirical equation available	$0.118 \leq a/h \leq 0.665$, $\beta = 90^\circ$
Müller (1995)	$1.25 \left(\frac{H}{h}\right)^{5/4} \left(\frac{H}{L}\right)^{-3/20} \left(\frac{90^\circ}{\beta}\right)^{1/5}$	$0.011 \leq a/h \leq 0.521$, $18.4^\circ \leq \beta \leq 90^\circ$
Evers and Boes (2019)	$2 \frac{a}{h} \exp\left(0.4 \frac{a}{h}\right) \left(\frac{90^\circ}{\beta}\right)^{0.20}$	$0.007 \leq a/h \leq 0.690$, $10^\circ \leq \beta \leq 90^\circ$

In an attempt to provide a unique and reliable prediction approach for non-breaking solitary and impulse wave run-ups, Evers and Boes (2019) suggested a new

equation based on 359 experiments from previous studies (Table 2.1). Their equation predicts the laboratory R with less than 20% deviation, while previous equations tend to underestimate R for $a/h < 0.1$.

When R is greater than the available freeboard f , wave overtoppings are observed (Fig. 2.3). These are relevant for either dams (Fig. 2.3a), with potentially disastrous consequences, or onshore structures, such that the waves overtop the shore transforming into overland flows (Fig. 2.3b). Fuchs and Hager (2015) performed 2D laboratory experiments in a 0.50 m (width) \times 11.00 m (length) \times 1.00 m (depth) wave flume to investigate the transformation of solitary waves into overland flows. Several experiments have been conducted with the investigated ranges of $0.1 \leq a/h \leq 0.7$, relative shore freeboards $0.04 \leq z_f/h \leq 0.56$ and shore inclinations $11^\circ \leq \beta_s \leq 34^\circ$. The overland flow depth h_s and velocity u_s were expressed as

$$h_s = h_{s0} \left\{ 1 - \tanh \left[0.54 \left[\frac{x_{of}}{z_f + h} \left(\frac{z_f + h}{h} \right)^{5.3 \tan \beta - 1.4} \right]^{0.39} \right] \right\} \text{ and} \quad (2.16)$$

$$u_s = 1.6c \tanh \left[2.2 \left(\frac{a_{eff}}{z_f + h} \right)^{0.75} \right], \quad (2.17)$$

with the streamwise overland flow coordinate x_{of} (Fig. 2.3b), the overland flow depth at $x_{of} = 0$

$$h_{s0} = \frac{(0.4 \tan \beta_s + 0.9)a_{eff}}{[(z_f + h)/h]^{0.45 \cot \beta_s}} \quad (2.18)$$

and the effective wave amplitude

$$a_{eff} = a - \frac{z_f (\tan \beta_s)^{0.05}}{3}. \quad (2.19)$$

These equations can be complemented with the model of Cross (1967) (Eq. 2.14) to evaluate surge forces on onshore structures.

2D overtopping of dams has been recently investigated by Kobel et al. (2017) in a 0.50 m (width) \times 11.00 m (length) \times 1.00 m (depth) wave flume. The wave overtopping volume Ψ and the maximum overtopping depth over the dam crest d_0

were measured with a high-speed camera. Solitary waves with $0.1 \leq a/h \leq 0.7$ and dam inclinations $\beta = 18.4, 45.0$ and 90.0° were investigated. The laboratory data were approximated as

$$\Psi = 1.35 \left(\frac{a}{H} \right)^{1.5} \left[\frac{a}{h} \left(\frac{h}{l} \right)^{(2h/a)(\beta/90^\circ)^{0.25}} \left(\frac{a-f}{s} \right)^{0.12} \right]^{0.7} h^2 \text{ and} \quad (2.20)$$

$$d_0 = 1.32 \left[\frac{a}{h} \left(\frac{h}{l} \right)^{4[(\beta/90^\circ)^{-0.21} - a/h]} \left(\frac{\beta}{90^\circ} \right)^{0.16} \right] l, \quad (2.21)$$

with the dam height l and thickness s . However, Eq. (2.20) can be applied for $a > f$ only.

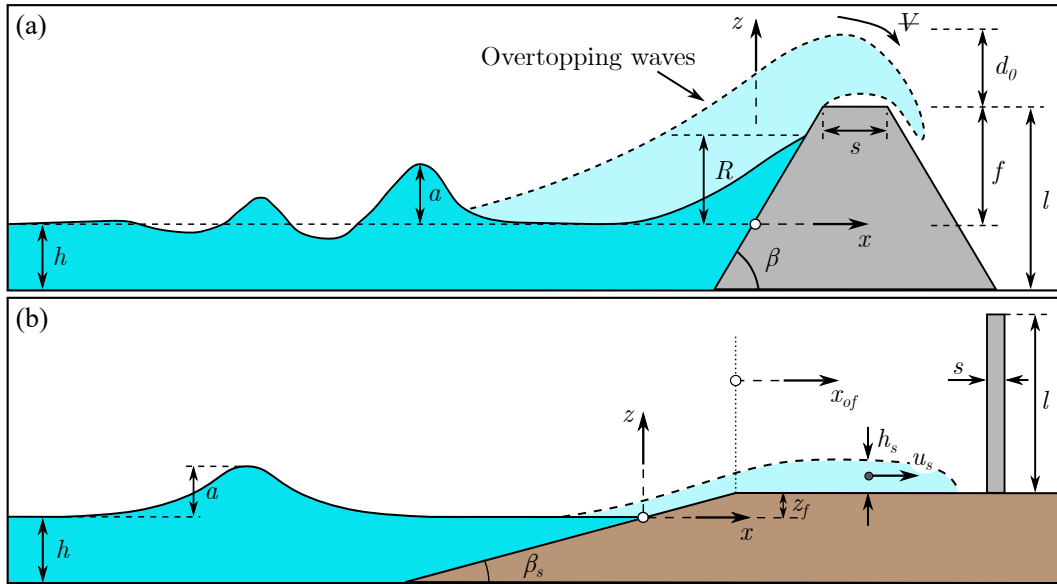


Figure 2.3. Sketches with the main parameters for (a) wave run-up and overtopping of a dam and (b) solitary wave transformation to overland flow.

Selected studies (Mallayachari and Sundar, 1995; Ramsden, 1996; Didier et al., 2014) about wave impact pressures and forces are addressed hereafter. Mallayachari and Sundar (1995) conducted 2D experiments in a 0.30 m (width) \times 10.00 m (length) wave flume with $h = 0.315$ m (Fig. 2.4). The wave flume was equipped with a paddle-type wave maker and a 4.5 mm thick plastic plate, which was located approximately 9 m downwave of the wave maker. The plate was supported by a steel structure and equipped with 4 pressure transducers. Experiments involved regular and random

waves with $0.53 \text{ s} \leq T \leq 1.25 \text{ s}$ and maximum (subscript *max*) $H_{max} = 0.10 \text{ m}$. The measured p at the plate was successfully compared with the solution of Tadjbakhsh and Keller (1960) in a few experiments (Section 3.3.1.1).

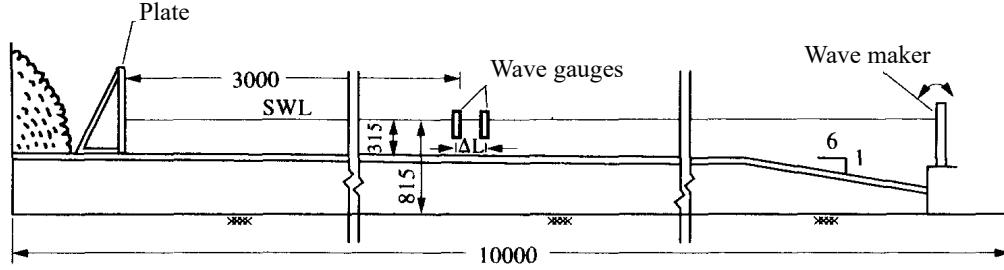


Figure 2.4. Side view of the experimental set-up from Mallayachari and Sundar (1995).

Ramsden (1996) conducted laboratory tests in a 0.396 m (width) \times 36.600 m (length) \times 0.610 m (height) wave tank. The solitary wave horizontal (subscript H) forces F_H and bending moments M_H on a vertical wall were measured. These measurements were approximated by Evers et al. (2019), taking over the concepts introduced in the first version of the manual Heller et al. (2009), as

$$F_H = [1 - 1.5(a/h)]^{1/6} (1/2) \rho_w g (2a + h)^2 \text{ and} \quad (2.22)$$

$$M_H = [1 - 1.5(a/h)]^{1/6} (1/6) \rho_w g (2a + h)^3. \quad (2.23)$$

A triangular distribution of the pressure was assumed at the plate, as

$$p(z) = [1 - 1.5(a/h)]^{1/6} \rho_w g (2a - z). \quad (2.24)$$

Eqs. (2.22) and (2.23) are valid for $0.0 \leq a/h \leq 0.6$ and rely on a few experiments only. For overtopping waves, Eq. (2.24) was reduced to a trapezoidal distribution by disregarding the triangular section above the dam crest. This resulted in the reduced (subscript *red*) force

$$F_{H,red} = \frac{(h + f)}{2} \left[p_K + \frac{2F_H}{2a + h} \right] \quad (2.25)$$

where F_H is given from Eq. (2.22) and p_K is the pressure at the dam crest

$$p_K = \frac{2F_H}{(2a+h)^2}(2a-f). \quad (2.26)$$

More recently, Didier et al. (2014) conducted experiments of waves interacting with a offshore breakwater in a 1.60 m (width) \times 49.40 m (length) \times 1.20 m (height) wave flume. The flume was equipped with a piston-type wave maker, resistance-type wave gauges and pressure sensors at the front of the breakwater. Experiments involved several wave conditions with $H = 0.10$ m, $T = 1.30$ s and $0.266 \text{ m} \leq h \leq 0.325$ m. The time series of F_H at the wall showed a first peak of relatively short duration, followed by a second peak due to the collapse of the water column. These experiments were specifically designed to validate a particle-based numerical model (Fig. 2.11).

2.3.1.2 Flexible walls

The dam break wave involving an elastic plate (Antoci et al., 2007) and the dam break wave impacting a flexible obstacle (Liao et al., 2015) represent two of the most significant WFSI benchmark cases. Antoci et al. (2007) used a tank with an elastic gate fixed at the top end and free at the bottom end (Fig. 2.5a). The tank was filled with water of depth $h = 0.140$ m and an external support was used to close the gate. The external support was suddenly removed allowing the gate to deform under the water flow. Large deformations of the gate were observed, with the maximum displacements occurring near the top end.

Liao et al. (2015) conducted a series of quasi 2D tests in a 0.60 m (height) \times 0.20 m (width) \times 0.80 m (length) wave tank (Fig. 2.5b). A water column was confined at the upwave side of the tank and an elastic plate was located 0.20 m from the downwave side. This consisted of silicon rubber with solid (subscript s) density $\rho_s = 1161.54$ kg/m³ and Young's modulus $E = 3.50$ MPa. Experiments consisted in abruptly lifting the gate with $h = 0.2, 0.3$ and 0.4 m, generating a dam break wave.

During the initial stage of the wave impact, the plate showed the largest displacement at the top end with a first mode of vibration. After the wave was reflected by the downwave side, higher modes of vibration were observed with decreasing displacements. These 2 studies have been widely used to validate WFSI numerical models (Section 2.3.2).

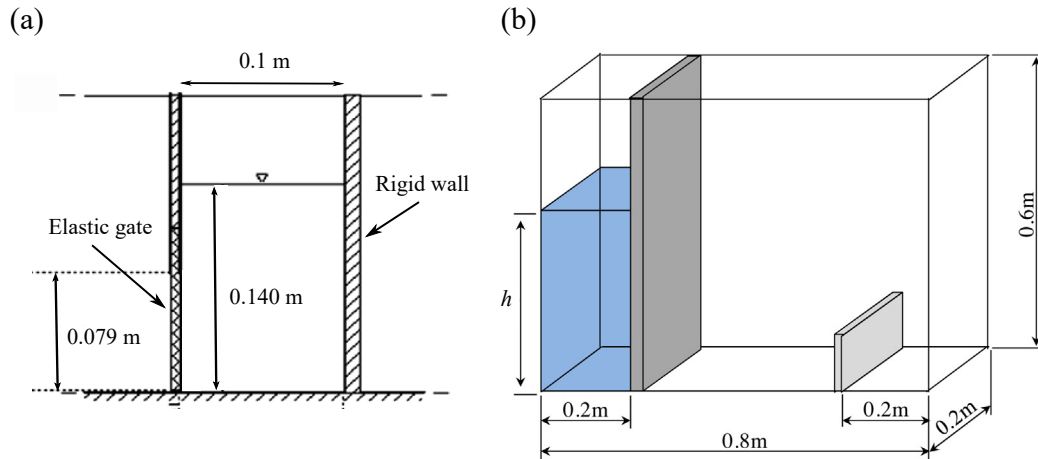


Figure 2.5. Dam break wave: (a) side view of the tank with elastic gate experiment from Antoci et al. (2007) and (b) overview of the experiments of Liao et al. (2015).

Kimmoun et al. (2009) conducted a laboratory investigation of solitary waves impacting plastic plates. The set-up consisted of a wave flume with a 1:15 sloped shore and a 1.00 m high plate (Fig. 4.12a). A range of a and plate thicknesses s were investigated. Wave breaking occurred in proximity of the plate in most tests, leading to a challenging wave-plate interaction. Snapshots of the wave impact and the plate deformation were recorded, establishing a new database for the validation of numerical models. However, the data were published only partially and the wave force on the plate was not measured.

Large-scale experiments have been conducted by Linton et al. (2013) to investigate tsunamis interacting with wood walls. As shown in Fig. 2.6, the set-up consisted of a 28.6 m flat section with a 1:12 sloped shore followed by an horizontal shore where the wall was located. Different timber sizes and spacings were used to reinforce the wall, resulting in 3 configurations. Solitary waves with $0.09 \text{ m} \leq a \leq 1.04 \text{ m}$ were

investigated. Transient and quasi-static F were observed in each experiment. The transient F was defined as the force occurring shortly after the initial impact. The quasi-static F was calculated as the average value over 1 s, starting 0.5 s after the transient force was observed. Larger a resulted in larger F , following a linear trend. A good agreement between Eq. (2.14) and the transient experimental F was observed. The most deformable wall configuration resulted in approximately 25% smaller F than the stiffest configuration.

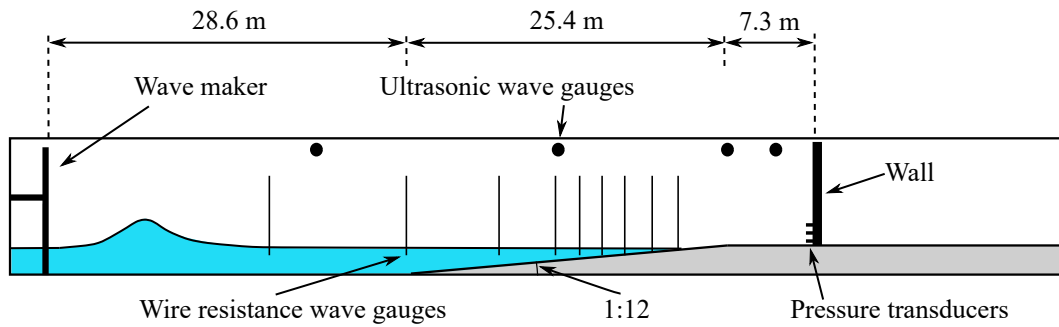


Figure 2.6. Side view of the experimental set-up with location of the measurement systems in the study of Linton et al. (2013).

Mai et al. (2020) investigated the effects of the structure elasticity in water-structure impacts. Tests of a plate impacting onto a water surface and waves impacting a vertical plate have been conducted. The plates were designed to be fixed to the support frames or connected by springs, mimicking rigid and flexible conditions. It is important to note that different structure elasticities have been modelled by changing the boundary conditions of the support frame (Mai et al., 2020), rather than the plate elasticity, e.g. Young's modulus, as in the present and other studies.

Under both the rigid and flexible conditions, the stiffness of the structure had an effect on F . Smaller impact F were observed for the elastic plate impacting onto a water surface compared to the rigid one at high impact velocities.

For wave impact on a vertical plate, the elastic plates resulted in smaller F than the rigid ones for high aeration condition. On the other hand, for slightly breaking waves, larger p were observed for the elastic plates.

Further investigation of waves impacting buildings of different stiffnesses was

conducted by Krautwald et al. (2022). Large-scale experiments of wave impacts on onshore rigid and elasto-plastic structures were performed to investigate the structural collapse under extreme waves. For small offshore wave heights, F on rigid and elasto-plastic structures showed similar values. For larger offshore wave heights and consequently larger F , the elasto-plastic structure showed smaller F during the first stage of the impact. In the second stage of the impact, similar F were observed for the different structures, with the rigid one not necessarily resulting in the largest F .

2.3.2 Numerical findings

Given the reliability and maturity of Computational Fluid Dynamics (CFD) and Computational Structural Dynamics (CSD), numerical modelling has been largely applied to WFSI phenomena in the last decade. The fluid and solid governing equations are solved within a unique solver in the monolithic approaches (Rao et al., 2017; Liu and Zhang, 2019). These are characterised by higher accuracy and robustness compared to partitioned approaches, however, at higher computational cost. Partitioned techniques consist in coupling the fluid and solid domains through an exchange of information at the fluid-solid interface (Sotiropoulos and Yang, 2014). This is generally performed by imposing continuity of displacements, velocity and equilibrium of stresses at the interface. Although they may be less accurate than monolithic approaches, partitioned approaches are more efficient and existing CFD and CSD solvers can be used.

Both mesh-based, e.g. Finite Element Method (FEM, Hartmann and Katz, 2004) and Finite Volume Method (FVM, Tuković et al., 2018), and mesh-free methods, e.g. Smoothed Particle Hydrodynamics (SPH, Didier et al., 2014) and Moving Particle Semi-implicit (MPS, Rao et al., 2017), have been applied to WSI. Mesh-based methods are highly reliable for both CFD and CSD and computationally efficient. However, they may be inaccurate for large deformations. On the other hand, mesh-free approaches can tackle large deformations efficiently. However, they may be computationally expensive and less accurate for the structural analysis compared to mesh-

based methods (Kumar et al., 2015; Liu and Zhang, 2019). Mesh-based and -free approaches have also been combined to minimise the disadvantages of each. This takes the advantages of each approach, however, making the fluid-solid coupling even more challenging, with particular emphasis to the energy balance at the interface (Degroote, 2013).

2.3.2.1 Mesh-based models

He and Kashiwagi (2012) investigated nonlinear waves interacting with a vertical plate based on a newly developed numerical model. This consisted of a Mixed Eulerian Lagrangian (MEL) method for the fluid and FEM for the solid within a monolithic coupling. After validation with an analytical and another numerical model, solitary waves impacting plates with different stiffnesses have been simulated. The numerical results showed that the hydroelastic behaviour was strongly influenced by the plate stiffness and support conditions.

Liao et al. (2015) developed a Finite Difference Method FDM coupled with a FEM approach to model free surface flows interacting with elastic structures. The fluid was solved with the FDM and FEM was adopted for the structural analysis with a moving Lagrangian framework. The coupling was performed by transferring the fluid forces to the structure first. The solid was then solved and its displacements were used to update the fluid. This model was successfully validated with a dam break wave impacting a flexible plate (Figs. 2.7 and 2.13).

Given the reliability, maturity and flexibility of OpenFOAM (OF), several WFSI codes have been developed in the OF framework (Higuera et al., 2013; Chen et al., 2014; Higuera et al., 2014; Hu et al., 2016; Rege and Hjertager, 2017; Martínez-Ferrer et al., 2018; Tuković et al., 2018; Cardiff et al., 2018; Chen et al., 2019; Chen et al., 2020; Romano et al., 2020; Di Paolo et al., 2021; Wang et al., 2023). To be concise, only a few of the OF studies will be presented hereafter.

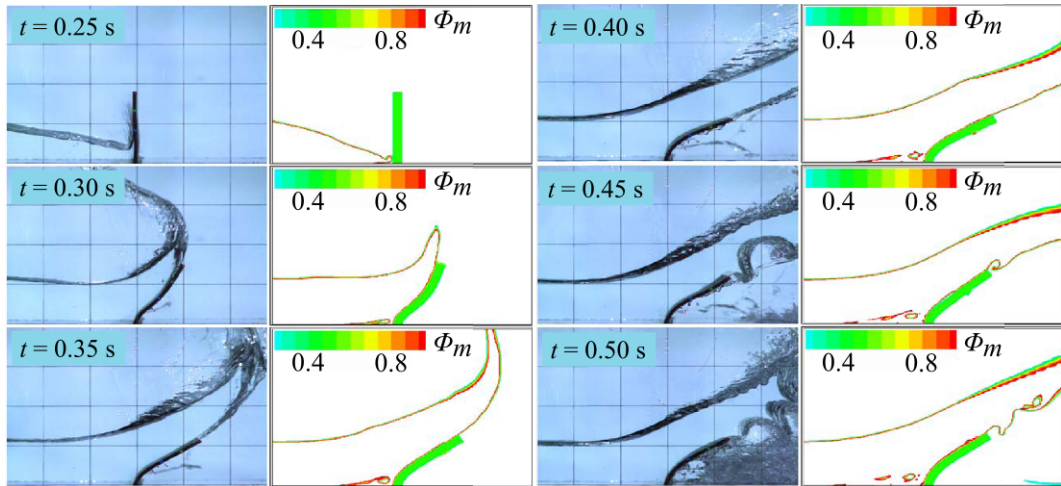


Figure 2.7. Comparison between experimental and numerical results of a dam break wave impacting a flexible plate (Liao et al., 2015). The colour function ϕ_m denotes the water, air and solid phases.

Chen et al. (2014) and Hu et al. (2016) implemented new boundary conditions in OF for the generation of regular, random and focused waves. Both models have been successfully validated with ad hoc experiments of waves interacting with cylinders. However, the structural analysis was not provided.

Tuković et al. (2018) developed the fluid-solid toolbox fsifoam implemented in Foam-Extend (FE, OpenFOAM extension, 2016). The fluid and solid domains were solved with FVM with a partitioned coupling approach. This consisted of imposing kinematic and dynamic boundary conditions at the fluid-solid interface. The accuracy of the structural analysis has been successfully verified with the analytical solution for a uniformly loaded plate with a circular hole. This toolbox was employed by Rege and Hjertager (2017) to investigate vibrations of a flexible structure due to turbulent flows, showing the capability of fsifoam to model such complex phenomena.

Chen et al. (2020) and Romano et al. (2020) developed new approaches in the OF framework for the modelling of moving bodies interacting with a water basin. Chen et al. (2020) presented a novel numerical methodology based on the Immersed Boundary Method (IBM). This was validated with large-scale laboratory experiments of tsunamis generated by iceberg calving (Heller et al., 2021). A new 3D model based on the overset mesh technique was presented and validated by Romano et al. (2020).

Di Paolo et al. (2021) also proposed a multi-domain method for the simulation of WFSI phenomena in OF. The computation domain was divided into subdomains where the governing equations are solved, with the benefit of reducing the computational time.

Hu et al. (2023) suggested a fully-coupled WFSI numerical model implemented in FE. This model combined the IHFOAM toolbox (Higuera et al., 2013) for the wave modelling with an available fluid-solid coupling approach (Tuković et al., 2018; Cardiff et al., 2018). After validation with numerical and laboratory observations, nonlinear waves interacting with flexible plates have been investigated. A range of wave and plate parameters have been modelled to provide insight into the effect of the structural elasticity on the wave run-up, force and reflection. It has been found that the wave reflection is reduced for more flexible plates, with smaller F on the flexible compared to the rigid plates. Empirical equations were also suggested to predict wave run-ups R and F , taking the plate flexibility into account.

2.3.2.2 Coupled mesh-based and mesh-free models

Kumar et al. (2015) developed a coupled FVM-SPH to solve free surface flows with large deformations. This model was implemented in OF and did not provide the structural analysis. The entire domain was solved with FVM first and SPH was then applied to optimise the solution where FVM may be inaccurate. The FVM-SPH coupling was performed by locating the SPH particles at the centre of the FVM cells and estimating their density from the p at the corresponding cells. This model was successfully validated with a dam break experiment (Colagrossi and Landrini, 2003).

Solitary waves interacting with elastic structures have been investigated by Rao et al. (2017) with a MPS-FEM approach based on a partitioned coupling approach. The model was validated with experimental observations of a dam break wave involving an elastic gate, as shown in Fig. 2.8. Solitary waves impacting rigid and flexible plates were investigated then. The flexible plate showed smaller and delayed F_{max} compared to the rigid one.

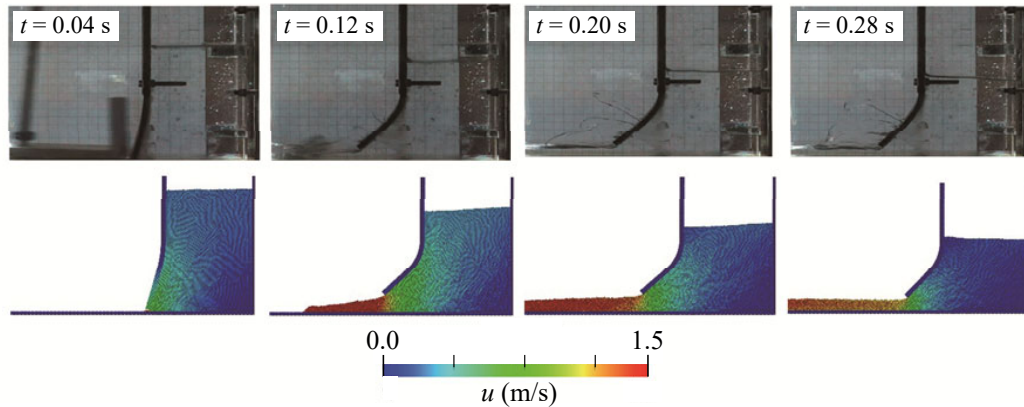


Figure 2.8. Validation of the numerical model of Rao et al. (2017) with a dam break laboratory experiment (Antoci et al., 2007).

Zhang et al. (2019a) proposed a partitioned coupled MPS-FEM model. The coupling was performed by transferring the solid displacements to the fluid and the fluid forces to the solid. Additional layers of fluid and solid ghost particles were used to guarantee an accurate pressure field at the interface. A novel hybrid approach combining a Lagrangian Smoothed FEM (S-FEM) with a particle method was developed by Zhang et al. (2019b). S-FEM was applied to solve both the fluid and solid domains in the first stage of the simulation. The regions of fluid with large deformations were then modelled with a Decoupled Finite Particle Method (DFPM). This model was validated with the experiment of Antoci et al. (2007), as shown in Fig. 2.9.

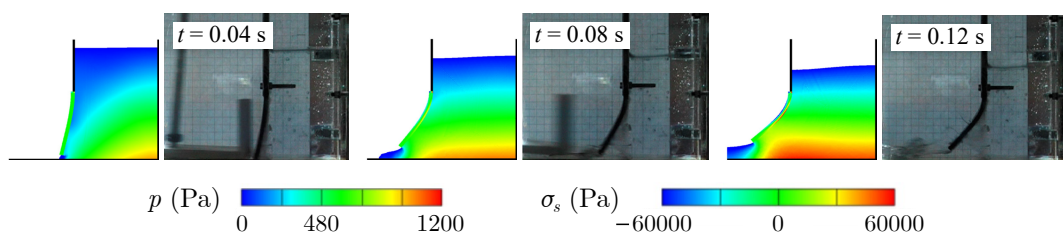


Figure 2.9. Comparison between the experiment of Antoci et al. (2007) and numerical results of Zhang et al. (2019b), showing the pressure p and stress σ_s fields.

2.3.2.3 Mesh-free models

Antoci et al. (2007) validated an in-house SPH model based on their dam break experiment. Both the fluid and solid were solved with SPH imposing kinematic and

dynamic boundary conditions at the interface. The numerical model captured the gate deformation and the evolution of the flow well, however, the gate displacements were slightly overpredicted (Fig. 2.10).

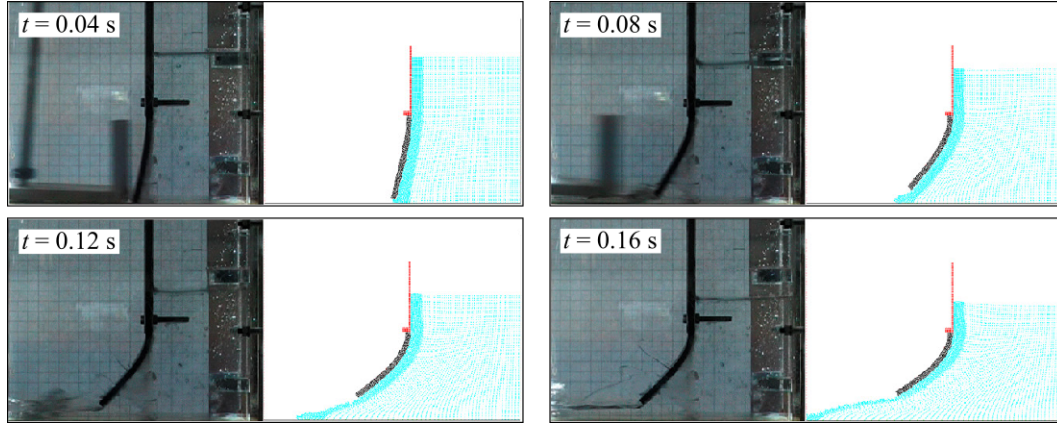


Figure 2.10. Dam break wave with an elastic gate: comparison between laboratory measurements and numerical observations of Antoci et al. (2007).

Didier et al. (2014) validated an SPH model with own experimental observations (Section 2.3.1.1). A weakly-compressible SPH method implemented in the open source code SPHysics (Gomez-Gesteira et al., 2012) was used, however, no structural analysis was included. The wave generation was performed through a numerical piston-type wave maker with the same amplitude and movement as observed in the physical tests. The numerical findings successfully captured the experimental observations (Fig. 2.11).

A fully mesh-free method was developed by Khayyer et al. (2018). The fluid was solved with an incompressible SPH method and an SPH discretisation was used for the solid. The coupling consisted in treating the solid particles as a moving boundary for the fluid, satisfying kinematic and dynamic boundary conditions at the interface. This model successfully simulated a dam break with an elastic gate test (Antoci et al., 2007). Based on the same coupling procedure, Khayyer et al. (2019) developed an MPS-based solver. The comparison with the dam break experiment from Liao et al. (2015) showed a good agreement overall.

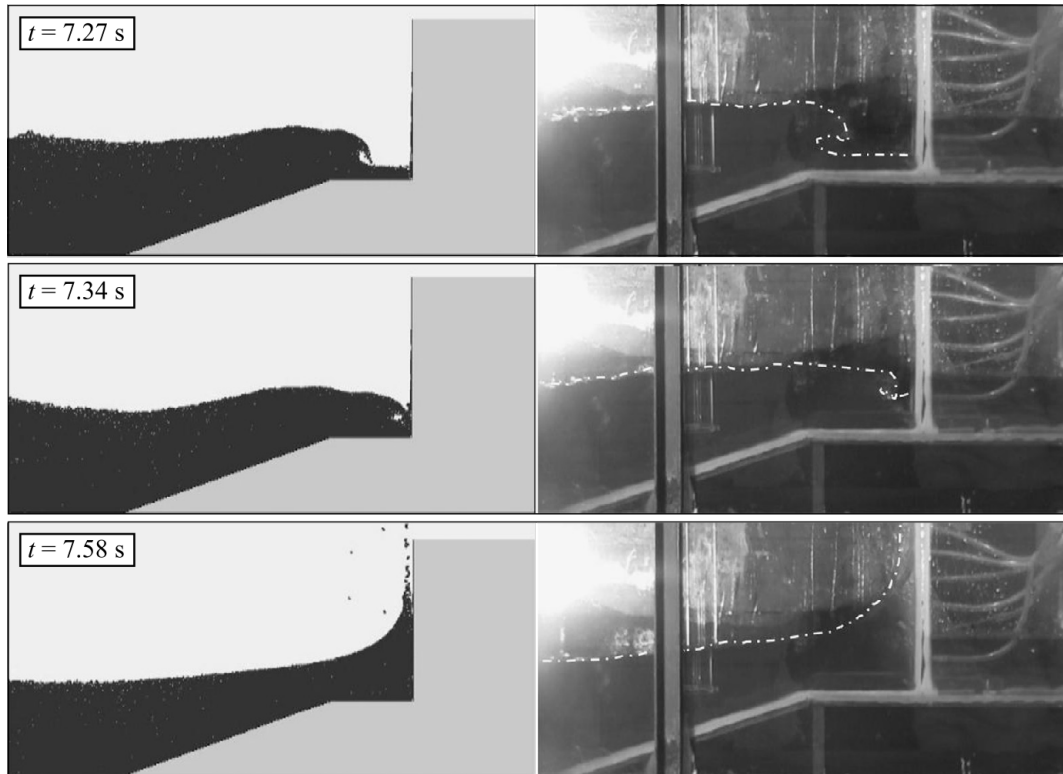


Figure 2.11. Numerical-laboratory modellings of wave impacts on a rigid onshore wall (Didier et al., 2014).

Sun et al. (2019) presented a fluid δ -SPH model coupled with a total Lagrangian particle method applied to the structure. The δ -SPH scheme is an SPH method where an extra term was included into the continuity equation for preventing oscillations of p . An Adaptive Particle Refinement (APR) technique was also implemented to increase the resolution in certain areas, e.g. around the structure. This numerical model was validated with the dam break wave benchmark test of Liao et al. (2015) (Figs. 2.12 and 2.13). This showed the capability of the numerical model of capturing the water flow, the plate deformation and the air cavity evolution well. However, some discrepancies were observed, pertaining with the initial deflection of the plate and the cavity behaviour in the final stage of the tests. These deviations may be due to 3D effects, which were not modelled in the simulations.

O'Connor and Rogers (2021) proposed a unified SPH approach for single-phase flows interacting with flexible structures. Fluid and solid governing equations were monolithically coupled within a unique framework. The challenges of SPH to accu-

rately tackle structural dynamics were addressed by using a total Lagrangian formulation with kernel function. The comparison with a dam break wave impacting a flexible obstacle (Fig. 2.13) showed a good agreement between the numerical and laboratory plate displacement during the initial impact. However, larger deviations are observed for $t \geq 0.45$ s. In this phase, the wave entrapped an air pocket which was not accurately modelled in the simulations, explaining the observed deviations. The numerical models reviewed in this section are summarised in Table 2.2, including the fluid and solid solvers and the coupling approach.

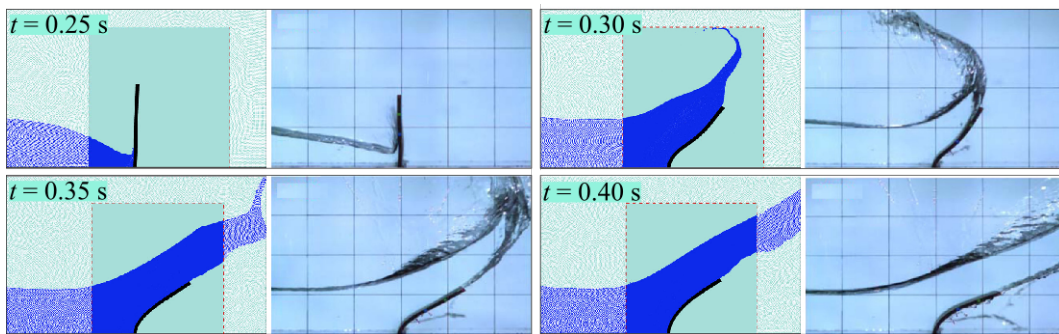


Figure 2.12. Dam break wave impacting a flexible obstacle: comparison between laboratory experiments (Liao et al., 2015) and simulations of Sun et al. (2019).

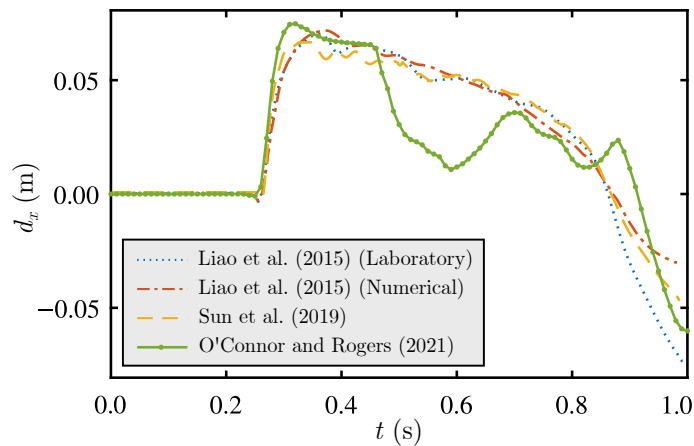


Figure 2.13. Dam break wave impacting a flexible obstacle: comparison of the horizontal plate displacement d_x between laboratory (Liao et al., 2015) and numerical (Liao et al., 2015; Sun et al., 2019; O'Connor and Rogers, 2021) experiments.

Table 2.2. Overview of numerical models for WSI.

	Reference	Fluid	Solid	Coupling
Mesh-based	He and Kashiwagi (2012)	MEL	FEM	Monolithic approach
	Chen et al. (2014)	FVM	-	-
	Liao et al. (2015)	FDM	FEM	Partitioned approach
	Hu et al. (2016)	FVM	-	-
	Tuković et al. (2018)	FVM	FVM	Partitioned approach
	Chen et al. (2020)	IBM	IBM	Partitioned approach
	Romano et al. (2020)	FVM	-	Overset mesh technique
	Di Paolo et al. (2021)	FVM	-	-
	Hu et al. (2023)	FVM	FVM	Partitioned approach
Mesh-based-mesh-free	Kumar et al. (2015)	SPH-FVM	-	-
	Rao et al. (2017)	MPS	FEM	Partitioned approach
	Zhang et al. (2019a)	MPS	FEM	Partitioned approach
	Zhang et al. (2019b)	S-FEM DFPM	S-FEM	Ghost particle approach
Mesh-free	Antoci et al. (2007)	SPH	SPH	Partitioned approach
	Didier et al. (2014)	SPH	-	-
	Khayyer et al. (2018)	SPH	SPH	Moving wall approach
	Khayyer et al. (2019)	SPH	SPH	Moving wall approach
	Sun et al. (2019)	δ -SPH	δ -SPH	Ghost particle approach

2.4 Model-prototype similarity

2.4.1 Introduction

Complex phenomena are often investigated based on laboratory modelling to provide physical insight, inform design solutions and to calibrate and validate numerical solvers. Laboratory tests are carried out at reduced size with the aim of capturing the main physical aspects of the full-size prototype. Exact model-prototype similarity is achieved when geometric, kinematic and dynamic similarities are satisfied (Kobus, 1980; Hughes, 1993; Heller, 2011).

Geometric similarity is satisfied when the ratios between lengths in the prototype and model are constant. The ratio between a characteristic length in the prototype (subscript P) and model (subscript M) is defined as the geometric scale factor

$$\lambda = \frac{h_P}{h_M}. \quad (2.27)$$

Consequently, areas and volumes are scaled with λ^2 and λ^3 for the model, respectively. Kinematic similarity requires that the motion in the prototype and model are proportional at all times. This is achieved with constant ratios of time, velocity and acceleration between the prototype and its model.

On top of geometric and kinematic similarities, dynamic similarity implies that all force ratios must be identical between the prototype and its model. The most relevant forces in fluid dynamics include inertial, gravity, viscous, surface tension, compressibility and elastic forces (Hughes, 1993; Heller, 2011). Their ratios are defined as the Froude number $Fr = (\text{inertial force/gravity force})^{1/2}$, Reynolds number $Re = (\text{inertial force/viscous force})$, Weber number $We = (\text{inertial force/surface tension force})$, Cauchy number $Ca = (\text{inertial force/elastic force})$ and the Mach number $Ma = (\text{inertial force/compressibility force})$.

Unfortunately, it is unpractical, even impossible in some cases, to keep all force ratios identical between the prototype and model. Therefore, it is common practice not to conserve some of the force ratios in favour of more feasible laboratory models. This results in deviations between the upscaled model results and the prototype observations, known as scale effects (Le Méhauté, 1976; Hughes, 1993; Heller, 2011).

Non-negligible differences between the upscaled model results and the prototype observations may also result due to model effects (Kobus, 1980; Hughes, 1993). These are due to the incorrect and/or idealised modelling of the prototype features, including the geometry, e.g. the modelling of a 3D phenomenon in 2D, the fluid properties, such as fresh instead of sea water, and the structure properties, e.g. the mass. In addition, measurement effects may be the reason of model-prototype deviations due to different measurement techniques used in the prototype and its model.

2.4.2 Froude similarity

Froude similarity is often applied for hydraulic models (Le Méhauté, 1976; Hughes, 1993, Heller, 2011; Sheng et al., 2014). This consists in satisfying the criterion

$$\text{Fr}_M = \text{Fr}_P. \quad (2.28)$$

Based on Eq. (2.28), the scaling laws for all the physical parameters can be derived (Table 2.3). Although Froude similarity is particularly convenient for scaling laminar or fully turbulent pure water flows (Heller, 2017), it is often applied to air-water flows. In these cases, Froude similarity typically provide incorrect predictions at small scales when ordinary water and air are used in the model, such that Re , We and Ma are not conserved.

2.4.3 Cauchy similarity

The geometry and elastic properties of the structure must also be appropriately scaled to achieve full similarity for WFSI (Hudson et al., 1979; Hughes, 1993; Heller, 2011; Martinelli et al., 2011; Krautwald et al., 2022). When elastic forces are significant, the scaling laws follow the Cauchy similarity. A combined Froude-Cauchy similarity is typically applied to WFSI phenomena (Le Méhauté, 1965). Under this scaling approach, the scaling laws of the structural properties can be derived in multiple ways. For example, by defining the elastic forces as EA_{\perp} (Hughes, 1993), with E as the Young's modulus and A_{\perp} as the cross-sectional area of the structure, the scaling law of E results in λ when the forces are scaled with λ^3 (Table 2.3). This scaling law can also be derived based on the proportionality of the bending stiffness EI , with I as the second moment of inertia, between the prototype and the model (Chakrabarti, 2005; Krautwald et al., 2022).

Given that several restrictions need to be fulfilled under Froude-Cauchy similarity, it might be challenging to find a material with the appropriate physical and mechanical properties for the model. However, an incorrect scaling of the structural properties

in the model result in an incorrect representation of the structure dynamics.

Table 2.3. Scaling laws for relevant parameters under Froude-Cauchy similarity, with the 3 units length [L], mass [M] and time [T].

Parameter	Unit	Scaling law
Length	[L]	λ
Area	[L ²]	λ^2
Volume	[L ³]	λ^3
Time	[T]	$\lambda^{1/2}$
Velocity	[L/T]	$\lambda^{1/2}$
Acceleration	[L/T ²]	1
Mass	[M]	λ^3
Force	[ML/T ²]	λ^3
Pressure	[M/(LT ²)]	λ
Young's modulus	[M/(LT ²)]	λ

2.4.4 Scale effects

Scale effects are due to non identical force ratios between the prototype and its model. Under Froude similarity, scale effects are commonly due to a non conservation of Re, We and/or Ma when ordinary water and air are used in the model. A common strategy for reducing scale effects under Froude similarity is based on the concept of Re invariance (Heller, 2017). This refers to a fluid state achieved at high Re, where the effect of the viscosity is negligible. Re invariance can be achieved with relatively small viscosity and/or relatively large model size, with the boundary limit strictly depending on the investigated phenomenon.

For wave impacts on vertical rigid seawalls, scale effects have been widely investigated under Froude similarity (Hughes, 1993; Peregrine, 2003; Cuomo et al., 2010b; Martinelli et al., 2011; Bredmose et al., 2015). Although negligible scale effects have been observed for non-breaking wave impacts (Hughes, 1993; Cuomo et al., 2010b), breaking wave impacts may need scale corrections (Hudson et al., 1979; Hughes, 1993; Peregrine, 2003; Cuomo et al., 2010b; Martinelli et al., 2011; Bredmose et al., 2015).

The unscaled water and air properties, e.g. viscosity and surface tension, result in

different air effects in the models, leading to incorrect predictions of the pressures and forces. Based on historical data and the theoretical work of Takahashi et al. (1985), Cuomo et al. (2010b) proposed an approach to remove scale effects in the upscaling of breaking wave pressures. This is based on the Bagnold number Ba , being an estimate of the wave impact strength (Bagnold, 1939). For breaking wave impacts on walls, Ba can be estimated as (Cuomo et al., 2010b)

$$Ba = \frac{0.2(1 - \pi/12) \rho_w g (h + H)}{\pi/12 p_0}, \quad (2.29)$$

with the atmospheric pressure p_0 . The maximum pressures $p_{max,P}$ and $p_{max,M}$ can be estimated by entering Fig. 2.14a with Ba_P and Ba_M (Eq. 2.29), move up to the solid line and reading the corresponding values of p on the vertical axis. The corrected pressure scaling law

$$\lambda_p = \frac{p_{max,P}}{p_{max,M}}. \quad (2.30)$$

can then be evaluated. In order to take more complex processes into account, including air leakage and air entrainment at the impact, an equivalent energy loss E_l was introduced, resulting in the dashed lines in Fig. 2.14a. Consequently, from the interception between the measured $p_{max,M}$ and Ba_M , the corresponding E_l curve can be identified. Therefore, by moving along this curve, the correct value of $p_{max,P}$ can be read at Ba_P .

This approach demonstrated that the Froude scaling laws tend to overpredict breaking wave impact pressures. These findings were confirmed by the numerical observations of Bredmose et al. (2015). For violent wave impacts, they found that the wave impact pressures follow the Bagnold-Mitsuyasu scaling law for $p \geq 3.18p_0$. This was generalised for 3D air pockets of arbitrary shape as

$$C_{B-M} \frac{\rho_w u^2}{p_0} = \left(\frac{p_{max}}{p_0} + 1 \right)^{0.4/1.4} + 0.4 \left(\frac{p_{max}}{p_0} + 1 \right)^{-1/1.4} - 1.4, \quad (2.31)$$

with the scale-independent constant C_{B-M} (Bredmose et al., 2015) and the fluid

velocity u . On the other hand, the Froude scaling laws accurately predict p for impact pressures below $3.18p_0$. Eq. (2.31) is shown in Fig. 2.14b, along with the line based on the Froude scaling laws. By entering Fig. 2.14b with $p_{max,M}/p_0$, the corresponding abscissa value can be read. This is multiplied by λ to obtain the abscissa values for the prototype and consequently $p_{max,P}/p_0$ can be read on the vertical axis.

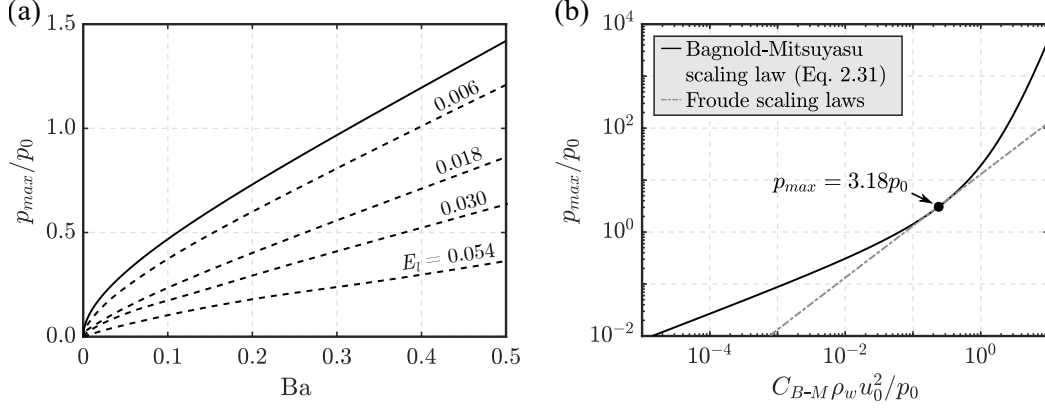


Figure 2.14. Upscaling approaches to remove scale effect in wave impact pressures: (a) p_{max}/p_0 versus Ba from Cuomo et al. (2010b) and (b) pressure scaling curves based on Bagnold-Mitsuyasu and the Froude scaling laws (after Bredmose et al., 2015).

More recently, novel scaling laws have been suggested by Catucci et al. (2021, 2023) to avoid scale effects in air-water flows. These were derived based on the self-similarity of the governing equations, allowing the modelling of air-water flows without Re , We and Ma scale effects. The new scaling laws for all the flow parameters have been derived, being more flexible than Froude scaling laws, such that different scaling configurations can be obtained. These were successfully validated based on the simulations of air-water flow phenomena, including a dam break wave impacting an obstacle, a plunging water jet and a Taylor bubble.

Nevertheless, an investigation of scale effects involving flexible structures is still lacking. For WFSI, additional scale effects may occur if the Cauchy similarity is not satisfied. This may be due to the challenge of finding a material for the model with the desired physical and mechanical properties, e.g. when the prototype is made of rubber. The unscaled structural properties lead to scale effects which may be significant

for both the wave loading and structural response and need to be appropriately investigated.

2.5 Summary and research gaps

In this Chapter 2, theoretical insight into wave theories was addressed first. Available theoretical models (Sainflou, 1928; Tadjbakhsh and Keller, 1960; Cross, 1967) for wave loading on rigid walls were then described in Section 2.2.2. The models of Sainflou (1928) and Tadjbakhsh and Keller (1960) provide a good estimation of the wave pressures for unexceptional real events, e.g. wind waves. However, they may be inaccurate for more extreme waves. A prediction approach for impulse waves impacting onshore plates was proposed by Cross (1967). The surge force was expressed as a function of the overland flow features, which, however, may be challenging to accurately predict.

The most relevant laboratory studies of WSI were reviewed in Section 2.3.1. This included laboratory investigations with plates which are rigid, e.g. solitary wave impacts on a wall (Ramsden, 1996), and flexible, e.g. dam break wave involving an elastic plate (Antoci et al., 2007). Despite of several benchmark studies, a comprehensive case for wave impact on plates of different stiffnesses is still lacking. This should provide the wave parameters, e.g. water surface elevation and force, and plate response, e.g. displacement, under several configurations, enabling a systematic validation of numerical models.

Given the maturity of CFD and CSD, the numerical modelling of WFSI has been largely developed in the last decade. The most relevant WSI and WFSI numerical studies were addressed in Section 2.3.2. Most of these studies proposed to separately solve the fluid and solid domains with the so-called partitioned approach. On the other hand, monolithic models were applied in a few studies, in which a unique solver is used for both domains (Table 2.2). Given the reliability and efficiency of OF for both CFD and CSD, an OF toolbox (Cardiff et al., 2018) was used in the present

study, however, requiring further validation for WFSI.

The review of the most relevant WSI laboratory and numerical studies revealed the need to further validate existing approaches for the prediction of impulse wave loads on vertical rigid walls (Eqs. 2.22 and 2.23). Physical insight into the wave pressure is also required. A systematic investigation of impulse wave impacts on rigid walls, including both 2D and 3D tests, would address this shortcoming.

As showed in Sections 2.3.1 and 2.3.2, evidence regarding the effect of the plate flexibility on the wave forces is still inconclusive. An accurate understanding of the wave-structure interaction effects is still lacking, requiring a thorough investigation with a range of incident waves and plate stiffnesses. This would enhance the physical understanding of WFSI and support the design of coastal and offshore structures.

Finally, the main aspects related to scaling laws and scale effects were addressed in Section 2.4. The Froude and Cauchy similarities were reviewed, being the most common scaling laws applied in hydraulics and for WFSI. The sources of scale effects in WFSI were briefly discussed and available approaches to remove them in breaking wave impacts on rigid walls were presented. However, scale effects in WFSI have not yet systematically been investigated. A comprehensive investigation along with a new and more practical scaling approach would support laboratory investigations of WFSI.

Chapter 3

A numerical investigation of tsunamis impacting dams

This chapter is comprised of the following journal article:

Attili, T., Heller, V. and Triantafyllou, S., 2021. A numerical investigation of tsunamis impacting dams. *Coastal Engineering* 169, 103942.

Despite of the different layout, the article is entirely included within this chapter with the following differences:

1. Section, page, figure, table and equation numbers are amended to ensure consistency across the thesis.
2. The reference to journal details, e.g. volume and page numbers, are omitted.
3. The email addresses of the authors have not been included.
4. Dates of submission, revision and acceptance have not been included.
5. Minor adjustments have been made to some equations, figures and text to correct a minor typo, provide more details and ensure consistency across the thesis.
6. The nomenclature and references list are provided at the end of this thesis.

A numerical investigation of tsunamis impacting dams

Tommaso Attili¹, Valentin Heller¹, Savvas Triantafyllou²

¹Environmental Fluid Mechanics and Geoprocesses Research Group, Faculty of Engineering, University of Nottingham, Nottingham NG7 2RD, UK

²Institute for Structural Analysis and Aseismic Research, School of Civil Engineering, National Technical University of Athens, Athens, Greece

Abstract

Landslides, rockfalls, and iceberg calving impacting into a water body generate large landslide-tsunamis posing a serious hazard in lakes and reservoirs. These waves can impact and even overtop dams as in the 1963 Vajont disaster in Italy. However, estimating the effects of tsunamis on dams, e.g. pressures and forces, and 3D effects is challenging. An accurate prediction of these effects is also important for a range of coastal and offshore applications. The present study focuses on the numerical modelling of landslide-tsunamis impacting dams with the open source toolbox solids4foam. After a validation with theoretical, experimental, and numerical results, 5th order Stokes, cnoidal, and solitary waves were simulated in 72 2D experiments with dams of steep to vertical inclinations. The wave loading on dams was found to be in agreement with predictions based on an existing empirical approach, significantly expanding its limited validation conditions. New empirical equations are suggested to predict the wave run-up height together with the overtopping volume and depth. These address the cases where no empirical equations are available or existing equations result in large deviations from the numerical results. Novel insight in the dynamic pressure is provided, supported by new semi-empirical equations. Further, simulations in 3D were performed to quantify the effects of the dam curvature and asymmetrical wave impact angles. Both effects combined induce an increase in

the run-up height at dam flanks of up to 32%. Such findings support the design of dams and tsunami hazard assessment.

3.1 Introduction

3.1.1 Background

Landslide-tsunamis, also called landslide-generated impulse waves, are generated by landslides, rockfalls, and iceberg calving in water bodies such as lakes and reservoirs (Heller and Hager, 2010; Heller et al., 2016; Bullard et al., 2019; Evers et al., 2019; Meng et al., 2020; Heller et al., 2021; Rauter et al., 2021; Ruffini et al., 2021). The energies of such gravity-driven masses are transferred into waves propagating across water bodies and potentially interacting with dams. This may result in significant run-ups and even overtoppings (Kobel et al., 2017; Evers and Boes, 2019; Evers et al., 2019). Several destructive landslide-tsunamis have been documented in the recent past. Among these, the one generated in the Vajont reservoir in Italy, in 1963, caused approximately 2000 casualties (Panizzo et al., 2005b). More recently, the 2014 Lake Askja event on Iceland resulted in a run-up height of 71 m (Gylfadóttir et al., 2017). Such events represent a persistent danger in regions with a large number of lakes, fjords, and/or reservoirs such as China and Norway.

Studies into the risk of tsunamis must be carried out for large water bodies (Swiss Federal Office of Energy, 2015), including tsunami impact and dam overtopping. In addition to the hydrostatic force from the still water, tsunami forces may be relevant (Ramsden, 1996) and an accurate prediction is important for the design of dams and a range of further coastal and offshore structures, e.g. oil and gas rigs, offshore wind turbine platforms, breakwaters, flood protection systems, and wave energy converters. Nevertheless, the estimation of tsunami forces is still associated with large uncertainties. Available prediction methods are based on a small number of 2D laboratory experiments (Ramsden, 1996). Moreover, 3D effects, e.g. the dam curvature and/or asymmetrical wave impact angles, often have to be neglected due

to a lack of knowledge (Heller et al., 2009). Wave run-ups are also important for the design of dams, e.g. to prevent dam overtoppings. This may cause severe damage to the dam, e.g. at the crest or downstream slope, and/or to the downstream area.

The present study focuses on the numerical investigation of tsunamis impacting dams to enhance hazard assessment. Tsunamis are modelled with idealised wave types representing a wide range of impulse waves, e.g. generated by earthquakes, landslides, and icebergs. Computational Fluid Dynamics (CFD) shows a great potential in modelling tsunamis (Yavari-Ramshe and Ataie-Ashtiani, 2016), waves impacting walls (He and Kashiwagi, 2012; Chen et al., 2014; Didier et al., 2014; Hu et al., 2016), and impulsive wave forces acting on recurved parapets (Castellino et al., 2018; Martinelli et al., 2018; Castellino et al., 2021; Dermentzoglou et al., 2021). Mesh-based methods, e.g. the Finite Volume Method (FVM, Tuković et al., 2018), and mesh-free methods (particle-based), e.g. Smoothed Particle Hydrodynamics (SPH, Didier et al., 2014), have been successfully applied. However, mesh-based methods are more computationally efficient and demonstrate a good convergence behaviour (Yavari-Ramshe and Ataie-Ashtiani, 2016).

Recently, new approaches have been developed for modelling waves generated by rigid bodies such as landslides. Chen et al. (2020) and Romano et al. (2020) presented new methods based on the Immersed Boundary Method and Overset Mesh Technique, respectively, in the OpenFOAM framework. Lagrangian approaches, e.g. the Particle Finite Element Method, have also been applied as they are efficient in solving large deformations (Franci et al., 2020; Mulligan et al., 2020). Furthermore, a new multi-domain method was developed by Di Paolo et al. (2021) to simulate wave-structure interactions in OpenFOAM. The present study relies on an available FVM toolbox in Foam-Extend 4.0 (FE 4.0), capable of simulating both the fluid and structure.

3.1.2 Previous work

An accurate prediction of the effects of tsunamis on dams is still challenging. The total pressure p at the dam is composed of the dynamic p_d and hydrostatic components. An

analytical formulation of p_d for linear waves propagating offshore in a water body was developed by Dean and Dalrymple (1991) (Section 3.3.2.3). Sainflou (1928) derived an analytical solution for p_d from nonlinear and standing waves on a vertical wall. Tadjbakhsh and Keller (1960) provided the theoretical p_d and water surface elevation η in function of the time t and the spatial coordinate x for periodic waves impacting a vertical wall. As the methods of Sainflou (1928) and Tadjbakhsh and Keller (1960) were originally developed for wind waves, they may be inappropriate to predict wave pressures for more extreme cases, such as tsunamis.

Landslide-tsunamis can be approximated with Stokes (Dean and Dalrymple, 1991), cnoidal (Dingemans, 1997), solitary (Boussinesq, 1871), and bore (Le Méhauté, 1976) waves (Heller and Hager, 2011; Heller and Spinneken, 2015; Xue et al., 2019). These different wave types result in different effects when impacting dams. Bore-like waves are typically created in the generation zone and transform into cnoidal- or solitary-like waves further offshore (Heller and Hager, 2011) or they are generated during wave breaking near the shore. Wave breaking rarely occurs at a dam as the water depth tends to increase and the wave amplitude tends to decrease towards the dam; hence, solitary-like waves represent the most extreme case in most situations (Heller et al., 2009; Kobel et al., 2017).

A mathematical investigation of solitary waves impacting a vertical wall was conducted by Cooker et al. (1997). The numerically deduced values of the wave force and the run-up height R were successfully validated with the numerical results of Fenton and Rienecker (1982). However, no prediction method for the pressure distribution at the wall was provided.

Ramsden (1996) conducted laboratory experiments in a 0.610 m (height) \times 0.396 m (width) \times 36.6 m (length) wave tank to investigate the effects of solitary waves on a vertical wall. The horizontal (subscript H) force F_H and bending moment M_H relative to the foundation resulting from the solitary wave and hydrostatic pressure from the still water combined were measured. In an effort to present a coherent methodology to predict the effects of tsunamis in lakes and reservoirs, Heller et al.

(2009) approximated the empirical data of Ramsden (1996). They found for a wave amplitude a to water depth h ratio range $0 \leq a/h \leq 0.6$

$$F_H = [1 - 1.5(a/h)]^{1/6} (1/2) \rho_w g (2a + h)^2, \quad (3.1)$$

$$M_H = [1 - 1.5(a/h)]^{1/6} (1/6) \rho_w g (2a + h)^3 \quad (3.2)$$

with the water (subscript w) density ρ_w and the gravitational acceleration g . Eqs. (3.1) and (3.2) provide the force and moment per unit width of the dam based on a triangular distribution of the pressure

$$p(z) = [1 - 1.5(a/h)]^{1/6} \rho_w g (2a - z) \quad (3.3)$$

with a maximum water level of $2a + h$ and z as the vertical coordinate. This is reduced to a trapezoidal distribution in the case of wave overtoppings (Appendix 3.A), i.e. for a dam height $l \leq (2a + h)$, the triangular section above the dam crest is removed (Heller et al., 2009). This results in the reduced (subscript *red*) force $F_{H,red}$ (Eq. 3.A.1) and moment $M_{H,red}$. This approach was taken over by Evers et al. (2019) in their effort to update the manual Heller et al. (2009). Eqs. (3.1) and (3.2) require further validation as they rely on a limited number of experiments and wave conditions.

The most recent prediction methods for R and dam overtopping were summarised by Evers et al. (2019). For R , the semi-empirical equation of Evers and Boes (2019) was proposed and for the wave overtopping volume Ψ , duration and the maximum wave overtopping depth d_0 , the methods of Kobel et al. (2017) were recommended. Unfortunately, the empirical equation for Ψ cannot be applied if a is larger than the freeboard f , being one of the shortcomings addressed in the present work. These methods will be compared and discussed with the results of the present article in Sections 3.3 and 3.4.

3.1.3 Aims and structure

The present study aims to:

- Provide new physical insight into tsunamis impacting dams of steep to vertical inclinations based on 2D and 3D numerical modelling.
- Provide insight and propose a new semi-empirical approach to predict the dynamic pressure of tsunamis on dams in analogy to the theory of Dean and Dalrymple (1991).
- Expand the validation conditions of the prediction methods of Evers et al. (2019) for tsunami forces on dams with and without overtopping.
- Provide a new empirical equation for the run-up height to support tsunami hazard assessment.
- Provide new empirical equations for the overtopping volume and depth for cases where the equations of Kobel et al. (2017) cannot be applied or result in significantly different predictions from the numerical results.

The remainder of this article is organised as follows. In Section 3.2 the numerical toolbox is addressed along with the numerical set-ups and the test programme. The validation of the numerical toolbox with laboratory data, an analytical solution, and another numerical solver is presented in Section 3.3. Thereafter, the investigation of tsunami forces, run-ups, overtoppings, and dynamic pressures for waves with and without overtopping in 2D is addressed. A discussion of the results and the 3D simulations can be found in Section 3.4 followed by the main conclusions in Section 3.5. The appendices include the overtopping wave force method of Evers et al. (2019) (Appendix 3.A), the convergence tests (Appendix 3.B), and the dynamic pressure (Appendix 3.C) for overtopping waves.

3.2 Methodology

The open source toolbox solids4foam (Cardiff et al., 2018) implemented in FE 4.0 (OpenFOAM extension, 2016) was used in the present study to model tsunamis impacting dams. This toolbox solves fluid-solid interaction problems with a Finite Volume discretisation for both domains and a partitioned coupling approach is applied.

3.2.1 Governing equations of fluid

The governing equations of an incompressible Newtonian fluid are the continuity and the Reynolds-Averaged Navier-Stokes (RANS) equations

$$\nabla \cdot \bar{\mathbf{u}} = 0 \quad (3.4)$$

$$\frac{\rho \partial \bar{\mathbf{u}}}{\partial t} + \rho(\bar{\mathbf{u}} \cdot \nabla) \bar{\mathbf{u}} = -\nabla \bar{p} + \rho \nabla \cdot (\mu \nabla \cdot \bar{\mathbf{u}} - \overline{\mathbf{u}'\mathbf{u}'} + \rho \mathbf{g}). \quad (3.5)$$

In Eqs. (3.4) and (3.5) $\bar{\mathbf{u}} = (\bar{u}_x, \bar{u}_y, \bar{u}_z)$ is the mean fluid velocity vector, \bar{p} the mean pressure, ρ the fluid density, μ the fluid dynamic viscosity, $\overline{\mathbf{u}'\mathbf{u}'}$ the turbulent stress tensor (with $\overline{\mathbf{u}'\mathbf{u}'} = 0$ for laminar flow) and \mathbf{g} the gravitational acceleration vector. Based on the Boussinesq approximation (Jasak, 1996)

$$\overline{\mathbf{u}'\mathbf{u}'} = \nu_t(\nabla \cdot \bar{\mathbf{u}} + (\nabla \cdot \bar{\mathbf{u}})^T) + \frac{2}{3}k_t\mathbf{I}, \quad (3.6)$$

where \mathbf{I} is the identity matrix and ν_t and k_t are the kinematic turbulent viscosity and the turbulent kinetic energy per unit mass defined by the selected turbulence model in FE 4.0 (Ferziger, 1987). For the simulations of the present study, the laminar flow model has been used (Streeter and Wylie, 1985). This assumption provides accurate results while reducing the associated computational costs, as demonstrated in the validation tests (Section 3.3.1.1 and 3.3.1.3), with a tendency to operate on the safe side.

The solver interFoam is applied in FE 4.0 to solve Eqs. (3.4) and (3.5). These

are discretised into a set of algebraic equations based on the spatial and temporal partition of the domain using the cell-centered FVM and solved with the PIMPLE loop (Aguerre et al., 2013). Time integration is governed by the Courant-Friedrichs-Lewy (CFL) convergence condition (Courant et al., 1928), which is expressed in two dimensions as

$$C = \frac{\bar{u}_x \Delta t}{\Delta x} + \frac{\bar{u}_z \Delta t}{\Delta z} \leq 1. \quad (3.7)$$

In Eq. (3.7), C is the Courant number, Δt the time step and Δx and Δz are the cell sizes in the x and z direction, respectively. Once the solver started, the initial Δt was continuously adapting to satisfy the CFL condition.

The Volume Of Fluid (VOF) method (Hirt and Nichols, 1981) is employed in interFoam to solve water-air flows based on the fraction of volume α ; α varies from 0 to 1, with $\alpha = 0$ denoting air, $\alpha = 1$ water and $0 < \alpha < 1$ the air-water interface. In the present study, $\alpha = 0.5$ was selected to track the water surface. The fluid properties ρ and μ are evaluated as

$$\rho = \rho_w \alpha + \rho_a (1 - \alpha) \quad (3.8)$$

$$\mu = \mu_w \alpha + \mu_a (1 - \alpha) \quad (3.9)$$

with the subscript a standing for air. Once the fluid velocity field is solved, α is updated through the following transport equation over time

$$\frac{\partial \alpha}{\partial t} + \nabla \cdot (\bar{\mathbf{u}} \alpha) + \nabla \cdot [\alpha(1 - \alpha) \mathbf{u}_r] = 0. \quad (3.10)$$

The artificial compression term $\nabla \cdot [\alpha(1 - \alpha) \mathbf{u}_r]$, including the compression velocity vector \mathbf{u}_r , was introduced by Weller et al. (1998) to reduce the numerical diffusion. The Euler first-order scheme was employed for temporal discretisation along with the Gauss linear second order for spatial gradients.

Wave generation was performed with the toolbox waves2Foam (Jacobsen et al., 2012). Several wave theories are implemented in waves2Foam, including linear, Stokes,

cnoidal, and solitary wave theory. The governing equations are implemented as in FE 4.0 with the only difference that Eq. (3.5) is written in terms of the pressure in excess to the hydrostatic one. The wave generation is based on the relaxation zone technique, consisting of a relaxation function applied to evaluate \bar{u} and α inside the relaxation zone (Jacobsen et al., 2012). In the present study, a relaxation zone of 3 times the wave length L was used in all the 2D tests (Fig. 3.1a).

3.2.2 Numerical set-up and test programme

The numerical set-up consisted of a 2D wave channel with a rigid dam (Fig. 3.1a). The dam with height $l = 50.00$ m and thickness $s = 2.50$ m was located $4L$ from the upstream boundary of the wave flume. Water depths of $h = 25, 36,$ and 48 m were used (Table 3.1), resulting in relative submergences of the dam of $h/l = 0.50, 0.72,$ and 0.96 with a minimum freeboard of $f = l - h = 2$ m, satisfying the criterion of the Bureau of Reclamation (2012). The simulations involved a range of wave types impacting dams of inclinations $\beta = 60, 75,$ and 90° . The wave types and corresponding wave features used in the simulations are shown in Table 3.1 where H is the wave height and T the wave period.

Table 3.1. The test programme for the 2D tests. Values marked with * were observed at $x = -h \cot \beta$ in simulations conducted without the dam and are slightly different, due to bottom friction, from the round values used at the input.

Parameter	Symbol	Unit	Range		Dimensionless range
Water depth	h	m	25, 36, 48	-	-
Dam height	l	m	50	-	-
Dam inclination	β	$^\circ$	60, 75, 90	-	-
Stokes 5th order waves	H	m	6.56 to 6.86*	H/h	0.13 to 0.26
	T	s	15, 20	$T(g/h)^{1/2}$	6.8 to 12.5
Cnoidal waves	H	m	5.56 to 6.60*	H/h	0.13 to 0.26
	T	s	15 to 30	$T(g/h)^{1/2}$	7.2 to 18.8
Solitary waves	a	m	2.53 to 15.70*	a/h	0.10 to 0.60

The mesh was generated using the "blockMesh" utility, consisting of structured hexahedral cells. In the cnoidal and Stokes wave tests a resolution of $\Delta x = L/310$ and $\Delta z = 50.00$ cm, with $\Delta x = L/1240$ and $\Delta z = 12.50$ cm in the $L/4 \times 80$ m refined

area, was employed. In the solitary wave tests, the domain was discretised with square cells of $\Delta x = \Delta z = 25.00$ cm and a higher resolution of $\Delta x = \Delta z = 6.25$ cm in a $25 \text{ m} \times 80 \text{ m}$ area in front of the dam (Fig. 3.1a). Finer resolutions were investigated in a few tests, requiring higher computation times without any significant difference in the results (Appendix 3.B.1).

Some initial tests were run with and without solving the governing equations of the solid. The computation times decreased by approximately 60% for the latter cases, and negligible differences (≈ 1 to 2%) were observed in the wave forces on the dam. Consequently, all tests in Table 3.1 were conducted by solving the fluid governing equations only. The simulations were conducted on the High Performance Computing cluster Augusta at the University of Nottingham using 40 Central Processing Unit (CPU) cores and 120 GB of memory. Stokes and cnoidal wave tests (≈ 0.4 million of cells) took approximately 12 h of computation time to simulate 140 to 200 s. A simulation time of 25 s for a solitary wave test (≈ 1.3 millions of cells) required approximately 6 h of computation time.

3.2.2.1 3D simulations

In order to provide some insight into the effects of the curvature of the dam and/or asymmetrical wave impact angles, 3D simulations were also conducted. The numerical set-up consisted of a 50 m wide wave tank with a 50 m high dam and $h = 25$ m (Fig. 3.1). Given the high computational costs, only 4 selected tests were simulated. These included solitary waves with $a/h = 0.30$ and propagation angles of $\gamma = 0$ and 30° (Fig. 3.1c, d) impacting gravity and arch dams (Fig. 3.1a, b). A straight axis was assumed for the gravity dam (Fig. 3.1a, c) and the upstream face of the arch dam (Fig. 3.1b, d) was designed with vertical and horizontal radii of 30 and 115 m (Bureau of Reclamation, 2013). The domain was discretised with square cells of $\Delta x = \Delta y = \Delta z = 25.00$ cm and with a higher resolution of $\Delta x = \Delta y = \Delta z = 6.25$ cm in a refined area in front of the dam (Fig. 3.1a, b).

For $\gamma = 0^\circ$, only half of the domain ($0 \text{ m} \leq y \leq 25 \text{ m}$) was simulated given

the symmetry of the wave field (≈ 40 million cells). The boundary condition for the plane $y = 0$ m was set as “symmetryPlane” (OpenFOAM documentation, 2020). At $y = 25$ m, the “noSlip” and “zeroGradient” conditions were used for the velocity and pressure fields. These simulations were conducted using 40 CPU cores and 600 GB of memory, requiring approximately 6 days of computation time to simulate 10 s.

For $\gamma = 30^\circ$, the whole domain was used (≈ 75 million cells). At $y = -25$ and 25 m, the boundary conditions were set as “noSlip” for the velocity and “zeroGradient” for the pressure (OpenFOAM documentation, 2020). The oblique waves were generated in waves2foam by changing the cosines representing the direction vector. Based on the wave type used and the relatively narrow domain, the wave generation is expected to be satisfactory for the purpose of the present study. Given the high computational costs, the wave front was located 50 m upstream of the dam (Fig. 3.1) to reduce the length of the domain and the time of simulation. A simulation time of 5 s took approximately 6.5 days of computation time with 80 CPU cores and 600 GB of memory.

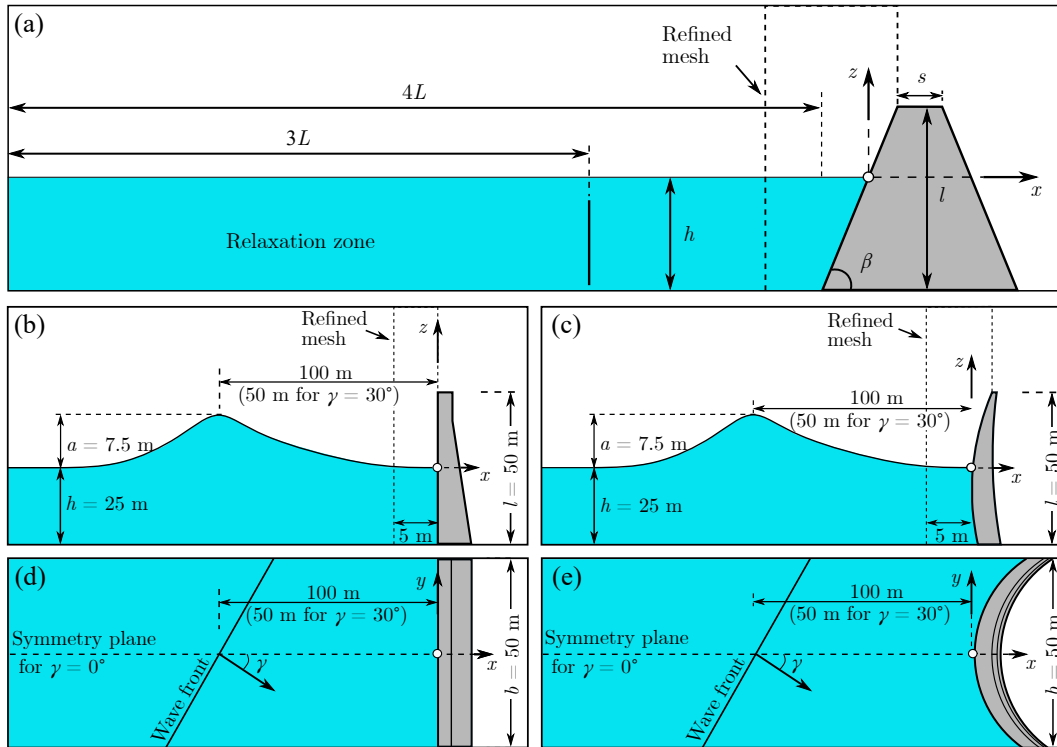


Figure 3.1. Numerical set-ups: (a) 2D tests, (b, c) lateral and (d, e) top views of the 3D tests with (b, d) showing the gravity and (c, e) the arch dam.

3.3 Results

3.3.1 Validation of the numerical toolbox

3.3.1.1 Comparison with experiments and an analytical solution

The numerical toolbox was validated with the laboratory measurements of Mallayachari and Sundar (1995) and the analytical solution of Tadjbakhsh and Keller (1960) for linear waves impacting a vertical wall. The numerical simulations were conducted with the identical set-up as in Mallayachari and Sundar (1995). A mesh resolution of $\Delta x = \Delta z = 0.0015$ m was employed, resulting from the convergence analysis in 3.B.2. The dynamic pressure p_d (Dean and Dalrymple, 1991), defined as

$$p_d(z) = \begin{cases} p(z) & \text{for } 0 < z \leq \eta, \\ p(z) + \rho_w g z & \text{for } -h \leq z \leq 0, \end{cases} \quad (3.11)$$

where $p(z)$ is the measured pressure in the simulations, is compared with the experimental and analytical results for two selected tests with intermediate-water waves in Fig. 3.2.

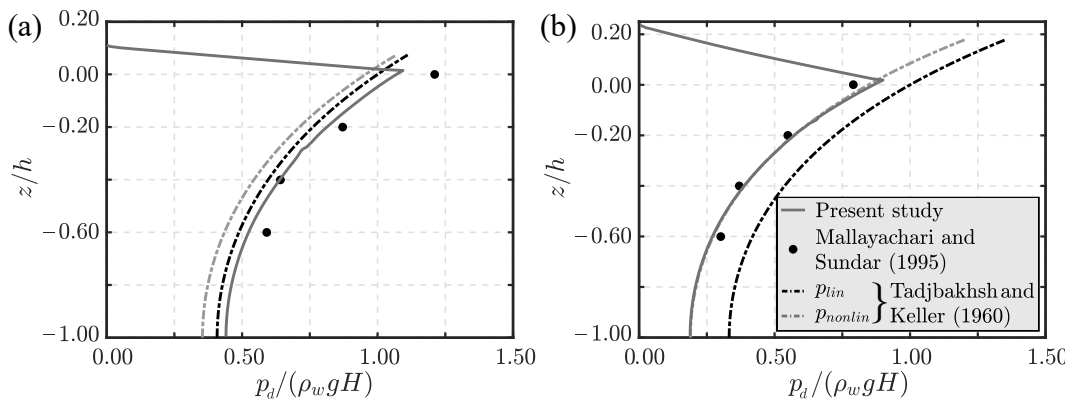


Figure 3.2. Comparison of the numerical pressure $p_d/(\rho_w g H)$ versus z/h with laboratory measurements (Mallayachari and Sundar, 1995) and analytical p_{lin} and p_{nonlin} (Tadjbakhsh and Keller, 1960) for (a) $H = 0.023$ m and $T = 0.950$ s and (b) $H = 0.048$ m and $T = 0.873$ s (after Attili et al., 2020).

The analytical solution p_{lin} takes only the linear term into account whereas p_{nonlin} considers up to the third order term (Tadjbakhsh and Keller, 1960). The normalised root mean square error

$$nRMSE = \frac{\sqrt{\frac{1}{N_d} \sum_i^{N_d} (p_{d,ref,i} - p_{d,num,i})^2}}{(p_{d,num,max} - p_{d,num,min})} \quad (3.12)$$

was computed, with the experimental or analytical (subscript *ref*) and the numerical (subscript *num*) value, respectively, N_d is the number of considered p_d values and the subscripts *max* and *min* stand for the maximum and minimum values. Eq. (3.12) was applied for $z \leq 0$ m only, due to the lack of experimental data for $z > 0$ m. In addition, the analytical solution does not result in atmospheric pressure ($p_d = 0$) as observed in the simulations at $z = \eta$ (Fig. 3.2). In both experiments the numerical toolbox captures the experimental data and the analytical model well. This resulted in $nRMSE = 0.14$ and 0.08 for the experimental data in Fig. 3.2a, b, respectively, and $nRMSE = 0.07$ to 0.14 and 0.02 to 0.21 for the analytical solution in Fig. 3.2a, b, respectively.

3.3.1.2 Comparison with numerical solutions

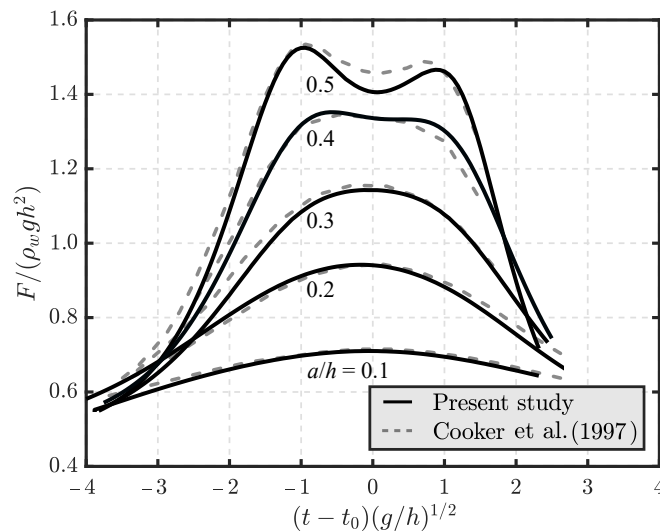


Figure 3.3. Comparison of the time series of the dimensionless forces $F/(\rho_w g h^2)$ at the dam with that of Cooker et al. (1997) for $a/h = 0.1, 0.2, 0.3, 0.4,$ and 0.5 .

The time series of the solitary wave forces F at a vertical dam were compared with the numerical results of Cooker et al. (1997). The numerical simulations herein were performed with the set-up shown in Fig. 3.1a, for $0.1 \leq a/h \leq 0.5$. The dimensionless

force $F/(\rho_w g h^2)$ versus the dimensionless time $(t - t_0)(g/h)^{1/2}$ is shown in Fig. 3.3, where t_0 is the instant when the maximum R occurs. The present study is in good agreement with Cooker et al. (1997), showing a maximum deviation of only 5% for $a/h = 0.5$ at $t = t_0$. In further agreement, F is maximum at $t = t_0$ for $a/h \leq 0.3$, while a double peak is observed in proximity of $t = t_0$ for $a/h \geq 0.4$ (Fig. 3.3).

3.3.1.3 Validation for overtopping waves with laboratory experiments

The numerical solver was validated with 2 laboratory experiments of Kobel et al. (2017) for the overtopping volume Ψ and depth d_0 of solitary waves impacting a vertical dam. The numerical set-up consisted of a 2D wave flume with a 0.30 m high plate representing the dam and $h = 0.25$ m. A mesh resolution of $\Delta x = \Delta z = 1.50$ mm was employed (Appendix 3.B).

The comparison between laboratory and numerical results for experiment 1 (Table 3.2) is shown in Fig. 3.4 for a section of the wave flume of approximately $0.85 \text{ m} \times 0.30 \text{ m}$. The free water surface is compared at several adjusted times $\tau = t - t_{d0}$, with t_{d0} as the time during the maximum d_0 . This reveals that the main features of the phenomenon are captured by the simulation. The experimental (subscript *exp*) and numerical Ψ/h^2 and d_0/h are addressed in Table 3.2. The numerical Ψ/h^2 and d_0/h are well predicted in both experiments with a maximum deviation of 14%.

Table 3.2. Overview of the main parameters in the comparison with experiments of Kobel et al. (2017).

Experiment	a/h	$\frac{\Psi_{exp}}{h^2}$	$\frac{\Psi_{num}}{h^2}$	$\Delta\Psi$	$\frac{d_{0,exp}}{h}$	$\frac{d_{0,num}}{h}$	Δd_0
1	0.30	0.25	0.27	8%	0.28	0.27	4%
2	0.50	0.55	0.60	9%	0.56	0.64	14%

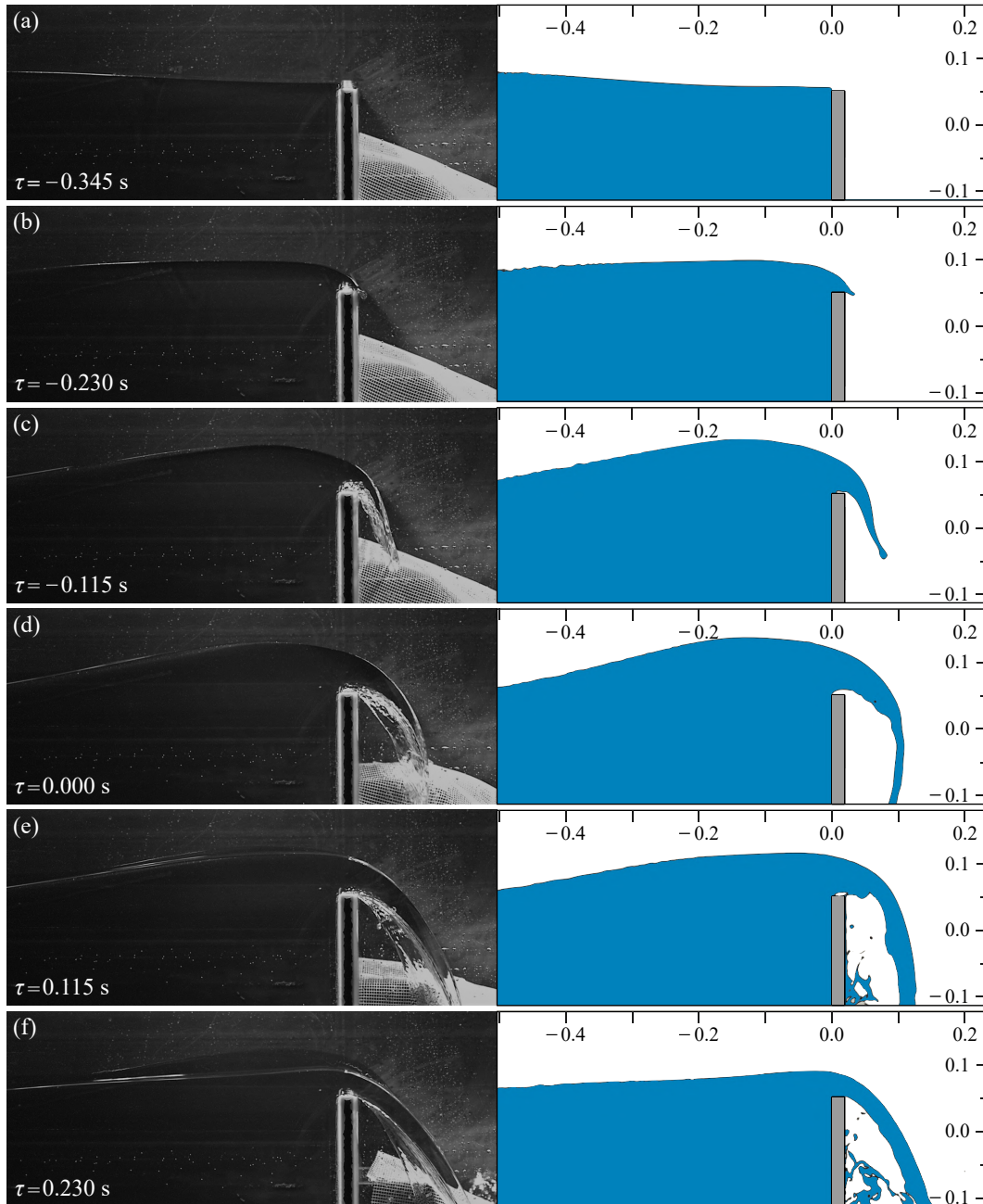


Figure 3.4. Comparison between laboratory (Kobel et al., 2017) and numerical snapshot series of a solitary wave impact on a vertical dam with overtoppings with $a/h = 0.30$. The units of the x and z axes are m.

3.3.2 No overtopping

The tsunamis travelled along the numerical flume, impacted and run-up the dam before being reflected. This is shown in the snapshot series in Fig. 3.5 for a solitary wave with $a/h = 0.31$ and $\beta = 90^\circ$.

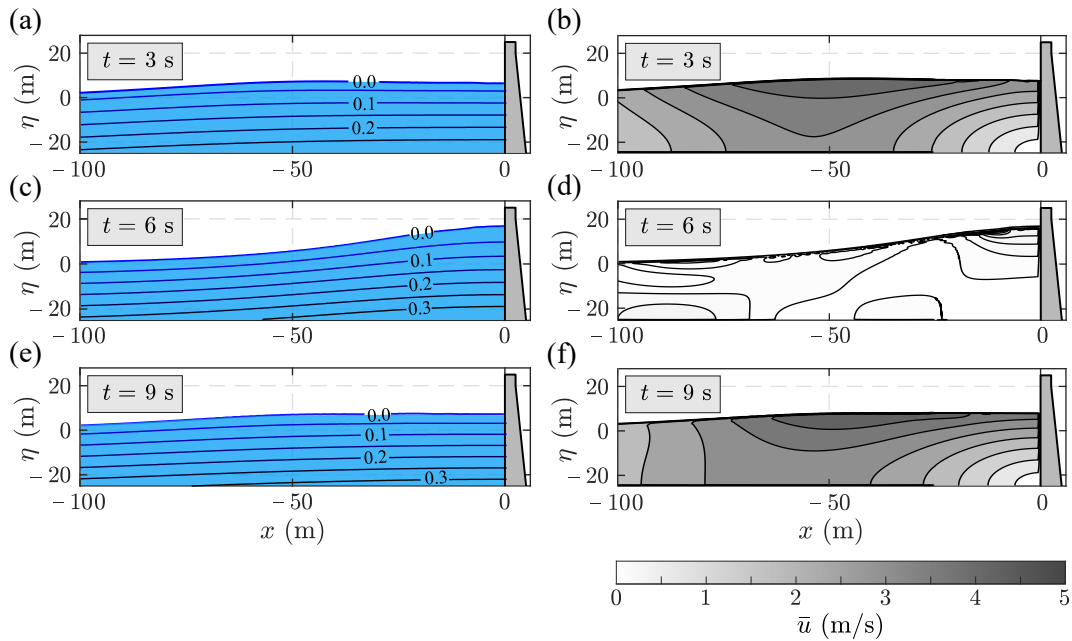


Figure 3.5. Snapshot series of a solitary wave impact on a dam without overtopping with $a/h = 0.31$ with (a, c, e) pressure contours in MPa and (b, d, f) mean velocity $\bar{u} = \sqrt{\bar{u}_x^2 + \bar{u}_z^2}$ contours.

3.3.2.1 Run-up

The simulations to investigate the run-up heights R at the dam were conducted with smooth slopes. Although they do not represent all types of dam surfaces, Teng et al. (2000) found that the effect of the roughness on R can be neglected for relatively steep slopes $\beta \geq 20^\circ$.

The maximum R/h observed in each test is shown in Fig. 3.6a versus a/h . In agreement with Cooker et al. (1997), the instant t_0 (Section 3.3.1.2) does not necessarily coincide with t when the maximum F is observed (Fig. 3.3). R/h increases with a/h following approximately a linear trend (Fig. 3.6a). Some of the cnoidal wave tests with $\beta = 60$ or 75° show larger values compared to the other tests for the same a/h . This is due to the smaller β resulting in larger R , as also observed for the solitary tests (Fig. 3.6a) and the splash generated during the wave impacts in these simulations.

Using the linear trend between R and a/h shown in Fig. 3.6a, R/h was approxi-

mated as

$$\frac{R}{h} = \frac{9}{4} \left(\frac{90^\circ}{\beta} \right)^{1/3} \frac{a}{h}, \quad (3.13)$$

where the pre-term and exponent were optimised through a regression analysis based on the least-square approach algorithm trust-region (Fig. 3.6b). The coefficient of determination

$$R^2 = 1 - \frac{\sum_i (Y_{num,i} - Y_{pred,i})^2}{\sum_i (Y_{num,i} - \bar{Y})^2}, \quad (3.14)$$

was computed with $Y_{num,i}$ as the numerical values, \bar{Y} as the mean of the numerical values and $Y_{pred,i}$ as the predicted values (subscript *pred*).

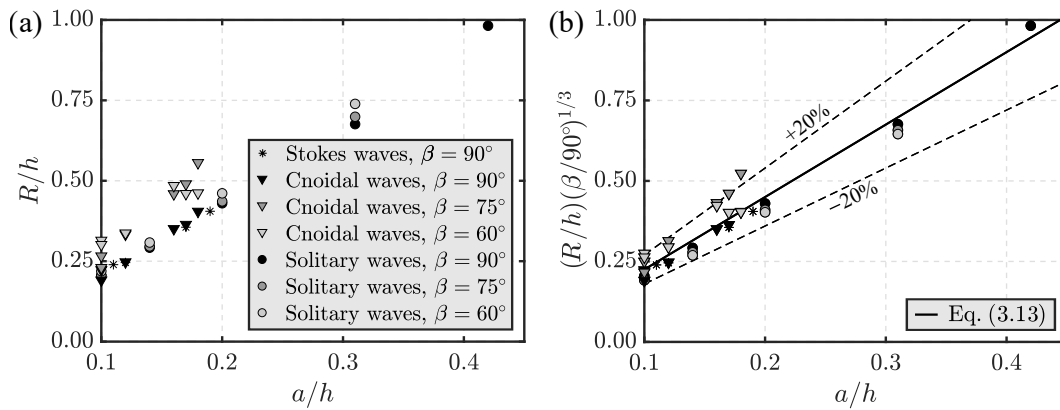


Figure 3.6. (a) Relative run-up height R/h and (b) $(R/h)(\beta/90^\circ)^{1/3}$ with Eq. (3.13) ($R^2 = 0.94$) versus the relative wave amplitude a/h .

3.3.2.2 Force and bending moment

The horizontal force F_H and bending moment M_H are compared with predictions based on Evers et al. (2019). For the tests with $\beta = 60$ and 75° , $F_H = F \sin \beta$ and $M_H = F_H z_H$ were computed, with z_H as the elevation of the resultant of F_H from $-h$. F_H and M_H are normalised with the hydrostatic force $F_h = (1/2)\rho_w g(2a + h)^2$ and moment $M_h = (1/6)\rho_w g(2a + h)^3$, respectively. F_H/F_h and M_H/M_h are shown with double logarithmic axes in Fig. 3.7 together with the predictions from Evers et al. (2019) (Eqs. 3.1 and 3.2) and the experimental data of Ramsden (1996).

Eqs. (3.1) and (3.2) predict the numerical F_H and M_H well, operating on the safe side, and most of the data are within the $\pm 10\%$ bounds (Fig. 3.7). The 4 tests

conducted with Stokes waves represent less extreme cases with approximately 10% smaller wave loadings than predicted with Evers et al. (2019) (Fig. 3.7). Marginally higher values for F_H and M_H of the cnoidal waves for larger T are observed. However, this dependence on T may be neglected for the investigated range $7.2 \leq T(g/h)^{1/2} \leq 18.8$ such that Eqs. (3.1) and (3.2) deliver also good approximations for cnoidal waves. The solitary wave loadings on the dam are in good agreement with Eqs. (3.1) and (3.2).

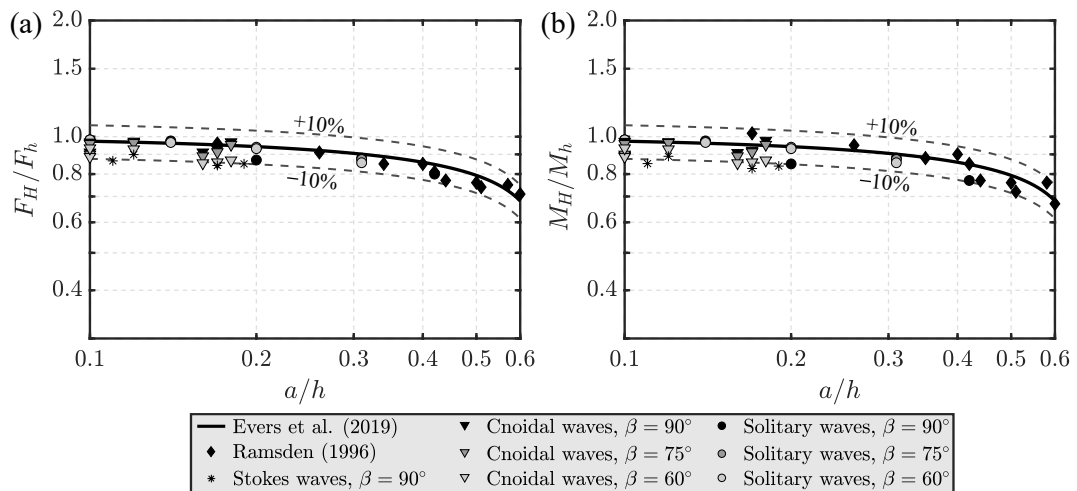


Figure 3.7. Comparison of the horizontal dimensionless (a) force F_H/F_h and (b) moment M_H/M_h at the dam versus a/h with predictions from Evers et al. (2019) and data of Ramsden (1996).

3.3.2.3 Dynamic pressure

The total pressure p at the wall is composed of the dynamic p_d and hydrostatic $-\rho_w g z$ components. The component p_d represents the excess pressure due to the waves, corresponding to p above ($z > 0$) and to $p + \rho_w g z$ below the still water surface ($z \leq 0$) (Eq. 3.11).

According to Dean and Dalrymple (1991), the pressure field of linear waves propagating offshore in a water body can be determined from the unsteady Bernoulli equation resulting in $p_d = K_p(z)p(z=0)$, for $z \leq 0$. K_p is the pressure response factor

$$K_p(z) = \frac{\cosh[k(h+z)]}{\cosh(kh)}, \quad (3.15)$$

where $k = 2\pi/L$ is the wave number. K_p reaches the maximum value of 1 at $z = 0$ and decreases for $z < 0$ proportionally to $\cosh(h + z)$.

The unsteady Bernoulli equation can also be used to describe the pressure field of waves impacting walls (Tadjbakhsh and Keller, 1960). In order to define p_d of nonlinear waves impacting dams, in analogy to Dean and Dalrymple (1991), the pressure response factor at the wall (subscript w) K_{pw} is introduced herein such that

$$p_d(z) = \begin{cases} p(z) & \text{for } z > 0, \\ K_{pw}p(z=0) & \text{for } -h \leq z \leq 0, \end{cases} \quad (3.16)$$

where $p(z)$ can be predicted with Eq. (3.3) (Evers et al., 2019).

Despite of the different conditions compared to linear waves propagating offshore in a water body, K_{pw} in the numerical tests showed similar trends as K_p (Eq. 3.15) and are approximated in function of a/h , z/h , and a coefficient A as

$$K_{pw}(a/h, z/h) = \frac{\cosh[A(a/h)(1 + z/h)]}{\cosh[A(a/h)]}. \quad (3.17)$$

A was optimised for each test with a least squares regression analysis resulting in $1.28 \leq A \leq 15.06$. Eq. (3.17) captures the numerical results well with coefficients of determination of $R^2 = 0.95$ to 1.00, as shown in Fig. 3.8 for 4 representative tests.

To eventually express K_{pw} as a function of a/h and z/h only, the coefficients A were defined separately for Stokes and cnoidal (Eq. 3.18) and solitary waves (Eq. 3.19) with

$$A = (a/h)^{-1} \text{ and} \quad (3.18)$$

$$A = (a/h)^{-2/3}. \quad (3.19)$$

Eq. (3.19) captures the data within deviations of $\pm 20\%$ for the solitary waves (Fig. 3.9b), while larger deviations are observed for Eq. (3.18) for Stokes and cnoidal waves (Fig. 3.9a). However, most of the data lie within the $\pm 30\%$ bounds. Combining Eq.

(3.17) with Eqs. (3.18) and (3.19) results in

$$K_{pw}(z/h) = \frac{\cosh(1 + z/h)}{\cosh(1)}, \text{ for Stokes and cnoidal waves and} \quad (3.20)$$

$$K_{pw}(a/h, z/h) = \frac{\cosh[(a/h)^{1/3}(1 + z/h)]}{\cosh[(a/h)^{1/3}]}, \text{ for solitary waves.} \quad (3.21)$$

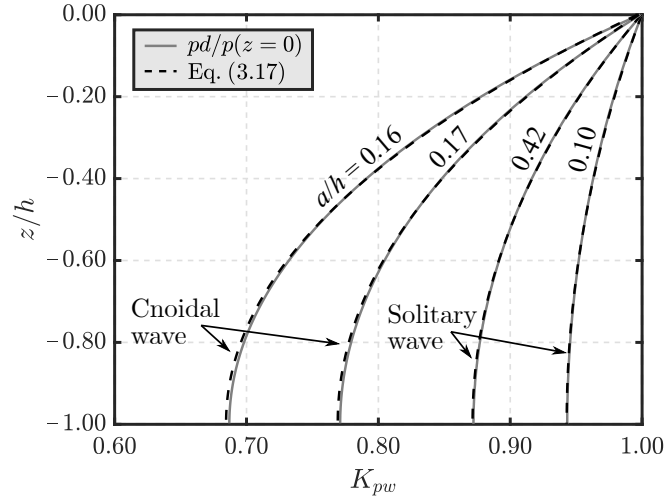


Figure 3.8. Distribution of the pressure response factor at the wall K_{pw} with z/h for $\beta = 90^\circ$ and Eq. (3.17) for $a/h = 0.10$ ($R^2 = 1.00$), 0.16 ($R^2 = 1.00$), 0.17 ($R^2 = 1.00$), and 0.42 ($R^2 = 1.00$) and $A = 3.47, 5.79, 4.45$, and 1.28 , respectively.

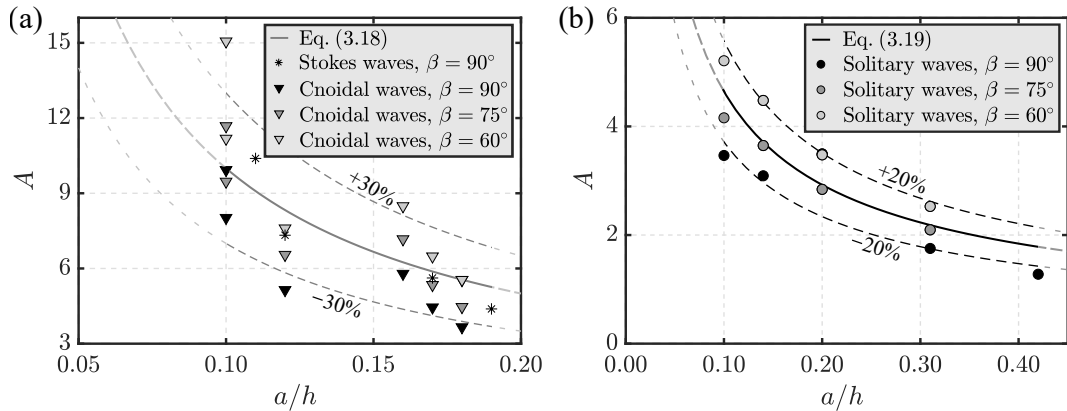


Figure 3.9. Coefficient A versus the relative wave amplitude a/h and (a) Eq. (3.18) for Stokes and cnoidal waves ($R^2 = 0.59$) and (b) Eq. (3.19) for solitary waves ($R^2 = 0.72$).

Eq. (3.21) shows that K_{pw} decays slower with z/h for smaller a/h than in Eq.

(3.20). K_{pw} for Stokes and cnoidal waves is a function of z/h only and would coincide with Eq. (3.21) for $a \rightarrow h$. Therefore, Eq. (3.21) operates on the safe side for $a/h < 1$ and can be used for Stokes and cnoidal waves also, i.e. the wave type does not need to be determined.

To summarise, semi-empirical equations for the pressure response factor at the wall K_{pw} were presented in this Section 3.3.2.3. These Eqs. (3.20) and (3.21), combined with the prediction of the total pressure p from Evers et al. (2019) (Eq. 3.3), directly provide the dynamic component of the pressure p_d (Eq. 3.16). To confirm these equations, the numerical $p(z)$ and $p_d(z)$ are compared with predictions of Evers et al. (2019) ($nRMSE = 0.017$ to 0.043) and Eq. (3.16) ($nRMSE = 0.04$ to 0.14) in Fig. 3.10 for 4 representative tests. The good agreement confirms the suitability of the new semi-empirical equations for engineering applications.

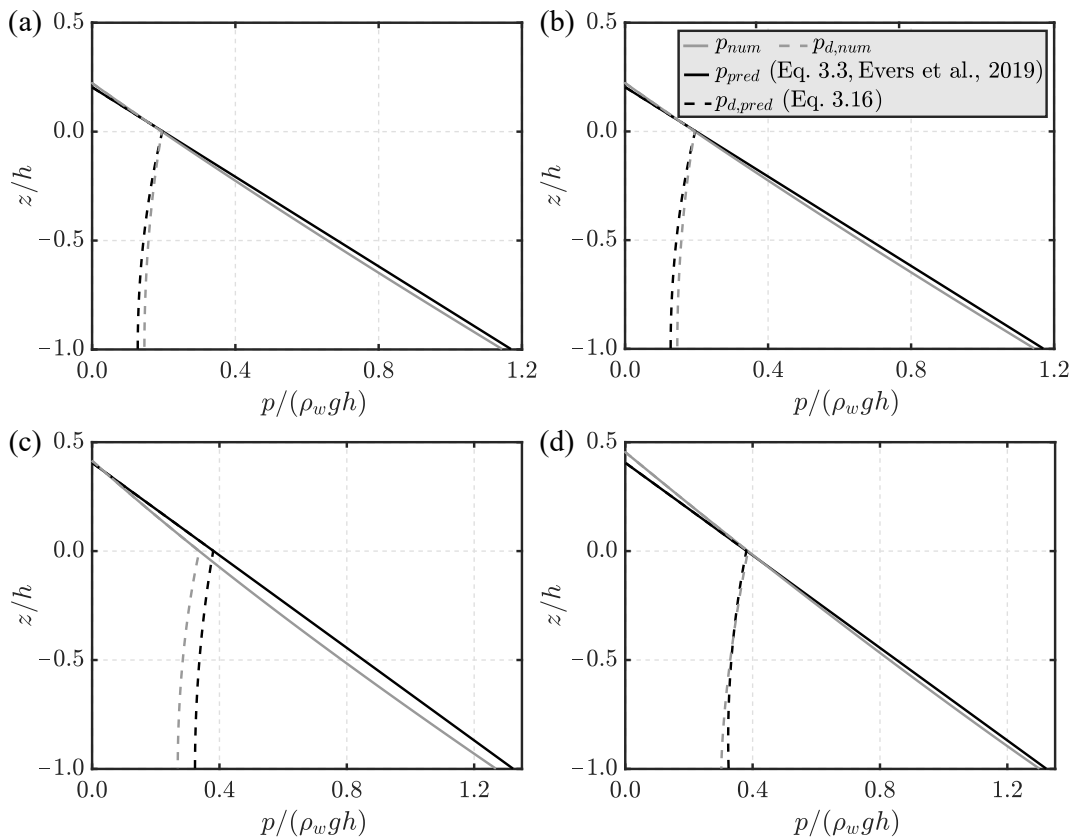


Figure 3.10. Comparison of the total $p/(\rho_w g h)$ and dynamic pressure $p_d/(\rho_w g h)$ with predictions from Evers et al. (2019) (Eq. 3.3) and Eq. (3.16) for cnoidal waves with $a/h = 0.10$ and (a) $\beta = 90$ and (b) 60° and solitary waves with $a/h = 0.20$ and (c) $\beta = 90$ and (d) 60° .

3.3.3 Overtopping waves

3.3.3.1 Force and bending moment

In 37 of the 72 tests (Table 3.1) R exceeded the freeboard f and the waves overtopped the dam, as shown in Fig. 3.11 for a solitary wave with $a/h = 0.28$, $f = 14$ m, and $\beta = 90^\circ$. In these cases, only a part of the wave loading is transferred on the dam (Appendix 3.A). The ratios $F_{H,red}/F_h$ and $M_{H,red}/M_h$ versus a/h are shown in Fig. 3.12a, c. Moreover, Fig. 3.12b, d shows $F_{H,red}/F_h$ and $M_{H,red}/M_h$ versus f/h . $F_{H,red}/F_h$ and $M_{H,red}/M_h$ decrease with increasing a/h for a constant f/h , except for the solitary wave test with $a/h = 0.6$ and $\beta = 90^\circ$, whereas larger f/h result in larger wave loadings for a constant a/h (Fig. 3.12b, d).

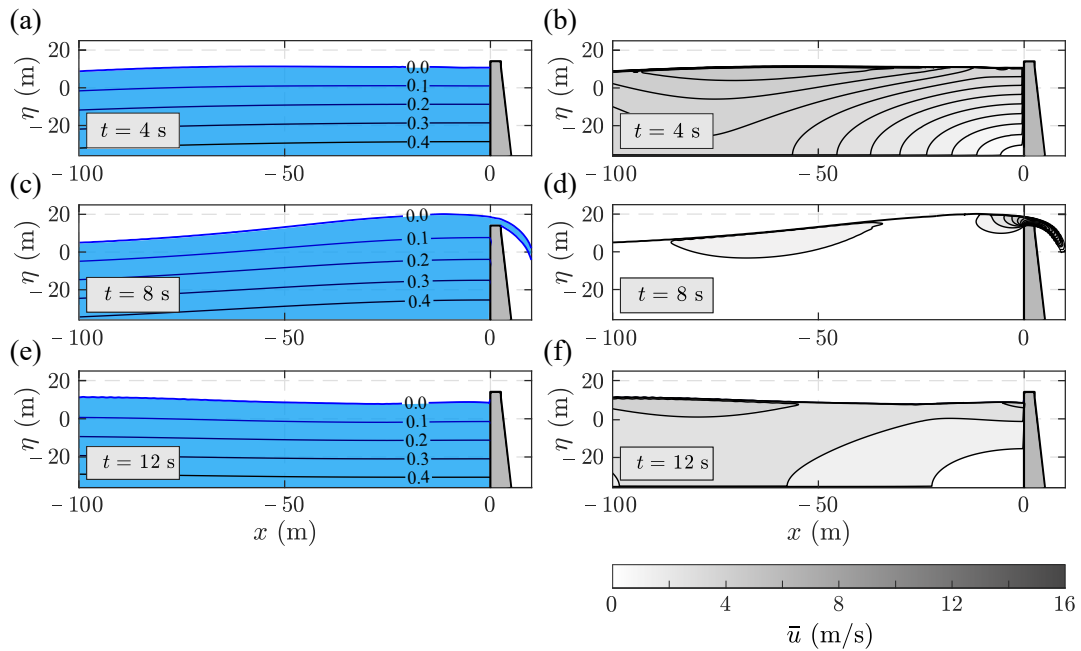


Figure 3.11. Snapshot series of a solitary wave impact on a dam with overtopping with $a/h = 0.28$ with (a, c, e) pressure contours in MPa and (b, d, f) mean velocity \bar{u} contours.

Fig. 3.12e, f shows $F_{H,red}$ and $M_{H,red}$ versus the predicted values for $F_{H,red}$ and $M_{H,red}$ based on Evers et al. (2019). Their method disregarding the top part of the pressure distribution on F_H and M_H (Appendix 3.A) agrees with the numerical results. This method results in predictions of $F_{H,red}$ and $M_{H,red}$ on the safe side for most of the experiments with deviations of up to approximately 15 and 20%,

respectively (Fig. 3.12e, f).

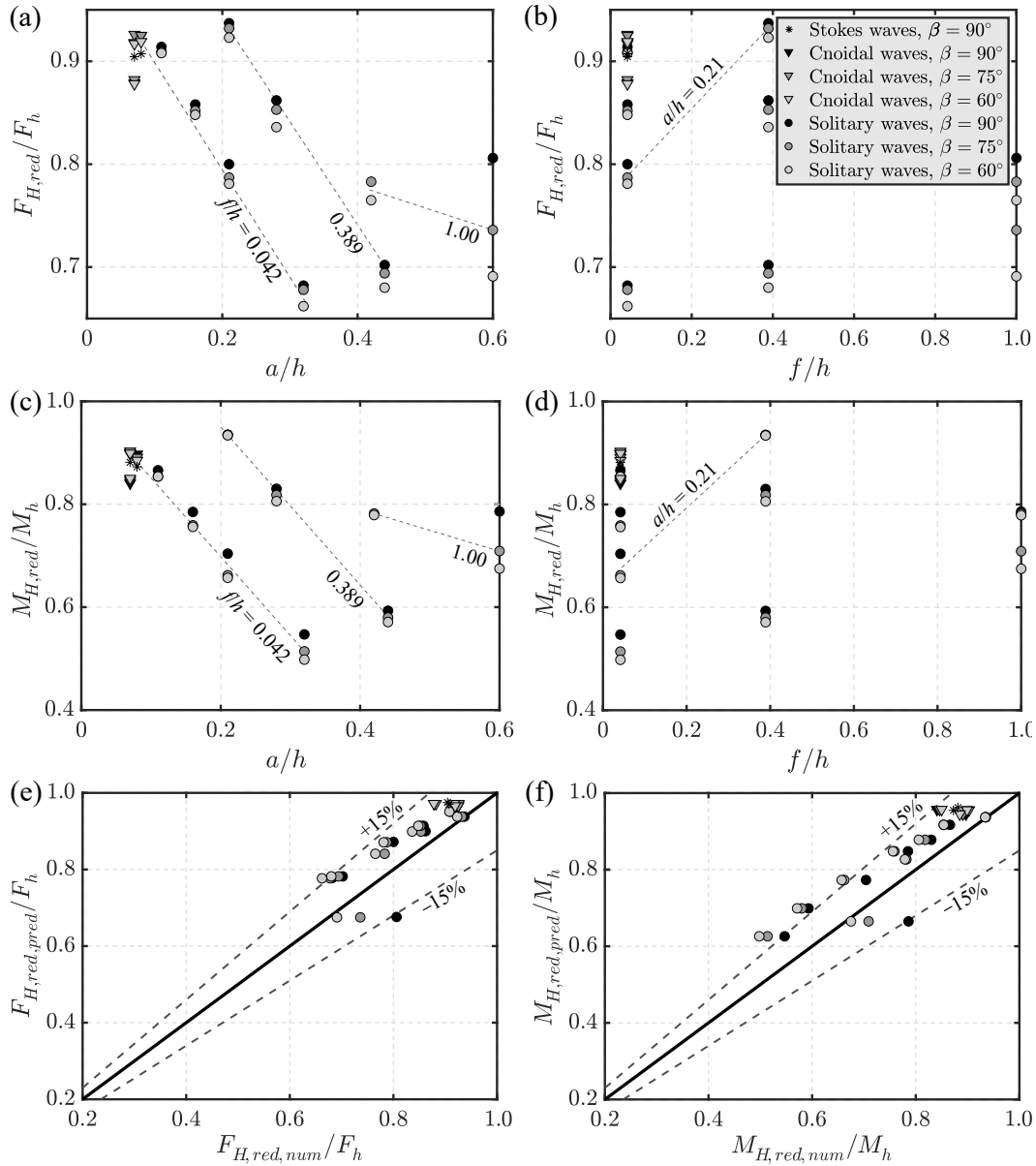


Figure 3.12. Overtopping waves: relative reduced horizontal force $F_{H,red}/F_h$ versus (a) a/h and (b) f/h , moment $M_{H,red}/M_h$ versus (c) a/h and (d) f/h , and comparison of the predicted (Evers et al., 2019) and numerical (e) $F_{H,red}/F_h$ and (f) $M_{H,red}/M_h$ at the dam.

Only the 3 solitary waves with $a/h = 0.6$ are underestimated, namely by up to 19%, compared to the numerical results (Fig. 3.12e, f). In these extreme cases, due to the relatively large wave steepness $a/L \approx 0.065$ (with L from Eq. 3.25), surging breaking was initiated in proximity of the dam. Surging breakers usually occur in proximity of steep slopes and are characterised by little foam (Galvin, 1968). Surging

breaking may be the reason for the observed deviations.

3.3.3.2 Overtopping

The overtopping volume per unit dam width Ψ and the maximum overtopping depth over the dam crest d_0 were also investigated. The numerical toolbox was first validated with the laboratory experiments of Kobel et al. (2017) (Section 3.3.1.3). Ψ was evaluated at the upstream corner of the dam crest as

$$\Psi = \sum_t \frac{q(t) + q(t+1)}{2} \Delta t, \quad (3.22)$$

with the discharge per unit dam width $q(t)$ defined as $\sum_z \bar{u}_x(z) \Delta z$, for $f \leq z \leq (f + d_0)$.

Ψ/h^2 and d_0/h are shown in function of a/h in Fig. 3.13. Both Ψ/h^2 and d_0/h increase with increasing a/h for a constant f/h , except for the solitary wave with $a/h = 0.6$ and $\beta = 90^\circ$. In this test the splash generated during wave impact may explain the relatively larger values of d_0/h compared to the remaining tests (Fig. 3.13b).

In addition to a/h , β and f/h have also a significant effect on the investigated parameters. Smaller β result in smaller Ψ/h^2 and larger d_0/h (Fig. 3.13a), while both Ψ/h^2 and d_0/h decrease with increasing f/h . An exception is once more the solitary wave with $a/h = 0.6$ and $\beta = 90^\circ$.

For the Stokes and cnoidal wave tests, the effects of T on Ψ and d_0 are also important. They become even more relevant in combination with the effects of a/h and β . In the cnoidal wave tests with $\beta = 90^\circ$, an increase of T by 33% results in a 25% larger Ψ . The same increase of T resulted in 77 and 96% greater Ψ for $\beta = 60$ and 75° , respectively.

Ψ/h^2 and d_0/h can be predicted with the empirical equations of Kobel et al. (2017) (Eqs. 3.26 and 3.27). They are compared with the present data in Section 3.4.3. However, for $a \leq f$, Eq. (3.26) cannot be applied and Eq. (3.27) is in poor

agreement with the present study. Based on the numerical data, Ψ/h^2 and d_0/h were approximated for $a \leq f$ in function of a , f , h , and β as

$$\frac{\Psi}{h^2} = 44 \left(\frac{a}{h}\right)^{10.6} \left(\frac{f}{h}\right)^{-7.5} \left(\frac{\beta}{90^\circ}\right)^{-0.1} \quad \text{and} \quad (3.23)$$

$$\frac{d_0}{h} = 24 \left(\frac{a}{h}\right)^{7.1} \left(\frac{f}{h}\right)^{-4.5} \left(\frac{\beta}{90^\circ}\right)^{1.5}. \quad (3.24)$$

These correlations were optimised with a least-squares regression analysis and are shown in Fig. 3.13c, d together with the numerical data. The aforementioned effects of each parameter are consistent with the pre-sign of the exponents in Eqs. (3.23) and (3.24) and for both equations the most dominant parameter resulted in a/h , followed by f/h .

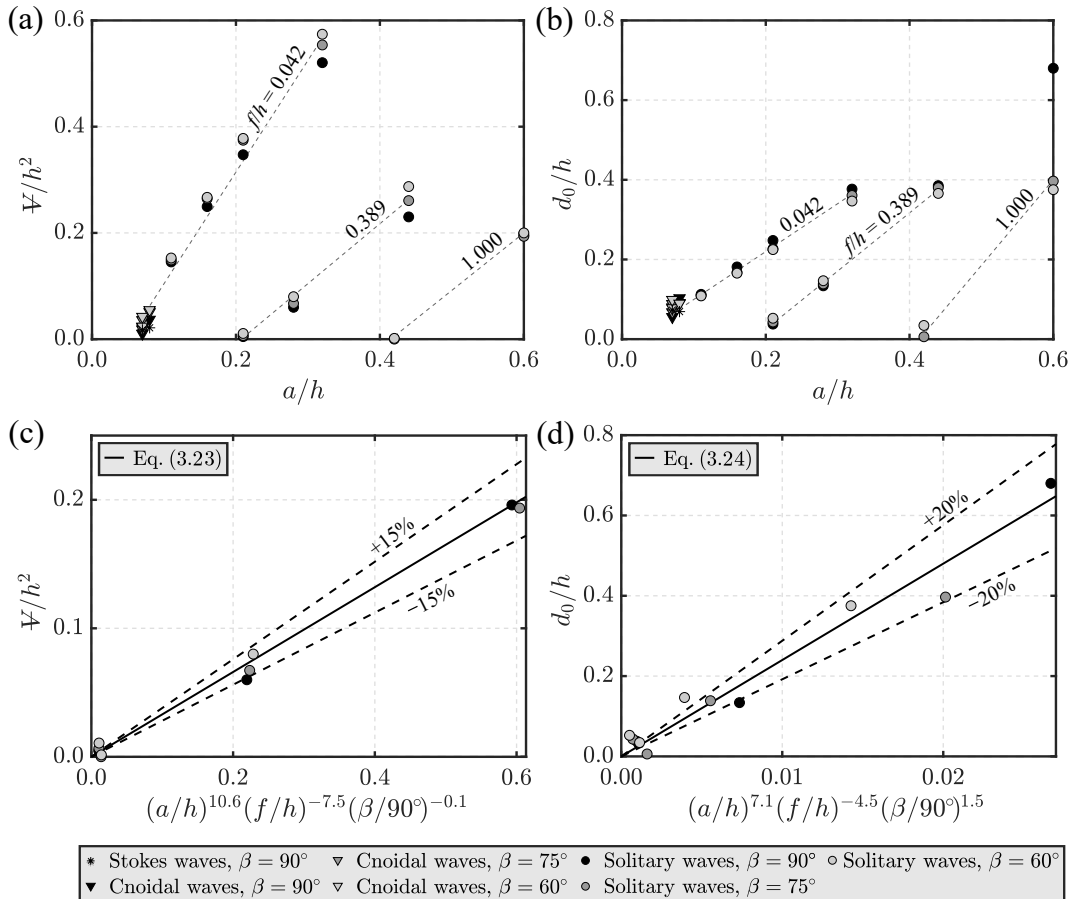


Figure 3.13. Relative overtopping (a) volume Ψ/h^2 and (b) maximum depth d_0/h versus a/h and correlations of (c) Ψ/h^2 with Eq. (3.23) ($R^2 = 0.99$) and (d) d_0/h with Eq. (3.24) ($R^2 = 0.96$).

3.4 Discussion of results

3.4.1 Validation of the available prediction method and limitations

The prediction method for tsunami forces on dams of Evers et al. (2019) was validated for a wide range of wave conditions and dam inclinations with 72 numerical tests (Figs. 3.7 and 3.12e, f). The numerical experiments replicate hypothetical, yet realistic, cases at real-world scale without scale effects (Heller, 2011; Bredmose et al., 2015). To apply Eqs. (3.1) and (3.2) and the equations for waves with overtoppings (Appendix 3.A) in nature, the dimensionless wave parameters need to be within the investigated ranges, i.e., $0.07 \leq a/h \leq 0.60$, $0.13 \leq H/h \leq 0.26$, and $7.2 \leq T(g/h)^{1/2} \leq 18.8$, for 5th order Stokes, cnoidal, and/or solitary waves, and dam inclinations of $60^\circ \leq \beta \leq 90^\circ$.

Table 3.3 includes some historical subaerial landslide-tsunamis. The dimensionless maximum a/h and $T(g/h)^{1/2}$ for these events are all within the limits of the present study, apart from $T(g/h)^{1/2}$ of the Lake Askja event. Further, the investigated values for β in the present study are typical for concrete dams.

Table 3.3. Main parameters of some subaerial landslide-tsunami events.

Event	h [m]	a/h [-]	$T(g/h)^{1/2}$ [-]	References
Pontesei Lake, 1959	47	0.40	Not available	Panizzo et al. (2005a)
Cabrera Lake, 1965	50 to 200	0.125 to 0.500	Not available	Watt et al. (2009)
Chehalis Lake, 2007	120	0.47	9.35	Wang et al. (2015); Evers (2017)
Lake Askja, 2014	138	0.25	6.30	Gylfadóttir et al. (2017); Ruffini et al. (2019)

3.4.2 Run-up height

Predictions with Eq. (3.13) are compared with laboratory measurements of Street and Camfield (1967), Maxworthy (1976), and Müller (1995) (Table 3.4) in Fig. 3.14a. Only data within the limitations of β of the present study were selected. The predicted R/h capture the experimental R/h and most of the tests lie within $\pm 20\%$ of the

prediction.

Fig. 3.14b shows the predicted R/h with the equations included in Table 3.4 versus the numerical R/h from the present study. Hall and Watts (1953) and Evers and Boes (2019) expressed R/h as a function of a/h and β only, while Müller (1995) includes H/h , H/L , and β (Table 3.4). This requires the wave length for solitary waves, which can be approximated as (Lo et al., 2013)

$$L = 2\pi h / (0.75a/h)^{1/2}. \quad (3.25)$$

Table 3.4. Predictions and limitations of the run-up height R in the present and other studies.

Reference	R/h	Limitations
Hall and Watts (1953)	$3.05 \tan(\beta)^{-0.13} \left(\frac{a}{h}\right)^{1.15 \tan(\beta)^{0.02}}$	$0.050 \leq a/h \leq 0.564$, $10^\circ \leq \beta \leq 45^\circ$
Street and Camfield (1967)	No empirical equation available	$0.100 \leq a/h \leq 0.645$, $\beta = 90^\circ$
Maxworthy (1976)	No empirical equation available	$0.118 \leq a/h \leq 0.665$, $\beta = 90^\circ$
Müller (1995)	$1.25 \left(\frac{H}{h}\right)^{5/4} \left(\frac{H}{L}\right)^{-3/20} \left(\frac{90^\circ}{\beta}\right)^{1/5}$	$0.011 \leq a/h \leq 0.521$, $18.4^\circ \leq \beta \leq 90^\circ$
Evers and Boes (2019)	$2 \frac{a}{h} \exp\left(0.4 \frac{a}{h}\right) \left(\frac{90^\circ}{\beta}\right)^{0.20}$	$0.007 \leq a/h \leq 0.690$, $10^\circ \leq \beta \leq 90^\circ$
Eq. (3.13)	$\frac{9}{4} \left(\frac{90^\circ}{\beta}\right)^{1/3} \frac{a}{h}$	$0.100 \leq a/h \leq 0.420$, $60^\circ \leq \beta \leq 90^\circ$

Hall and Watts (1953) are applied for $\beta = 60$ and 75° only, as their equation involves the tangent of the inclination β preventing estimates for $\beta = 90^\circ$. The equation of Hall and Watts (1953) underestimates the numerical R/h by up to 64%, apart from a few tests. These deviations are partially due to the violation of the limitations of β (Table 3.4). The equation of Müller (1995) successfully predicts most of the cnoidal wave tests, while the solitary waves are underestimated by up to 42%. Similar agreements are achieved by Evers and Boes (2019) and Eq. (3.13) based on

the numerical R/h . Most of the tests show relatively small deviations and only a few cases are underestimated, namely by up to 39% by the equation of Evers and Boes (2019) and by up to 32% by Eq. (3.13) (Fig. 3.14b).

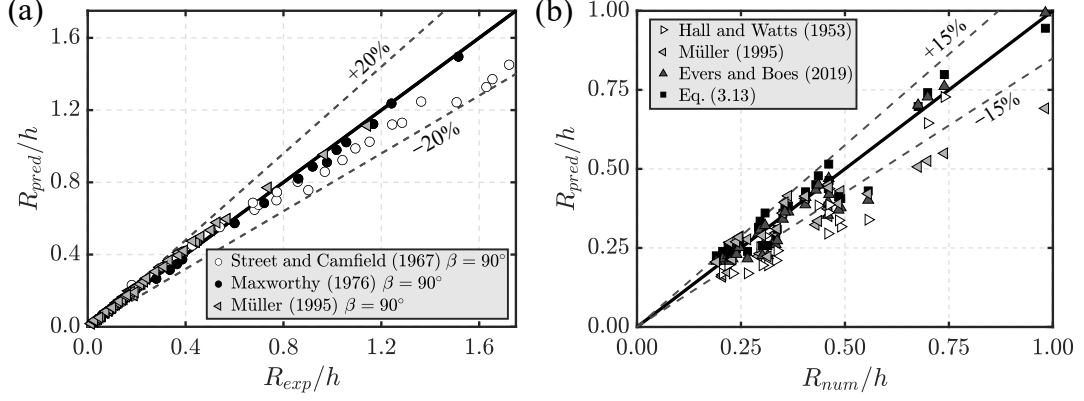


Figure 3.14. Predicted relative run-up heights R_{pred}/h (a) based on Eq. (3.13) versus the experimental R_{exp}/h of Street and Camfield (1967), Maxworthy (1976), and Müller (1995) with $\beta = 90^\circ$ and (b) based on Hall and Watts (1953), Müller (1995), Evers and Boes (2019), and Eq. (3.13) (Table 3.4) versus the numerical R_{num}/h of the present study.

3.4.3 Overtopping

The overtopping volume Ψ and the maximum overtopping depth over the dam crest d_0 (Section 3.3.3.2) are compared with the empirical predictions of Kobel et al. (2017), which are

$$\Psi = 1.35 \left(\frac{a}{H} \right)^{1.5} \left[\frac{a}{h} \left(\frac{h}{l} \right)^{(2h/a)(\beta/90^\circ)^{0.25}} \left(\frac{a-f}{s} \right)^{0.12} \right]^{0.7} h^2 \quad \text{and} \quad (3.26)$$

$$d_0 = 1.32 \left[\frac{a}{h} \left(\frac{h}{l} \right)^{4[(\beta/90^\circ)^{-0.21} - a/h]} \left(\frac{\beta}{90^\circ} \right)^{0.16} \right] l. \quad (3.27)$$

The comparison is shown in Fig. 3.15. For $a \leq f$, overtoppings occur due to the increase in η once the wave is reflected at the dam and Ψ/h^2 cannot be predicted with Eq. (3.26). Instead, Eq. (3.23) can be used. Eq. (3.26) successfully captures the numerical results, with most of the data showing a deviation on the safe side of less than 15%. Stokes and cnoidal waves show relatively large deviations with

overestimations of up to 75%; these are attributed to the fact that Eq. (3.26) is based on solitary wave laboratory tests.

Fig. 3.15b shows the predicted d_0/h with Kobel et al. (2017) and Eq. (3.24), applicable for $a \leq f$ only, versus the numerical d_0/h . Eq. (3.27) agrees with the numerical results for the tests with $a > f$, showing the largest deviations of up to 36% for the Stokes and cnoidal wave tests, once more because Eq. (3.27) is based on a different wave type. Most of the tests with $a \leq f$ (encircled data in Fig. 3.15b) are overpredicted by Eq. (3.27) with relatively large deviations. Eq. (3.24) results in smaller deviations, however, the prediction of the overtopping waves with $a \leq f$ remains even then challenging. Table 3.5 shows a summary of the most suitable equations for the prediction of wave run-ups and overtoppings.

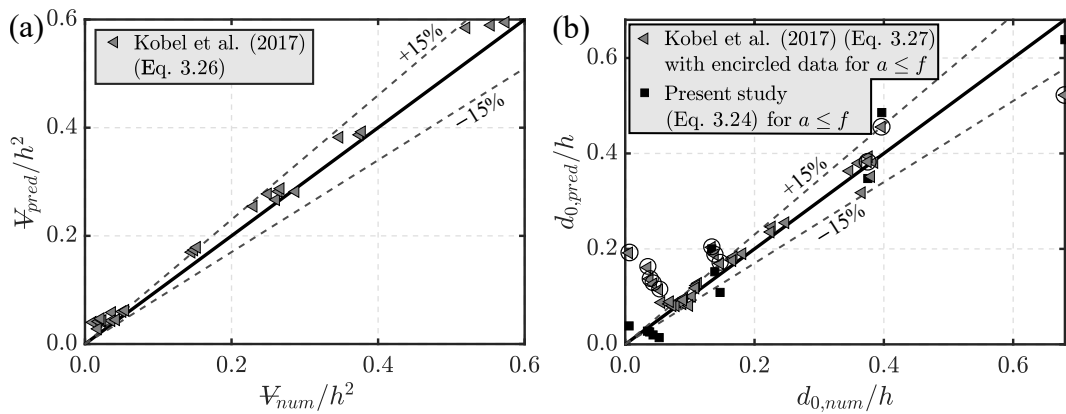


Figure 3.15. Comparison of the predicted and numerical relative overtopping (a) volume \mathcal{V}/h^2 and (b) maximum depth d_0/h with encircled data predicted by Kobel et al. (2017) for $a \leq f$.

Table 3.5. Summary of the most suitable equations to predict landslide-tsunami run-ups and overtoppings.

		No overtopping	Overtopping	
			$a \leq f$	$a > f$
Run-up height	R	Eq. (3.13)	-	-
Overtopping volume	\mathcal{V}	-	Eq. (3.23)	Eq. (3.26) (corresponding to Eq. 2 in Kobel et al., 2017)
Overtopping depth	d_0	-	Eq. (3.24)	Eq. (3.27) (corresponding to Eq. 4 in Kobel et al., 2017)

Note that the new methods introduced herein also provide good estimates of non-

breaking tsunami forces, pressures, and overtoppings for a range of steep to vertical coastal engineering structures. Therefore, such estimates support tsunami hazard assessment in coastal environments in general.

3.4.4 3D simulations to investigate 3D effects

3.4.4.1 Symmetrical wave impact angle

For the gravity dam with normal wave impact ($\gamma = 0^\circ$, Fig. 3.1b, d) the different boundary conditions used at $y = 0$ and 25 m result in small deviations of the main parameters, e.g. p and α , across the dam width (Section 3.2.2.1). R/h is constant across y/h and $R_{max}/h = 0.68$ agrees with the predicted value of 0.68 from Eq. (3.13) (Fig. 3.16).

Fig. 3.16 shows η/h across the arch dam (Fig. 3.1c, e) with $\gamma = 0^\circ$ during R_{max}/h at $y = 25$ m. The dam curvature induces an increase in R/h of approximately 10% close to the lateral flanks of the reservoir. At $y = 0$ m, $R_{max}/h = 0.66$ at $t = 6.2$ s, which is still well captured by Eq. (3.13) with $\beta = 90^\circ$. At $y = 25$ m, $R_{max}/h = 0.72$ is delayed and approximately 9% larger than at $y = 0$ m (Fig. 3.16).

For the arch dam, the force vector per unit dam width \mathbf{F} was calculated as

$$\mathbf{F}(y, t) = \sum_i^N p(y, z_i, t) \mathbf{n}_i \Delta z, \quad (3.28)$$

with $p(y, z_i, t)$ as the numerical pressure at the cell (y, z_i) , N as the number of $p(z)$ values, and \mathbf{n}_i as the normal vector to the dam surface. Similarly, the force vector acting over the entire dam is

$$\mathbf{F}_{3D}(t) = \sum_i^N \sum_j^P p(y_i, z_j, t) \mathbf{n}_{i,j} S_{i,j}, \quad (3.29)$$

with $p(y_i, z_j, t)$ as the numerical pressure at the cell (y_i, z_j) , N and P as the number of p values along y and z , and $S_{i,j}$ as the cell area. Hence, the horizontal components F_H and $F_{H,3D}$ were calculated as the resultant of the x and y components.

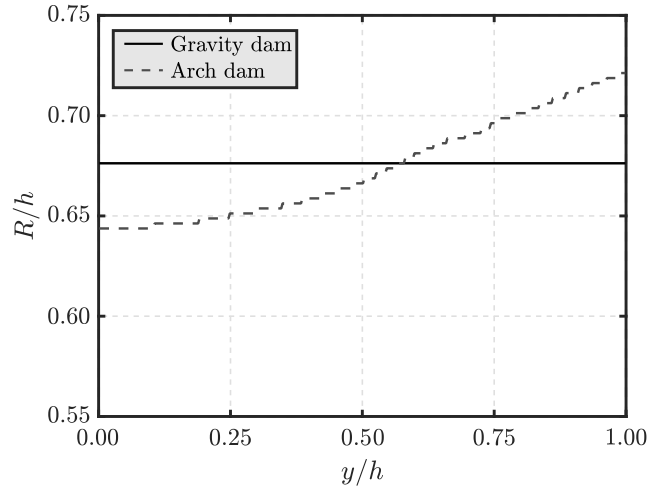


Figure 3.16. Maximum relative run-up height R_{max}/h versus y/h for the gravity dam and R/h versus y/h for the arch dam at $t = 6.8$ s, with $a/h = 0.3$ and $\gamma = 0^\circ$.

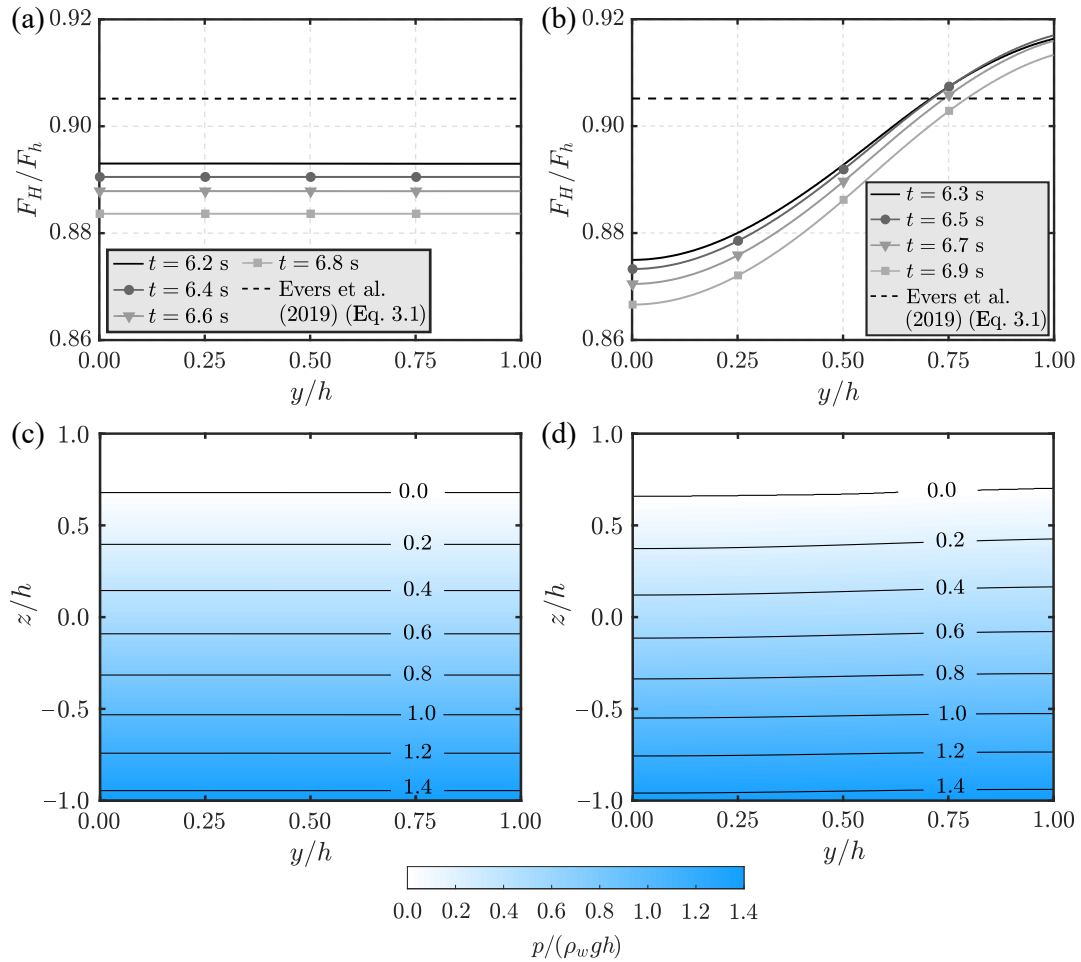


Figure 3.17. Symmetrical wave impact ($\gamma = 0^\circ$): dimensionless force F_H/F_h versus the relative dam width y/h at the (a) gravity and (b) arch dam and pressure $p/(\rho_wgh)$ versus y/h and z/h during the maximum force at the (c) gravity and (d) arch dam.

Fig. 3.17a, b shows F_H/F_h versus y/h for the gravity and arch dam. The gravity dam shows constant values of F_H/F_h across the width with the maximum F_H/F_h overestimated by only 1.3% by the prediction based on Evers et al. (2019) (Eq. 3.1). A larger F_H/F_h in proximity of the flanks acts on the arch dam (Fig. 3.17b). However, the effect of the curvature on F_H/F_h may be neglected as the deviations between $y = 0$ and 25 m are only up to 4.7% and the maximum F_H/F_h is only 1.3% greater compared to the prediction based on Evers et al. (2019) (Eq. 3.1). The maximum force acting over the whole dam $F_{H,3D}$ was normalised with $bF_h/2$, with the dam width $b = 50$ m. This resulted in 0.89 and 1.01, for the gravity and arch dam, respectively, and $p/(\rho_w g h)$ during the maximum F_{3D} is shown in Fig. 3.17c, d.

3.4.4.2 Asymmetrical wave impact

Fig. 3.18 shows a snapshot series in the xy plane for the gravity dam and asymmetrical wave impact. In these tests the wave travelled along the wave tank with direction $\gamma = 30^\circ$ (Fig. 3.1). The wave was reflected by the tank boundary at $y = -25$ m ($y/h = -1$) with a concentration of energy at the corresponding dam corner. Diffraction occurred at the opposite side of the wave tank with lateral spread of the wave energy. The solitary wave impact on the gravity and arch dam, respectively, for asymmetrical wave impact, are shown in Fig. 3.19.

The concentration of energy at the dam flank at $y/h = -1$, resulted in a significant increase of R/h for both the gravity and arch dam. For the gravity dam, R/h overall increases across the dam width (Fig. 3.19a, b, c). For $t \geq 2.5$ s, R/h is approximately constant at $-1.00 \leq y/h \leq -0.75$, reaching the maximum $R/h = 0.82$ at $t = 3.0$ s. This is 64 and 21% larger compared to the maximum R/h at $y/h = 1$ and the prediction with Eq. (3.13), respectively. The effect of the asymmetrical wave impact is even more relevant in combination with the effect of the curvature of the dam. As revealed by Fig. 3.19d, e, f, R/h reaches the maximum of 0.90 at $y/h = -1$ and $t = 4.0$ s for the arch dam, which is 32% larger than the prediction with Eq. (3.13). The maximum $R/h = 0.55$ at $y/h = 1$ occurs at $t = 3.0$ s and is 63% smaller than

at $y/h = -1$.

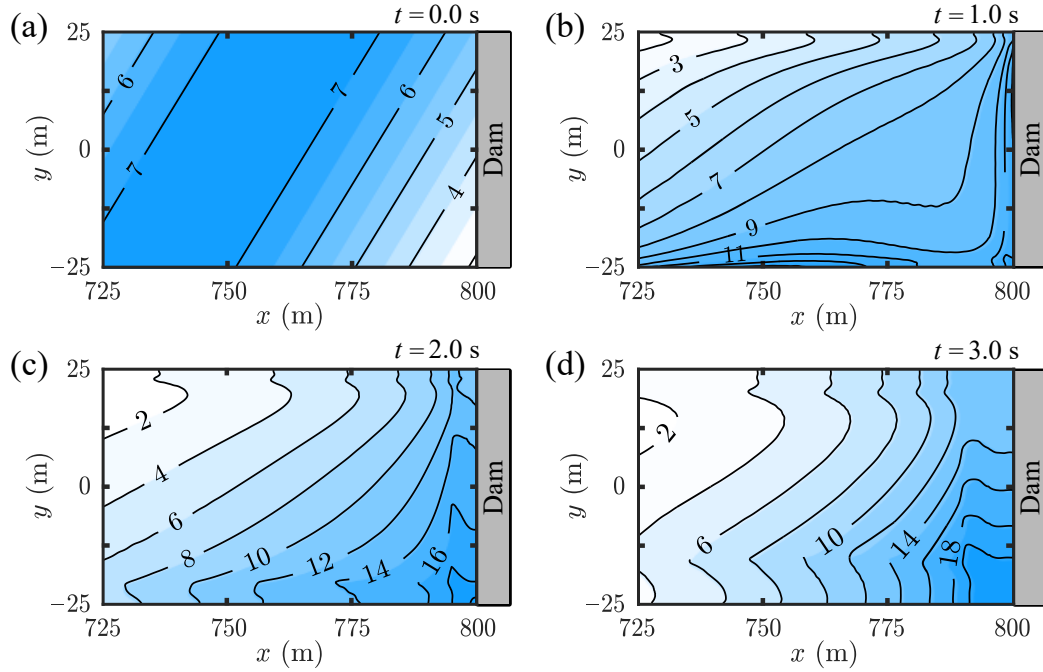


Figure 3.18. Snapshot series with surface elevation contours in m of a solitary wave impact on the gravity dam with $a/h = 0.3$ and $\gamma = 30^\circ$ at $t =$ (a) 0.0, (b) 1.0, (c) 2.0, and (d) 3.0 s.

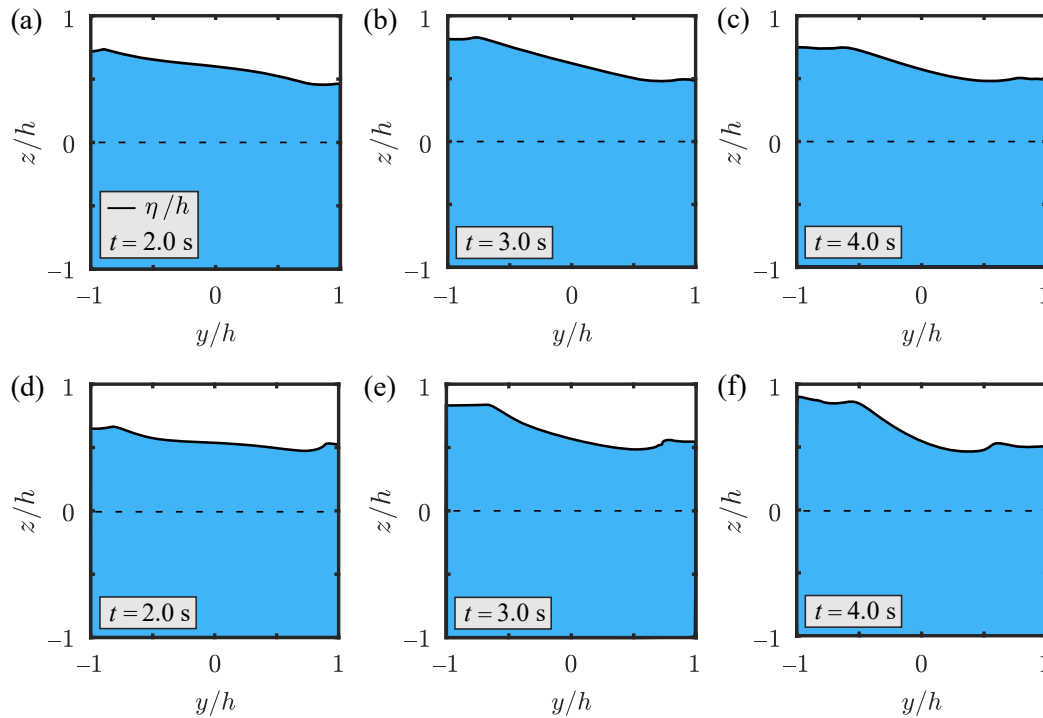


Figure 3.19. Snapshot series of a solitary wave impact on the (a, b, c) gravity and (d, e, f) arch dams with $a/h = 0.3$ and $\gamma = 30^\circ$ at $t = 2, 3,$ and 4 s.

Fig. 3.20a, b shows F_H/F_h versus y/h for the gravity and arch dams. F_H/F_h

increases with smaller y/h for the gravity dam, reaching a maximum of 0.91 at $y/h = -1$. F_H/F_h is approximately constant for the arch dam at $0.6 < y/h \leq 1.0$, decreases for $0.3 \leq y/h \leq 0.6$ and increases for $y/h < 0.3$, reaching the maximum $F_H/F_h = 0.97$ at $y/h = -1$. The gravity and arch dams show similar values of F_H/F_h for $y/h > 0.6$, while the curvature of the arch dam induces larger F_H/F_h in proximity of the flank at $y/h = -1$. Although F_H may not be normal to the dam axis, due to $\gamma \neq 0^\circ$ and the curvature of the dam, the maximum F_H/F_h is once more well predicted by Eq. (3.1) for both the gravity and arch dams, with small underestimations of a maximum of 7%. The maximum $F_{H,3D}/(bF_h)$ resulted in 0.87 and 0.88 and the contours of p at t during the maximum F_{3D} are shown in Fig. 3.20c, d.

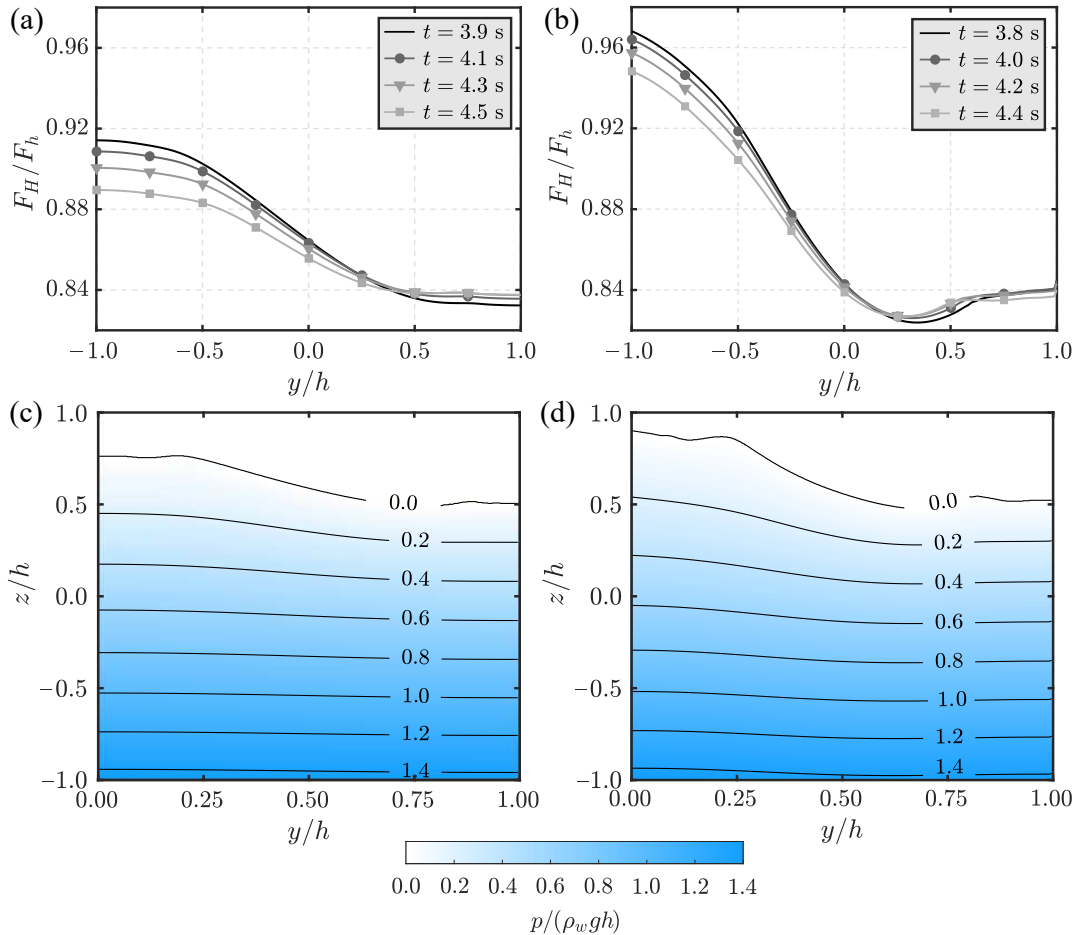


Figure 3.20. Asymmetrical wave impact ($\gamma = 30^\circ$): dimensionless force F_H/F_h versus the relative dam width y/h at the (a) gravity and (b) arch dam and pressure $p/(\rho_w g h)$ versus y/h and z/h during the maximum force at the (c) gravity and (d) arch dam.

As discussed above, the boundaries of the reservoir confine the tsunami with a significant concentration of energy in proximity of the dam. The dam curvature and asymmetrical wave impact resulted both in higher R at the dam flanks. These two effects combined resulted in an increase of R of up to 32%. In contrast, these 3D effects can be neglected for F_H . Although in nature some reservoirs have a similar geometry as the one investigated in the present study, e.g. the Derwent reservoir in England and the Luzzone reservoir in Switzerland, in most cases, the reservoir geometry is less idealised. Furthermore, the waves may approach the dam with a more extreme angle than $\gamma = 30^\circ$ and the bathymetry may not be flat. Therefore, the wave behaviour can be more complex (Couston et al., 2015; Ruffini et al., 2019).

3.5 Conclusions

The present article aimed to investigate landslide-tsunamis impacting dams with the numerical toolbox `solids4foam` in `foam-extend`. This investigation was motivated by the limited validation of available prediction methods for tsunami pressures and forces on dams, which is also a drawback for a range of offshore and coastal engineering applications. Moreover, additional methods to predict the overtopping waves under certain conditions were required.

The numerical toolbox `solids4foam` was successfully validated with available laboratory measurements, an analytical model, and a numerical solution for pressures, forces, and overtoppings of waves impacting a vertical wall. A total of 72 2D numerical experiments with 5th order Stokes, cnoidal, and solitary waves impacting dams of inclinations $60^\circ \leq \beta \leq 90^\circ$ were performed. The tsunami forces and moments on dams were in agreement with predictions based on Evers et al. (2019), extending their validation ranges.

New empirical equations for the wave run-up heights R , overtopping volumes Ψ , and maximum depths over the dam d_0 were proposed. R was expressed in function of the wave amplitude relative to the water depth a/h and β (Eq. 3.13). Ψ and d_0

were expressed in function of a , h , f , and β (Eqs. 3.23 and 3.24) for the tests with $a \leq f$. Larger waves resulted in larger Ψ and d_0 . In contrast, Ψ and d_0 decreased with increasing freeboard f for a given wave (Fig. 3.13). A summary of the most suitable equations to predict R , Ψ , and d_0 is shown in Table 3.5. Further, a new semi-empirical approach for the dynamic pressure of tsunamis impacting dams was presented in Section 3.3.2.3. This approach, combined with the prediction of the total pressure from Evers et al. (2019), provides the dynamic component of the pressure.

Furthermore, a total of 4 3D simulations were conducted with either a straight or an arch dam impacted by solitary waves normal or at an angle of 30° (Section 3.4.4). For a normal wave impact, the curvature of the dam induced larger R at the dam flanks of up to 9%, while the effects on the force can be neglected such that the 2D equations of Evers et al. (2019) apply. For a solitary wave with asymmetrical wave impact of 30° , R was 21 and 32% larger for the gravity and arch dam, respectively, compared to the prediction for normal wave impact.

Future work will focus on waves interacting with flexible structures. The effects of the structural deformation on the wave field will be investigated together with scale effects for both rigid and flexible structures.

3.A Overtopping wave forces at dams

Waves overtop a dam when the run-up height R exceeds the freeboard f . For $f < 2a$, Evers et al. (2019) followed Heller et al. (2009) by suggesting a reduction of the force effects due to hydrostatic and wave pressures by removing the triangular section of the pressure above the dam crest (Fig. 3.11b in Evers et al., 2019). This results in a trapezoidal distribution of the pressure and the reduced horizontal force per unit dam width is

$$F_{H,red} = \frac{(h + f)}{2} \left[p_K + \frac{2F_H}{2a + h} \right]. \quad (3.A.1)$$

In Eq. (3.A.1) F_H is the force that would act on the dam without overtopping (Eq. 3.1) and p_K is the pressure at the dam crest

$$p_K = \frac{2F_H}{(2a + h)^2} (2a - f). \quad (3.A.2)$$

3.B Convergence tests

3.B.1 Convergence of the main tests

The numerical set-up used for the main tests and its discretisation is presented in Section 3.2.2. Convergence tests with a solitary wave of $a/h = 0.31$ have been conducted to find the optimal cell sizes. Resolutions of $\Delta x = \Delta z = 50.000, 25.000, 12.500, 6.250,$ and 3.125 cm have been investigated. The finest resolutions $\Delta x = \Delta z = 12.500, 6.250,$ and 3.125 cm were applied in a $25 \text{ m} \times 80 \text{ m}$ area in front of the dam and $\Delta x = \Delta z = 25.000$ cm was used in the rest of the domain (Fig. 3.1a). The convergence is shown here in terms of the force

$$F(t) = \sum_i^N \frac{p(z_i, t) + p(z_{i+1}, t)}{2} \Delta z, \quad (3.B.1)$$

with $p(z_i, t)$ as the numerical pressure at a certain height z and N as the number of $p(z)$ values. The maximum $F/(\rho_w g h^2/2)$ versus Δx ($= \Delta z$) is shown in Fig. 3.B.1a.

The values of $F/(\rho_w g h^2/2)$ increase with decreasing cell sizes and the deviations

between each Δx and $\Delta x/2$ decrease for smaller Δx (Fig. 3.B.1a). $\Delta x = \Delta z = 6.250$ cm was used for the main tests as convergence is achieved, resulting only in a 0.18% smaller value for $F/(\rho_w g h^2/2)$ than for $\Delta x = \Delta z = 3.125$ cm and requiring only 1/6 of the computation time.

3.B.2 Convergence of the validation tests

The numerical set-up for the validation tests in Section 3.3.1.1 has the same geometry as the experimental set-up of Mallayachari and Sundar (1995). The domain was discretised with squared cells and mesh resolutions of $\Delta x = \Delta z = 6.00, 3.00, 1.50,$ and 0.75 mm were investigated. The last two were applied only in a $L/4 \times 0.630$ m area in front of the plate and $\Delta x = \Delta z = 3.00$ mm was used in the rest of the domain.

Convergence tests were performed for the experiment shown in Fig. 3.2a. F on the plate is shown in Fig. 3.B.1b in function of the mesh sizes. Considering the small increment of $F/(\rho_w g h^2/2)$ of 1.4% between $\Delta x = \Delta z = 1.50$ and 0.75 mm (Fig. 3.B.1b), the larger computational efforts and some instability issues which occurred for $\Delta x = \Delta z = 0.75$ mm, $\Delta x = \Delta z = 1.50$ mm resulted in the optimal resolution (Fig. 3.B.2).

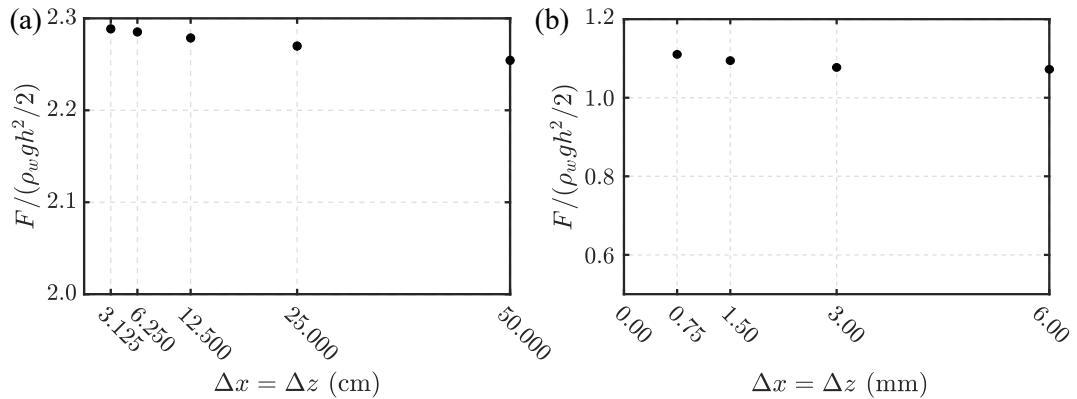


Figure 3.B.1. Convergence tests of the relative force $F/(\rho_w g h^2/2)$ with the mesh size $\Delta x = \Delta z$ for the (a) main and (b) validation tests.

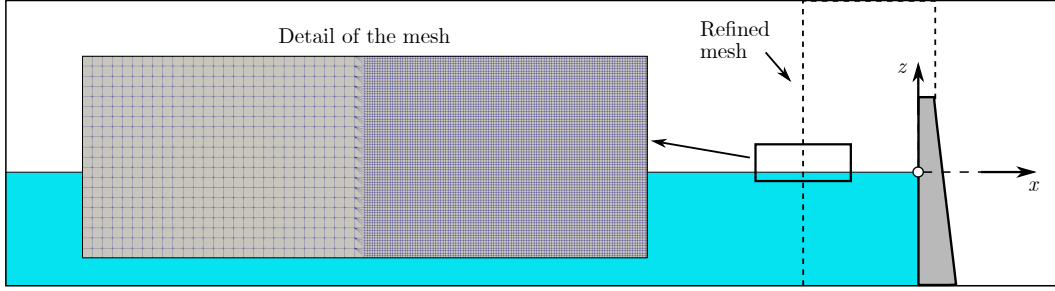


Figure 3.B.2. Numerical set-up with a detail of the mesh.

3.C Overtopping waves: dynamic pressure

The dynamics of the overtopping water may have a significant effect on p_d due to the additional water depth and larger velocities $u_x(z)$ in proximity of the crest compared to the waves which do not overtop. Fig. 3.C.1a, b shows the distribution of p and p_d in 2 solitary wave tests with $a/h = 0.21$, at $h = 36$ and 48 m, respectively. Due to the larger f/h of the test in Fig. 3.C.1a compared to Fig. 3.C.1b, smaller values of p were observed in proximity of the dam crest. In other words, a larger d_0 was observed in Fig. 3.C.1b, resulting in a larger p at the dam crest compared to Fig. 3.C.1a.

For the Stokes and cnoidal wave tests, with $0.07 \leq a/h \leq 0.08$ and $f/h = 0.042$, K_{pw} is poorly captured by Eq. (3.20) with $nRMSE$ of up to 3.13 (Fig. 3.C.1c). For the solitary wave tests with $0.21 \leq a/h \leq 0.44$ and $0.389 \leq f/h \leq 1.000$, the overtopping dynamics does not modify the pressure field significantly. In these cases, K_{pw} is captured by Eq. (3.21) with $nRMSE = 0.06$ to 0.41 for most tests apart from two with 0.79 and 1.86. For larger values of a/h and/or smaller f/h a different trend of $K_{pw}(z)$ is observed. In these cases, K_{pw} is larger than 1, reaches a peak in proximity of $z/h = -0.20$ and decreases then, as shown in Fig. 3.C.1d for some representative tests. This trend is likely due to the larger d_0 compared to the cases with smaller a/h and/or larger f/h .

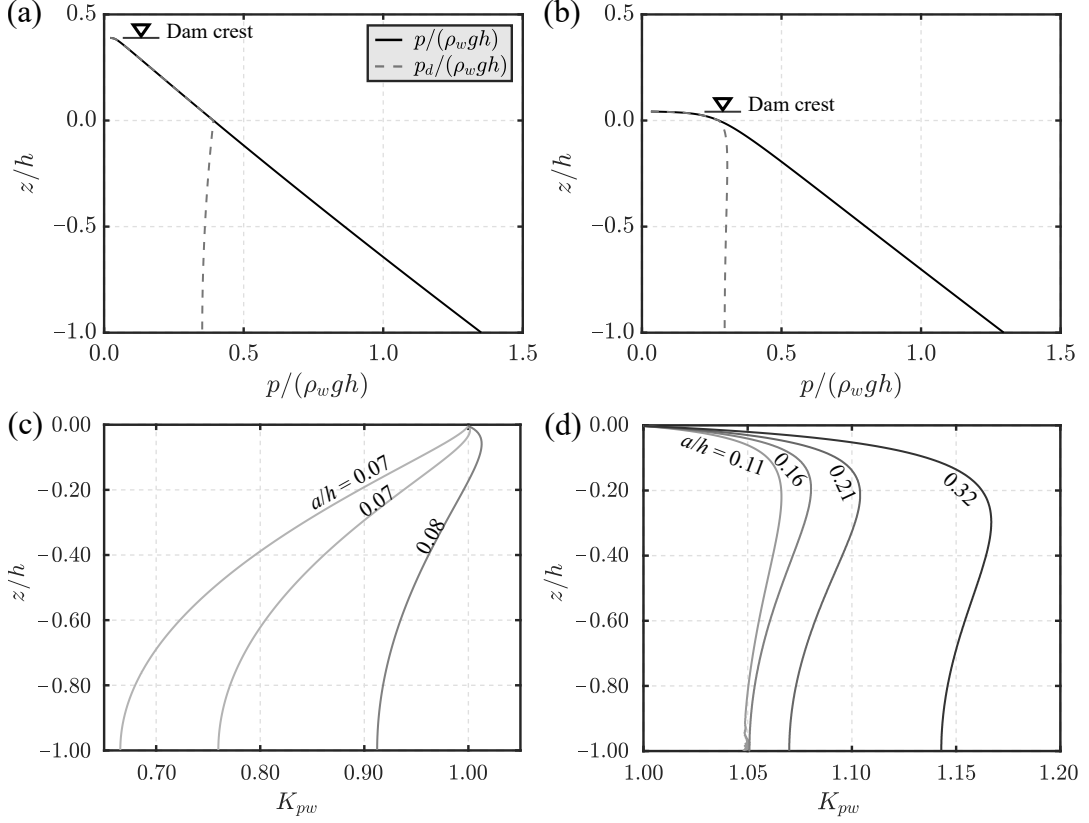


Figure 3.C.1. Total pressure p and dynamic pressure p_d at the dam in two overtopping tests with $a/h = 0.21$ and $\beta = 90^\circ$ with (a) $f/h = 0.389$ and (b) $f/h = 0.042$ and pressure response factor at the wall K_{pw} versus z/h for $f/h = 0.042$ for some representative (c) cnoidal and (d) solitary wave overtopping tests for $\beta = 90^\circ$.

The pressure $p(z)$ can be approximated with the trapezoidal distribution proposed by Evers et al. (2019) (Appendix 3.A) for engineering applications with wave overtoppings. For $0.21 \leq a/h \leq 0.44$ and $0.389 \leq f/h \leq 1.000$, the component p_d can be predicted as for waves without overtopping (Eq. 3.16) with K_{pw} defined in Eq. (3.21). For larger a/h and/or smaller f/h , it is challenging to find an expression for $K_{pw}(z)$ (Fig. 3.C.1c, d). However, a good preliminary estimation of p_d can be achieved in these cases by subtracting the hydrostatic component of the pressure from $p(z)$ (Eq. 3.11).

This page was intentionally left blank.

Chapter 4

Wave impact on rigid and flexible plates

This chapter is comprised of the following journal article:

Attili, T., Heller, V. and Triantafyllou, S., 2023. Wave impact on rigid and flexible plates. *Coastal Engineering* 182, 104302.

Despite of the different layout, the published paper is entirely included within this chapter with the following differences:

1. Section, page, figure, table and equation numbers are amended to ensure consistency across the thesis.
2. The reference to journal details, e.g. volume and page numbers, are omitted.
3. The email addresses of the authors have not been included.
4. Dates of submission, revision and acceptance have not been included.
5. Minor adjustments have been made to some equations, figures and text to provide more details and ensure consistency across the thesis.
6. The nomenclature and references list are provided at the end of this thesis.

Wave impact on rigid and flexible plates

Tommaso Attili¹, Valentin Heller¹, Savvas Triantafyllou²

¹Environmental Fluid Mechanics and Geoprocesses Research Group, Faculty of Engineering, University of Nottingham, Nottingham NG7 2RD, UK

²Institute for Structural Analysis and Aseismic Research, School of Civil Engineering, National Technical University of Athens, Athens, Greece

Abstract

Wave impact on offshore and coastal structures, such as oil and gas rigs, offshore wind turbine platforms, breakwaters, flood protection systems and wave energy converters, involve complex wave-structure interactions. These interactions are particularly challenging for flexible structures and may result in structural damage in extreme cases. Some studies found reduced wave forces on flexible compared to rigid walls. However, the technical literature includes inconclusive results on this aspect and an accurate understanding of wave-structure interaction is still lacking. The present study comprehensively investigates wave-structure interaction with the numerical toolbox `solids4foam` to resolve this shortcoming. The numerical pressures, forces and plate deformations have been successfully validated with new and already available laboratory experiments, e.g. the numerical plate displacement deviates less than 35% from the laboratory observation. 117 Two-Dimensional (2D) tests of waves impacting plates of different stiffnesses located in the open sea (offshore) and on the coast (onshore) were then conducted, complemented with 2 Three-Dimensional (3D) tests with offshore plates. For most of the offshore and onshore tests, the plate stiffness had a negligible effect on the upwave force. However, for the most flexible offshore plates, the downwave water depth increased due to plate deformation, resulting in up to 40% smaller total forces on the flexible than the rigid plates. This was also

confirmed in the 3D tests. The response of the offshore plates was then successfully examined in view of the Euler-Bernoulli beam theory. In the onshore tests, the wave force showed two peaks confirming previous observations. The second force peak was up to 3.3 times larger than the first one, with the rigid plates not necessarily resulting in the largest peaks. New semi-theoretical correlations to predict wave forces on onshore plates are finally suggested, as a simple function of the offshore wave energy. Such findings enhance the physical understanding of wave-structure interaction and are aimed at supporting the design of coastal and offshore structures.

4.1 Introduction

4.1.1 Background

Waves pose a challenge for a range of coastal structures. These include oil and gas rigs, offshore wind turbine platforms, breakwaters, flood protection systems and Wave Energy Converters (WECs). Such structures may experience significant deformations under wave loading leading to a mutual interplay between the waves and the structure, referred to as Wave-Structure Interaction (WSI). WSI resulted in structural damage and even failure in extreme cases. For example, an offshore platform in the Gulf of Mexico collapsed during the 2002 hurricane Lili (Moan, 2018) and the Dawlish seawall breached in 2014 due to a severe storm (Dawson et al., 2016).

Analytical, laboratory and numerical modelling of WSI traditionally addressed rigid structures (Sainflou, 1928; Cross, 1967; Mallayachari and Sundar, 1995; Higuera et al., 2014; Attili et al., 2021). Nevertheless, recent applications, e.g. the use of deformable materials for WECs (Chaplin et al., 2012; Collins et al., 2021) and vegetation for shore protection (van Veelen et al., 2021), raised the need to model the structure as flexible, making WSI even more significant.

Some researchers (Linton et al., 2013; Rao et al., 2017; Zhang et al., 2019a) observed benefits, e.g. reduced wave forces, when a deformable rather than a rigid wall is used. A few studies (Laya et al., 1984; Yuan and Huang, 2015) suggested reduc-

tion terms in the Morison equation (Morison et al., 1950), providing wave loading on stationary rigid cylinders, if the cylinders are moving. This opens up promising potential solutions by partially or fully replacing rigid coastal structures with flexible ones. However, current studies are still inconclusive; elastic walls showed larger wave pressures and forces under certain conditions compared to rigid ones (Mai et al., 2020).

An accurate understanding of the plate flexibility effect on wave loading is still a major challenge and an exhaustive analysis involving rigid and flexible structures is lacking. The present study focuses on an extensive investigation of WSI mimicking a range of real applications. This relies on numerical modelling of waves impacting rigid and flexible plates, located either offshore or onshore, using an available toolbox in foam-extend 4.0 (FE 4.0).

4.1.2 Previous work

4.1.2.1 Laboratory studies

Most laboratory studies of WSI have been conducted for the validation of numerical models. The most relevant benchmark cases include dam break waves involving elastic gates (Antoci et al., 2007), waves impacting rigid and flexible walls (Kimmoun et al., 2009; Linton et al., 2013; Didier et al., 2014) and dam break waves impacting flexible obstacles (Liao et al., 2015).

Kimmoun et al. (2009) conducted laboratory experiments of solitary waves impacting a flexible plate. Wave breaking was initiated in proximity of the plate in most tests, resulting in a complex wave-plate interaction. The wave-plate impact and the plate deflection were recorded, establishing a new database for numerical validation. Linton et al. (2013) conducted large-scale experiments in a 104 m long, 3.66 m wide and 4.57 m deep flume to investigate tsunamis impacting timber walls. The most flexible wall experienced smaller forces compared to stiffer walls. The measured peak forces were in good agreement with the equation (Cross, 1967)

$$F_I = \frac{1}{2}\rho_w g h_s^2 + C_f \rho_w h_s \bar{u}_s^2, \quad (4.1)$$

predicting the force on a vertical and rigid wall due to a surge, where ρ_w is the water (subscript w) density, g the gravitational acceleration, h_s the shore (subscript s) water depth, \bar{u}_s the depth-averaged velocity and C_f is a force coefficient related to the inclination of the free water surface.

Mai et al. (2020) experimentally investigated the effects of the structural elasticity during wave impacts on a vertical plate and vertically falling plate impact onto a water surface. In both cases, the structural elasticity had an effect on the impact load. Reduced forces and pressures were observed in the slamming tests for the elastic plates compared to rigid ones at high impact velocities only. The wave loading on the flexible plates was smaller than on the rigid plate under certain conditions, namely for high aeration waves. For slightly breaking waves, however, the elastic plates showed larger pressures and forces.

Large-scale laboratory tests have been conducted by Krautwald et al. (2022) to analyse the failure of rigid and elasto-plastic buildings under extreme wave loadings. These involved waves transforming into bores and impacting onshore buildings. For small wave heights, the structure stiffness had a negligible effect on the measured forces. For increasing wave heights, the elasto-plastic structures showed less pronounced force peaks compared to rigid ones. However, the forces were similar for both structures during the second stage of the impact, with the deformable structure experiencing even larger forces in some cases.

To the best of the authors' knowledge, a comprehensive benchmark case for wave impact on flexible structures is still lacking. This should provide the wave parameters, e.g. water surface elevation, pressure and force, as well as the plate displacement and/or deformation. In addition, the effect of the structure elasticity on the wave force is still uncertain requiring further study.

4.1.2.2 Numerical modelling

Given the maturity of Computational Fluid Dynamics (CFD) and Computational Structural Dynamics (CSD), numerical modelling has been increasingly applied to WSI phenomena (Liu and Zhang, 2019). Both mesh-based, e.g. the Finite Volume Method (FVM, Tuković et al., 2018), and mesh-free, e.g. Smoothed Particle Hydrodynamics (SPH, Didier et al., 2014), methods have been successfully applied with either monolithic (Rao et al., 2017; Liu and Zhang, 2019) or partitioned (Sotiropoulos and Yang, 2014) coupling approaches. In the monolithic approaches the fluid and solid governing equations are solved within a single solver. On the other hand, partitioned techniques individually solve the fluid and solid domains with an exchange of information at the fluid-solid interface.

Mesh-based methods are highly reliable for both CFD and CSD and also computationally efficient. However, they may become inaccurate for large deformations. He and Kashiwagi (2012) proposed a mixed Eulerian Lagrangian method monolithically coupled with a Finite Element Method (FEM). Solitary waves impacting elastic plates were investigated, showing that the hydroelastic behaviour strongly depends on the plate stiffness. Several models have been developed in the OpenFOAM (OF) framework (Higuera et al., 2013; Chen et al., 2014; Higuera et al., 2014; Hu et al., 2016; Rege and Hjertager, 2017; Tuković et al., 2018; Cardiff et al., 2018; Chen et al., 2019; Chen et al., 2020; Romano et al., 2020; Di Paolo et al., 2021; Hu et al., 2023), showing a great potential in tackling WSI phenomena (Huang et al., 2022).

Mesh-free approaches typically handle moving interfaces and large deformations more efficiently than mesh-based methods. However, they show instabilities and inaccuracies in the structural stresses (Liu and Zhang, 2019) and are more computationally expensive (Kumar et al., 2015). New developments in the SPH method have been presented by Antoci et al. (2007), Didier et al. (2014), Huang et al. (2018), Khayyer et al. (2018), Sun et al. (2019) and O'Connor and Rogers (2021). These have been validated with benchmark cases such as dam break waves involving an elastic gate (Antoci et al., 2007), a wave impacting an offshore wall (Didier et al.,

2014) and a dam break wave impacting a flexible obstacle (Liao et al., 2015). Overall, SPH models showed the capability of capturing the physics of WSI phenomena, with some deviations related to the structural response in most cases (Antoci et al., 2007; Sun et al., 2019; O’Connor and Rogers, 2021).

Mesh-based and mesh-free methods have eventually been coupled to combine their strengths. In these hybrid approaches, however, the fluid-solid coupling is even more challenging. This concerns particularly the energy balance at the interface (Degroote, 2013). Kumar et al. (2015) developed an SPH-FVM model within the OF framework, showing a good agreement for a dam break experiment. However, the solid analysis was not provided. A Moving Particle Semi-implicit (MPS, Khayyer et al., 2019) method was coupled with FEM by Rao et al. (2017). This approach was used to investigate solitary waves impacting rigid and flexible plates. Results showed larger pressures acting on the rigid than on the elastic plates. Zhang et al. (2019a) proposed a coupled MPS-FEM approach to investigate regular waves interacting with a horizontal plate. Comparisons with laboratory observations indicated the capability of this approach to accurately solve WSI phenomena.

The open source software OF is robust, stable and supports two-phase flows with a range of turbulence models and wave theories. Given the reliability and flexibility of the OF models, the available toolbox `solids4foam` (Cardiff et al., 2018) was used in the present study. This toolbox is capable of modelling both the fluid and structure with a partitioned coupling (Section 4.2). This numerical model has already been successfully applied to fluid-solid interaction phenomena (Mohammadi et al., 2021; Girfoglio et al., 2021). However, further validation is required, being one of the shortcomings addressed in the present study.

4.1.3 Aims and structure

The present study is aimed at:

- Validating the numerical model `solids4foam` with new laboratory experiments and the one from Kimmoun et al. (2009).

- Providing new physical insight into linear and solitary waves impacting plates of different stiffnesses and inclinations located in the open sea (offshore).
- Providing new physical insight into broken solitary waves impacting plates of different stiffnesses located on the coast (onshore).

The remainder of this article is organised as follows. The numerical model is presented in Section 4.2 along with the numerical set-ups and the test programme. The laboratory experiments are discussed in Section 4.3. Section 4.4 includes the validation of the numerical toolbox along with the numerical wave forces and plate responses for the offshore and onshore tests. In Section 4.5, the results are discussed and compared with existing prediction methods. The main conclusions are then summarised in Section 4.6. The appendices include the convergence tests (Appendix 4.A), the Euler-Bernoulli beam theory for the offshore tests (Appendix 4.B) and new correlations for the onshore plate displacements and stresses (Appendix 4.C).

4.2 Numerical model

The numerical investigation was conducted with the open source toolbox `solids4foam` (Cardiff et al., 2018) implemented in FE 4.0 (OpenFOAM extension, 2016). This toolbox solves fluid-solid interaction phenomena employing the FVM discretisation for both domains and with a partitioned coupling approach.

4.2.1 Governing equations and coupling method

The fluid was modelled as an incompressible Newtonian fluid satisfying the continuity and the Reynolds-Averaged Navier-Stokes (RANS) equations

$$\nabla \cdot \bar{\mathbf{u}} = 0 \quad (4.2)$$

$$\frac{\rho \partial \bar{\mathbf{u}}}{\partial t} + \rho(\bar{\mathbf{u}} \cdot \nabla) \bar{\mathbf{u}} = -\nabla \bar{p} + \rho \nabla \cdot (\mu \nabla \cdot \bar{\mathbf{u}} - \overline{\mathbf{u}' \mathbf{u}'}) + \rho \mathbf{g} + f_{\sigma}, \quad (4.3)$$

where $\bar{\mathbf{u}} = (\bar{u}_x, \bar{u}_y, \bar{u}_z)$ is the mean fluid velocity vector, \bar{p} the mean pressure, ρ the fluid density, μ the fluid dynamic viscosity, $\overline{\mathbf{u}'\mathbf{u}'}$ the turbulent stress tensor, t the time, \mathbf{g} the gravitational acceleration vector and f_σ the surface tension force per unit volume (Brackbill et al., 1992). The tensor $\overline{\mathbf{u}'\mathbf{u}'}$ is defined according to the turbulence model considered (Ferziger, 1987; Jasak, 1996). The k - ε model (Launder and Spalding, 1974) has been used herein. This standard model ensures fast convergence and reliability in modelling fully-turbulent processes.

Eqs. (4.2) and (4.3) were discretised into a set of algebraic equations and solved with the PIMPLE loop (Aguerre et al., 2013). The Courant-Friedrichs-Lewy (CFL) convergence condition (Courant et al., 1928)

$$C = \frac{\bar{u}_x \Delta t}{\Delta x} + \frac{\bar{u}_y \Delta t}{\Delta y} + \frac{\bar{u}_z \Delta t}{\Delta z} \leq 1 \quad (4.4)$$

was used to control the time integration. In Eq. (4.4), C is the Courant number and Δx , Δy and Δz are the cell sizes in the x , y and z direction, respectively. The initial time step Δt was dynamically adapted to satisfy the CFL condition throughout the simulation, with the mean C typically not exceeding 0.012.

The water-air flows herein were solved by employing the Volume Of Fluid (VOF) method (Hirt and Nichols, 1981) with the fraction of volume α ; α varies from 0 to 1, with $\alpha = 0$ denoting air (subscript a), $\alpha = 1$ water and $0 < \alpha < 1$ the air-water interface. In the present study, $\alpha = 0.5$ was used to track the water surface. The physical properties ρ and μ are computed as

$$\rho = \rho_w \alpha + \rho_a (1 - \alpha) \quad (4.5)$$

$$\mu = \mu_w \alpha + \mu_a (1 - \alpha). \quad (4.6)$$

Once Eqs. (4.2) and (4.3) were solved, α was updated based on the transport equation

$$\frac{\partial \alpha}{\partial t} + \nabla \cdot (\bar{\mathbf{u}} \alpha) + \nabla \cdot [\alpha (1 - \alpha) \mathbf{u}_r] = 0. \quad (4.7)$$

The compression term $\nabla \cdot [\alpha(1 - \alpha)\mathbf{u}_r]$, where \mathbf{u}_r is the compression velocity vector, was introduced by Weller et al. (1998) to reduce the numerical diffusion.

The waves were generated with the toolbox waves2Foam (Jacobsen et al., 2012). The wave generation was based on the relaxation zone technique, consisting of a relaxation function applied to evaluate $\bar{\mathbf{u}}$ and α inside the relaxation zone (Jacobsen et al., 2012). A relaxation zone of 3 times the wave length L was used in all tests of the present study (Fig. 4.1a).

A Lagrangian approach was adopted for the solid domain. In the present study, large displacement kinematics were considered along with the Neo-Hookean elastic constitutive law. The momentum equation is

$$\rho_s \frac{\partial^2 \mathbf{d}_s}{\partial t^2} + \nabla \cdot [(J\mathbf{D}_F^{-T}) \cdot \boldsymbol{\sigma}_s] = \rho_s \mathbf{g}, \quad (4.8)$$

where \mathbf{d}_s is the solid (subscript s) displacement vector, ρ_s the solid density, $\mathbf{D}_F = \mathbf{I} + (\nabla \mathbf{d}_s)^T$ the deformation gradient, with the identity matrix \mathbf{I} , J the determinant of \mathbf{D}_F and $\boldsymbol{\sigma}_s$ the stress tensor in Voigt notation.

The fluid-solid coupling was performed through a partitioned approach. The fluid domain was solved with a Dirichlet condition for the mean velocity vector $\bar{\mathbf{u}}$ at the interface and the solid with a stress boundary condition (Cardiff et al., 2018). For each time step, the fluid velocity and pressure fields were updated with Eqs. (4.2) and (4.3) through the PIMPLE loop (Aguerre et al., 2013), and Eq. (4.7) was solved to track the water-air interface. Thereafter, the fluid forces acting on the solid were evaluated and applied to the solid interface. The traction Neumann condition was employed at the solid interface, where the boundary condition for the displacement was set as “solidTraction” (Cardiff et al., 2018). The solid domain was solved, then the new solid velocities were transferred to the fluid using an under-relaxation technique (Cardiff et al., 2018). This involved multiplying the new solid velocities by a relaxation factor ≤ 1 to optimise the numerical convergence. Consequently, the fluid mesh was updated and the loop was performed until convergence was achieved.

4.2.2 Numerical set-up and test programme

Linear and solitary waves impacting plates located either offshore or onshore were investigated with the 2D set-ups shown in Fig. 4.1. These idealised wave types represent a range of real-world applications, from wind waves to more extreme cases such as tsunamis. In the offshore tests, the plate was located $4L$ from the upstream boundary of the flume (Fig. 4.1a). The plate, with a height $l = 30$ m and thickness $s = 2$ m, was fixed on a substructure with height $l_s = 35$ m and submerged by 25, 50 or 75% of l . This design is related to the concepts of the MOSE mobile gate (Erbisti, 2014) and Oyster WEC (Lagoun et al., 2010).

Young's moduli $E = 1, 30$ and 1000 GPa were used, modelling extreme scenarios of real applications, with $E = 1$ GPa representing a variety of plastics and $E = 1000$ GPa as an upper bound for rigid plates. Inclinations of the plate $\beta = 60, 75$ and 90° were investigated. Linear and solitary waves with various wave amplitudes a , heights H and periods T were simulated within a total of 72 tests (Table 4.1). A resolution of $\Delta x = \Delta z = 0.15$ m in a 25.00 m \times 32.00 m refined area (Appendix 4.A) was employed, with $\Delta x = \Delta z = 0.60$ m in the remainder of the domain (Fig. 4.1a).

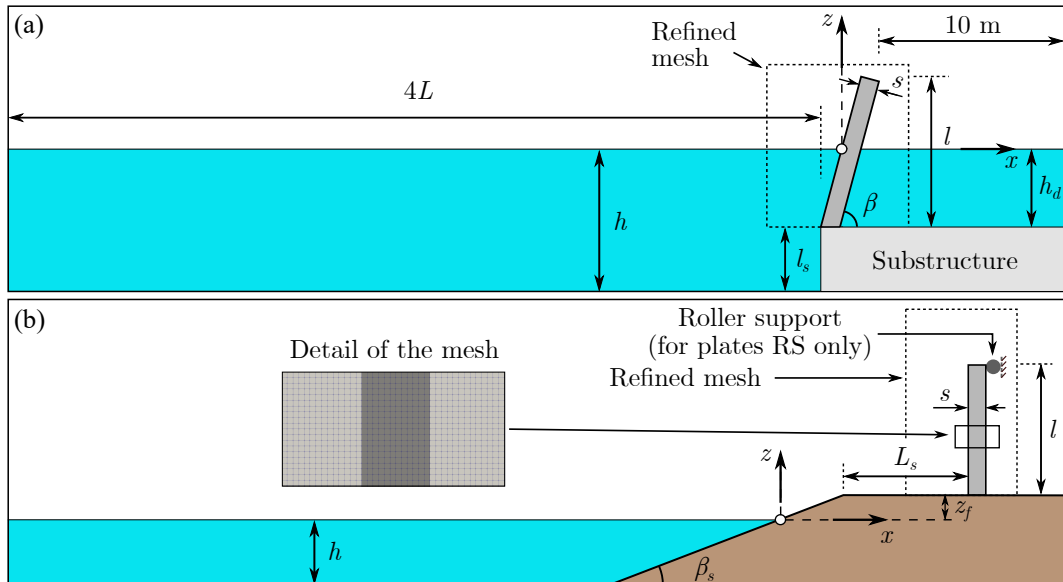


Figure 4.1. Side views of the numerical set-ups: (a) offshore and (b) onshore.

In the onshore tests, the plate was located on the horizontal section of the shore

at a distance of $L_s = 4$ m from the transition point (Fig. 4.1b). An inclination of the shore of $\beta_s = 30^\circ$ was used, as a typical value for the friction angle of sand. Water depths of $h = 2, 3$ and 4 m were investigated, resulting in freeboards of $z_f = 0, 1$ and 2 m. For each wave condition, 5 plates with different E , boundary conditions and thicknesses were used (Table 4.2), resulting in a total of 45 tests. For the Rigid (R) and “Top Free” (TF) cases the plate was fixed to the foundation and the top end was free to move. In the “Roller Support” (RS) case the plate was fixed to the foundation and the horizontal displacement d_x at the top end was prevented. The fundamental natural frequency f_s of the plates R, TF1 and TF2 (Table 4.2) was computed as (Gibson, 2007)

$$f_s = \frac{(1.875)^2}{2\pi l^2} \sqrt{\frac{Es^2}{12\rho_s}}. \quad (4.9)$$

A resolution of $\Delta x = \Delta z = 0.0250$ m, with $\Delta x = \Delta z = 0.0125$ m in a 1.40 m \times 3.00 m refined area, was used (Fig. 4.1b).

Table 4.1. Test programme for the 2D numerical tests.

Parameter	Symbol	Unit	Offshore	Onshore
Water depth	h	m	42.5, 50.0, 57.5	2, 3, 4
Plate height	l	m	30	3
Plate inclination	β	$^\circ$	60, 75, 90	90
Young’s modulus	E	GPa	1, 30, 1000	1, 1000
Plate thickness	s	m	2	0.15, 0.30
Dimensionless rigidity	$Es^3/(12\rho_wgh^4)$	-	0.006 to 20.830	0.112 to 1.433×10^4
Plate density	ρ_s	kg/m ³	1500, 8000	1500, 8000
Plate boundary condition	-	-	Top free	Top free, roller support
Shore freeboard	z_f	m	-	0, 1, 2
Shore length	L_s	m	-	4
Shore inclination	β_s	$^\circ$	-	30
	H	m	2.62 to 3.55	-
	H/h	-	0.046 to 0.080	-
Linear waves	T	s	6, 8, 10	-
	$T(g/h)^{1/2}$	-	2.48 to 3.84	-
	a	m	3.56 to 3.75	0.9, 1.2, 1.5
Solitary waves	a/h	-	0.06 to 0.09	0.225 to 0.750
Number of tests	-	-	72	45

The simulations were run on the High Performance Computing (HPC) cluster Augusta at the University of Nottingham using 40 Central Processing Units (CPUs)

and 150 GB of memory. In the offshore layout (≈ 0.1 million cells), the solitary wave tests took up to approximately 10 h to simulate 30 to 33 s and linear wave tests took 34 h for a simulation time of 110 s. Onshore tests (≈ 0.5 million cells) required up to 20 h to simulate 6 to 10 s.

Table 4.2. Classification of the 5 plates used in the onshore tests.

Notation	E (GPa)	ρ_s (kg/m ³)	s (m)	Boundary condition	f_s (Hz)
R	1000	8000	0.30	Top free	60.20
RS1	1	1500	0.30	Roller support	-
RS2	1	1500	0.15	Roller support	-
TF1	1	1500	0.30	Top free	4.40
TF2	1	1500	0.15	Top free	2.20

4.2.3 3D simulations

3D simulations have been conducted with the 15 m wide wave flume shown in Fig. 4.2. The plate, with the same width as the flume, was 30 m high with $s = 0.30$ m and supported at both ends. A volume of water with depth $h_d = 15$ m was retained downwave (subscript d) of this plate. This scenario mimics a section of the hull of a Floating Production Storage and Offloading (FPSO) unit.

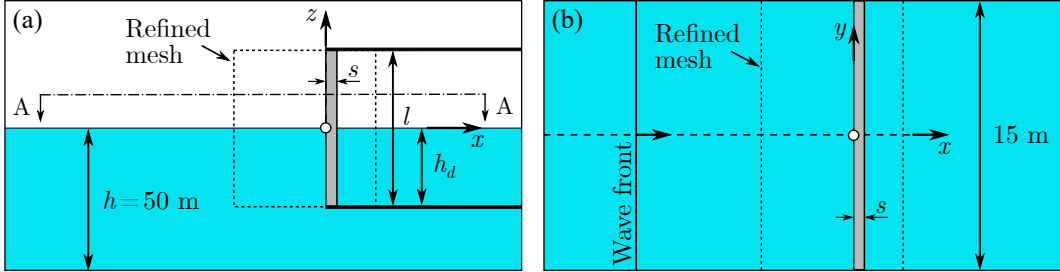


Figure 4.2. 3D simulations: (a) lateral view and (b) section AA of the 3D numerical set-up with the hull of a FPSO unit.

The simulations involved flexible and rigid plates with $E = 2 \cdot 10^2$ and $2 \cdot 10^4$ GPa, respectively, impacted by a solitary wave with $a/h = 0.07$. The density of the plate was $\rho_s = 8000$ kg/m³ in both cases. A resolution of $\Delta x = \Delta y = \Delta z = 0.15$ m was used in a 30.00 m \times 15.00 m \times 30.00 m refined volume, with $\Delta x = \Delta y = \Delta z = 0.60$ m in the remainder of the domain resulting in ≈ 6 million cells. The numerical tank boundaries at $y = -7.5$ and 7.5 m were modelled as smooth walls. The simulations

were again run on Augusta using 40 CPUs and 120 GB of memory. The rigid plate test took approximately 28 h and the flexible case 150 h to simulate 30 s.

4.3 Physical model

Laboratory experiments were conducted in an approximately 15 m long, 0.245 m wide and 0.460 m deep flume, as shown in Fig. 4.3a. Cartesian coordinates (x, y, z) are used in this study, with the origin at the still water surface. The tests involved linear and solitary waves impacting a $0.55 \text{ m} \times 0.24 \text{ m}$ plate. The flume was equipped with a piston-type wave maker. The plate was located 11.43 m downwave the wave maker and supported by a movable angled ramp, enabling several plate inclinations β . A gap of 2.0 to 2.5 mm between the plate and the lateral walls of the flume allowed for a free movement of the plate. A 4 mm thick acrylic (Young's modulus $E = 3.30 \text{ GPa}$) and a 3 mm thick stainless steel plate ($E = 200 \text{ GPa}$) were used in the tests to model flexible and rigid structures.

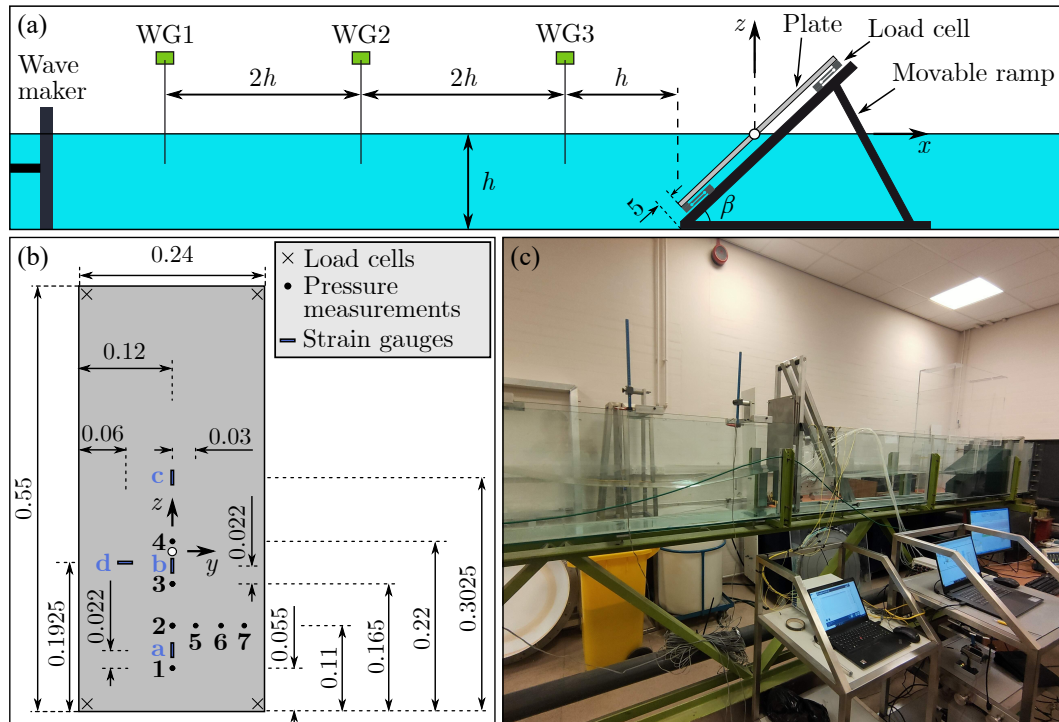


Figure 4.3. Experimental set-up: (a) side view of the wave flume and plate, (b) frontal view of the plate (dimensions in m) and (c) overview of the flume with the instrumentation.

The water surface elevations were recorded at 3 locations with resistance-type Wave Gauges (WGs, Fig. 4.3a). They recorded at 100 Hz with an accuracy of ± 1 mm. An array of MPXV5004GC7U (RS Components UK) Precision Pressure Transducers (PPTs) was used to measure the water pressure at the plate. Each PPT was attached to the lateral wall of the flume and connected with a water-filled pipe to the plate. The locations of the pressure measurements is shown in Fig. 4.3b. The PPTs sampled at 100 Hz with an estimated accuracy of ± 10 Pa. Both the WGs and PPTs were calibrated daily by changing the still water levels.

Load Cells (LCs) have been manufactured in-house to measure the wave forces on the plates. These consisted of stainless steel S beams equipped with fibre optic strain gauges and the data were interrogated with a FS22SI BraggMETER. The 4 LCs were located at the corners of the plate and fixed to the movable angled ramp (Fig. 4.3a). They have been individually calibrated resulting in an overall accuracy of ± 0.3 N. The force was recorded at 1 kHz. In addition, KFWB Series Waterproof Strain Gauges (SGs) were mounted on both the upwave and downwave sides of the acrylic plate to measure deflections (Fig. 4.3b). They recorded at 100 Hz with an accuracy of $\pm 10^{-6}$.

4.4 Results

4.4.1 Offshore

4.4.1.1 Validation of solids4foam with new laboratory experiments

The validation of solids4foam for rigid plates was addressed in Attili et al. (2021). The numerical model for flexible plates is validated herein with 2 new laboratory experiments (Section 4.3) of solitary waves impacting a stainless steel and a plastic plate. An overview of the main experimental parameters is given in Table 4.3. The numerical set-up consisted of a 3D wave flume mimicking one half ($0.00 \text{ m} \leq y \leq 0.12 \text{ m}$) of the experimental flume given the symmetry of the wave field and plate. Small strains were considered for the plates in these simulations with the linear elastic

constitutive law.

Table 4.3. Main parameters in the validation with 2 laboratory experiments. Values marked with * were observed at WG1 in tests conducted without the plate.

Experiment	h (m)	a (m)	s (m)	E (GPa)	ρ_s (kg/m ³)	β (°)
1	0.250	0.064*	0.003	200.000	8000	90
2	0.250	0.064*	0.004	3.300	1200	90

To accurately model the dynamics of the acrylic plate by reducing computational cost, a plate with $s = 0.008$ m, $E = 412.5$ MPa and $\rho_s = 600$ kg/m³ was used in the simulation. This has the same flexural rigidity EI and natural period T_s as the laboratory plate where I is the moment of inertia. The numerical model experienced instabilities when the same physical properties as in the laboratory test were used. These were likely due to the relatively small thickness of the plate. A mesh resolution of $\Delta x = \Delta y = \Delta z = 0.0040$ m was used for the fluid domain in both experiments and $\Delta x = \Delta y = \Delta z = 0.0015$ m and $\Delta x = \Delta y = \Delta z = 0.0020$ m were employed for the solid domain in experiment 1 and 2, respectively.

The relative water surface elevations η/h observed at the 3 WGs (Fig. 4.3a) are shown in Fig. 4.4 for both experiments. The wave travelled along the flume, impacted the plate and was reflected. During wave impact, vibrations of the pipes connecting the PPTs were observed in the laboratory tests. As a result, oscillations of the pressure p , which are not directly related to wave pressures, were observed, as shown in Fig. 4.5. However, as also revealed by low-pass filter analyses, these oscillations follow the overall trend of the wave pressure such that these measurements are still valuable. In the end, the laboratory measurements were not low-pass filtered to avoid attenuating significant high frequencies due to plate vibrations.

The comparison between laboratory and numerical results shows a good agreement for η/h and $p/(\rho_w gh)$ (Figs. 4.4 and 4.5a, b, c, d). The incident and reflected waves, as well as their superposition, are well captured by the numerical model with less than 12% deviations. The numerical (subscript *num*) p_{num} at PPT1, 2, 3 and 6 shows similar trends as the experimental (subscript *exp*) p_{exp} , apart from the previ-

ously mentioned oscillations. The normalised root mean square error was computed as

$$nRMSE = \frac{\sqrt{\frac{1}{N} \sum_i^N (p_{num,i} - p_{exp,i})^2}}{(p_{exp,max} - p_{exp,min})}, \quad (4.10)$$

where N is the number of the considered p values and the subscripts max and min stand for the maximum and minimum values.

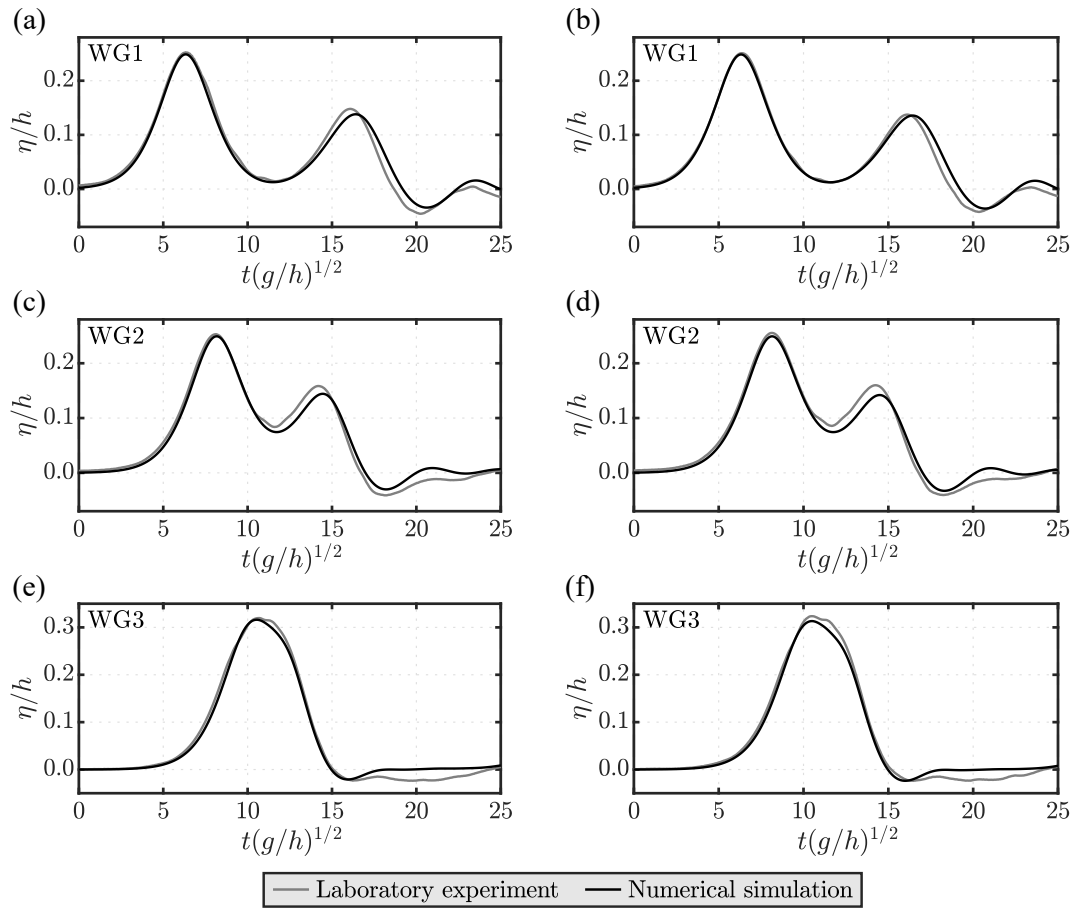


Figure 4.4. Comparison of the experimental and numerical water surface elevations η/h at all 3 WGs for experiment 1 (a, c, e) and 2 (b, d, f) of Table 4.3.

Deviations of less than 7.6% were observed for p_{exp} across the plate between PPT2, 5, 6 and 7 in experiment 1. This was confirmed by the numerical results, where p_{num} showed negligible deviations ($< 1\%$) between $y = 0.00$ m and $y = 0.10$ m. However, reduced p_{num} were observed in proximity of the plate sides as a result of larger velocities due to the gaps between the plate and the flume walls. This effect

induced 24.5% smaller p_{num} at $y = 0.12$ m than at $y = 0$ m. Similar results were observed in experiment 2.

The 3D experimental and numerical total forces $F_{3D} = F_{3D,u} - F_{3D,d}$, where $F_{3D,u}$ is the upwave (subscript u) and $F_{3D,d}$ the downwave force, are compared in Fig. 4.5e, f. The force is overestimated by the numerical simulations by up to 18 and 33% for experiment 1 and 2, respectively. These deviations may be explained by the inability of the numerical model to fully capture the 3D effects due to the lateral gaps. The numerical simulations tend to overpredict the laboratory p in proximity of the gaps, as indicated by the comparison at PPT7, resulting in larger F_{3D} on the plate.

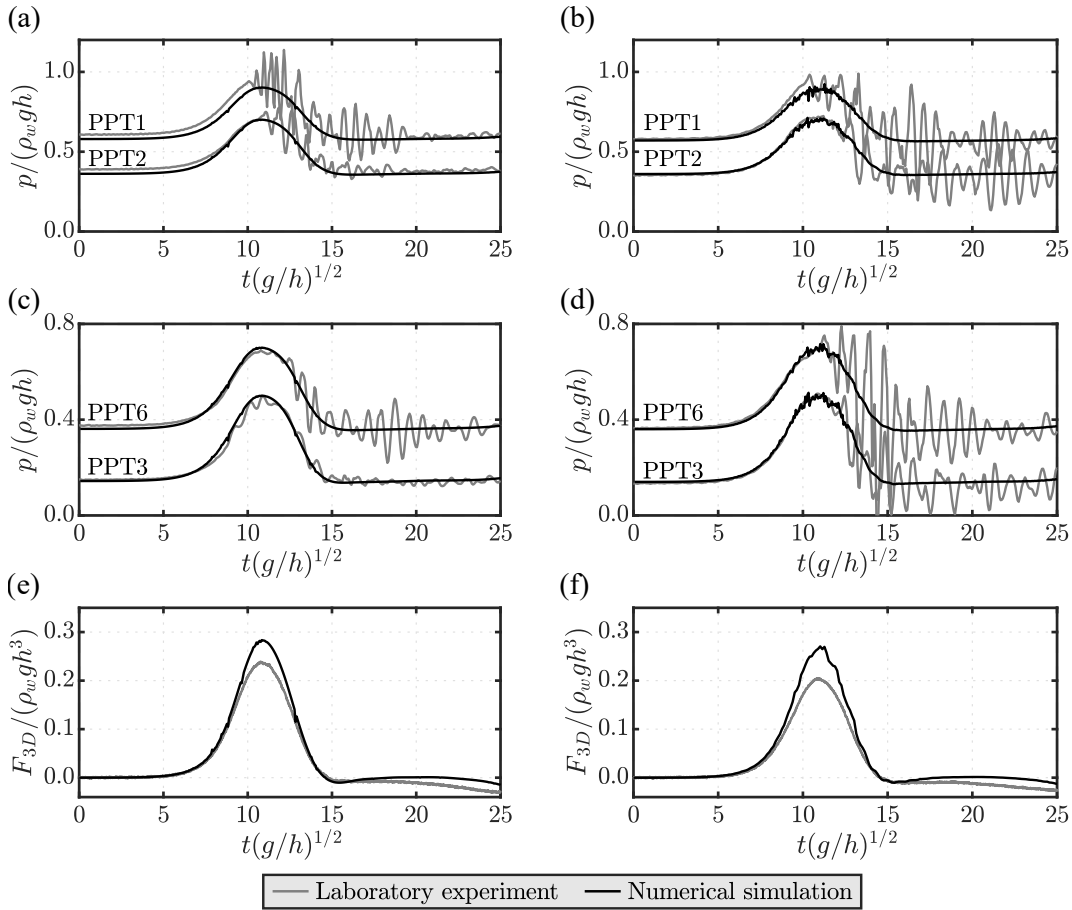


Figure 4.5. Comparison of the experimental and numerical pressures $p/(\rho_wgh)$ at (a) PPT1 ($nRMSE = 0.097$) and 2 ($nRMSE = 0.085$), (c) 3 ($nRMSE = 0.041$) and 6 ($nRMSE = 0.078$) and (e) force $F_{3D}/(\rho_wgh^3)$ for experiment 1 and $p/(\rho_wgh)$ at (b) PPT1 ($nRMSE = 0.108$) and 2 ($nRMSE = 0.115$), (d) 3 ($nRMSE = 0.094$) and 6 ($nRMSE = 0.102$) and (f) $F_{3D}/(\rho_wgh^3)$ for experiment 2 of Table 4.3.

Fig. 4.6 shows the numerical and experimental strain ε_{zz} at the upwave SGb and

SGc (Fig. 4.3b) for experiment 2. The largest deformations of the plate were observed at SGb followed by SGc. This behaviour is captured in the numerical simulation, however, with up to 45.2 and 59.7% deviations for SGb and SGc. The overestimation of the wave force in combination with the absence of physical damping in solids4foam (Section 4.4.2.1) may explain the observed deviations. To sum up, the validation of solid4foam with new laboratory tests showed its capability of capturing the water surface elevation and the wave pressures well, however, it overestimates the wave forces and plate deformation.

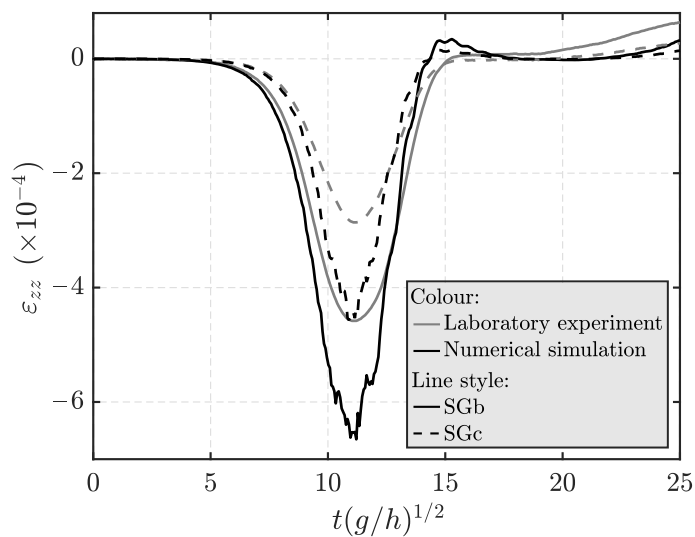


Figure 4.6. Comparison of the experimental and numerical strains ε_{zz} at SGb and SGc for experiment 2 of Table 4.3.

4.4.1.2 A numerical representative test

Fig. 4.7 shows an offshore test with wave impact and reflection. In the present study, $t = 0.0$ s is the instant when the wave front reaches the plate. The horizontal (subscript H) relative forces acting on a rigid and flexible plate with $E = 1000$ and 1 GPa, respectively, for a linear wave with $a/h = 0.038$ and $T(g/h)^{1/2} = 3.54$, are shown in Fig. 4.8a.

Both the force acting on the upwave side of the plate $F_{H,u}$ and the total force $F_H = F_{H,u} - F_{H,d}$ due to the hydrostatic and wave pressures are shown in Fig. 4.8a. The stiffness of the plate results in negligible deviations of $F_{H,u}/(\rho_w g h^2)$. On the

other hand, slightly larger deviations, of up to 6%, are observed for $F_H/(\rho_w g h^2)$. These are due to the increase in the downwave water depth h_d for the flexible plates. The time series of the relative d_x/l are shown in Fig. 4.8b.

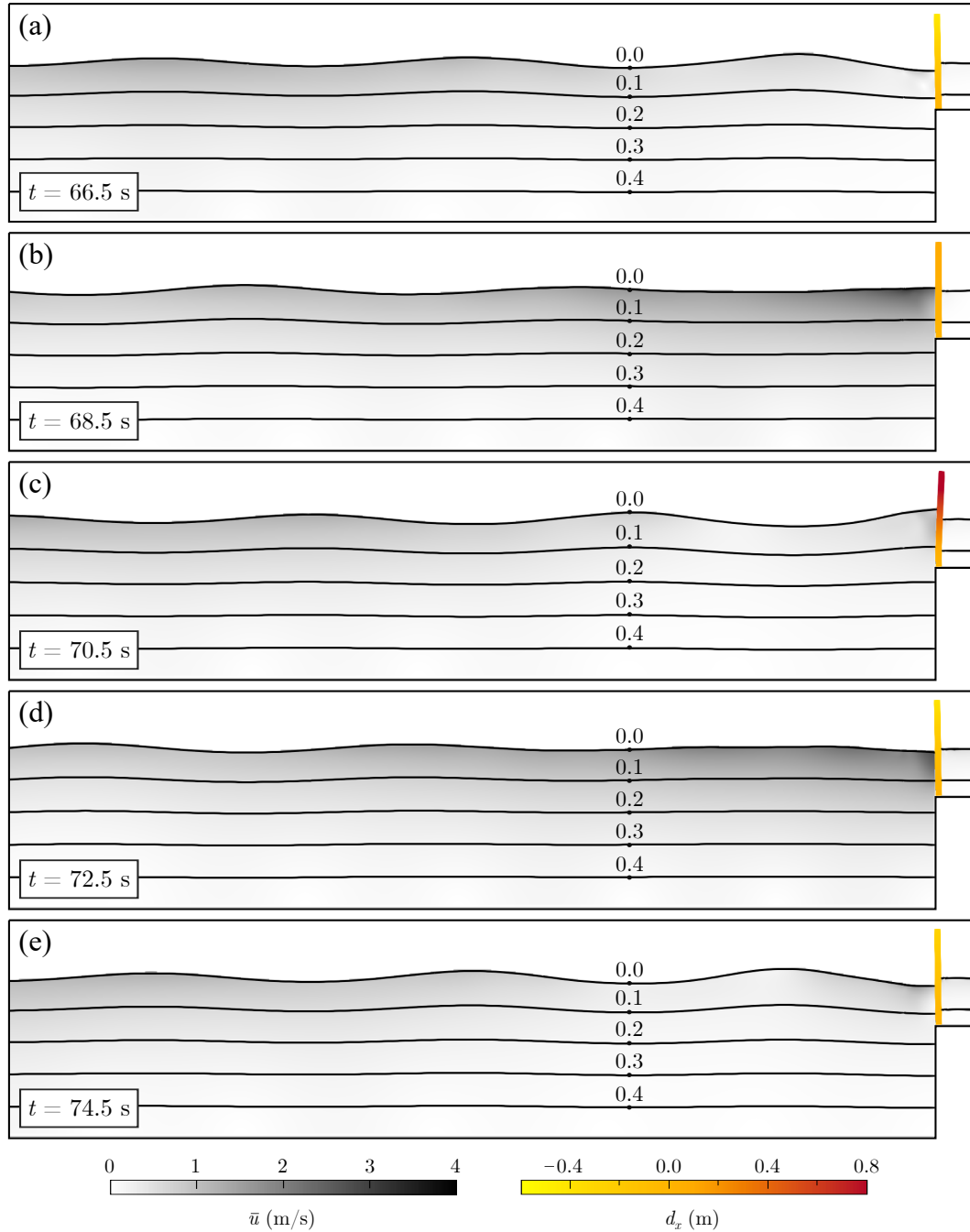


Figure 4.7. Snapshot series of a 2D linear wave impacting a plate with $a/h = 0.038$, $T(g/h)^{1/2} = 3.54$, $s = 2.00$ m and $E = 1.00$ GPa showing the mean velocity $\bar{u} = \sqrt{\bar{u}_x^2 + \bar{u}_z^2}$, pressure contours (MPa) and horizontal displacement d_x .

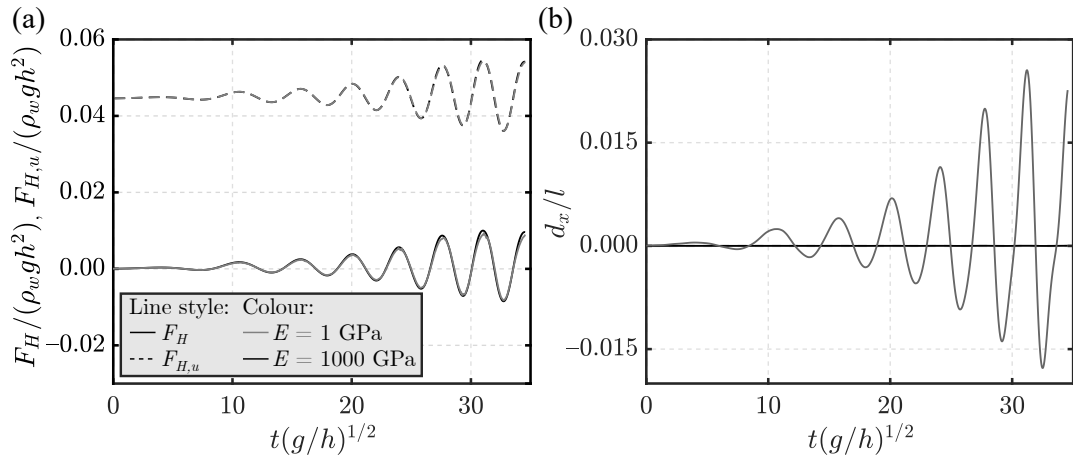


Figure 4.8. Offshore tests: time series of the relative (a) total $F_H/(\rho_w g h^2)$ and upstream $F_{H,u}/(\rho_w g h^2)$ forces and (b) horizontal displacement d_x/l at the top end of the offshore plates (Fig. 4.1a) with $E = 1$ and 1000 GPa and $\beta = 90^\circ$ for a linear wave with $a/h = 0.038$ and $T(g/h)^{1/2} = 3.54$.

4.4.1.3 Numerical run-up and force

The maximum dimensionless run-up heights R/h are shown in Fig. 4.9a versus a/h for the linear and solitary wave tests. Overall, R/h increases with increasing a/h , following a linear trend in the solitary wave tests. The most deformable plates show slightly smaller R/h with delays compared to the rigid plates, however, with small deviations. The numerical R_{num}/h are compared with predicted (subscript *pred*) R_{pred}/h based on the equations included in Table 4.4 (Fig. 4.9b). The linear wave tests were predicted with the theoretical equation from Miche (1951) and the empirical equation of Müller (1995) was used for solitary waves, with $L = 2\pi h/(0.75a/h)^{1/2}$ (Lo et al., 2013). The linear wave R_{num}/h are well predicted by Miche (1951) for $\beta = 90^\circ$, while deviations of up to 116% are observed for $\beta = 60$ and 75° . These deviations are due to the assumption of complete wave reflection in the theoretical equation. In contrast, the incident waves are only partially reflected from sloped walls (Ursell et al., 1960). The equation of Müller (1995) successfully captures the solitary wave tests, with relatively small deviations.

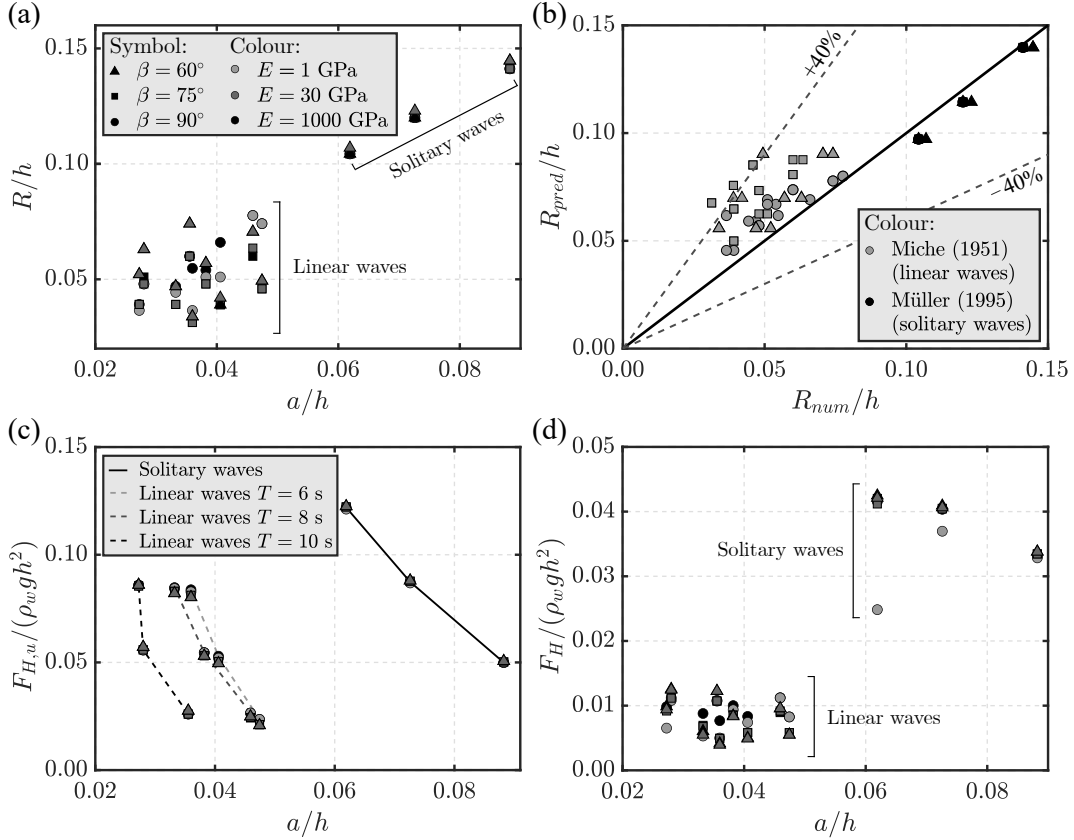


Figure 4.9. Offshore tests: (a) relative run-up height R/h versus a/h , (b) predicted R_{pred}/h with Miche (1951) for the linear and Müller (1995) for the solitary wave tests (Table 4.4) versus the numerical R_{num}/h , (c) upwave $F_{H,u}/(\rho_w g h^2)$ and (d) total $F_H/(\rho_w g h^2)$ forces versus a/h for the different plates shown in Table 4.1.

Table 4.4. Run-up height R prediction equations of Miche (1951) and Müller (1995).

Reference	R/h	Wave type
Miche (1951)	$\frac{H}{h} \left(\frac{90^\circ}{\beta} \right)^{1/2}$	Linear waves
Müller (1995)	$1.25 \left(\frac{a}{h} \right)^{5/4} \left(\frac{a}{L} \right)^{-3/20} \left(\frac{90^\circ}{\beta} \right)^{1/5}$	Solitary waves

Fig. 4.9c, d shows the relative $F_{H,u}/(\rho_w g h^2)$ and $F_H/(\rho_w g h^2)$ versus a/h . $F_{H,u}/(\rho_w g h^2)$ decreases with increasing a/h for all tests and increases with increasing T in the linear wave tests. However, T has a small influence on $F_{H,u}$. The plate stiffness results in negligible deviations of $F_{H,u}/(\rho_w g h^2)$ for the investigated conditions. The larger h_d observed for the flexible plates result in larger forces acting on the downwave side and consequently smaller F_H . As shown in Fig. 4.9d, this effect is relatively small for most of the tests. In a few tests with $E = 1$ GPa, the plate deformation induced up

to 16% larger h_d , with larger p_d acting on the plate, compared to $E = 1000$ GPa. As a result, F_H for $E = 1$ GPa was up to 40% smaller than for $E = 1000$ GPa under these conditions. The data in Fig. 4.9 will be further discussed and compared with available prediction methods in Section 4.5.

4.4.1.4 Numerical plate response

In the offshore tests the natural period of the plate T_s varied from 0.24 to 3.11 s. This was estimated as $1/f_s$ (with f_s from Eq. 4.9) with a reduced plate density due to the initial submergence. In the solitary wave tests, the wave exerts a quasi static loading on the plate. The ratio T/T_s is relatively large as $T \rightarrow \infty$ and the plate does not oscillate over the loading time. On the other hand, the ratio $T/T_s = 1.92$ to 42.16 is relatively small for the linear wave tests. In these tests, the wave impact is of short duration and the plate oscillates with a period close to T (Fig. 4.8b). No resonance has been observed in the investigated tests.

Fig. 4.10a shows the maximum $d_{x,max}/l$ versus a/h observed in all offshore tests. The largest $d_{x,max}/l$ were observed in the solitary wave tests and overall $d_{x,max}/l$ decreases for smaller h with constant a . The maximum relative stress component $\sigma_{zz,max}/(\rho_s gl)$ observed along the inner fibre (upwave) versus a/h are shown in Fig. 4.10b for the solitary wave tests. $\sigma_{zz,max}/(\rho_s gl)$ were observed at or close to the foundation of the plate. The flexible plates show larger $\sigma_{zz,max}/(\rho_s gl)$ compared to the rigid plate.

Based on the Euler-Bernoulli beam theory, d_x and σ_{zz} can be predicted as shown in Appendix 4.B. The maximum predicted $d_{x,max,pred}$ with Eq. (4.B.11) versus the numerical $d_{x,max,num}$ are shown in Fig. 4.10c. The coefficient of determination is applied as

$$R^2 = 1 - \frac{\sum_i (Y_{num,i} - Y_{pred,i})^2}{\sum_i (Y_{num,i} - \bar{Y})^2}, \quad (4.11)$$

where $Y_{num,i}$ and $Y_{pred,i}$ are the numerical and predicted values and \bar{Y} is the mean of $Y_{num,i}$. The theoretical model tends to overpredict the numerical observations with

deviations of up to 149%, whilst in other tests $d_{x,max,num}$ is underestimated by Eq. (4.B.11).

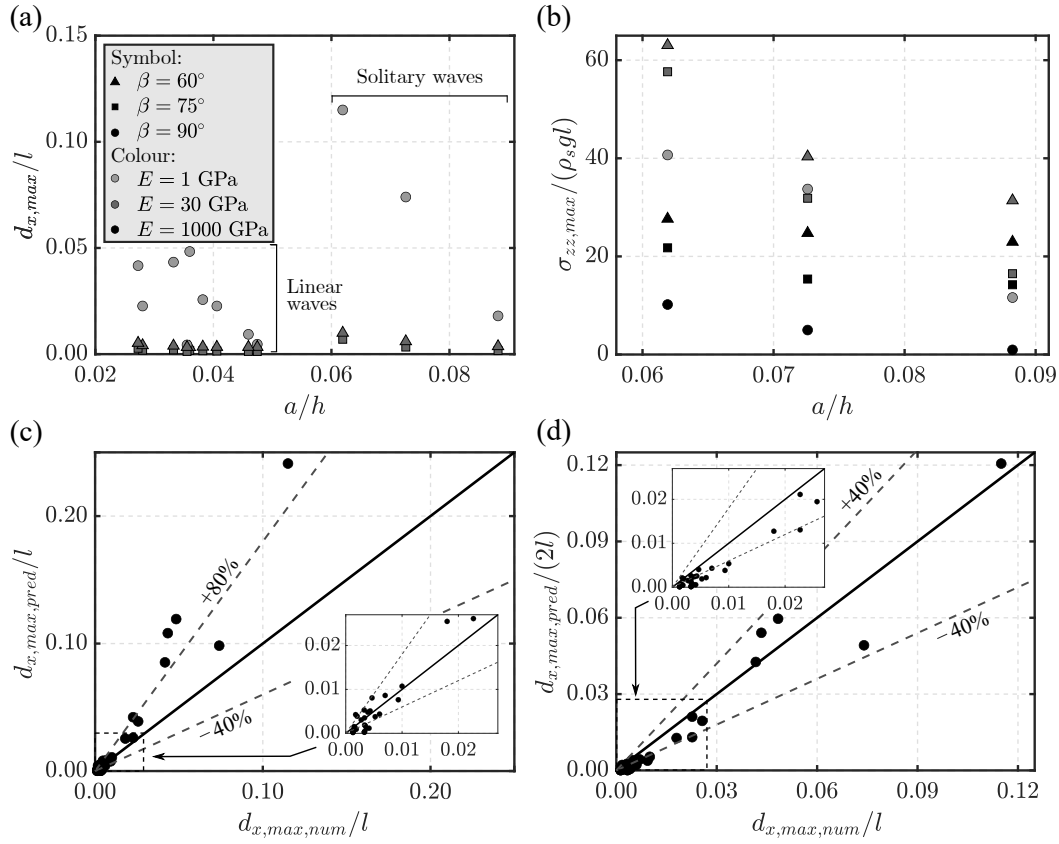


Figure 4.10. Plate response for offshore tests: (a) relative maximum displacement $d_{x,max}/l$ versus a/h , (b) relative maximum vertical stress component $\sigma_{zz,max}/(\rho_s g l)$ versus a/h for the solitary wave tests and (c, d) comparison between $d_{x,max,num}/l$ and (c) $d_{x,max,pred}/l$ ($R^2 = -0.42$) and (d) $d_{x,max,pred}/(2l)$ ($R^2 = 0.94$).

The observed deviations are partially due to the violation of some of the assumptions for the beam equation. The critical distributed load was assumed static in the beam theory analysis. Conversely, the critical wave pressure distribution is momentarily applied to the plate as a consequence of the dynamic nature of the wave loading. Therefore, the beam theory represents an upper bound estimate of the time varying plate deflections. A further assumption in Appendix 4.B is that the run-up height R corresponds to $2a$. However, this overestimates R_{num} by up to 50%, also contributing to the observed deviations. On the other hand, an estimation of the plate slope $d_{x,max}/l \leq 0.12$ reveals that the small slope assumption is satisfied in all tests. A significantly improved agreement and R^2 values can be achieved by applying

an empirical prefactor of $1/2$ to $d_{x,max,pred}$, as shown in Fig. 4.10d.

4.4.1.5 Numerical 3D tests

Negligible deviations of the main parameters, e.g. p and d_x , have been observed across the plate width in the 3D tests (Section 4.2.3). Fig. 4.11a shows the relative upwave $F_{3D,H,u}/(\rho_w g h^3)$ and total $F_{3D,H}/(\rho_w g h^3)$ forces on the 3D rigid and flexible offshore plates. As observed in the 2D simulations (Fig. 4.8a), the stiffness of the plate results in negligible deviations of $F_{3D,H,u}$, with slight deviations of $F_{3D,H}$ of less than 2%. These are again due to the increase of h_d , and consequently p_d (Fig. 4.11b), for the flexible plate.

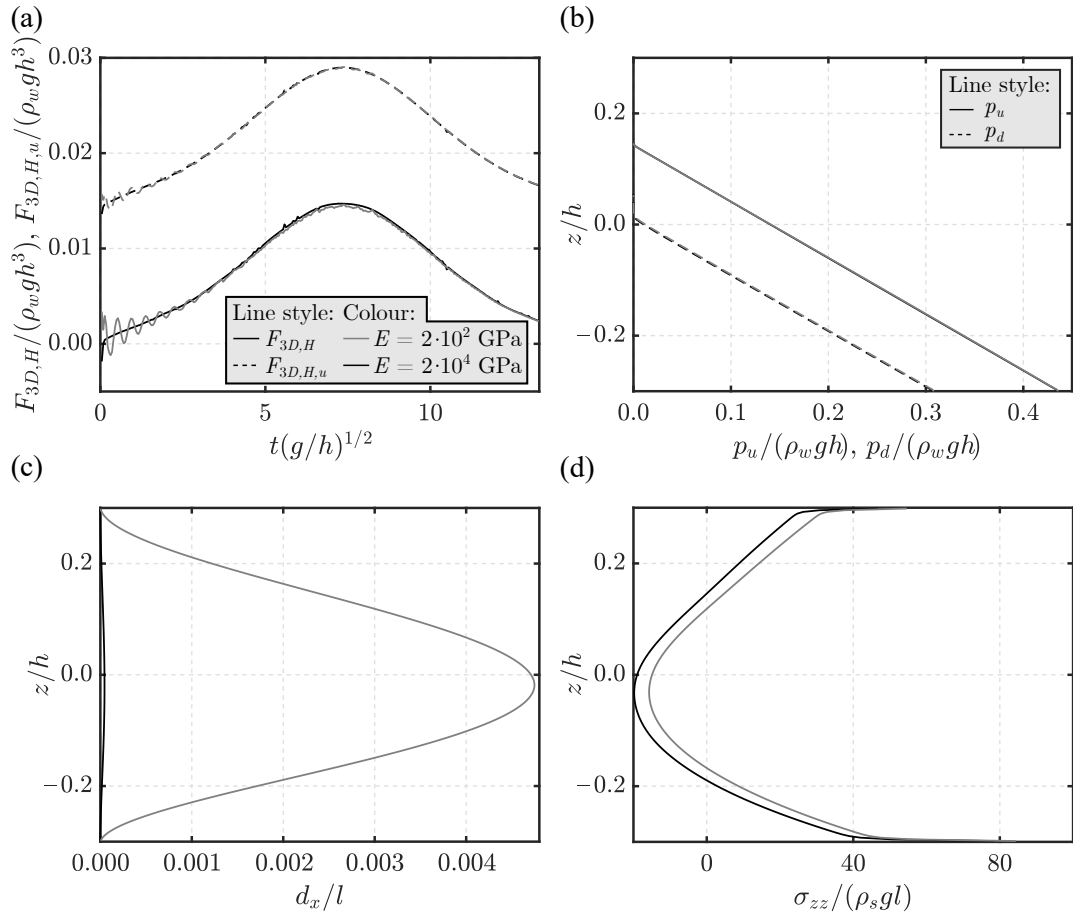


Figure 4.11. 3D simulations of offshore tests: (a) relative forces $F_{H,3D}/(\rho_w g h^3)$ and $F_{H,u,3D}/(\rho_w g h^3)$ versus $t(g/h)^{1/2}$, (b) relative pressures $p_u/(\rho_w g h)$ and $p_d/(\rho_w g h)$ along z/h at $y = 7.5$ m, (c) relative displacements d_x/l and (d) relative stresses $\sigma_{zz}/(\rho_s g l)$ at the inner fibre along z/h at $y = 7.5$ m during the maximum force for $E = 2 \cdot 10^2$ and $2 \cdot 10^4$ GPa.

Fig. 4.11c, d shows the relative displacements d_x/l and stresses $\sigma_{zz}/(\rho_s g l)$ along z/h during the maximum $F_{H,3D}$. As expected, the rigid plate shows negligible d_x/l compared to the flexible plate. The maximum $d_{x,max}/l$ was observed near the centre of the plate at the instant during the maximum $F_{H,3D}$. The maximum $\sigma_{zz,max}/(\rho_s g l)$ were observed at the bottom of the plates, with a deviation between the rigid and flexible plates of 7% only.

4.4.2 Onshore

4.4.2.1 Validation of solids4foam with an available laboratory experiment

The numerical model was further validated with a laboratory solitary wave experiment from Kimmoun et al. (2009). The experimental set-up consisted of a flume with a 1:15 sloped shore and a 1.00 m high plate (Fig. 4.12a). A solitary wave with $a/h = 0.12$ impacting a plastic plate with $s = 5.0$ mm, $E = 3.25$ GPa and $\rho_s = 1190$ kg/m³ is discussed herein. The plate was fixed at the bottom end and supported at $z = 0.872$ m. The water surface and plate deflections were recorded with 2 cameras. A mesh resolution of $\Delta x = \Delta z = 4.0$ mm was used for the fluid and $\Delta x = 2.5$ mm and $\Delta z = 2.0$ mm for the solid domain. A simulated time of 6 s took approximately 12 days of computation time with 40 CPUs and 500 GB of memory.

The wave overturned in front of the plate and entrapped an air pocket when impacting the plate. This resulted in a complex wave-plate interaction (Peregrine, 2003; Bredmose et al., 2015). Fig. 4.12b shows the experimental and numerical snapshots at $t = 0.03$ s, where $t = 0.00$ s is the instant when the wave reaches the plate. The water surface elevation is captured well in the simulation, however, the volume of the air pocket is smaller than in the laboratory experiment.

The plate displacements d_x at $z = 0.35$ m are compared in Fig. 4.12c. The experimental and numerical d_x show similar trends, apart from some deviations. For $t \leq 0$ s, $d_x < 0$ m was measured in the laboratory experiments, while $d_x = 0$ m is expected. The two peaks of d_x observed in the laboratory experiments at $t \approx 0.08$ and 0.45 s are captured in the simulation, with deviations of up to 35%.

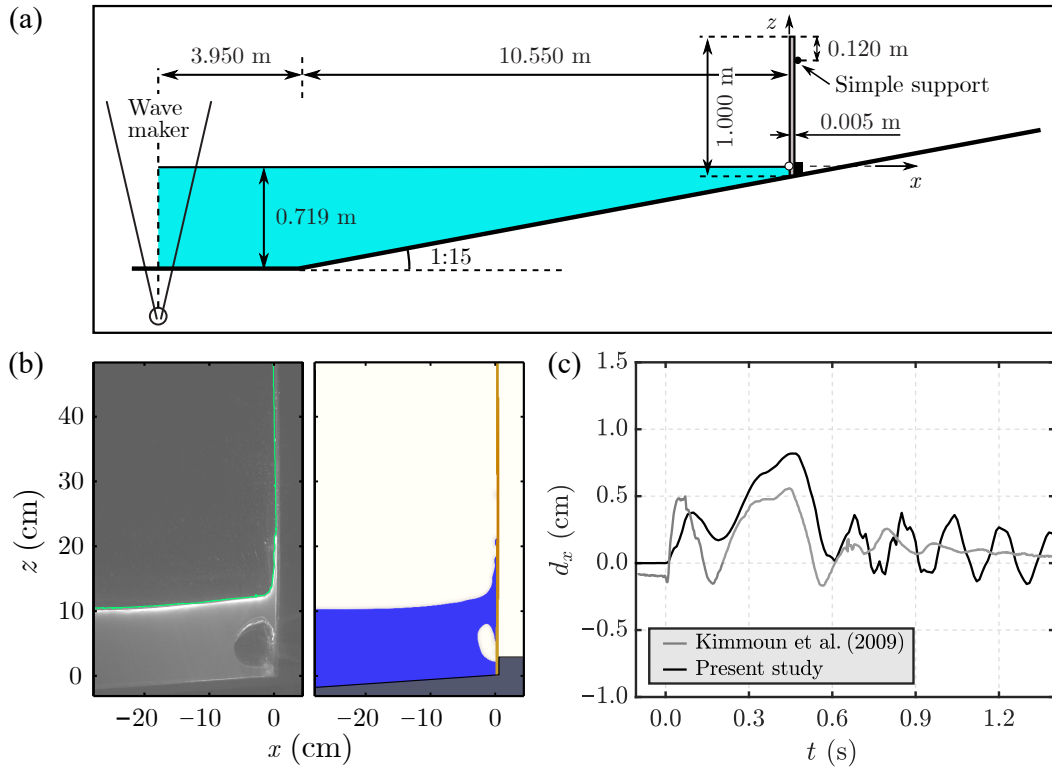


Figure 4.12. Validation of solids4foam with an experiment of Kimmoun et al. (2009): (a) experimental set-up, (b) comparison between the laboratory and numerical snapshots at $t = 0.03$ s and (c) horizontal plate displacement d_x at $z = 0.35$ m (after Attili et al., 2022b).

Once the wave was reflected and propagated towards $x \leq 0$ m, the plate oscillated with a certain frequency, as shown in Fig. 4.12c for $t \geq 0.6$ s. In this phase, the comparison reveals that the laboratory results are affected by a relatively larger damping than the simulation results. In the latter, damping is due to numerical effects only, e.g. temporal discretisation, as physical damping is not modelled in solids4foam. The damping ratio based on the logarithmic decrement of d_x can be evaluated as

$$\zeta = \frac{1}{\sqrt{1 + \left[2\pi / \left(\ln \frac{d_{x,i}}{d_{x,i+1}} \right) \right]^2}} \quad (4.12)$$

with $d_{x,i}$ and $d_{x,i+1}$ as the displacements of two successive peaks. For $0.6 \text{ s} \leq t \leq 1.4$ s, the averaged ζ resulted in 0.058 and 0.022 for the laboratory and numerical d_x , respectively. The larger ζ and the negative d_x for $t \leq 0$ s shown in the laboratory experiments, in addition to the assumption of incompressible fluid in the simulation, may explain the observed deviations.

4.4.2.2 A numerical representative test

Fig. 4.13 shows a snapshot series of an onshore test for a solitary wave with $a/h = 0.4$ impacting the plate TF2 (Table 4.2). A water column following the wave run-up was observed in front of the plate, which collapses after its kinetic energy is transformed into potential energy (Fig. 4.13c, d).

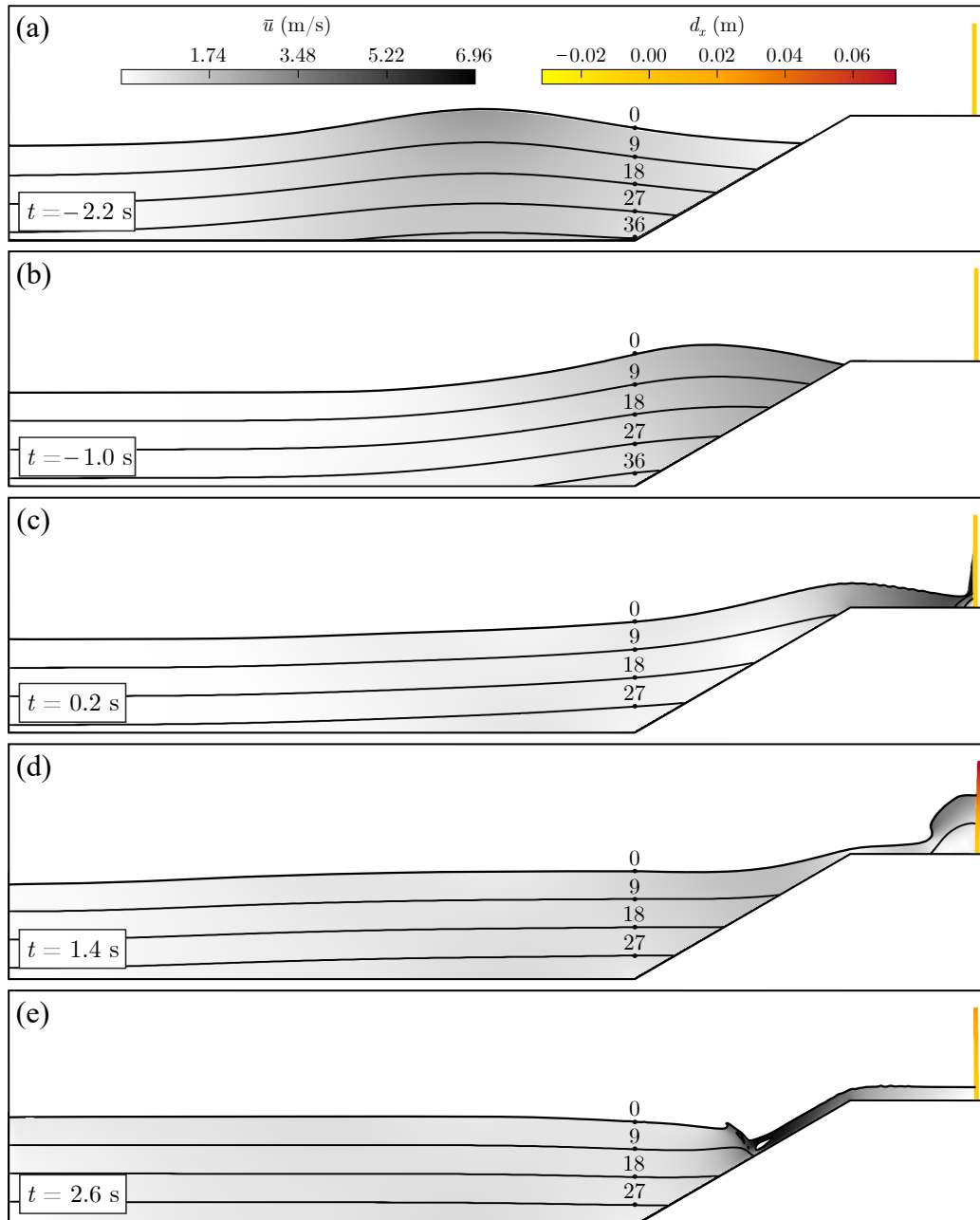


Figure 4.13. Snapshot series of a 2D solitary wave impacting an onshore plate with $a/h = 0.40$, $s = 0.15$ m and $E = 1.00$ GPa showing the mean velocity $\bar{u} = \sqrt{\bar{u}_x^2 + \bar{u}_z^2}$, pressure contours (kPa) and horizontal displacement d_x .

4.4.2.3 Numerical force

The horizontal force F_H acting on the plate shows a first peak F_I at the initial impact followed by a second peak F_{II} (Fig. 4.14a, b), confirming previous laboratory observations (Linton et al., 2013; Didier et al., 2014). F_{II} is a consequence of the collapse of the water column following the wave run-up at the plate. All tests show a double peak apart from the 5 tests with $a/h = 0.225$ and $z_f/h = 0.000$. In these tests a single peak of F_H was observed, most likely due to the relatively small a/h and large wave length L .

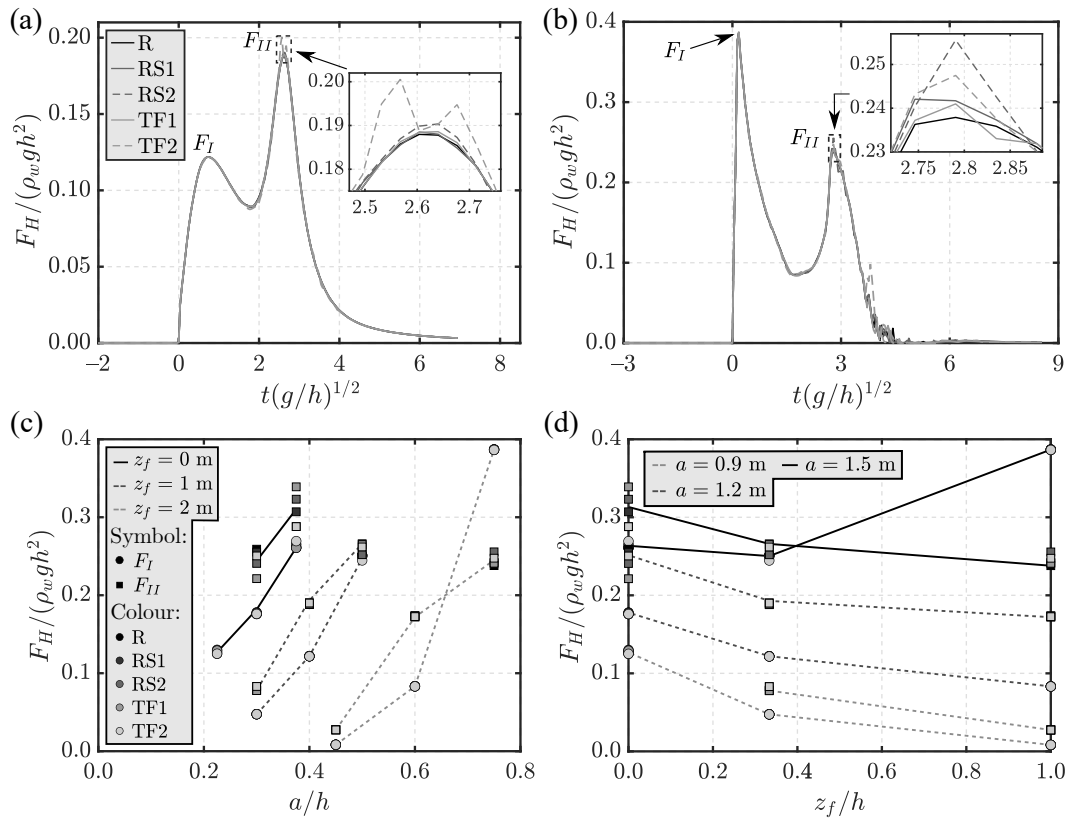


Figure 4.14. Plate forces at the 5 plates shown in Table 4.2 for onshore tests: relative force $F_H / (\rho_w g h^2)$ versus t with (a) $a/h = 0.40$ and (b) $a/h = 0.75$ and (c, d) $F_H / (\rho_w g h^2)$ versus (c) a/h and (d) z_f/h .

F_{II} is up to 3.3 times larger than F_I , apart from the tests with $a/h = 0.75$ (Fig. 4.14b). In these tests, due to the relatively large steepness $a/L = 0.09$, surging breaking was observed in proximity of the shore. This resulted in a violent impact on the plate. Fig. 4.14c, d shows $F_H / (\rho_w g h^2)$ versus a/h and z_f/h . $F_H / (\rho_w g h^2)$ increases

with increasing a/h for a constant z_f . For a constant a , $F_H/(\rho_wgh^2)$ decreases with increasing z_f/h , except for the tests with $a/h = 0.75$.

An important finding of this study is that the rigidity of the onshore plate tends to have a negligible effect on F_H (Fig. 4.14c, d). The largest deviations between the 5 plates under constant wave conditions are observed for large a/h and/or small z/h . Plate R does not necessarily result in the maximum F_H , with deviations of the flexible plates in relation to plate R of up to 3.0% and 17.7% for F_I and F_{II} , respectively. As a result, the design of flexible onshore plates can be based on design approaches for rigid plates combined with a safety factor of 1.2 to account for the observed force variations.

4.4.2.4 Numerical plate response

The plate deformation depends on the flexural rigidity and the wave loading. The plate R shows negligible horizontal displacements d_x . Maximum deformations were observed for the most flexible plates, namely RS2, TF1 and TF2 (Table 4.2). Fig. 4.15a, b shows d_x/l along the centroidal axis and $\sigma_{zz}/(\rho_sgl)$ along the inner fibre of the plate for a representative test with $a/h = 0.4$ at the instant when F_{II} occurred. The plates RS2 showed a maximum $d_{x,max}$ near the centre, while this is observed at the top end for TF1 and TF2. Note that $d_{x,max}$ do not necessarily occur at the instant when the maximum F are observed.

Plate TF2 shows the largest $\sigma_{zz}/(\rho_sgl)$ due to the largest deformation. For all 5 plates, the largest $\sigma_{zz}/(\rho_sgl)$ are observed at the fixing point of the plate. The maximum $d_{x,max}/l$ and $\sigma_{zz,max}/(\rho_sgl)$ are shown as a function of a/h in Fig. 4.15c, d for plates RS2, TF1 and TF2. Overall, both $d_{x,max}/l$ and $\sigma_{zz,max}/(\rho_sgl)$ increase with increasing a/h for a constant z_f/h . $d_{x,max}/l$ of TF1 are close and/or slightly larger than $d_{x,max}/l$ of RS2. In contrast, $\sigma_{zz,max}/(\rho_sgl)$ of TF1 are smaller than for RS2. Once the wave was reflected, the plate oscillated with a certain frequency f_s . As expected, plates TF1 and TF2 oscillated with f_s close to their natural frequencies (Table 4.2), namely at $f_s = 4.55$ and 2.27 Hz.

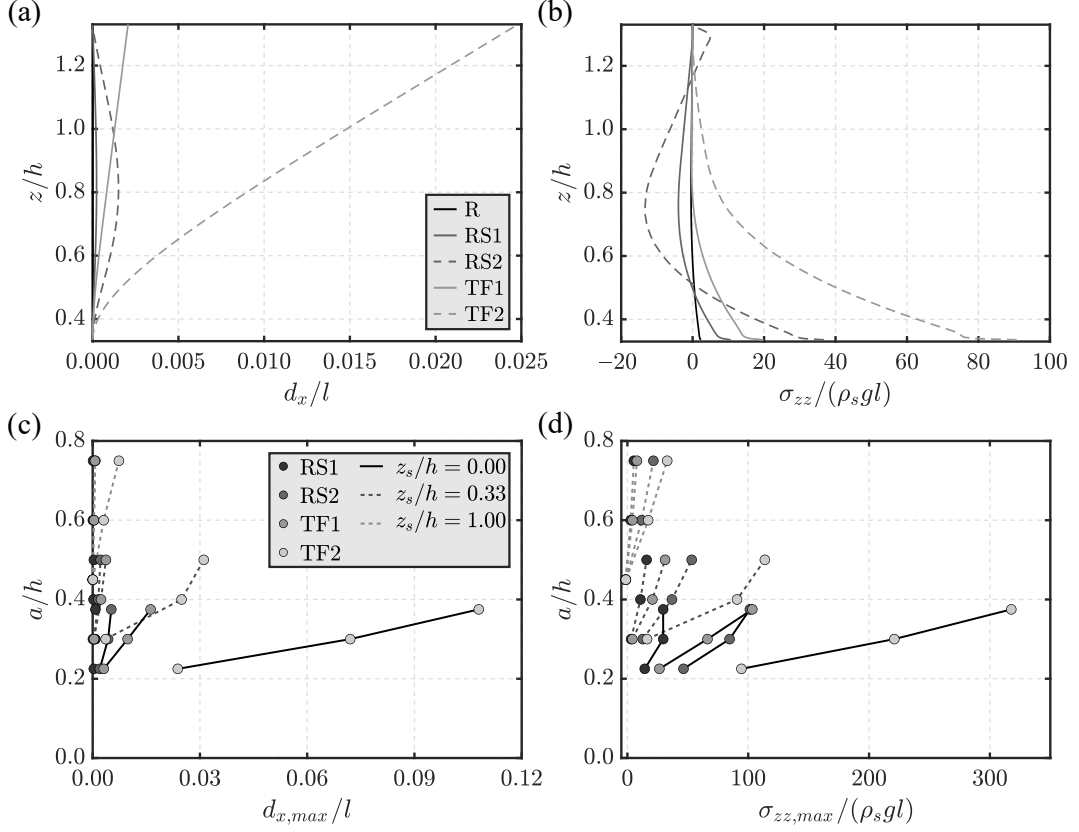


Figure 4.15. Plate response for the 5 plates (Table 4.2) in the onshore tests: (a) dimensionless horizontal displacement d_x/l and (b) vertical stress component $\sigma_{zz}/(\rho_s g l)$ along z/h at $t(g/h)^{1/2} = 2.64$ with $a/h = 0.4$ and maximum (c) $d_{x,max}/l$ and (d) $\sigma_{zz,max}/(\rho_s g l)$ versus a/h .

4.5 Discussion of results

4.5.1 Offshore

4.5.1.1 Force

The numerical $F_{H,u,num}/(\rho_w g h^2)$ in the offshore tests are compared with predictions based on Evers et al. (2019) and Heller et al. (2009). The prediction equation of Evers et al. (2019) has been slightly modified into

$$F_{H,u} = [1 - 1.5(a/h)]^{1/6} (1/2) \rho_w g (2a + h - l_s)^2, \quad (4.13)$$

to disregard the trapezoidal section of $p(z)$ acting on the substructure at $-h \leq z < (-h + l_s)$. The comparison in Fig. 4.16 reveals that $F_{H,u,num}$ are captured by the prediction method of Evers et al. (2019), operating on the safe side for all tests. The solitary wave tests are predicted well by Eq. (4.13), with deviations of less than 22% for all investigated stiffnesses. The linear wave tests show the largest underestimations, namely up to 73%. These deviations are likely due to the fact that Eq. (4.13) relies on more extreme waves, including Stokes 5th order, cnoidal and solitary waves (Attili et al., 2021; Hess et al., 2023).

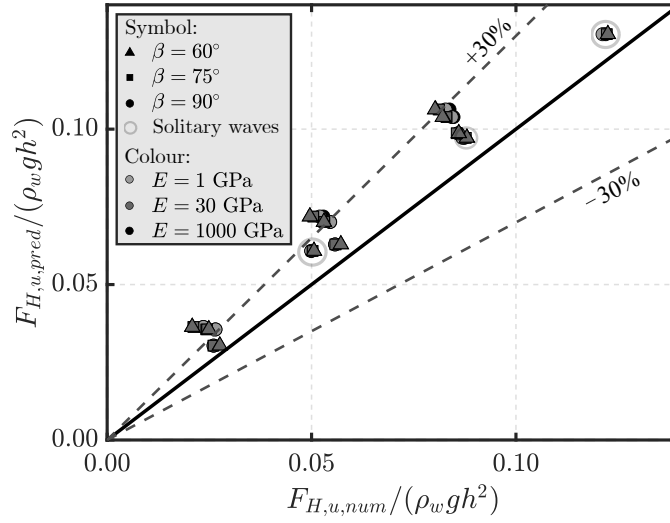


Figure 4.16. Comparison of the predicted $F_{H,u,pred}/(\rho_w g h^2)$ (Evers et al., 2019) and numerical $F_{H,u,num}/(\rho_w g h^2)$ for the linear and solitary (encircled) wave tests.

4.5.2 Onshore

4.5.2.1 Transformation into overland flow

Once the waves run-up the shore, they transformed into overland flows before impacting the plates (Fig. 4.17). The overland flow is characterised by the depth h_s and the depth-averaged velocity \bar{u}_s . These are defined at $x = z_f \cot \beta_s + L_s/2$ in the present study. The first force peak F_I (Fig. 4.14a, b) can be theoretically predicted as a function of h_s and \bar{u}_s with Eq. (4.1) (taken from Cross, 1967). Fig. 4.10a shows the predicted $F_{I,pred}/(\rho_w g h^2)$ based on Eq. (4.1) versus the numerical values $F_{I,num}/(\rho_w g h^2)$ for the tests with plate R. $F_{I,pred}$ was predicted assuming $C_f = 1$

and with the numerical h_s and \bar{u}_s resulting in the maximum $F_{I,pred}$. The comparison shows a good agreement between $F_{I,pred}$ and $F_{I,num}$, however, the predictions of h_s and \bar{u}_s remain challenging. Fuchs and Hager (2015) proposed empirical equations to predict $h_s(x)$ and $\bar{u}_s(x)$, which, however, result in unsatisfactory agreements in the present study with deviations of up to 117%. Further guidelines for the prediction of h_s and \bar{u}_s can be found in design standards (ASCE/SEI 7-16, 2017). In the following section, F_I and F_{II} are directly related to the offshore wave energy E_w such that h_s and \bar{u}_s are no longer required.

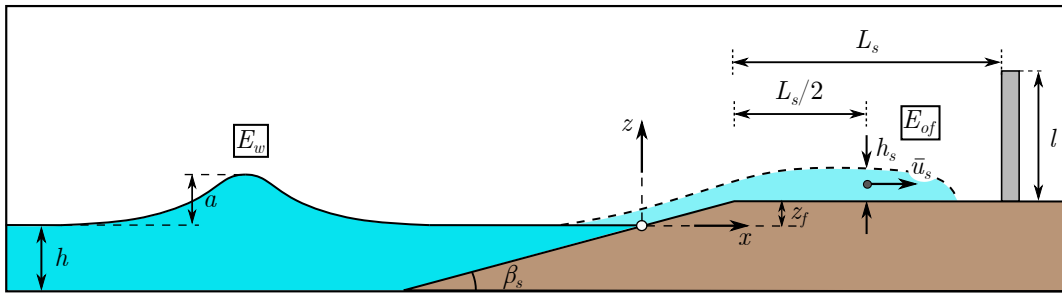


Figure 4.17. Sketch with the main parameters of a solitary wave and its transformation to overland flow.

When a wave propagates and runs-up a slope, its offshore wave energy is transformed into potential and kinetic energies of the overland flow. A portion of the wave energy is consumed during this process by various mechanisms, including bottom friction, reflection from the shore and wave breaking. The energy associated with the reflection from the shore was found to be negligible in the study of Li and Raichlen (2003) and von Häfen et al. (2022) found that the energy dissipated by wave breaking is proportional to a .

The wave energy per unit width E_w is composed of the kinetic and potential energies. According to Li and Raichlen (2003), E_w of a solitary wave is

$$E_w = \frac{8}{3\sqrt{3}}\rho_w g (ah)^{3/2}. \quad (4.14)$$

The total energy per unit area of the overland flow E_{of} due to the kinetic and potential components is

$$E_{of} = \frac{1}{2}\rho_w h_s \bar{u}_s^2 + \rho_w g h_s (h + z_f + h_s/2). \quad (4.15)$$

Based on the energy balance, it can be assumed that E_w is directly proportional to E_{of} . By employing a least-square approach algorithm, the following equation has been derived (Fig. 4.18b)

$$\frac{E_{of}}{[\rho_w g (h + z_f + a)^2]} = \frac{5}{2} \frac{E_w}{[\rho_w g (h + z_f + a)^3]} - 0.06. \quad (4.16)$$

The intercept 0.06 in Eq. (4.16) takes the energy consumed by bottom friction, reflection from the shore and wave breaking into account. The forces F_I and F_{II} observed at the 5 plates (Table 4.2) were also expressed as a function of E_w as (Fig. 4.18c, d)

$$\frac{F_I}{[\rho_w g (h + z_f + a)^2]} = \frac{5}{4} \frac{E_w}{[\rho_w g (h + z_f + a)^3]} - 0.04, \quad (4.17)$$

$$\frac{F_{II}}{[\rho_w g (h + z_f + a + l)^2]} = \frac{2}{3} \frac{E_w}{[\rho_w g (h + z_f + a)^3]} - 0.02. \quad (4.18)$$

The constants in Eqs. (4.17) and (4.18) have been optimised based on a least-square approach algorithm. Eqs. (4.17) and (4.18) capture the numerical results well and most of the data deviate less than $\pm 30\%$. Eq. (4.17) underestimates the tests with $a/h = 0.75$ by a factor of up to 2.43. Once again, the surging breaking and relatively violent impact on the plate may be the reason for the observed deviations. In this case, advanced turbulence models could provide more accurate results (Larsen and Fuhrman, 2019; Xie and Chu, 2019). Similar correlations are shown in Appendix 4.C to predict $d_{x,max}$ and $\sigma_{zz,max}$.

Eqs. (4.17) and (4.18) can be used to predict the maximum surge forces on on-shore buildings and infrastructures. To apply these equations, the main dimensionless parameters need to be within the investigated ranges, namely $0.225 \leq a/h \leq 0.750$, $1 \leq L_s/h \leq 2$, $0 \leq z_f/h \leq 1$ and $\beta_s = 30^\circ$. However, Eqs. (4.17) and (4.18) may still

provide good preliminary estimates when these limitations are moderately violated.

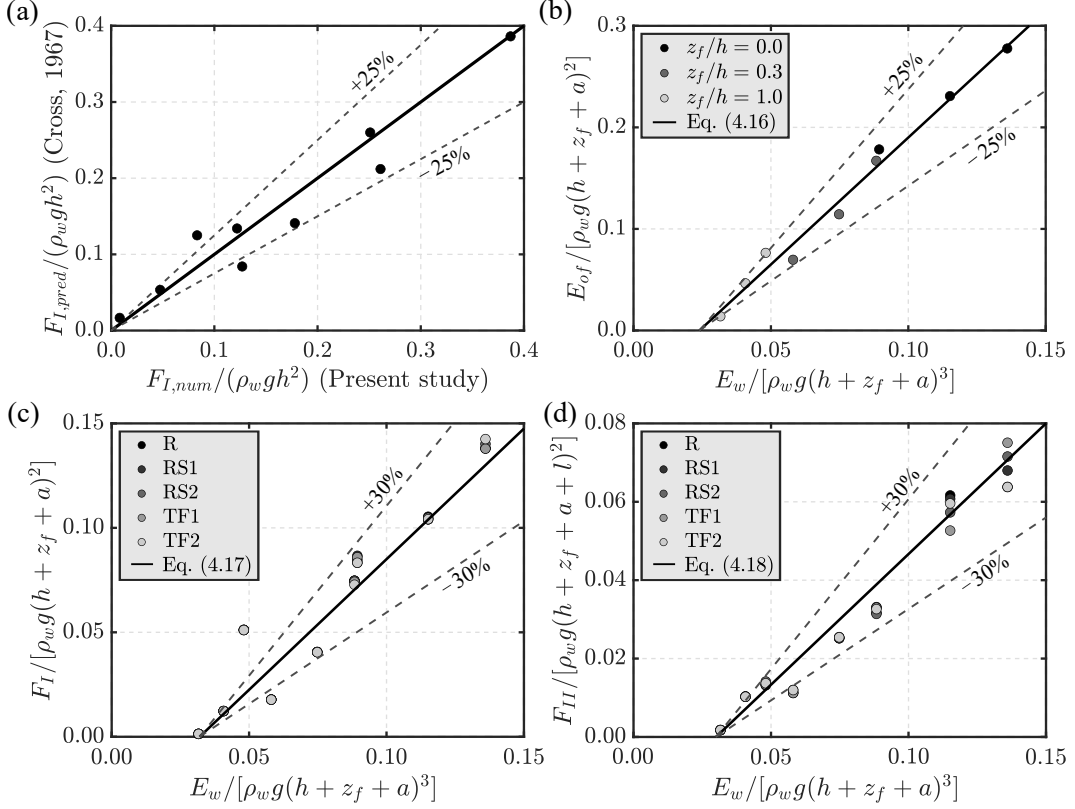


Figure 4.18. Overland flow: (a) comparison of the predicted (Cross, 1967) and numerical $F_I/(\rho_w g h^2)$ ($R^2 = 0.93$) at plate R, (b) energy of the overland flow $E_{of}/[\rho_w g (h + z_f + a)^2]$ with Eq. (4.16) ($R^2 = 0.98$) for plate R, (c) $F_I/[\rho_w g (h + z_f + a)^2]$ with Eq. (4.17) ($R^2 = 0.90$) versus the wave energy $E_w/[\rho_w g (h + z_f + a)^3]$ and (d) $F_{II}/[\rho_w g (h + z_f + a + l)^2]$ versus $E_w/[\rho_w g (h + z_f + a)^3]$ with Eq. (4.18) ($R^2 = 0.96$) for all 5 plates in Table 4.2.

4.5.2.2 Run-up height

The maximum run-up heights R at the onshore plates are predicted relative to the shore height $(h + z_f)$ as (Fig. 4.19)

$$\frac{R}{(h + z_f)} = \frac{9}{2} \frac{a}{(h + z_f)} - 0.6. \quad (4.19)$$

As discussed for Eqs. (4.17) and (4.18), a requirement for applying Eq. (4.19) is that the dimensionless parameters in nature are within the investigated ranges and $\beta_s = 30^\circ$. For solitary wave transformation into overland flow, β_s has an effect on the bottom friction, e.g. smaller β_s result in larger propagation distances, and on

the reflection from the shore. For relatively steep slopes, the energy dissipated by bottom friction and reflection from the shore is negligible compared to the energy dissipated by wave breaking (Li and Raichlen, 2003). As a result, a is the most important parameter, such that Eq. (4.19) provides a reasonable prediction of R even for $\beta_s \neq 30^\circ$. However, for rough slopes and relatively small β_s , the energy dissipation due to bottom friction would have to be taken into account such that Eq. (4.19) may overestimate R .

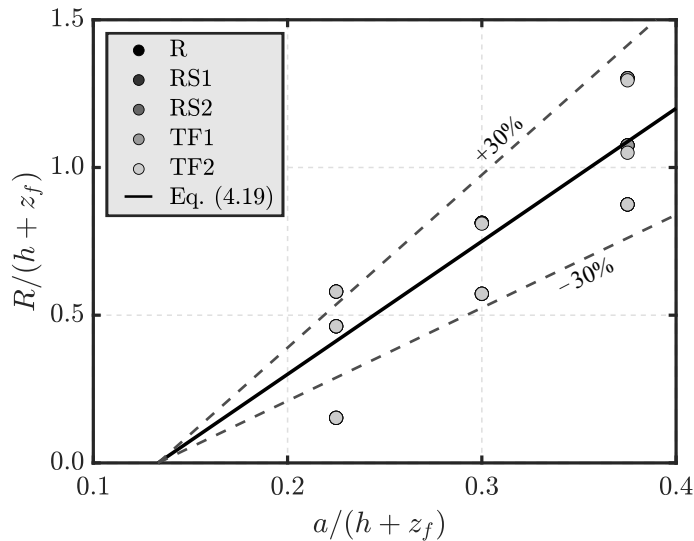


Figure 4.19. Dimensionless run-up $R/(h + z_f)$ versus the dimensionless wave amplitude $a/(h + z_f)$ with Eq. (4.19) ($R^2 = 0.75$).

4.6 Conclusions

Waves impacting rigid and flexible plates were investigated based on laboratory and numerical modelling. This study was motivated by the limited knowledge of Wave-Structure Interaction (WSI) effects and the need to further investigate the effect of the plate stiffness on wave forces. The main conclusions are summarised hereafter.

Small-scale laboratory tests of wave impact on offshore plates of different stiffnesses were conducted to validate the numerical model solids4foam. This resulted in a good agreement with the laboratory observations for 2 representative tests, apart from the strain where deviations of up to 59.7% have been observed. The numerical model was further validated with a solitary wave impacting an onshore flexible plate

experiment from Kimmoun et al. (2009). A total of 117 numerical tests were conducted to investigate wave impacts on offshore and onshore plates with 2D set-ups. These involved a range of linear and solitary waves with plates of different stiffnesses. The standard k - ε model has been used because the turbulence effect was small in the offshore tests and fully turbulent flows were observed in the onshore tests. However, more advanced models, e.g. the Re-Normalised Group k - ε and Shear Stress Transport k - ω models, should be employed for more complex processes with strong turbulence and air entrainment (Larsen and Fuhrman, 2019; Xie and Chu, 2019).

The simulations were conducted assuming elastic plates, hence, no energy dissipation due to the material was taken into account. This approximation is suitable for real applications, where energy dissipation is expected to be relatively small.

In the offshore tests, the linear wave run-up heights R were up to 116% overpredicted by the equation of Miche (1951) whilst the solitary wave R were in good agreement with predictions from the equation of Müller (1995) (Fig. 4.9b). The upstream horizontal forces $F_{H,u}$ were captured by the prediction method based on Evers et al. (2019) for all investigated stiffnesses. The total forces F_H were up to 40% smaller for the tests with Young's moduli $E = 1$ GPa than for tests with $E = 1000$ GPa. These deviations were mostly due to an increase in the downstream water depth h_d as a consequence of the plate deformation. The offshore plate responses were successfully analysed based on the Euler-Bernoulli beam theory (Appendix 4.B). Solitary wave impact on 3D rigid and flexible plates was also simulated. Negligible deviations of the pressures have been observed across the plate width. Once again, the plate stiffness had negligible effects on the wave forces, with relatively small deviations observed in the total force.

The force acting on the onshore plates showed a first F_I and second F_{II} peak, confirming available laboratory observations (Linton et al., 2013; Didier et al., 2014). With the exception of a few tests where surging breaking was observed, F_{II} was up to 3.3 times larger than F_I . The rigidity of the plate had a negligible effect on the wave force in most of the tests (Fig. 4.14c, d). For constant wave conditions, the largest

deviations between the 5 plates (Table 4.2) were observed for large wave amplitude relative to the water depth a/h and/or small relative shore freeboard z_f/h . The rigid plate did not necessarily result in the maximum wave forces, with deviations of the flexible plates in relation to the rigid one of up to 3.0 and 17.7% for F_I and F_{II} , respectively.

The solitary wave transformation into overland flow was also analysed for the onshore tests. New semi-theoretical correlations based on the solitary wave energy were derived. These provide the wave forces for both F_I and F_{II} and plate responses, including the horizontal displacement and vertical stresses. In addition, the maximum R were approximated in function of a , h and z_f .

To sum up, the flexible plates did not necessarily result in smaller wave forces compared to the rigid ones for the investigated conditions. In the offshore tests, the plate stiffness had a negligible effect on the upwave forces. However, smaller total forces were observed for more deformable offshore plates. Based on that, the actual stiffness of the plate needs to be taken into account for the design of offshore plates. The total forces on the onshore plates were unaffected by the plate stiffness in most tests. Up to 17% deviations were observed in a few tests, however, with the rigid plate not always resulting in the largest force. Therefore, the design of both rigid and flexible onshore plates can be based on design approaches for rigid plates combined with a safety factor of 1.2 to account for the observed force variations within this study.

Ongoing and future work will focus on the scaling and scale effects in WSI phenomena. This, along with the findings of Attili et al. (2021) and of the present article, are aimed at enhancing the physical understanding and modelling as well as support the design of coastal and offshore structures.

4.A Convergence tests

Convergence tests were conducted for both the offshore and onshore set-ups (Fig. 4.1). Resolutions of $\Delta x = \Delta z = 0.075, 0.150, 0.300$ and 0.600 m were investigated in the offshore case. The finest resolutions $\Delta x = \Delta z = 0.075, 0.150$ and 0.300 m were used in a $25 \text{ m} \times 32 \text{ m}$ refined area only (Fig. 4.1a), with larger meshes $\Delta x = \Delta z = 0.300$ and 0.600 m in the remainder of the domain.

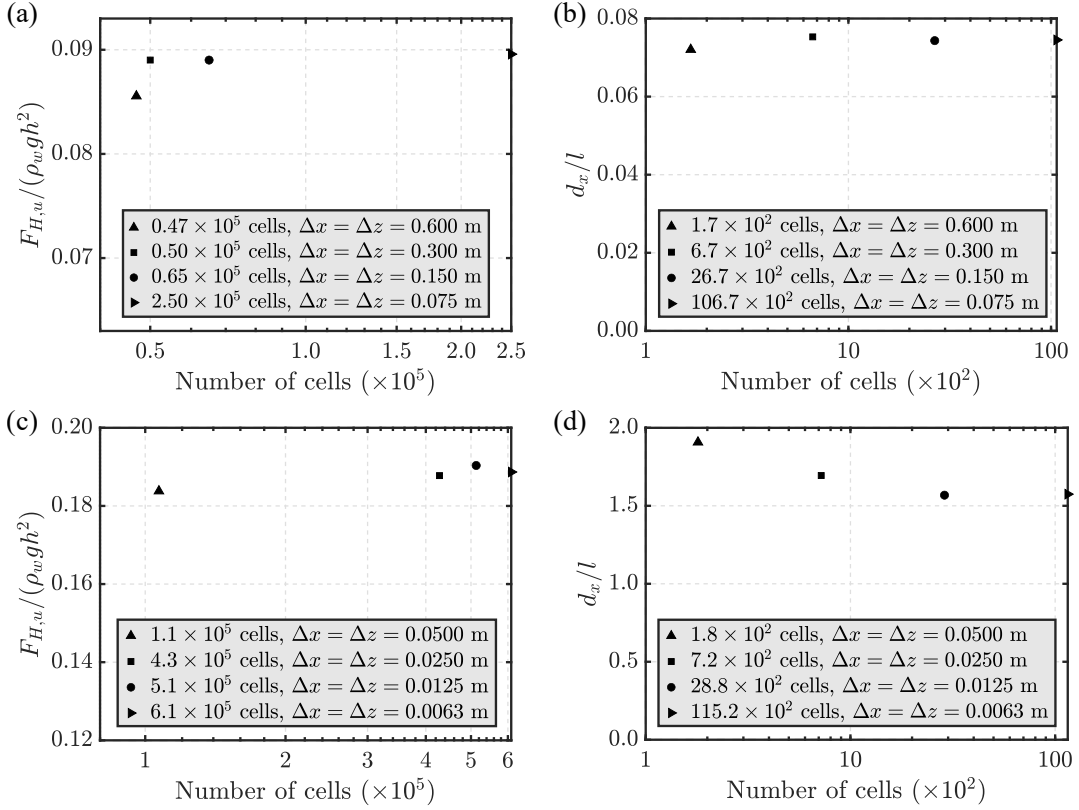


Figure 4.A.1. Convergence tests: semi-logarithmic diagramme for the relative (a, c) force $F_{H,u}/(\rho_w g h^2)$ and (b, d) horizontal displacement d_x/l with the number of cells and mesh size $\Delta x = \Delta z$ for an (a, b) offshore and (c, d) onshore test.

Convergence tests were conducted with a solitary wave with $a/h = 0.073$ and $L = 2\pi h/(0.75a/h)^{1/2} = 1346$ m (Lo et al., 2013) impacting a plate with $E = 1$ GPa. $F_{H,u}/(\rho_w g h^2)$ and d_x/l are shown versus the number of cells and mesh sizes in Fig. 4.A.1a, b. $\Delta x = \Delta z = 0.150$ m was used for the main tests as convergence is achieved. This resulted in negligible differences ($< 1\%$) with $\Delta x = \Delta z = 0.075$ m, for both $F_{H,u}$ and d_x , requiring approximately 1/4 of the computational time.

A solitary wave with $a/h = 0.4$ and $L = 2\pi h/(0.75a/h)^{1/2} = 34.4$ m (Lo et al., 2013) impacting plate RS2 (Table 4.2) has been simulated to investigate the optimal mesh resolution for the onshore tests. Resolutions of $\Delta x = \Delta z = 0.0063, 0.0125, 0.0250$ and 0.0500 m were investigated. The finest resolutions $\Delta x = \Delta z = 0.0063$ and 0.0125 m were used in a $1.40 \text{ m} \times 3.00 \text{ m}$ area surrounding the plate, while $\Delta x = \Delta z = 0.0250$ m was used in the rest of the domain (Fig. 4.1b). $F_{H,u}/(\rho gh^2)$ overall decreases with rougher resolutions, while d_x/l increases (Fig. 4.A.1c, d). $\Delta x = \Delta z = 0.0125$ m resulted in the optimal mesh resolution. This shows deviations of only 0.9% and 0.4% for $F_{H,u}/(\rho_w gh^2)$ and d_x/l , respectively, in relation to $\Delta x = \Delta z = 0.0063$ m and required 1/2 of the computational time.

4.B An application of the Euler-Bernoulli beam theory for offshore plates

The Euler-Bernoulli beam theory describes the behaviour of beams under axial forces and bending (Timoshenko, 1983). By assuming that plane beam sections remain plane and perpendicular to the deformed neutral axis and the slope dd_x/dz is small, the beam deflection results in

$$EI \frac{d^4 d_x}{dz^4} = p(z). \quad (4.B.1)$$

In Eq. (4.B.1), $I = bs^3/12$ is the moment of inertia of the beam cross-section, with b as the beam width, and $p(z)$ represents a distributed static load. The moment curvature relation is

$$M = -EI \frac{d^2 d_x}{dz^2} \quad (4.B.2)$$

and the shear force is evaluated as

$$Q = -EI \frac{d^3 d_x}{dz^3}. \quad (4.B.3)$$

In the present study the bending moment in the beam is defined positive when it produces a compressive stress at the downwave face of the beam.

Based on the numerical observations, the offshore plate response may be assumed quasi-static as it is in phase with the excitation and no transient oscillations emerge. Under these assumptions, Eq. (4.B.1) can be applied to the offshore plates where $b = 1$ m and $p(z)$ due to hydrostatic and wave pressures is approximated as shown in Fig. 4.B.1, with $p = \rho_w g 2a [1 - 1.5(a/h)]^{1/6}$ (Heller et al., 2009; Evers et al., 2019). By integrating Eq. (4.B.1) between points 0-1, 1-2 and 2-3 (Fig. 4.B.1) the following 3 equations were obtained

$$EId_x(z_1) = p \frac{z_1^4}{24} + C_1 \frac{z_1^3}{6} + C_2 \frac{z_1^2}{2} + C_3 z_1 + C_4, \quad \text{for } 0 \leq z_1 < h, \quad (4.B.4)$$

$$EId_x(z_2) = p \left(1 - \frac{z_2}{10a}\right) \frac{z_2^4}{24} + C_5 \frac{z_2^3}{6} + C_6 \frac{z_2^2}{2} + C_7 z_2 + C_8, \quad \text{for } 0 \leq z_2 < 2a \quad \text{and} \quad (4.B.5)$$

$$EId_x(z_3) = C_9 \frac{z_3^3}{6} + C_{10} \frac{z_3^2}{2} + C_{11} z_3 + C_{12}, \quad \text{for } 0 \leq z_3 \leq (l - h - 2a). \quad (4.B.6)$$

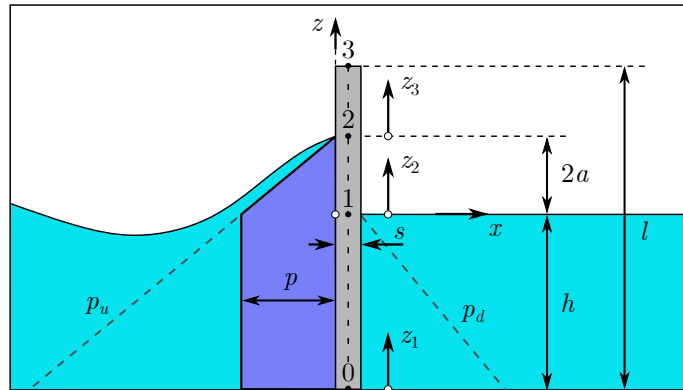


Figure 4.B.1. Sketch with the main parameters and pressure distribution of a wave impact on offshore plates.

For the sake of conciseness, the substructure has been omitted herein and $\beta = 90^\circ$ has been used. In the presence of a substructure (Fig. 4.1a), Eqs. (4.B.4) and (4.B.6)

are valid for $0 \leq z_1 < (h - l_s)$ and $0 \leq z_3 < (l - h + l_s - 2a)$, respectively. For $\beta < 90^\circ$, Eqs. (4.B.4) to (4.B.6) rely on the x - and z -axis rotated clockwise by $(90^\circ - \beta)$ compared to $\beta = 90^\circ$.

A number of boundary conditions can be imposed at points 0, 1, 2 and 3 (Table 4.B.1). These include zero displacement and rotation at point 0, continuity of the displacement, rotation, moment and shear force at points 1 and 2 and zero moment and shear force at point 3. These boundary conditions result in a system of 12 linear equations with C_i , for $i = 1, \dots, 12$ unknowns, with the solution shown in Table 4.B.2.

Table 4.B.1. Boundary conditions at the 4 significant points for the offshore plate of Fig. 4.B.1.

Point 0	Point 1	Point 2	Point 3
$d_x(z_1 = 0) = 0$	$d_x(z_1 = h) = d_x(z_2 = 0)$	$d_x(z_2 = 2a) = d_x(z_3 = 0)$	-
$\left. \frac{dd_x}{dz_1} \right _{z_1=0} = 0$	$\left. \frac{dd_x}{dz_1} \right _{z_1=h} = \left. \frac{dd_x}{dz_2} \right _{z_2=0}$	$\left. \frac{dd_x}{dz_2} \right _{z_2=2a} = \left. \frac{dd_x}{dz_3} \right _{z_3=0}$	-
-	$M(z_1 = h) = M(z_2 = 0)$	$M(z_2 = 2a) = M(z_3 = 0)$	$M(z_3 = l - h - 2a) = 0$
-	$Q(z_1 = h) = Q(z_2 = 0)$	$Q(z_2 = 2a) = Q(z_3 = 0)$	$Q(z_3 = l - h - 2a) = 0$

The Euler-Bernoulli beam equation can also be used to describe the distribution of the vertical stresses at the inner fibre of the beam

$$\sigma_{zz}(z) = \frac{s}{2} E \frac{d^2 d_x}{dz^2}. \quad (4.B.7)$$

By combining Eq. (4.B.7) with the second derivatives of Eqs. (4.B.4) to (4.B.6)

$$\sigma_{zz}(z) = \frac{s}{2I} \left(p \frac{z_{s1}^2}{2} + C_1 z_{s1} + C_2 \right), \text{ for } 0 \leq z_{s1} < h, \quad (4.B.8)$$

$$\sigma_{zz}(z) = \frac{s}{2I} \left[p \left(1 - \frac{z_{s2}}{6a} \right) \frac{z_{s2}^2}{2} + C_5 z_{s2} + C_6 \right], \text{ for } 0 \leq z_{s2} \leq 2a \text{ and} \quad (4.B.9)$$

$$\sigma_{zz}(z) = 0, \text{ for } z_3 > 0. \quad (4.B.10)$$

Table 4.B.2. Values for the constants in Eqs. (4.B.4), (4.B.5) and (4.B.6).

Constant	Value
C_1	$-ph - pa$
C_2	$p\frac{h^2}{2} + pha + \frac{p}{6}(2a)^2$
C_3	0
C_4	0
C_5	$-pa$
C_6	$\frac{p}{6}(2a)^2$
C_7	$p\frac{h^3}{6} + p\frac{h^2}{2}a + p\frac{h}{6}(2a)^2$
C_8	$p\frac{h^4}{8} + p\frac{h^3}{3}a + p\frac{h^2}{12}(2a)^2$
C_9	0
C_{10}	0
C_{11}	$p\frac{h^3}{6} + p\frac{h^2}{2}a + p\frac{h}{6}(2a)^2 + \frac{p}{24}(2a)^3$
C_{12}	$p\frac{h^4}{8} + p\frac{h^3}{3}2a + p\frac{h^2}{3}(2a)^2 + p\frac{h}{6}(2a)^3 + \frac{p}{30}(2a)^4$

The comparisons between the numerical and predicted d_x/l and $\sigma_{zz}/(\rho_s gl)$ based on Eqs. (4.B.4) to (4.B.6) and Eqs. (4.B.8) to (4.B.10), respectively, with the constants in Table 4.B.2, are shown in Fig. 4.B.2 for 4 representative tests. The maximum $d_{x,max}$ at the plate top end results from Eq. (4.B.6) with $z_{s3} = l - h + l_s - 2a$ in

$$d_{x,max} = 12 \frac{C_{11}(l - h + l_s - 2a) + C_{12}}{E_s^3}. \quad (4.B.11)$$

While such an application of the static Euler-Bernoulli beam theory provides a reasonable prediction of the offshore plate responses, future studies should include time varying load distributions for more complex wave-plate interactions.

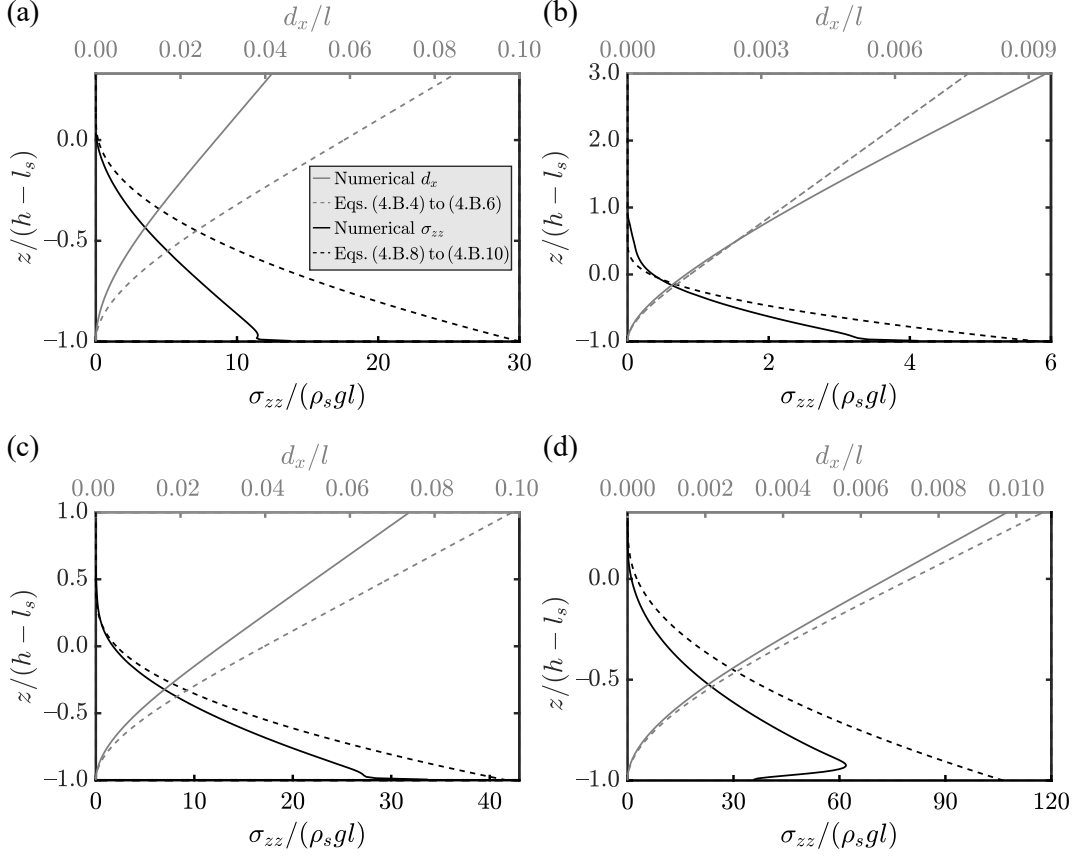


Figure 4.B.2. Comparison of the predicted and numerical (a) d_x/l ($nRMSE = 0.27$) and $\sigma_{zz}/(\rho_s gl)$ ($nRMSE = 0.22$) for a linear wave test with $a/h = 0.027$, $T(g/h)^{1/2} = 4.13$, $E = 1$ GPa and $\beta = 90^\circ$, (b) d_x/l ($nRMSE = 0.10$) and $\sigma_{zz}/(\rho_s gl)$ ($nRMSE = 0.09$) for a linear wave test with $a/h = 0.046$, $T(g/h)^{1/2} = 3.84$, $E = 1$ GPa and $\beta = 90^\circ$, (c) d_x/l ($nRMSE = 0.14$) and $\sigma_{zz}/(\rho_s gl)$ ($nRMSE = 0.10$) for a solitary wave test with $a/h = 0.073$, $E = 1$ GPa and $\beta = 90^\circ$ and (d) d_x/l ($nRMSE = 0.04$) and $\sigma_{zz}/(\rho_s gl)$ ($nRMSE = 0.17$) for a solitary wave test with $a/h = 0.062$, $E = 30$ GPa and $\beta = 60^\circ$.

4.C Correlations of the onshore plate response

The maximum $d_{x,max}$ and $\sigma_{zz,max}$ are expressed as a function of the offshore wave energy E_w for the onshore tests. For the roller support plates the following equations have been derived (Fig. 4.C.1a, b)

$$\frac{d_{x,max} E_s^3}{\rho_s g l^5} = \left(\frac{E_w}{[\rho_w g (h + z_f + a)^3]} \right)^2 - 8.0 \cdot 10^{-4}, \quad (4.C.1)$$

$$\frac{\sigma_{zz,max}s^2}{El^2} = 1.2 \cdot 10^{-4} \left(\frac{E_w}{[\rho_w g(h + z_f + a)^3]} \right) - 4.4 \cdot 10^{-6}. \quad (4.C.2)$$

For the top free plates, $d_{x,max}$ and $\sigma_{zz,max}$ are expressed as (Fig. 4.C.1c, d)

$$\frac{d_{x,max}Es^3}{\rho_s gl^5} = 19.0 \left(\frac{E_w}{[\rho_w g(h + z_f + a)^3]} \right)^2 - 0.04, \quad (4.C.3)$$

$$\frac{\sigma_{zz,max}s^2}{El^2} = 2.3 \cdot 10^{-3} \left(\frac{E_w}{[\rho_w g(h + z_f + a)^3]} \right)^2 - 3.6 \cdot 10^{-6}. \quad (4.C.4)$$

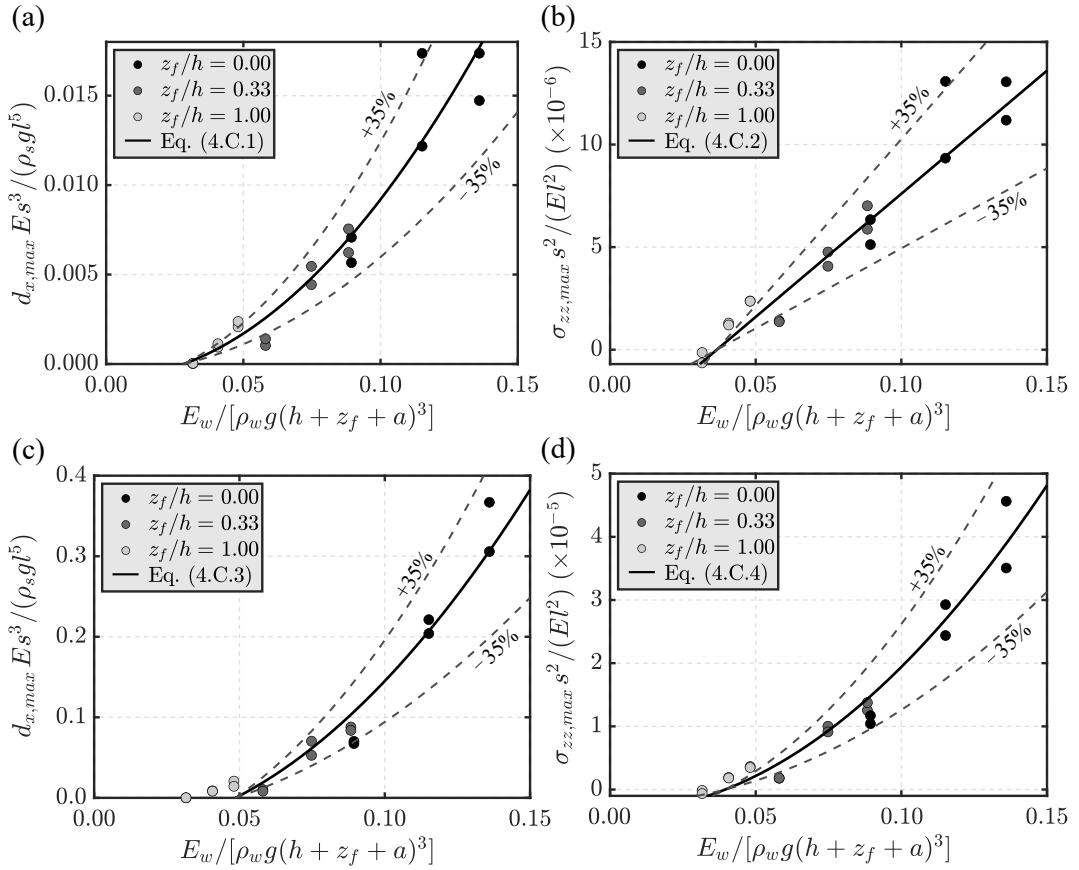


Figure 4.C.1. Plate response in the onshore tests: maximum relative (a) displacement $d_{x,max}Es^3/(\rho_s gl^5)$ with Eq. (4.C.1) ($R^2 = 0.93$) and (b) stress $\sigma_{zz,max}s^2/(El^2)$ with Eq. (4.C.2) ($R^2 = 0.93$) for plates RS and (c) $d_{x,max}Es^3/(\rho_s gl^5)$ with Eq. (4.C.3) ($R^2 = 0.95$) and (d) $\sigma_{zz,max}s^2/(El^2)$ with Eq. (4.C.4) ($R^2 = 0.96$) for plates TF versus the dimensionless wave energy $E_w/[\rho_w g(h + z_f + a)^3]$.

This page was intentionally left blank.

Chapter 5

Scaling approaches and scale effects in wave-flexible structure interaction

This chapter is comprised of the following journal article, which is currently in press for publication in the *Journal of Fluids and Structures*:

Attili, T., Heller, V. and Triantafyllou, S., 2023. Scaling approaches and scale effects in wave-flexible structure interaction. *Journal of Fluids and Structures* (in press).

To improve readability, the following adjustments have been made:

1. Section, page figure, table and equation numbers are amended to ensure consistency across the thesis.
2. The email addresses of the authors have not been included.
3. The nomenclature and references list are provided at the end of this thesis.

Scaling approaches and scale effects in wave-flexible structure interaction

Tommaso Attili¹, Valentin Heller¹, Savvas Triantafyllou²

¹Environmental Fluid Mechanics and Geoprocesses Research Group, Faculty of Engineering, University of Nottingham, Nottingham NG7 2RD, UK

²Institute for Structural Analysis and Aseismic Research, School of Civil Engineering, National Technical University of Athens, Athens, Greece

Abstract

Laboratory models are important for research, to inform design solutions and to calibrate and validate numerical models. Unfortunately, model-prototype similarity is often difficult to achieve in small models, resulting in scale effects. For Wave-Flexible Structure Interaction (WFSI), scale effects arise when the fluid and/or structure properties are incorrectly scaled. The present study provides a systematic investigation of scale effects for wave impacts on flexible and rigid plates based on numerical modelling supported by small-scale laboratory tests. Non-breaking and breaking wave impacts were simulated with regular and solitary waves for the prototypes and up to 40 times smaller models. These were scaled according to the scaling approaches (i) precise Froude (fluid and plate properties scaled), (ii) traditional Froude-Cauchy (fluid properties unscaled, plate properties scaled), (iii) traditional Froude (fluid and plate properties unscaled) and (iv) a new WFSI approach (partial conservation of the WFSI governing parameters). The numerical results confirmed the absence of scale effects for (i). Non-breaking wave impacts were correctly predicted for (ii), however, up to 132% scale effects were observed in the breaking wave pressures due to the unscaled fluid properties. The plate displacements were underestimated by up to 98% for (iii). The new approach (iv) was successfully validated based on non-breaking

waves, with less than 4.3% deviations for the maximum regular wave forces and plate displacements. Additionally, less than 3% deviations for the maximum solitary wave force and plate displacement were observed. The new scaling approach provides a more versatile alternative to traditional Froude-Cauchy scaling laws to support laboratory investigations of WFSI.

5.1 Introduction

5.1.1 Background

Wave-Structure Interaction (WSI) is relevant for numerous coastal and offshore structures, including breakwaters, floating and bottom-fixed wind turbines, wave energy converters and offshore oil and gas platforms (Cuomo et al., 2010a; He and Kashiwagi, 2012; Didier et al., 2014). For flexible structures undergoing non-negligible displacements, i.e. deflections larger than 0.5 to 2.0% of the structure length, called Wave-Flexible Structure Interaction (WFSI) herein, the involved physical processes are particularly complex. These structures may suffer from large stresses and deformations under wave loading and experience damage under extreme conditions. Given the complexity of these processes, e.g. variable geometries and complex flow fields, laboratory models (Linton et al., 2013; Krautwald et al., 2022; Attili et al., 2023b) are often used for research, to inform design solutions and to calibrate and validate numerical simulations.

A laboratory model is similar to its prototype if geometric, kinematic and dynamic similarities are satisfied (Kobus, 1980; Hughes, 1993; Heller, 2011). Exact model-prototype similarity is rarely achieved, due to the challenge of keeping all relevant force ratios constant between the prototype and its model. This results in scale effects, manifesting themselves in a variety of ways. For example, they can result in considerably different void fractions in air-water flows (Catucci et al., 2021) or non-identical pressures and forces in WSI between a model and its prototype (Abrahamson and Faltinsen, 2013; Bredmose et al., 2015).

Free-surface flow models are commonly scaled according to the Froude scaling laws (Le Méhauté, 1976; Hughes, 1993; Heller, 2011; Sheng et al., 2014), ensuring the same Froude number $Fr = (\text{inertial force/gravity force})^{1/2}$ in the prototype and model. When ordinary water and air are used in the model, other force ratios, such as the Reynolds number (inertial force/viscous force)

$$Re = \frac{g^{1/2}h^{3/2}}{\nu} \quad (5.1)$$

and Weber number (inertial force/surface tension force)

$$We = \frac{\rho_w g h^2}{\sigma} \quad (5.2)$$

are not conserved, introducing scale effects. In Eqs. (5.1) and (5.2), the shallow-water wave speed $(gh)^{1/2}$ was used as the characteristic velocity, with the gravitational acceleration g and the water depth h . The characteristic velocity and length can change with the investigated phenomenon. Further, ν is the kinematic viscosity, ρ_w the water (subscript w) density and σ the surface tension.

Re and We play a key role for air-water flows, e.g. for breaking waves (Kiger and Duncan, 2012) and plunging jets (Chanson et al., 2004; Catucci et al., 2021). Furthermore, the Mach number $Ma = (\text{inertial force/compressibility force})$ can be relevant when the air-water flow compressibility is important, e.g. for oscillating water columns (Falcão and Henriques, 2014) and violent wave impacts (Bredmose et al., 2015). For such processes, the Froude scaling laws typically provide unsatisfactory predictions (Hughes, 1993; Heller, 2011).

In WSI, scale effects are generally negligible for non-breaking waves under Froude similarity for commonly used laboratory scales, i.e. 1:10 to 1:50 (Hughes, 1993; Cuomo et al., 2010b). However, relevant scale effects are observed for breaking wave impacts (Hughes, 1993; Cuomo et al., 2010b; Blenkinsopp and Chaplin, 2011; Martinelli et al., 2011; Bredmose et al., 2015). Cuomo et al. (2010b) suggested an approach to remove scale effects in the upscaling process of wave impact pressures on rigid walls. Their

approach provides an estimate of the corrected pressure scaling law λ_p based on the Bagnold number Ba . This is a measure of the peak impact pressure and was expressed as (Cuomo et al., 2010b)

$$Ba = \frac{0.2(1 - \pi/12) \rho_w g (h + H)}{\pi/12 p_0}, \quad (5.3)$$

with the wave height H and the atmospheric pressure p_0 . Cuomo et al. (2010b) revealed that wave impact pressures on rigid coastal structures are overestimated by the Froude scaling laws. This was confirmed numerically by Bredmose et al. (2015), who found larger pressures in smaller models due to the relatively stiffer air. To overcome this, Bredmose et al. (2015) recommended to use the Bagnold-Mitsuyasu law for pressures larger than 3.18 times the atmospheric pressure, whilst for smaller pressures the Froude scaling laws provide good predictions. However, none of the aforementioned studies took potential structural deformations into account.

In WFSI, the geometry and elastic properties of the structure must also be appropriately scaled (Hudson et al., 1979; Hughes, 1993; Chakrabarti, 2005; Heller, 2011; Martinelli et al., 2011; Krautwald et al., 2022; Abrahamsen et al., 2023; Lambert et al., 2023). When elastic forces are relevant, scaling criteria follow the Cauchy similarity based on the Cauchy number $Ca = (\text{inertial force}/\text{elastic force})$. Froude and Cauchy similarities can be combined to the Froude-Cauchy similarity for WFSI phenomena (Le Méhauté, 1965; Chakrabarti, 2005; Krautwald et al., 2022), in which the Young's modulus E is scaled linearly with the geometrical scale factor between the prototype (subscript P) and model (subscript M) (Le Méhauté, 1965)

$$\lambda = \frac{h_P}{h_M}. \quad (5.4)$$

As the structure (subscript s) density ρ_s and Poisson ratio have to be constant between the prototype and its model, it is challenging to find an appropriate material for small scales. On the other hand, an incorrect scaling of the structural properties may have disastrous consequences, as in the case of the Sines breakwater which failed

in 1978, partially due to an underdesign informed by misleading laboratory results (Oumeraci, 1984; Le Méhauté, 1990). The most relevant WSI scaling studies are summarised in Table 5.1.

Table 5.1. Relevant scaling studies for various WSI phenomena.

Reference	Investigated phenomenon	λ	Comment
Cuomo et al. (2010b)	Wave impact pressures on vertical walls	1 to 40	Approach to upscale breaking wave pressures by removing scale effects
Abrahamsen and Faltinsen (2013)	Entrapped air pockets during slamming events	1 to 1200	New scaling laws for gas pocket pressures and rise times
Bredmose et al. (2015)	Breaking wave impacts on walls	1/16 to 16	New scaling law for breaking wave pressures
Catucci et al. (2021)	Dam break waves impacting an obstacle	1 to 16	Novel scaling laws excluding scale effects in air-water flows
Krautwald et al. (2022)	Bore wave impacts on (collapsing) timber structures	5	Large-scale experimental model under Froude-Cauchy similarity

A systematic investigation of scale effects in WFSI, including the modelling of both the fluid and the structure, is still lacking. The present study explores scale effects in wave impacts on rigid and flexible plates based on numerical modelling supported by small-scale laboratory experiments (Appendix 5.B). Dimensionless governing parameters are validated and used to define a new scaling approach which is more versatile than Froude-Cauchy scaling. Scale effects are systematically quantified for a range of scaling approaches to illustrate the benefits of this new approach.

5.1.2 Aims and structure

The present study is aimed at:

- Formulating and validating a set of governing parameters fully representing the underlying physics of WFSI.
- Formulating a new scaling approach for WFSI.
- Investigating scale effects in WSI based on different scaling approaches.

The remainder of this article is organised as follows. In Section 5.2, the numerical model is presented, including the governing equations and the numerical set-ups. This is followed by the governing parameters for WFSI, along with traditional scaling

laws and the new scaling approach. The main results are presented in Section 5.3, including the validation of the governing parameters and scale effects. These findings are discussed and applied to upscale new laboratory measurements in Section 5.4 and the main conclusions are summarised in Section 5.5. The appendices include the convergence tests (Appendix 5.A), a description of the physical experiments along with the main laboratory results (Appendix 5.B), used as illustrative examples for discussing scale effects and upscaling the results to hypothetical prototype scales, and additional data about the scaling and scale effects (Appendix 5.C).

5.2 Methodology

5.2.1 Numerical model

5.2.1.1 Governing equations and coupling technique

The open source toolbox solids4foam (Cardiff et al., 2018; Attili et al., 2021; 2022a; 2023b), implemented in foam-extend 4.0 (FE 4.0) (OpenFOAM extension, 2016), was used in the present study. The fluid and solid domains were solved based on the Finite Volume Method (FVM) discretisation and coupled with a partitioned approach. An incompressible Newtonian fluid model was used, satisfying the continuity

$$\nabla \cdot \bar{\mathbf{u}} = 0 \quad (5.5)$$

and Reynolds-Averaged Navier-Stokes (RANS) equations

$$\frac{\rho \partial \bar{\mathbf{u}}}{\partial t} + \rho(\bar{\mathbf{u}} \cdot \nabla) \bar{\mathbf{u}} = -\nabla \bar{p} + \rho \nabla \cdot (\mu \nabla \cdot \bar{\mathbf{u}} - \overline{\mathbf{u}' \mathbf{u}'}) + \rho \mathbf{g} + f_\sigma. \quad (5.6)$$

In Eqs. (5.5) and (5.6), $\bar{\mathbf{u}} = (\bar{u}_x, \bar{u}_y, \bar{u}_z)$ is the mean fluid velocity vector, \bar{p} the mean pressure, μ the fluid dynamic viscosity, $\overline{\mathbf{u}' \mathbf{u}'}$ the turbulent stress tensor, t the time, \mathbf{g} the gravitational acceleration vector and f_σ the surface tension force per unit volume (Brackbill et al., 1992). The k - ε turbulence model (Launder and Spalding, 1974) was used.

The time integration of Eqs. (5.5) and (5.6) was controlled based on the Courant-Friedrichs-Lewy (CFL) convergence condition (Courant et al., 1928)

$$C = \frac{\bar{u}_x \Delta t}{\Delta x} + \frac{\bar{u}_y \Delta t}{\Delta y} + \frac{\bar{u}_z \Delta t}{\Delta z} \leq 1 \quad (5.7)$$

where C is the Courant number, Δt the time step and Δx , Δy and Δz are the cell sizes in the x , y and z direction, respectively. Eqs. (5.5) and (5.6) were complemented with the Volume Of Fluid (VOF) method (Hirt and Nichols, 1981) to model air-water flows. This is based on the fraction of volume α , which varies from 0 to 1, with $\alpha = 0$ denoting air, $\alpha = 1$ water and $\alpha = 0.5$ was used to track the air-water interface. The wave generation and absorption was performed with the toolbox waves2Foam (Jacobsen et al., 2012), using a relaxation zone of 3 times the wave length L .

Contrary to the fluid, a Lagrangian approach was adopted for the solid domain. The momentum equation

$$\rho_s \frac{\partial^2 \mathbf{d}_s}{\partial t^2} + \nabla \cdot [(J \mathbf{D}_F^{-T}) \cdot \boldsymbol{\sigma}_s] = \rho_s \mathbf{g} \quad (5.8)$$

was solved, assuming large displacement kinematics with the Neo-Hookean elastic constitutive law. In Eq. (5.8), \mathbf{d}_s is the solid (subscript s) displacement vector, ρ_s the solid density, $\mathbf{D}_F = \mathbf{I} + (\nabla \mathbf{d}_s)^T$ the deformation gradient, with the identity matrix \mathbf{I} , J the determinant of \mathbf{D}_F and $\boldsymbol{\sigma}_s$ the stress tensor in Voigt notation.

The fluid-solid coupling was carried out with a partitioned approach (Tuković et al., 2018; Liu and Zhang, 2019). As such, after solving the fluid velocity and pressure fields, the fluid forces acting on the solid were evaluated. These were used as new boundary conditions to update the solid domain. Consequently, the new solid velocities were transferred to the fluid and the fluid mesh was updated. This was performed in a loop within each time step until convergence was achieved (Cardiff et al., 2018). This numerical model resulted in an overall good agreement with laboratory measurements for wave impacts on rigid and flexible plates (Attili et al., 2023b).

5.2.1.2 Numerical set-up and test programme

The numerical set-up involved a wave flume (2D) with a vertical offshore plate, as shown in Fig. 5.1a. Cartesian coordinates (x, y, z) are used in this study, with the origin at the still water surface. The plate, with $\rho_s = 8000 \text{ kg/m}^3$ and $E = 200 \text{ GPa}$, is 10 m high with a constant thickness $s = 0.15 \text{ m}$. Similarly as in Attili et al. (2023b), this design was inspired by the flood protection system MOSE (Erbisti, 2014) and the Oyster wave energy converter (Lagoun et al., 2010). A Poisson ratio of 0.3 was used in all tests.

A total of 3 prototype simulation tests have been conducted, involving non-breaking regular and solitary waves with the values for the wave height H , period T and amplitude a shown in Table 5.2. The simulations were run on the High Performance Computing (HPC) cluster Augusta at the University of Nottingham with 60 Central Processing Units (CPUs) and 150 GB of memory. A fluid resolution of $\Delta x = \Delta z = 0.05 \text{ m}$ was employed in a $11.00 \text{ m} \times 20.00 \text{ m}$ refined area, with $\Delta x = \Delta z = 0.10 \text{ m}$ in the remainder of the domain (Fig. 5.1, Appendix 5.A). A solid resolution of $\Delta x = \Delta z = 0.017 \text{ m}$ was used. The simulations were conducted with a fixed $\Delta t = 0.025 \text{ s}$ for the regular and $\Delta t = 0.017 \text{ s}$ for the solitary wave tests, satisfying Eq. (5.7). The regular wave tests took up to 50 h to simulate 102 s and a solitary wave test took approximately 20 h to simulate 20 s.

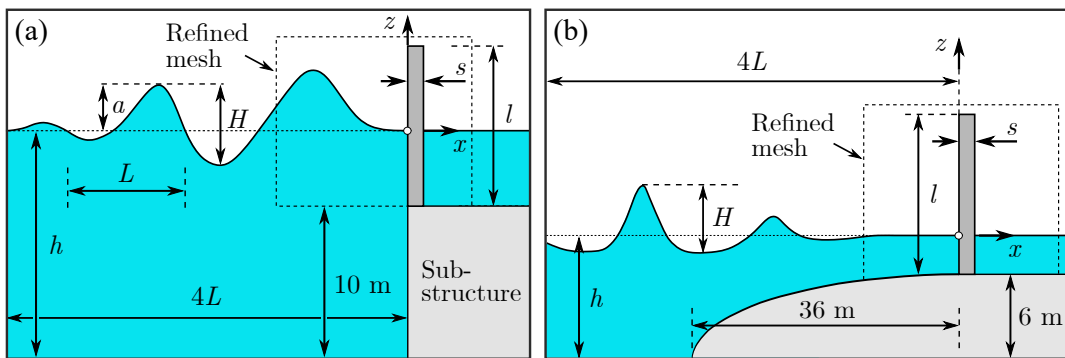


Figure 5.1. Side view of the prototype numerical set-ups for the (a) non-breaking wave and (b) breaking wave tests.

Table 5.2. Test programme for the prototype numerical tests.

Parameter	Symbol	Unit	Non-breaking waves	Breaking waves
Water depth	h	m	15	8.5
Plate height	l	m	10	10
Young's modulus	E	GPa	200	200, 400
Plate thickness	s	m	0.15	0.15, 0.50
Plate density	ρ_s	kg/m ³	8000	8000
	H	m	2	2.90
	H/h	-	0.13	0.34
Regular waves	T	s	5.5, 11	11.30
	$T(g/h)^{1/2}$	-	4.45, 8.90	12.14
	a	m	2	-
Solitary waves	a/h	-	0.13	-

5.2.1.3 Numerical simulation of breaking waves impacting plates

Additional numerical tests have been conducted to investigate breaking wave impacts on a plate. The numerical set-up was inspired by Bredmose et al. (2015), consisting of a wave flume with the plate located on top of a semi-elliptical shore (Fig. 5.1b). The 2 prototype tests involved a regular wave with $H = 2.9$ m and $T = 11.3$ s at $h = 8.5$ m, impacting a rigid and flexible plate with their mechanical properties summarised in Table 5.2. The same mesh resolution as for the tests in Section 5.2.1.2 was employed, with an adaptive Δt . Simulations were run on the HPC, taking up to 3.5 days to simulate 73 s.

5.2.2 Governing parameters in WFSI

For 2D wave interactions with flexible plates, 10 governing parameters were identified: H , T , h , ρ_w , ν , σ , the plate flexural rigidity $D = Es^3/12$, the plate mass per unit area $M_s = \rho_s s$, l and g . These involve the 3 units length [L], mass [M] and time [T], i.e. they can be reduced to a set of 7 dimensionless quantities based on the 3 reference parameters ρ_w , h and g (Buckingham, 1914). This results in the 7 dimensionless quantities shown in Table 5.3. Π_1 to Π_4 include the fluid parameters, with Π_1 and Π_2 representing the dimensionless wave height and period, and Π_3 and Π_4 the inverse of Re and We, respectively. The plate parameters are included in Π_5 to Π_7 , resulting in

the relative mass (Π_5), stiffness (Π_6) and height (Π_7). These dimensionless quantities can be used for a general dimensionless presentation of results without the need for upscaling (Section 5.3.1).

Table 5.3. Dimensionless governing parameters in 2D WFSI.

Π_1	Π_2	Π_3	Π_4	Π_5	Π_6	Π_7
$\frac{H}{h}$	$T \left(\frac{g}{h}\right)^{1/2}$	$\frac{\nu}{g^{1/2}h^{3/2}}$	$\frac{\sigma}{\rho_w g h^2}$	$\frac{M_s}{\rho_w h}$	$\frac{D}{\rho_w g h^4}$	$\frac{l}{h}$

5.2.3 Scaling approaches

The prototype tests (Table 5.2) have been simulated within a scale series (Heller et al., 2008) based on 4 different scaling approaches. These are summarised in Table 5.4 with the corresponding scaling laws for all relevant parameters. Simulations with geometrical scale factors $\lambda = 5, 10, 20$ and 40 were conducted for each scaling approach, with all initial conditions, mesh sizes and time steps scaled accordingly.

Table 5.4. Scaling laws for all WFSI relevant parameters under different scaling approaches.

Parameter	Unit	PFr	TFr _E	TFr	GP
H	m	λ	λ	λ	λ
T	s	$\lambda^{1/2}$	$\lambda^{1/2}$	$\lambda^{1/2}$	$\lambda^{1/2}$
ρ_w	kg/m ³	1	1	1	1
ν	m ² /s	$\lambda^{3/2}$	1	1	1
σ	N/m	λ^2	1	1	1
E	N/m ²	λ	λ	1	λ_E
ρ_s	kg/m ³	1	1	1	Unrestricted
s	m	λ	λ	λ	$\sqrt[3]{\lambda^4/\lambda_E}$
l	m	λ	λ	λ	λ
g	m/s ²	1	1	1	1

The precise Froude scaling (PFr) laws, in which the fluid and plate properties are correctly scaled (Catucci et al., 2021; 2023), were applied first. PFr do not involve any scale effects. Secondly, the traditional Froude-Cauchy scaling (TFr_E) laws, where ordinary water and air were used in the models, with the plate mechanical properties

scaled according to Cauchy similarity, were employed. Scale effects in the TFr_E laws are due to the non conservation of Re , We and Ma .

Traditional Froude scaling (TFr, Catucci et al., 2021; 2023) laws were also applied, relying on ordinary water and air at reduced scales and the plate stiffness was unscaled. Scale effects in TFr are expected due to a non conservation of Re , We , Ma and Ca . Finally, a new scaling approach based on the WFSI dimensionless governing parameters (Table 5.3), referred to as GP, was used. This is based on the conservation of Π_1 , Π_2 , Π_6 and Π_7 between the prototype and models.

By assuming Π_1 and Π_2 to be constant between the prototype and models, the same scaling laws as under Froude scaling resulted for H and T (Table 5.4). For practical reasons, ordinary water and air were used in the models, such that Π_3 and Π_4 were not conserved, with a potential for scale effects. By introducing the E scaling law

$$\lambda_E = \frac{E_P}{E_M} \quad (5.9)$$

and assuming the conservation of Π_6 between the prototype and models,

$$s_M = \frac{s_P}{\sqrt[3]{\lambda^4/\lambda_E}} \quad (5.10)$$

results. This requires that λ_E is constant over the applied force range, such that the material response is linear or remains proportional between the prototype and models. Finally, it can be derived that l scales linearly with λ by imposing Π_7 to be constant between the prototype and models. The derived scaling laws for the GP approach are summarised in the last column of Table 5.4.

Based on this approach, the plate material in the models can be freely selected, λ_E can then be evaluated (Eq. 5.9) and s can be estimated from Eq. (5.10). Acrylic plates ($E = 3.03 \text{ GPa}$ and $\rho_s = 1200 \text{ kg/m}^3$) were used for the GP models of the present study, resulting in $\lambda_E = 66.01$ for $E_P = 200 \text{ GPa}$. Note that Π_5 is intentionally not conserved in favour of a more versatile and practical approach.

Consequently, no restrictions are applied to ρ_s , which otherwise would have to scale with $\sqrt[3]{\lambda_E/\lambda}$ to ensure $\Pi_{5,P} = \Pi_{5,M}$. Therefore, model effects (Kobus, 1980; Hughes, 1993) are expected due to an incorrect representation of the plate mass and need to be appropriately discussed (Section 5.4.2). These might be negligible in WFSI processes where the plate mass is of secondary importance in relation to its stiffness, as in the typical case of light-weight and slender structures under long-periodic waves where the structure dynamics is mainly controlled by the external loading.

5.3 Results

5.3.1 Validation of the governing parameters

The WFSI dimensionless governing parameters (Table 5.3) were validated herein, confirming their capability to fully capture the physics of WFSI. A regular wave prototype test (Section 5.2.1.2), referred to as test 1, was compared with 3 tests conducted under different conditions with the same parameters Π_1 to Π_7 (Table 5.5). In tests 1a and 1b, the set-up, fluid properties and the wave features are identical to test 1. However, E in tests 1a is smaller than in test 1, with a larger s and smaller ρ_s . A thinner plate was used in test 1b, with both larger E and ρ_s compared to test 1.

Test 1c replicates an hypothetical, yet realistic, case at laboratory scale with $h = 1$ m. Consequently, H , T , ν , σ and l were evaluated by imposing the conservation of the corresponding $\Pi_1, \Pi_2, \Pi_3, \Pi_4$ and Π_7 . By assuming $E = 3$ GPa, s was evaluated based on the conservation of Π_6 and consequently ρ_s was calculated from Π_5 (Table 5.5). In this test case, the mesh sizes and the time step were scaled to maintain the same spatial, e.g. $s/\Delta x$ and $l/\Delta z$, and temporal, e.g. $T/\Delta t$, resolutions as in test 1. The initial conditions were also scaled accordingly.

Table 5.5. Test programme to validate the WFSI dimensionless parameters.

Symbol	Unit	Test 1	Test 1a	Test 1b	Test 1c
h	m	15	15	15	1
l	m	10	10	10	0.67
E	GPa	200	100	390	3
s	m	0.15	0.19	0.12	0.0165
ρ_s	kg/m ³	8000	6350	10000	4850
H	m	2	2	2	0.133
T	s	5.5	5.5	5.5	1.42
ν	m ² /s	$1.00 \cdot 10^{-6}$	$1.00 \cdot 10^{-6}$	$1.00 \cdot 10^{-6}$	$1.72 \cdot 10^{-8}$
σ	N/m	0.07	0.07	0.07	$3.11 \cdot 10^{-4}$
g	m/s ²	9.81	9.81	9.81	9.81
Π_1	-	0.13	0.13	0.13	0.13
Π_2	-	4.45	4.45	4.45	4.45
Π_3	-	$5.50 \cdot 10^{-9}$	$5.50 \cdot 10^{-9}$	$5.50 \cdot 10^{-9}$	$5.50 \cdot 10^{-9}$
Π_4	-	$3.17 \cdot 10^{-8}$	$3.17 \cdot 10^{-8}$	$3.17 \cdot 10^{-8}$	$3.17 \cdot 10^{-8}$
Π_5	-	0.08	0.08	0.08	0.08
Π_6	-	0.11	0.11	0.11	0.11
Π_7	-	0.67	0.67	0.67	0.67

Fig. 5.2 shows the dimensionless water surface elevations η/h at $x = 0$ m, horizontal (subscript H) forces $F_H/(\rho_w g h^2)$ and horizontal displacements at the top end of the plate d_x/l for the 4 experiments of Table 5.5. The wave travelled along the flume and interacted with the plate, which oscillated with a period close to T . In the present study, $t = 0.0$ s is the instant when the first wave front reaches the plate and $F_H = F_{H,u} - F_{H,d}$, with the upwave (subscript u) $F_{H,u}$ and the downwave (subscript d) $F_{H,d}$ forces. The 4 experiments show identical results with less than 2% deviations. This confirms that the derived WFSI dimensionless governing parameters are able to represent the underlying physical processes of the phenomenon.

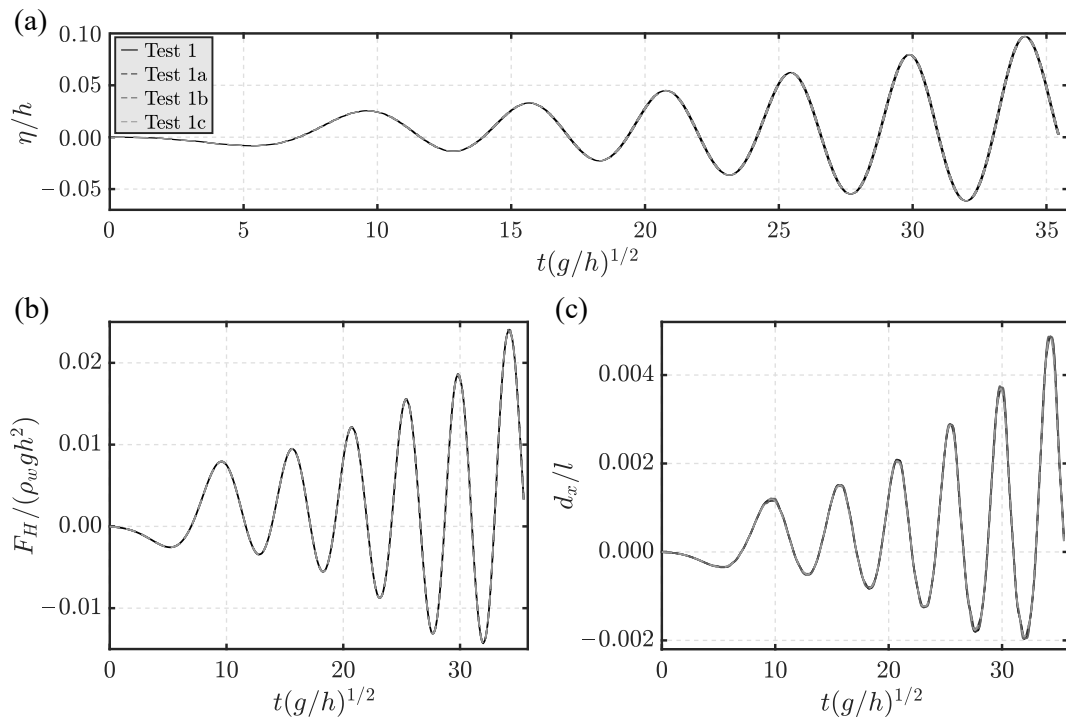


Figure 5.2. Validation of the dimensionless governing parameters: dimensionless time histories of the (a) water surface elevations η/h at $x = 0$ m, (b) forces $F_H/(\rho_w g h^2)$ and (c) displacements d_x/l for the tests of Table 5.5.

5.3.2 Non-breaking wave impacts

Scale effects are investigated in this section for the non-breaking wave tests (Table 5.2). Given the purpose of the present study, F_H and d_x at the top end of the plate were analysed. Further discussions of p and vertical stresses σ_{zz} are included in Section 5.4.2.

Figs. 5.3, 5.4 and 5.5 show the time histories of the dimensionless F_H and d_x for the 3 prototype tests of Table 5.2 and the scaled models based on the approaches in Table 5.4. The PFr models are identical to the prototype, confirming full similarity. The TFr_E approach correctly scaled WFSI in all 3 tests, showing negligible Re, We and Ma scale effects (Figs. 5.3c, d, 5.4c, d and 5.5c, d). In the regular wave tests the plate oscillated with a period close to T . On the other hand, the plate showed faster oscillations following T_s (Table 5.C.1) in the solitary wave test. In all tests, the plate oscillations were correctly captured in the PFr and TFr_E models. F_H were correctly modelled under TFr (Figs. 5.3e, 5.4e and 5.5e), however, d_x/l were underestimated

by up to 97.8% (Figs. 5.3f, 5.4f and 5.5f) due to the unscaled E .

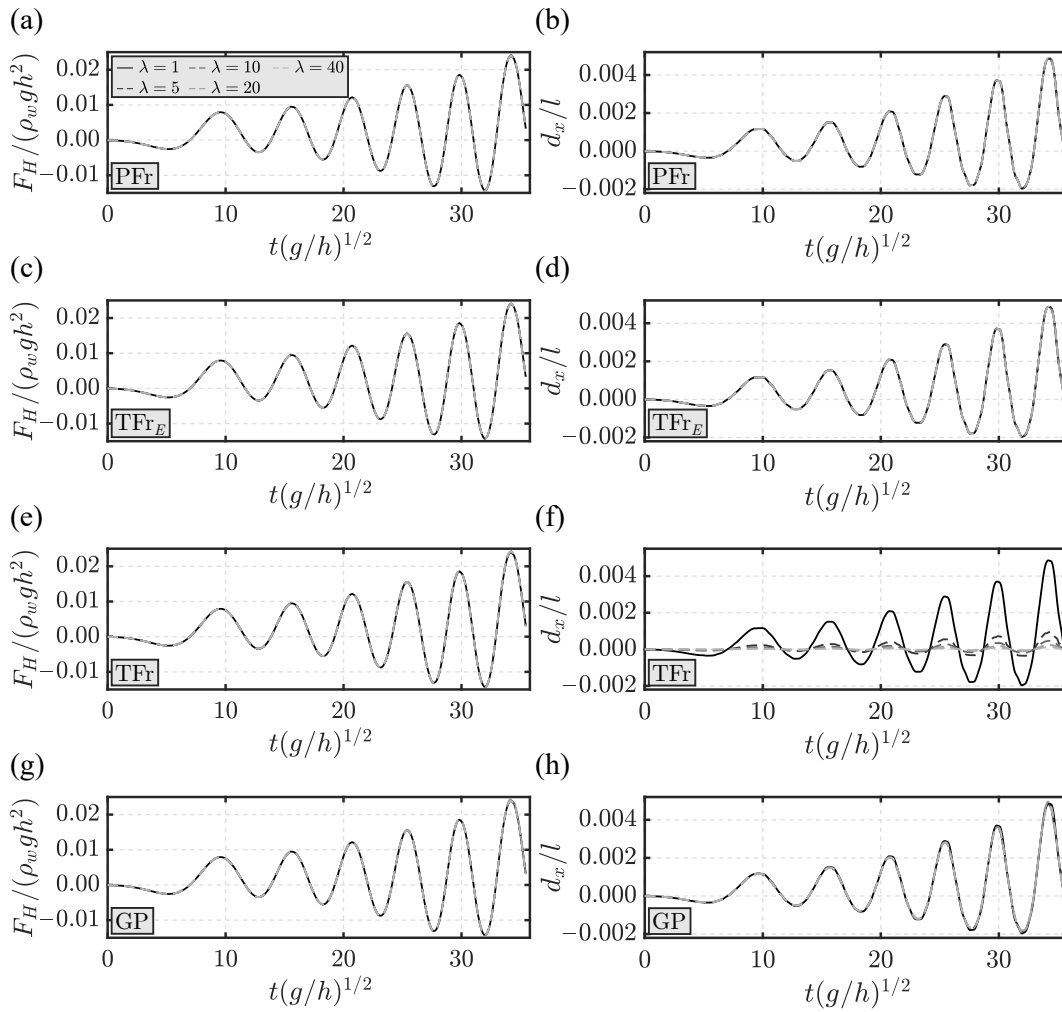


Figure 5.3. Scale series for a regular wave test with $H/h = 0.13$ and $T(g/h)^{1/2} = 4.45$: dimensionless $F_H/(\rho_w g h^2)$ and d_x/l versus $t(g/h)^{1/2}$ for the prototype ($\lambda = 1$) and scaled models according to (a, b) PFr, (c, d) TFr_E, (e, f) TFr and (g, h) GP approaches.

Finally, the scale series based on the new GP approach are shown in Figs. 5.3g, h, 5.4g, h and 5.5g, h. F_H were correctly predicted by the models, with less than 2.5% deviations compared to the prototype. The plate masses, hence the plate periods T_s (Table 5.C.1), were incorrectly scaled introducing model effects. In these tests, $T_{s,M}$ are up to 58% smaller than the correctly scaled values $T_{s,M} = \lambda^{1/2} T_{s,P}$.

Although $T_{s,M}$ were inexact, the model plate dynamics were nearly identical to the prototype in all 3 tests, confirming that the plate motion is mostly controlled by the wave action in absence of resonance. In the regular wave tests, the frequency of

the plate oscillations was correctly captured in the models (Figs. 5.3h and 5.4h). Deviations are observed at the peaks of d_x between the prototype and models, however, not exceeding 4.3% (Table 5.C.2).

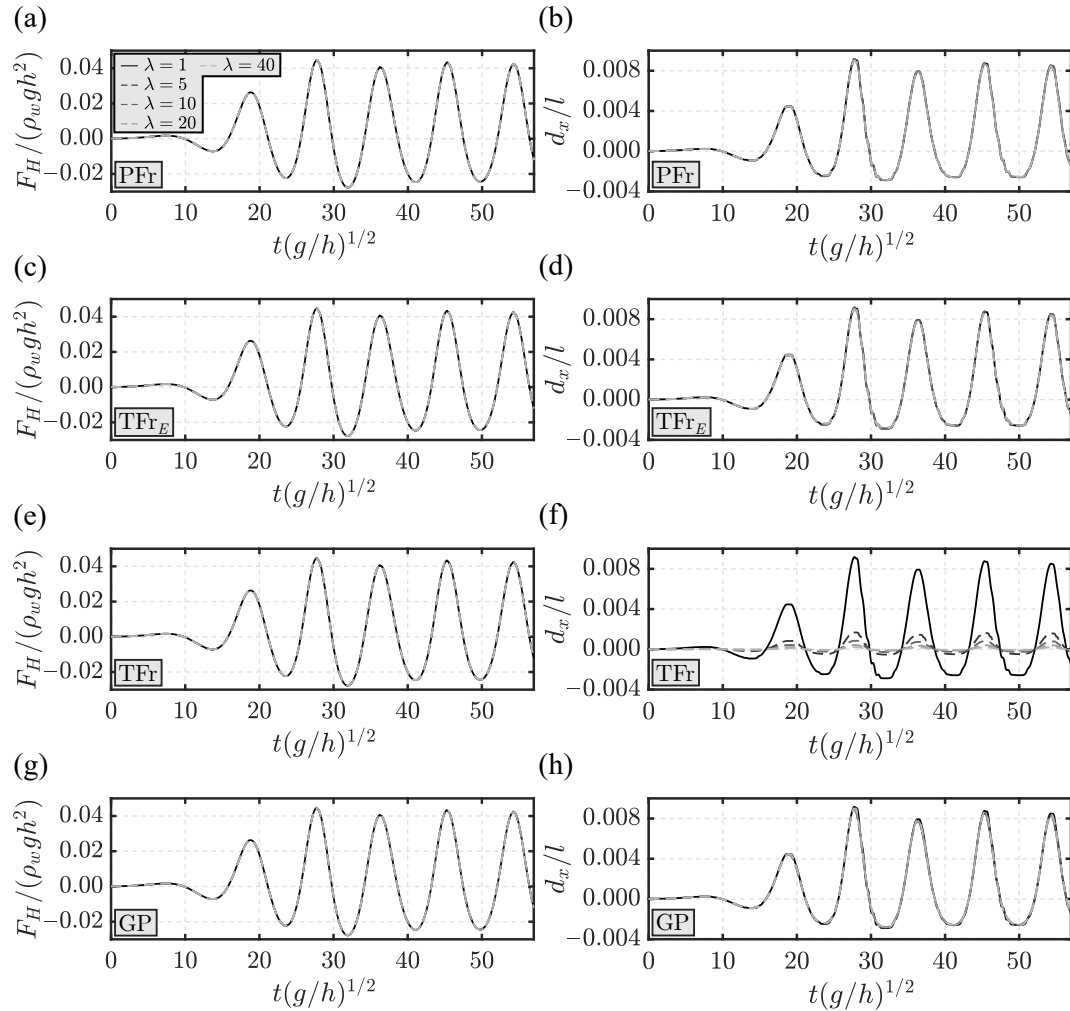


Figure 5.4. Scale series for a regular wave test with $H/h = 0.13$ and $T(g/h)^{1/2} = 8.90$: dimensionless $F_H/(\rho_w g h^2)$ and d_x/l versus $t(g/h)^{1/2}$ for the prototype ($\lambda = 1$) and scaled models according to (a, b) PFr, (c, d) TFr_E, (e, f) TFr and (g, h) GP approaches.

For the solitary wave tests, the models captured the main features of the plate deformation (Fig. 5.5h). The maximum (subscript *max*) $d_{x,max}/l$ in the models occurred slightly earlier in time compared to the prototype, with less than 3% deviations. However, the models were not able to capture the fastest oscillations shown in the prototype, particularly during wave run-down. Based on these findings, despite the deviations in the smaller frequency components of d_x , the GP approach predicted

F_H and the overall plate deformation well. The scale effects addressed in this section are summarised in Table 5.C.2 for each scaling approach and λ , including all 3 tests.

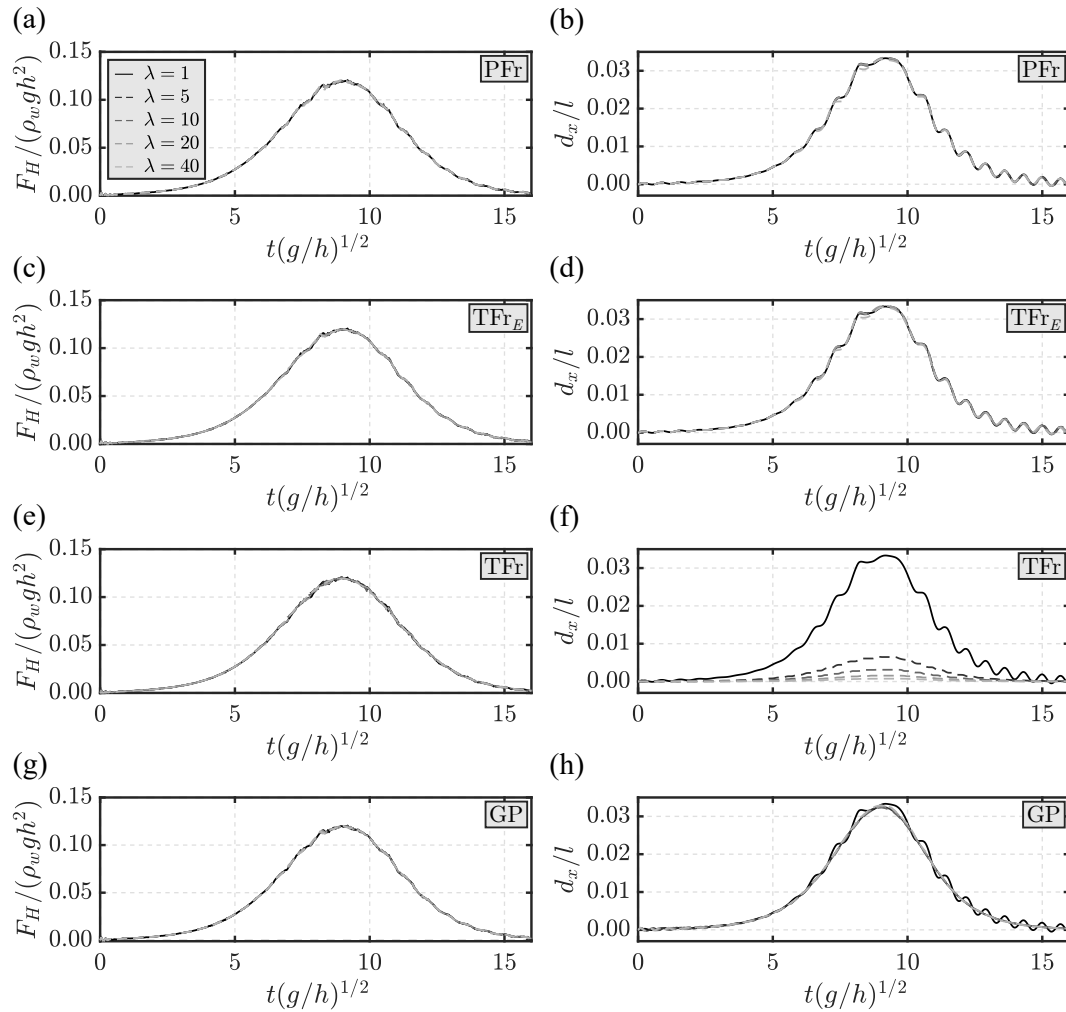


Figure 5.5. Scale series for a solitary wave test with $a/h = 0.13$: dimensionless $F_H/(\rho_w g h^2)$ and d_x/l versus $t(g/h)^{1/2}$ for the prototype ($\lambda = 1$) and scaled models according to (a, b) PFr, (c, d) TFr_E, (e, f) TFr and (g, h) GP approaches.

5.3.3 Breaking wave impacts

Scaled breaking wave impacts on plates (Table 5.2) under TFr_E laws are presented in this section. To be concise, only results from the flexible plate tests with $E_P = 200$ GPa and $s_P = 0.15$ m will be presented herein (Table 5.2). The wave pressures and forces from the scale series with $E_P = 400$ GPa and $s_P = 0.50$ m were similar to the flexible plate simulations and can be partially found in Section 5.4.3. In contrast to the non-breaking wave tests (Section 5.3.2), breaking wave impacts involve complex air-

water interactions (Peregrine, 2003; Croquer et al., 2023) such that significant scale effects are expected. Note that both air and water are modelled as incompressible in solids4foam, as further discussed in Section 5.4.3.

Fig. 5.6a, b shows the time histories of $F_H/(\rho_w gh^2)$ and d_x/l (at the top end of the plate) for the prototype and its models. The first incident wave was reflected by the plate without breaking, resulting in a peak of $F_H/(\rho_w gh^2) = 0.16$ and $d_x/l = 0.006$ at $t(g/h)^{1/2} = 16.5$. Negligible scale effects can be observed at this stage, with $F_H/(\rho_w gh^2)$ and d_x/l accurately predicted at smaller model sizes.

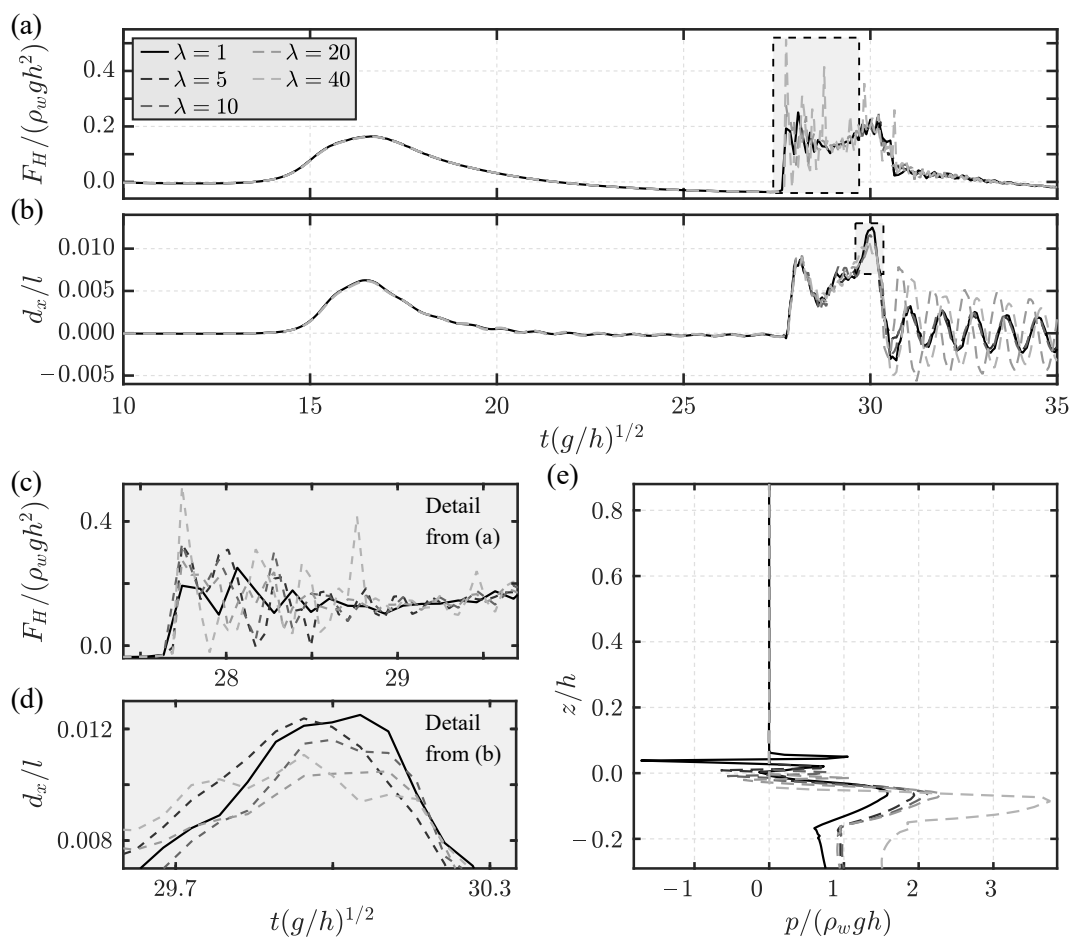


Figure 5.6. Breaking wave impacts for the prototype ($\lambda = 1$) and scaled after TFr_E: time histories of the dimensionless (a) forces $F_H/(\rho_w gh^2)$ and (b) displacements d_x/l , with details of (c) $F_H/(\rho_w gh^2)$ and (d) d_x/l , and (e) pressure $p/(\rho_w gh)$ distribution at the plate at $t(g/h)^{1/2} = 27.7$.

The second wave broke before the impact, entrapping an air pocket (Fig. 5.7). This led to a violent impact with a sharp peak of F_H , followed by oscillations during run-up

$27.7 \leq t/(g/h)^{1/2} \leq 29.2$. A further increase of F_H was observed at $t/(g/h)^{1/2} = 30.2$ due to the collapse of the water column following the wave run-up (Linton et al., 2013; Didier et al., 2014; Attili et al., 2023b).

These impact forces were incorrectly scaled under TFr_E , with significant Re , We and Ma scale effects (Fig. 5.6a). These effects can also be seen in Figs. 5.6c and 5.7, where the prototype and scaled wave impact $p/(\rho_w g h)$ for different snapshots are shown. Smaller model sizes tend to overpredict F_H and p (Cuomo et al., 2010b; Bredmose et al., 2015). As expected, the largest scale effects were observed at the smallest scale $\lambda = 40$, where F_H is up to twice the correctly scaled value. The air-water interfaces are inexactly modelled when air entrainment is important (Catucci et al., 2021); the models did not capture the complex free water surface observed for the prototype in detail. The shape, size and the pressures of the air pockets are also incorrectly scaled (Fig. 5.7).

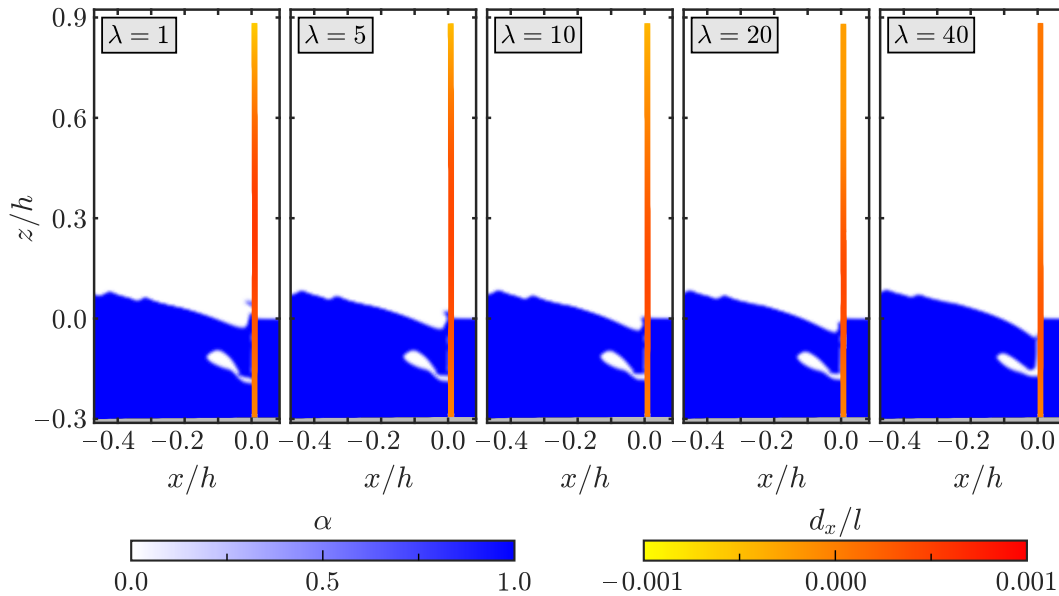


Figure 5.7. Snapshots of breaking wave impact on the flexible plate at $t/(g/h)^{1/2} = 27.7$ of the prototype ($\lambda = 1$) and TFr_E scaled models showing only minor scale effects.

The plate showed a peak of d_x due to the breaking wave impact at $t/(g/h)^{1/2} = 28.05$, followed by a second peak corresponding to the collapse of the water column (Fig. 5.6b). After the wave was reflected, the plate oscillated with $T_s/(g/h)^{1/2} = 0.86$,

being close to its natural period $T_s/(g/h)^{1/2} = 0.89$ (Gibson, 2007). As a consequence of the incorrect scaling of the breaking wave loading, the plate dynamics was not perfectly predicted by the models. The main differences concern the magnitude of the maximum peak, which is up to 17% underestimated by the models. Further, the d_x oscillations observed for $t(g/h)^{1/2} \geq 30.5$ were up to 2.5 times overpredicted at $\lambda = 20$ and 40, however, capturing their frequency correctly.

5.4 Discussion of results

5.4.1 Governing parameters

The governing parameters (Table 5.3) fully capture the underlying physical processes of WFSI (Fig. 5.2). These parameters can be used to define a range of physically-equivalent configurations, benefiting WFSI modelling, especially in laboratory scale models.

As an example, a prototype wood plate with $s = 0.15$ m, $E = 13$ GPa and $\rho_s = 1500$ kg/m³ at $h = 20$ m is considered. For $\lambda = 10$, the TFr_E scaled model results in $s_M = 0.015$ m, $E_M = 1.3$ GPa and $\rho_{s,M} = 1500$ kg/m³ at $h_M = 2$ m. Materials commonly used in the laboratory would not meet these requirements. However, based on the conservation of the WFSI governing parameters, a low density polyethylene plate with $s = 0.0237$ m, $E = 0.3$ GPa and $\rho_s = 950$ kg/m³ can be used. This is physically-equivalent to the TFr_E scaled model, revealing the potential of the WFSI parameters to achieve plate similarity.

The 2D WFSI dimensionless parameters in Table 5.3 can be extended to Three-Dimensional (3D) phenomena, e.g. asymmetrical wave fields and/or curved structures. By introducing the 3D plate mass $M_{3D,s} = \rho_s s b$ and flexural rigidity $D_{3D} = E b s^3 / 12$, with the plate width b , Π_5 and Π_6 for 3D were derived (Table 5.6). The remaining dimensionless parameters are identical to the 2D case. Due to the extensive computational cost, the 3D governing parameters were not validated, however, a similar behaviour as for the 2D case is expected (Fig. 5.2). This should be confirmed

by future studies.

Table 5.6. Dimensionless governing parameters in 3D WFSI.

Π_1	Π_2	Π_3	Π_4	Π_5	Π_6	Π_7
$\frac{H}{h}$	$T\left(\frac{g}{h}\right)^{1/2}$	$\frac{\nu}{g^{1/2}h^{3/2}}$	$\frac{\sigma}{\rho_w g h^2}$	$\frac{M_{3D,s}}{\rho_w h^2}$	$\frac{D_{3D}}{\rho_w g h^5}$	$\frac{l}{h}$

5.4.2 Scale effects in non-breaking waves

The investigated ranges of the main force ratios and WFSI dimensionless parameters are shown in Table 5.C.3 for the non-breaking wave numerical tests (Section 5.3.2).

Ca and Ma were computed as

$$\text{Ca} = \frac{\rho_w g h}{E}, \quad (5.11)$$

$$\text{Ma} = \frac{(gh)^{1/2}}{c_{sound}} \quad (5.12)$$

with the speed of sound in air $c_{sound} = (K_a/\rho_a)^{1/2}$ (Cramer, 1993), where K_a is the air (subscript a) bulk modulus. In the present study, $c_{sound} = 340$ m/s was assumed for the calculation of Ma. Although the air-water flows were modelled as incompressible, Ma is not conserved when ordinary water and air are used in the models due to the unscaled c_{sound} .

Non-breaking wave impacts on flexible plates were characterised by relatively small air-water interactions. The wave loading and plate behaviour were correctly scaled under the TFr_E approach, indicating that Re, We and Ma scale effects were relatively small in the investigated conditions (Table 5.C.2). This is further confirmed by p and σ_{zz} in the TFr_E models, as shown in Fig. 5.8 for a representative test. It can be concluded that non-breaking wave impact pressures and forces are correctly scaled under traditional Froude similarity (Hughes, 1993; Cuomo et al., 2010b; Windt et al., 2021) and the plate dynamics are correctly predicted for accurately scaled plates.

On the other hand, significant scale effects for d_x were observed under TFr due to the unscaled E . The numerical $d_{x,M}$ (Figs. 5.3f, 5.4f and 5.5f) are upscaled by

removing scale effects as (Fig. 5.9)

$$\frac{d_{x,P}}{l_P} = \frac{17}{16} \frac{\text{Ca}_P}{\text{Ca}_M} \frac{d_{x,M}}{l_M}, \quad (5.13)$$

with Ca calculated based on Eq. (5.11). Eq. (5.13) predicts the prototype plate displacements for incorrectly scaled models. However, it should be used for preliminary estimations only. Additional model effects due to the incorrect scaling of T_s might arise under TFr, which are not accounted for by Eq. (5.13) and need to be discussed on a case-by-case basis.

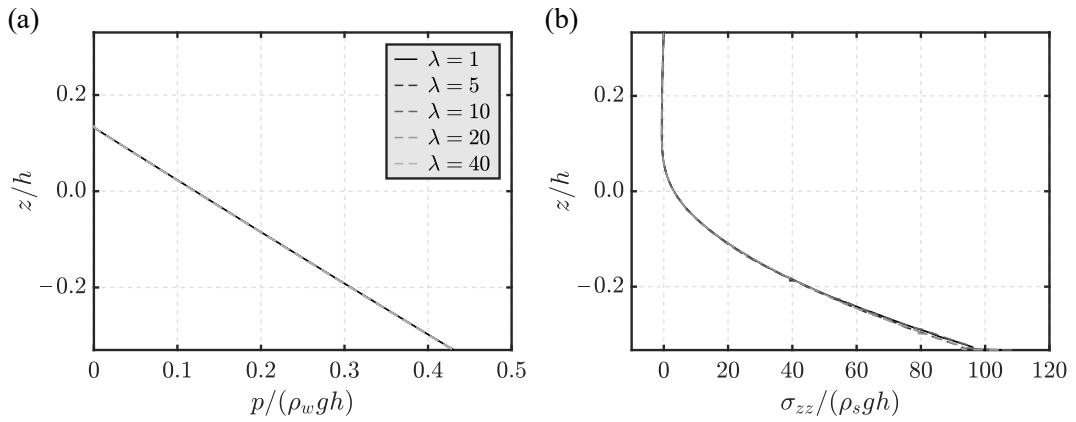


Figure 5.8. Regular wave test with $H/h = 0.13$ and $T(g/h)^{1/2} = 8.90$: prototype and TFr_E scaled (a) $p/(\rho_w g h)$ versus z/h and (b) $\sigma_{zz}/(\rho_s g l)$ along the inner fibre (upwave) of the plate at the instant during $F_{H,max}$.

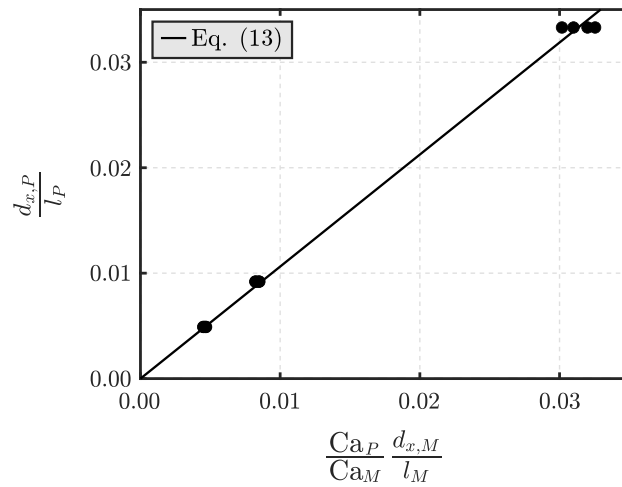


Figure 5.9. Upscaling of d_x under TFr with Eq. (5.13) to remove scale effects: comparison of the numerical $\frac{d_{x,P}}{l_P}$ and predictions based on Eq. (5.13).

The new GP approach was also applied to scale non-breaking wave impacts. Acrylic plates were used in all the models to overcome the challenge of finding an appropriate material for scaled plates. Despite the inexact modelling of T_s , the GP models predicted the wave impact forces and plate displacements well (Figs. 5.3g, h, 5.4g, h and 5.5g, h). Scale effects due to the use of ordinary water and air in the models were negligible, as discussed for the TFr_E models. Based on the numerical observations, it can be concluded that this approach is suitable for WFSI with relatively small T/T_s , e.g. for regular waves or relatively stiff plates. In these cases, the GP approach predicts the prototype correctly, representing a valuable and more versatile alternative to TFr_E. On the other hand, non-negligible model effects might arise for larger T/T_s , e.g. for long period waves. In the solitary wave tests, the GP approach did not accurately predict the fastest frequency components of d_x , while providing satisfactory results for F_H and $d_{x,max}$ (Fig. 5.5g, h). Therefore, this approach can also be applied for relatively large T/T_s , if the main aim is to predict the maximum displacement, being significantly more versatile than the TFr_E approach.

5.4.3 Scale effects in breaking waves

Relevant air-water interactions were observed for breaking waves impacting flexible plates (Section 5.3.3). The air-water compressibility may have a significant effect during wave impact, potentially resulting in reduced forces and pressures. However, the observed p_{max} were smaller than $3.18p_0$. Consequently, the air compression has a minor effect on the wave impact (Bredmose et al., 2015), such that the assumption of incompressible fluid in the simulation provides a suitable approximation. In addition, discrepancies of the numerical models from real observations do not affect the main conclusions of the present study as scale effects are quantified relative to numerical prototype observations.

By using ordinary water and air in the models, the TFr_E approach failed to correctly predict the prototype breaking wave impact (Figs. 5.6 and 5.7). The surface tension and air bulk modulus were overrepresented in the models, resulting in rela-

tively smaller and stiffer air pockets at reduced scales (Cuomo et al., 2010b; Bredmose et al., 2015; Seiffert et al., 2015). At this stage, scale effects were predominantly due to We and Ma . On the other hand, stronger turbulence was observed at a later stage with the resurfacing of the air pocket such that Re effects are expected to be more significant. Fig. 5.10 shows the comparison of $p_{max,P}/p_{max,M}$ versus the dimensionless group $\frac{Re_P}{Re_M} \frac{We_P}{We_M} \frac{Ma_P}{Ma_M}$ along with the Froude scaling predictions. The largest scales, $\lambda = 5$ and 10, show relatively small deviations from the Froude scaling laws, however, up to 60% deviations are observed at $\lambda = 20$ and 40. The decreasing values of Re , We and Ma at smaller scales explain the observed deviations (Heller, 2011; 2017).

The numerical (subscript *num*) wave impact $p_{max,num}$ (Fig. 5.10) were upscaled with the approach of Cuomo et al. (2010b) (Section 5.1.1) removing scale effects. Table 5.7 shows the predicted (subscript *pred*) and numerical p_{max}/p_0 and $\lambda_p = p_M/p_P$ for both experimental conditions (Table 5.2). The method suggested by Cuomo et al. (2010b) agrees overall with the results of the present study in both experiments. For the stiffer plate, $\lambda_{p,pred}$ consistently underestimates the numerical observations with 23 to 26% deviations. Although this approach was developed for rigid walls, it captured the flexible plate results well, underestimating λ_p by only 12% at $\lambda = 5, 10$ and 20. Once again, $\lambda = 40$ shows the largest deviations.

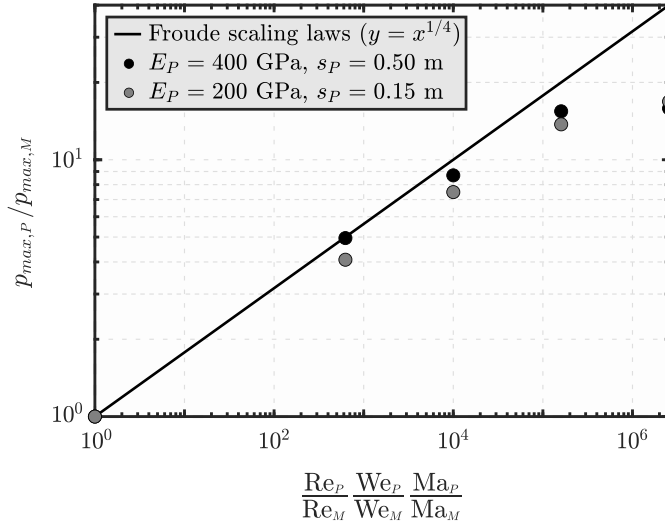


Figure 5.10. Scale effects in wave breaking impacts: (-) prediction based on the Froude scaling laws and data of numerical relative impact pressures $p_{max,P}/p_{max,M}$ versus $\frac{Re_P}{Re_M} \frac{We_P}{We_M} \frac{Ma_P}{Ma_M}$.

Table 5.7. Comparison of the upscaled relative breaking wave impact pressures $p_{P,max}/p_0$ based on the approach of Cuomo et al. (2010b) with the numerical results of the present study, where $p_0 = 101.325$ kPa and $\Delta\lambda_p$ is the deviation between $\lambda_{p,pred}$ and $\lambda_{p,num}$.

	λ	$(p_{P,max,pred}/p_0)$	$(p_{max,num}/p_0)$	$\lambda_{p,pred}$	$\lambda_{p,num}$	$\Delta\lambda_p$
$E_P = 400$ GPa $s_P = 0.50$ m	1	-	1.48	-	-	-
	5	1.15	0.30	3.8	5.0	23%
	10	1.15	0.17	6.7	8.7	23%
	20	1.15	0.10	12.0	15.4	23%
	40	1.10	0.09	11.7	15.8	26%
$E_P = 200$ GPa $s_P = 0.15$ m	1	-	1.30	-	-	-
	5	1.15	0.32	3.6	4.1	12%
	10	1.15	0.17	6.6	7.5	12%
	20	1.15	0.09	12.1	13.7	12%
	40	0.85	0.08	12.9	16.9	23%

Finally, the numerically derived pressure ratios p_{max}/p_0 are compared with the Bagnold-Mitsuyasu (Bredmose et al., 2015) and Froude scaling laws in Fig. 5.11. On the x -axis, the scale-invariant constant C_{B-M} depends on the air pocket characteristics, e.g. the volume, and u is the fluid velocity. The x values for the prototype data points were determined from the Froude scaling laws at $p_{P,max}$ and then scaled with λ for the models (Bredmose et al., 2015). According to Bredmose et al. (2015), the Bagnold-Mitsuyasu model might not be accurate for $p_{max} \leq 3.18p_0$ due to the relatively stiffer air pockets. These tend to behave as rigid boundaries at such small scales, resulting in an overestimation of p . Consequently, the Froude scaling laws should be used for $p_{max} \leq 3.18p_0$. However, for $p_{max} > 3.18p_0$ the compression of the air pocket has a significant effect, such that the Bagnold-Mitsuyasu scaling law can be used to remove scale effects.

The numerical p_{max} lie between predictions based on the Bagnold-Mitsuyasu and Froude scaling laws (Fig. 5.11). These do not fully agree with the observations of Bredmose et al. (2015), particularly at the smallest scales. However, the air-water flows were modelled as incompressible in the present study, explaining the larger p compared to Bredmose et al. (2015). In addition, smaller values of Re , We and Ma were investigated in the present study, resulting in larger scale effects. This high-

lights once again the complexity of scale effects and the importance of taking the investigated force ratios into account, rather than λ only (Heller, 2011).

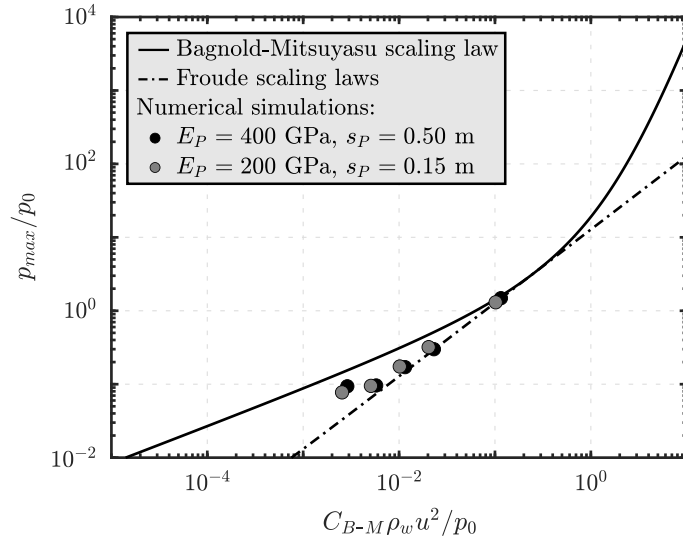


Figure 5.11. Comparison of the numerical p_{max}/p_0 with the predictions based on the Bagnold-Mitsuyasu and the Froude scaling laws (after Bredmose et al., 2015).

5.4.4 Upscaling of the laboratory tests

The laboratory measurements presented in Appendix 5.B are used in this section as practical examples to discuss scale effects and to upscale the results to real-world cases. Based on the findings of Fig. 5.B.2b and given that the waves did not break (Appendix 5.B.2), scale effects due to Re , We and Ma are expected to be small. In addition, the laboratory $Re = 3.92 \cdot 10^5$, $We = 8.76 \cdot 10^3$ and $Ma = 4.61 \cdot 10^{-3}$ are within or close to the ranges investigated in Section 5.3.2 (Table 5.C.3), indicating that scale effects are negligible.

By considering a hypothetical prototype scale with $h_P = 10.00$ m, $\lambda = 40$ results ($h_M = 0.25$, Table 5.B.1). The upscaled parameters under TFr_E are shown in Table 5.8 for the rigid and flexible laboratory plates. A representative solitary wave with $a = 0.085$ m resulted in the 3D forces $F_{3D,H} = 56.09$ and 45.45 N on the vertical rigid and flexible laboratory plates. This corresponds to $a = 3.40$ m and $F_{3D,H} = 3589.76$ and 2908.80 kN on the rigid and flexible prototype plates, respectively.

Table 5.8. Upscaled laboratory test parameters of the rigid and flexible plate under the TFr_E and GP approaches, with $\lambda = 40$.

	Unit	Rigid plate (TFr _E)	Flexible plate (TFr _E)	Flexible plate (GP)
E_P	GPa	8000	132	200
$\rho_{s,P}$	kg/m ³	8000	1200	8000
s_P	m	0.12	0.16	0.14
l_P	m	22.00	22.00	22.00
b_P	m	9.60	9.60	9.60
h_P	m	10.00	10.00	10.00

Model effects due to the inexact scaling of the plate mass under GP are also expected to be negligible for the maximum wave force and plate deformation, as discussed in Sections 5.3.2 and 5.4.2. However, inaccurate predictions of the smaller frequency components of the plate dynamics might be expected in the upscaling of the solitary wave tests. Given the interest of the GP approach, only the flexible plate tests are discussed. In addition to $\lambda = 40$, λ_E needs to be defined. By assuming that the prototype is made of stainless steel ($E_P = 200$ GPa), λ_E is 60.6 based on $E_M = 3.3$ GPa. The prototype thickness can be calculated from Eq. (5.10), resulting in $s_P = 0.14$ m. At the prototype scale, solitary waves with a ranging from 0.84 to 3.40 m induce $F_{3D,H} = 449.35$ to 2908.80 kN, with up to $-5.73 \cdot 10^{-4}$ deformation along the centroid line of the plate. Regular waves with $0.565 \text{ m} \leq H \leq 1.642 \text{ m}$ and $4.43 \text{ s} \leq T \leq 8.22 \text{ s}$, result in $144.17 \text{ kN} \leq F_{H,3D} \leq 563.80 \text{ kN}$ and maximum strains of $\varepsilon_{zz} = -5.73 \cdot 10^{-4}$ to $-4.05 \cdot 10^{-5}$.

5.5 Conclusions

Scale effects have been rarely investigated in Wave-Structure Interaction (WSI) and may lead to incorrect predictions of the prototype behaviour. Free-surface flows are typically scaled according to the Froude scaling laws, involving scale effects when ordinary water and air are used in the models. For Wave-Flexible Structure Interaction (WFSI), the solid properties, e.g. the Young's modulus, must also be scaled based on Cauchy similarity. This can be difficult to achieve at reduced scale due to the chal-

length of finding a material with the appropriate properties, with potential for scale and model effects. A systematic investigation of scale effects in WSI was conducted in the present study. Regular and solitary wave impacts on rigid and flexible plates have been investigated at different scales based on numerical modelling supported by small-scale laboratory experiments. The main conclusions are summarised hereafter.

The 7 governing parameters Π_1 to Π_7 for WFSI (Table 5.3) have been derived and validated numerically (Fig. 5.2). These can be used to define physically-equivalent configurations at any scale. A new scaling approach was derived by conserving $\Pi_1 = H/h$, $\Pi_2 = T(g/h)^{1/2}$, $\Pi_6 = D/(\rho_w g h^4)$ and $\Pi_7 = l/h$ between the prototype and models, with the wave height H , wave period T , water depth h , water density ρ_w , plate flexural rigidity D and the plate height l . This approach is more versatile than traditional Froude-Cauchy scaling (Section 5.2.3).

Non-breaking and breaking wave impacts have been simulated for 5 prototype tests (Table 5.2) and their models with geometrical scale factors $\lambda = 5, 10, 20$ and 40. These were scaled according to precise Froude (fluid and plate properties scaled), traditional Froude-Cauchy (fluid properties unscaled, plate properties scaled), traditional Froude (fluid and plate properties unscaled) and the new WFSI scaling approach. Accurate predictions of the prototype behaviour were achieved with precise Froude scaling. Traditional Froude-Cauchy scaling showed small scale effects for non-breaking waves. The wave pressures, forces and plate displacements were accurately predicted by the models with less than 2.1% deviations.

On the other hand, significant scale effects were observed for breaking wave impacts under traditional Froude-Cauchy similarity (Fig. 5.6). The models incorrectly predict the prototype behaviour due to the unscaled fluid properties. The wave pressures were overestimated by up to 132% at smaller scales with $\lambda = 40$. The scaled pressures resulted in a reasonable agreement with available approaches (Cuomo et al., 2010b; Bredmose et al., 2015), removing scale effects in the upscaling of breaking wave impacts on rigid plates. Smaller discrepancies were explained by the assumption of incompressible fluids and the smaller values of the Reynold, Weber and Mach numbers

used in the present study (Section 5.4.3).

Traditional Froude scaling showed significant scale effects due to the unscaled plate properties (Figs. 5.3f, 5.4f and 5.5f). These resulted in an up to 98% underestimation of the plate displacements at $\lambda = 40$. Scale effects can be removed in the upscaling of the plate displacements with the newly proposed Eq. (5.13).

The new scaling approach based on the WFSI governing parameters was successfully validated with non-breaking waves. The regular wave models showed accurately scaled wave pressures, forces and plate displacements, with less than 4.3% deviations (Figs. 5.3g, h and 5.4g, h). The solitary wave tests revealed that, despite non-negligible model effects due to the non conservation of T relative to the plate period T_s , the wave loadings and plate dynamics were predicted reasonably well (Fig. 5.5g, h). The maximum solitary wave force and plate displacement showed less than 3% deviations. While being more versatile than traditional Froude-Cauchy scaling laws, this approach is suitable for relatively small and large ratios of T/T_s , i.e. if the plate mass effects are small. However, this approach may not be appropriate for other WFSI processes where the inertia of the structure plays a significant role, such as for offshore floating platforms or offshore pipelines.

Future work should validate the new scaling approach in laboratory experiments and in other WFSI processes. This would also provide insight in related model effects.

5.A Convergence tests

Fig. 5.A.1 shows the convergence tests for a non-breaking solitary wave test (Fig. 5.1a). Mesh resolutions of $\Delta x = \Delta z = 0.200, 0.100, 0.050$ and 0.025 m were investigated for the fluid domain. The finest resolutions $\Delta x = \Delta z = 0.050$ and 0.025 m were employed in a $11 \text{ m} \times 22 \text{ m}$ refined area only, while $\Delta x = \Delta z = 0.10$ m was used in the remainder of the fluid domain. Convergence is achieved for $\Delta x = \Delta z = 0.05$ m, which was selected for the main tests. This showed deviations of only 1% compared to the finest resolutions, while requiring approximately 1/5 of the computational time.

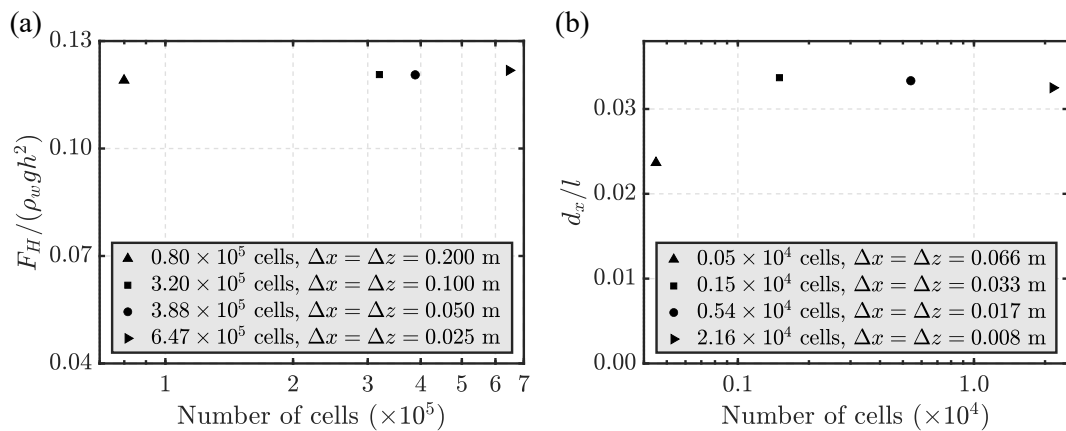


Figure 5.A.1. Convergence tests for a solitary non-breaking wave test with $a/h = 0.13$: semi-logarithmic diagramme for the relative (a) force $F_H / (\rho_w g h^2)$ and (b) horizontal displacement d_x / l with the mesh size $\Delta x = \Delta z$.

Resolutions of $\Delta x = \Delta z = 0.066, 0.033, 0.017$ and 0.008 m were investigated for the plate. $\Delta x = \Delta z = 0.017$ m was selected as the optimal mesh size for the main tests. This resulted in a 2.4% larger d_x / h compared to $\Delta x = \Delta z = 0.008$ m, while saving computational time.

5.B Physical model

5.B.1 Laboratory set-up

Laboratory tests were conducted in a 15.0 m long, 0.245 m wide and 0.460 deep flume (Fig. 5.B.1a). The flume was equipped with a piston-type wave maker. A $0.55 \text{ m} \times 0.24 \text{ m}$ plate was located approximately 11.50 m downwave the wave maker. The

plate was supported by a movable angled ramp to vary the plate inclinations β . A 2.0 to 2.5 mm gap between the plate and the lateral walls of the flume ensured a free movement of the plate.

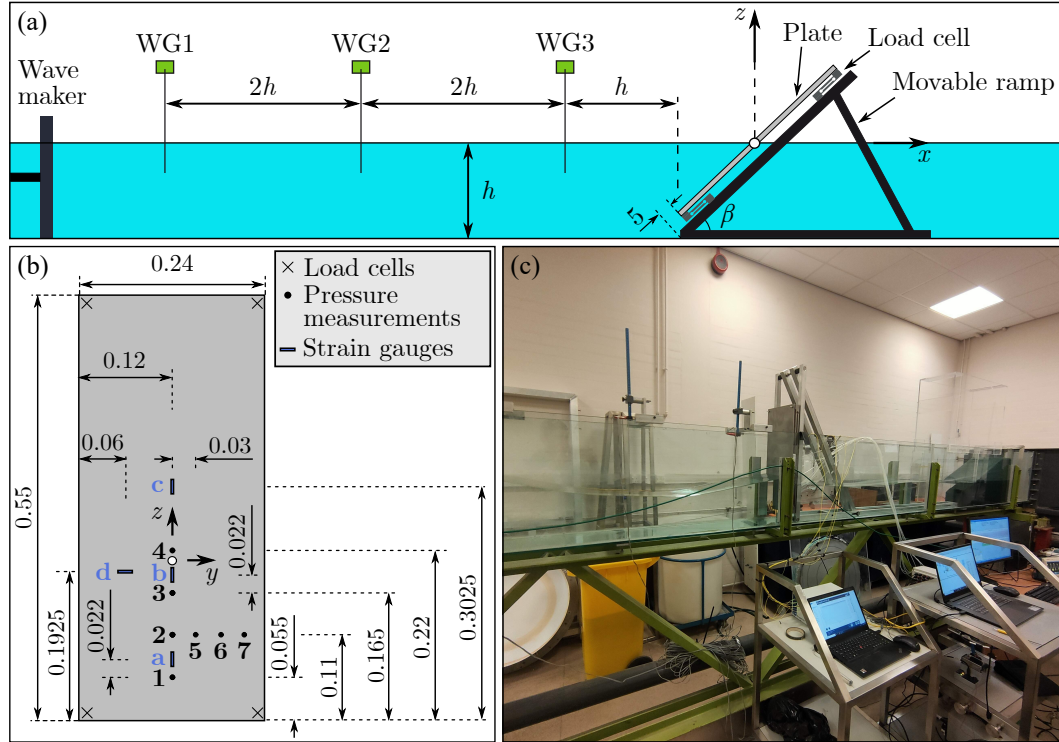


Figure 5.B.1. Laboratory set-up: (a) schematic side view of the wave flume and plate, (b) frontal view of the plate with location of the measurement systems and (c) picture of the wave flume with some of the instrumentation (Attili et al., 2023b).

Resistance-type Wave Gauges (WGs) were used at 3 locations to record water surface elevations. They sampled at 100 Hz with ± 1 mm accuracy. Water pressures on the plate were measured with an array of MPXV5004GC7U (RS Components UK) Precision Pressure Transducers (PPTs), which recorded at 100 Hz with an estimated accuracy of ± 10 Pa. In-house Load Cells (LCs) were mounted at the corners of the plate to measure the wave forces on the plate. Forces were recorded at 1 kHz with an overall accuracy of ± 0.3 N. Finally, KFWB Series Waterproof Strain Gauges (SGs) were glued to the flexible plate to measure deflections.

A total of 52 laboratory tests were conducted with $h = 0.25$ m. These involved a range of regular and solitary waves impacting a stainless steel ($E = 200.0$ GPa) and an acrylic ($E = 3.3$ GPa) plate with $\beta = 60$ and 90° . The laboratory test programme

is summarised in Table 5.B.1.

Table 5.B.1. Test programme for the laboratory tests.

Parameter	Symbol	Unit	Range
Water depth	h	m	0.25
Plate height	l	m	0.55
Plate width	b	m	0.24
Plate inclination	β	°	60, 90
Young's modulus	E	GPa	3.30, 200.00
Plate thickness	s	m	0.003, 0.004
Plate density	ρ_s	kg/m ³	1190, 8000
Regular waves	H	m	0.014 to 0.041
	H/h	-	0.056 to 0.164
	T	s	0.7 to 1.3
	$T(g/h)^{1/2}$	-	4.39 to 8.14
Solitary waves	a	m	0.021 to 0.085
	a/h	-	0.084 to 0.34

5.B.2 Laboratory results

Fig. 5.B.2a shows the horizontal 3D forces $F_{3D,H}$ versus a/h for the laboratory tests of Table 5.B.1. The flexible plate resulted overall in smaller forces than the rigid one. This effect was larger for $\beta = 90^\circ$ than for $\beta = 60^\circ$, with up to 29% deviations of $F_{3D,H}$ between $E = 3.30$ and 200 GPa. The laboratory $F_{3D,H}$ were approximated as (Fig. 5.B.2b)

$$\frac{F_{3D,H}}{\rho_w g h^3} = \left(\frac{a}{h}\right)^{7/6} \Pi_6^{1/12} \left(\frac{\beta}{90^\circ}\right)^{1/3}, \quad (5.B.1)$$

based on a least-squares regression analysis. Data points from the 3 numerical non-breaking wave prototype tests (Table 5.2) are shown in Fig. 5.B.2b along with Eq. (5.B.1) and the laboratory $F_{3D,H}$. The 2D numerical F_H were multiplied by λb_M to obtain $F_{3D,H}$, with the laboratory plate width $b_M = 0.24$ m and $\lambda = 60$. Despite the differences between the set-ups and the plate support conditions (Figs. 5.1a and 5.B.1), the dimensionless numerical and laboratory $F_{3D,H}$ show similar values. This

is a strong indication that scale effects are negligible in these laboratory experiments (Section 5.4.4).

The maximum strain ε_{zz} measured at the upwave Strain Gauge b (SGb, Fig. 5.B.1b) are shown in Fig. 5.B.2c. Note that the initial deformations due to the weight of the plate have been deducted. Larger ε_{zz} resulted from larger a/h following a linear trend. These were approximated as (Fig. 5.B.2d)

$$\varepsilon_{zz} = \frac{14}{8} \cdot 10^{-3} \frac{a}{h} \left(\frac{\beta}{90^\circ} \right)^{3/10}. \quad (5.B.2)$$

As shown in Fig. 5.B.2d, Eq. (5.B.2) captures the laboratory observations well, with most data lying within the $\pm 25\%$ limits.

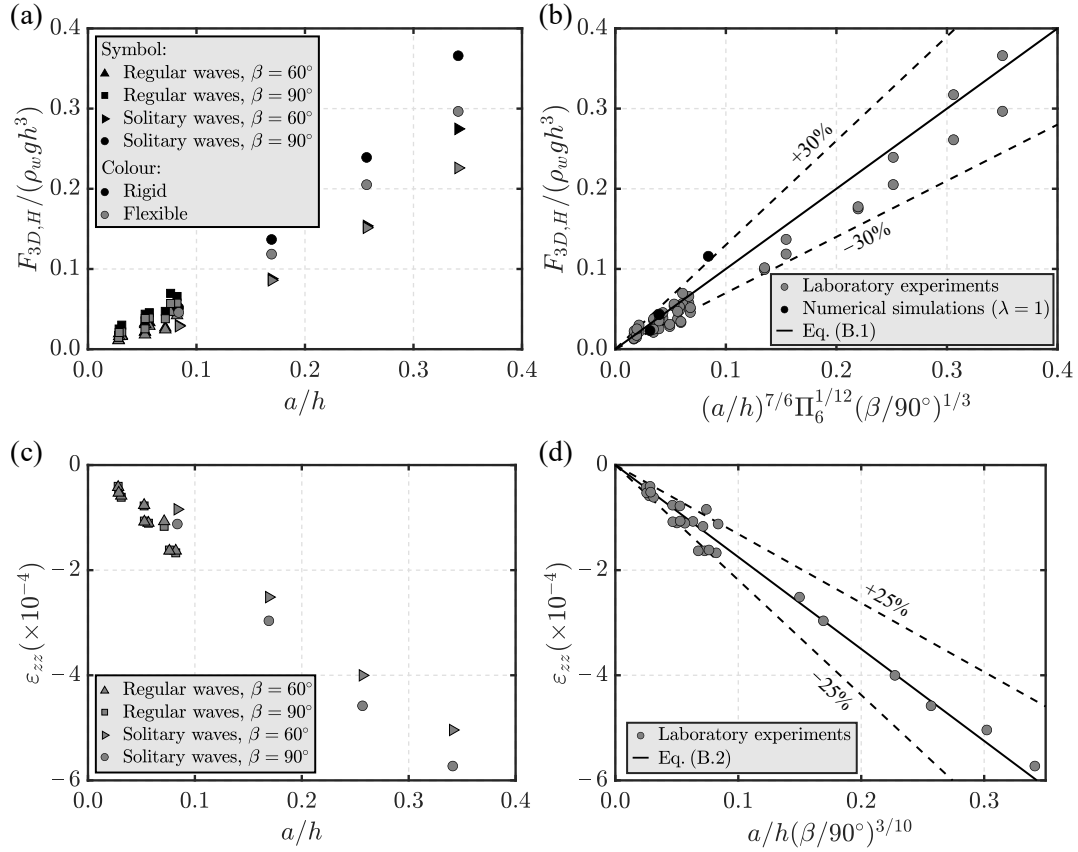


Figure 5.B.2. Laboratory experiments: (a) maximum relative forces $F_{3D,H}/(\rho_w g h^3)$ versus a/h for all tests of Table 5.B.1, (b) $F_{3D,H}/(\rho_w g h^3)$ with Eq. (5.B.1) (coefficient of determination $R^2 = 0.98$) and the data points of the non-breaking wave prototype ($\lambda = 1$) numerical tests (Table 5.2), (c) maximum ε_{zz} at SGb versus a/h for the flexible plate ($E = 3.30$ GPa) tests and (d) ε_{zz} at SGb with Eq. (5.B.2) ($R^2 = 0.98$).

5.C Supplementary tables

Table 5.C.1. Natural plate period $T_s = [2\pi l^2/1.875^2]\sqrt{12\rho_s/(Es^2)}$ (Gibson, 2007) and dimensionless plate period $T_s(g/h)^{1/2}$ for the non-breaking wave tests of Table 5.2 under the scaling approaches shown in Table 5.4.

		$\lambda = 1$	$\lambda = 5$	$\lambda = 10$	$\lambda = 20$	$\lambda = 40$
PFr	T_s (s)	0.83	0.37	0.26	0.18	0.13
	$T_s(g/h)^{1/2}$ (-)	0.67	0.67	0.67	0.67	0.67
TFr _E	T_s (s)	0.83	0.37	0.26	0.18	0.13
	$T_s(g/h)^{1/2}$ (-)	0.67	0.67	0.67	0.67	0.67
TFr	T_s (s)	0.83	0.17	0.08	0.04	0.02
	$T_s(g/h)^{1/2}$ (-)	0.67	0.30	0.21	0.15	0.11
GP	T_s (s)	0.83	0.22	0.14	0.09	0.05
	$T_s(g/h)^{1/2}$ (-)	0.67	0.40	0.35	0.32	0.28

Table 5.C.2. Scale effects $\Delta F_{H,max}$ and $\Delta d_{x,max}$ for the maximum force and displacement, respectively, for the non-breaking wave tests of Table 5.2 under the scaling approaches shown in Table 5.4.

		$\lambda = 5$	$\lambda = 10$	$\lambda = 20$	$\lambda = 40$
PFr	$\Delta F_{H,max} < 1.0\%$	$\Delta F_{H,max} < 1.0\%$			
	$\Delta d_{x,max} < 2.0\%$	$\Delta d_{x,max} < 1.0\%$	$\Delta d_{x,max} < 1.5\%$	$\Delta d_{x,max} < 1.5\%$	$\Delta d_{x,max} < 1.5\%$
TFr _E	$\Delta F_{H,max} < 1.0\%$	$\Delta F_{H,max} < 1.0\%$			
	$\Delta d_{x,max} \leq 2.1\%$	$\Delta d_{x,max} < 1.0\%$	$\Delta d_{x,max} < 2.0\%$	$\Delta d_{x,max} < 2.0\%$	$\Delta d_{x,max} < 2.0\%$
TFr	$\Delta F_{H,max} < 1.0\%$	$\Delta F_{H,max} \leq 1.0\%$			
	$80.4\% \leq \Delta d_{x,max} \leq 81.7\%$	$90.4\% \leq \Delta d_{x,max} \leq 90.8\%$	$95.3\% \leq \Delta d_{x,max} \leq 95.5\%$	$97.7\% \leq \Delta d_{x,max} \leq 97.8\%$	
GP	$\Delta F_{H,max} < 1.0\%$	$\Delta F_{H,max} < 1.0\%$	$\Delta F_{H,max} \leq 2.5\%$	$\Delta F_{H,max} \leq 1.4\%$	
	$1.0\% \leq \Delta d_{x,max} \leq 3.4\%$	$2.5\% \leq \Delta d_{x,max} \leq 4.3\%$	$1.9\% \leq \Delta d_{x,max} \leq 3.8\%$	$1.0\% \leq \Delta d_{x,max} \leq 2.4\%$	

Table 5.C.3. Ranges of Re, We, Ma, Ca and WFSI dimensionless parameters investigated in the non-breaking wave impact tests for different scaling approaches.

	Re		We		Ma		Ca		
PFr	$1.82 \cdot 10^8$		$3.15 \cdot 10^7$		$3.57 \cdot 10^{-2}$		$7.36 \cdot 10^{-7}$		
TFr _E	$7.19 \cdot 10^5$ to $1.82 \cdot 10^8$		$1.97 \cdot 10^4$ to $3.15 \cdot 10^7$		$5.64 \cdot 10^{-3}$ to $3.57 \cdot 10^{-2}$		$7.36 \cdot 10^{-7}$		
TFr	$7.19 \cdot 10^5$ to $1.82 \cdot 10^8$		$1.97 \cdot 10^4$ to $3.15 \cdot 10^7$		$5.64 \cdot 10^{-3}$ to $3.57 \cdot 10^{-2}$		$1.84 \cdot 10^{-8}$ to $7.36 \cdot 10^{-7}$		
	Π_1	Π_2	Π_3		Π_4		Π_5	Π_6	Π_7
GP	0.13	4.45 to 8.90	$5.50 \cdot 10^{-9}$ to $1.39 \cdot 10^{-6}$		$3.17 \cdot 10^{-8}$ to $5.07 \cdot 10^{-5}$		0.0142 to 0.08	0.113	0.67

This page was intentionally left blank.

Chapter 6

Conclusions and outlook

6.1 Conclusions

This thesis undertakes a comprehensive investigation of Wave-Structure Interaction (WSI), including both rigid and flexible (Wave-Flexible Structure Interaction, WFSI) plates, based on numerical modelling supported by small-scale laboratory experiments. This study was aimed at enhancing the physical understanding of WSI to support the design and laboratory modelling of a range of offshore and onshore structures. The general conclusions are summarised hereafter, in addition to the conclusions in each of the main Sections 3.5, 4.6 and 5.5.

The numerical toolbox `solids4foam` (Cardiff et al., 2018), implemented in `Foam-Extend 4.0`, was used to model WSI for a range of set-ups using both Two-Dimensional (2D) and Three-Dimensional (3D) geometries. These included tsunamis impacting dams and wave impacts on offshore and onshore plates of different stiffnesses, resulting in more than 230 tests. The numerical modelling was supported by a total of 52 laboratory experiments conducted in a 0.25 m (width) \times 15.00 m (length) \times 0.46 m (depth) wave flume (Section 4.3, Appendices 5.B and A). The laboratory tests involved a range of regular and solitary waves impacting a stainless steel (rigid) and an acrylic (flexible) plate. The water surface elevations, wave pressures, wave forces and the plate deformations were measured.

The numerical model was extensively validated for wave impact on rigid and flexible plates with analytical, laboratory and other numerical results. The validation for rigid plates showed the capability of solids4foam to capture the wave pressures, forces and overtoppings (Figs. 3.2, 3.3, 3.4, 4.4 and 4.5). For wave impact on flexible plates, solids4foam resulted overall in a reasonable agreement with available and new laboratory observations, however, overestimating the force and the plate deformations in some cases (Figs. 4.4, 4.5, 4.6 and 4.12).

Subsequently, a total of 72 numerical simulations were conducted to investigate 2D tsunamis impacting dams of steep to vertical inclinations (Chapter 3). These were complemented with 3D tests aimed at exploring the effects of the curvature of the dam and/or asymmetrical wave impact angles. Tsunamis were idealised with 5th order Stokes, cnoidal and solitary waves. The tsunami forces and pressures on dams agreed with the prediction approach of Evers et al. (2019), extending its validation ranges (Figs. 3.7 and 3.12e, f). New equations were proposed for the wave run-ups (Section 3.3.2.1) and overtoppings (Section 3.3.3.2), where existing approaches were lacking or inaccurate. Based on the 3D simulations, a solitary wave impacting an arch dam with an angle of 30° resulted in a 32% larger run-up compared to the 2D prediction (Section 3.4.4). For real reservoirs, where the geometries cannot be idealised as rectangular wave basins and asymmetrical wave impact may occur, the 3D effects can be even more relevant and should be taken into account.

Wave impacts on rigid and flexible plates, located either offshore or onshore, were then investigated in Chapter 4. A total of 119 numerical tests have been performed either in 2D or 3D. Linear and solitary waves impacting plates of different stiffnesses have been simulated, mimicking a range of real applications, such as wave impacts on a wave energy converter, on a hull of a floating production storage and offloading unit and surges impacting onshore walls. In the offshore tests, the upstream forces on the plate were in good agreement with the ones from the approach of Evers et al. (2019). The total forces, calculated by subtracting the downwave force from the upwave component, were up to 40% smaller for the flexible compared to the rigid

plate. These deviations were mostly due to increased downstream water depths as a result of the plate deformations (Section 4.4.1.3). In addition, the maximum plate deformations and stresses during the maximum force were successfully related to the Euler-Bernoulli beam theory (Appendix 4.B).

The onshore tests were characterised by 2 peaks of the force during the impact, as observed in previous studies (Linton et al., 2013; Didier et al., 2014). The plate mechanical properties showed a negligible effect on the onshore wave forces for most tests. Up to 17.7% deviations were observed between the different plates, with the rigid plate not necessarily resulting in the largest forces (Section 4.4.2.3). Additionally, new semi-theoretical correlations were proposed to predict the wave forces and run-ups on onshore plates as a function of the offshore wave energy (Section 4.5).

Finally, a systematic investigation of scale effects for WSI based on the numerical modelling supported by small-scale laboratory tests was presented in Chapter 5. A set of governing dimensionless parameters for WFSI was derived and validated based on the numerical simulations (Section 5.3.1). Consequently, regular and solitary waves impacting rigid and flexible plates have been simulated for the prototypes and up to 40 times smaller models under various scaling approaches. These included precise Froude (fluid and plate properties scaled), traditional Froude-Cauchy (fluid properties unscaled, plate properties scaled), traditional Froude (fluid and plate properties unscaled) and a new WFSI scaling approach (partial conservation of the WFSI governing parameters, Section 5.2.3).

The numerical results confirmed the absence of scale effects for precise Froude scaling (Section 5.3.2). Negligible scale effects ($\leq 2.1\%$) were observed for non-breaking wave impacts under traditional Froude-Cauchy similarity. On the other hand, significant scale effects were observed for breaking wave impacts, with an overestimation of the wave pressure of up to 132% at a geometrical scale factor $\lambda = 40$ (Sections 5.3.3 and 5.4.3). These scale effects resulted in a reasonable agreement with previous studies (Cuomo et al., 2010b; Bredmose et al., 2015).

As expected, large scale effects were observed under Traditional Froude scaling

due to the unscaled plate properties. These resulted in up to 98% underestimations of the plate displacements at $\lambda = 40$. A new equation to preliminarily remove scale effects under this approach was suggested (Eq. 5.13).

The new scaling approach based on the WFSI governing parameters was successfully validated based on numerical simulations. For regular waves, the wave pressures, forces and plate displacements were accurately scaled in the models, with less than 4.3% deviations (Section 5.4.2). Larger model effects were observed for the solitary waves, however, the wave forces and plate maximum displacements were correctly captured in the models with less than 3% deviations. This approach represents a more versatile alternative to Froude-Cauchy scaling.

In conclusion, the present thesis provides an extensive investigation of WSI based on numerical and laboratory modelling. Existing prediction approaches for tsunami forces and pressures on dams have been further validated and new equations for wave run-ups and overtoppings were suggested. New physical insights into WSI and WFSI were provided, revealing overall that more flexible plates do not necessarily result in smaller forces. Additionally, scale effects in WFSI have been investigated and a new and versatile scaling approach was derived. These findings enhance the physical understanding and laboratory modelling of a range of offshore and onshore structures, supporting their design and assessment.

6.2 Outlook

Future work should address important aspects of WSI and WFSI that require further investigation. Based on the limitations of the present study, potential directions for future research are pointed out hereafter.

The present study emphasised the importance of the 3D effects due to the dam geometry and/or asymmetrical wave impact angles. However, these were investigated for selected cases only. A systematic investigation including a range of wave impact angles, reservoir sections, e.g. converging and diverging channels, and dam types and

geometries would provide new insight into these effects and potentially expand the 2D prediction approaches to 3D phenomena.

As only the instant during the maximum force was considered for the application of the Euler-Bernoulli beam theory to the offshore plate deformations, future work should include time varying load distributions. This might be done by introducing the time varying wave pressures in Eqs. (4.B.4) to (4.B.6). Consequently, the plate displacements and stresses can be derived as shown in Appendix 4.B. This would provide a valuable analytical approach to accurately describe the plate dynamics over time.

Future work should additionally extend the validation conditions for the prediction of the surge forces and run-ups on onshore plates. Experiments of solitary wave impacts on onshore plates, involving a range of wave amplitudes, water depths, shore inclinations, shore heights and shore lengths, would further validate the equations (Eqs. 4.17 to 4.19) suggested in the present study.

As only incompressible fluids can be modelled in solids4foam, compressible solvers should be implemented. This would enable to investigate the fluid compressibility effect on WFSI. Furthermore, the different sources of scale effects could be separately quantified, i.e. by correctly scaling viscosity and surface tension, scale effects due to the Mach number only can be explored. This would deliver further knowledge into scale effects for WSI.

The 3D WFSI governing parameters suggested in Table 5.6 should be confirmed by numerical and/or laboratory results. This can be accomplished similarly as for the 2D WFSI governing parameters (Section 5.3.1). In addition, the new scaling approach presented in this study should be further validated based on numerical and laboratory experiments. This would expand its capabilities and provide insight into the related scale and model effects (Section 5.2.3). This approach should be applied to other WFSI phenomena and wider ranges of the dimensionless parameters should be explored, enhancing the physical modelling of WFSI.

This page was intentionally left blank.

Notation

A	Coefficient of the pressure response factor at the wall
A_{\perp}	Cross-sectional area of the structure, m^2
a	Wave amplitude, m
a_{eff}	Effective wave amplitude, m
b	Dam/plate width, m
Ba	Bagnold number
C	Courant number
$C_{1,2,\dots,12}$	Constants of the offshore plate displacement, $\text{Nm}^{0,1,2}$ or 3
C_{B-M}	Constant in the Bagnold-Mitsuyasu scaling law
C_f	Force coefficient of Cross (1967)
c	Wave celerity, m/s
c_{sound}	Speed of sound in air, m/s
Ca	Cauchy number
cn	Elliptic function
\mathbf{D}_F	Deformation gradient
D	Plate flexural rigidity in 2D, Nm
D_{3D}	Plate flexural rigidity in 3D, Nm^2
\mathbf{d}	Displacement vector, m
d_0	Maximum wave overtopping depth, m
d_x	Plate displacement component along x -axis, m
E	Young's modulus, N/m^2
E_l	Equivalent energy loss of Cuomo et al. (2010b)
E_{of}	Overland flow energy per unit area, J/m^2
E_w	Offshore wave energy per unit width, J/m

\mathbf{F}	Force vector per unit width resulting from a wave and hydrostatic pressure, N/m
\mathbf{F}_{3D}	Force vector resulting from a wave and hydrostatic pressure, N
F	Force per unit width resulting from a wave and hydrostatic pressure, N/m
F_{3D}	Force on plate resulting from a wave and hydrostatic pressure, N
F_h	Hydrostatic force per unit width due to still water, N/m
F_I	First force peak on plate per unit width resulting from a surge, N/m
F_{II}	Second force peak on plate per unit width resulting from a surge, N/m
f	Freeboard, m
f_s	Natural frequency of a plate, Hz
f_σ	Surface tension force per unit volume, N/m ³
Fr	Froude number
\mathbf{g}	Gravitational acceleration vector, m/s ²
g	Gravitational acceleration, m/s ²
H	Wave height, m
H_s	Significant wave height, m
h	Water depth, m
h_{s0}	Overland flow depth at the transition point ($x_{of} = 0$), m
\mathbf{I}	Identity matrix
I	Second moment of inertia, m ⁴
i	Index for the i -th data value
J	Determinant of \mathbf{D}_F
K	Bulk modulus, N/m ²
K_e	Complete elliptic integral of the first kind
K_p	Pressure response factor
k	Wave number, 1/m
k	Turbulent kinetic energy per unit mass in the k - ε model, m ² /s ²
k_s	Spring stiffness, N/m
k_t	Turbulent kinetic energy per unit mass, m ² /s ²
L	Wave length, m

L_s	Shore length, m
l	Dam/plate height, m
l_s	Substructure height, m
M	Bending moment, Nm
$M_{3D,s}$	Mass per unit length, kg/m
M_h	Bending moment per unit width relative to the foundation due to the hydrostatic pressure, Nm/m
M_s	Mass per unit area, kg/m ²
m	Elliptic parameter
Ma	Mach number
N, P	Numbers of the considered pressure values
N _d	Number of the considered dynamic pressure values
n	Normal vector to the dam surface
$nRMSE$	Normalised Root Mean Square Error
p	Pressure, N/m ²
\bar{p}	Mean pressure, N/m ²
p_0	Atmospheric pressure, N/m ²
p_d	Dynamic pressure, N/m ²
$p_{d,1}$	Dynamic pressure at the sea bed of Sainflou (1928), N/m ²
$p_{d,2}$	Dynamic pressure at the still water surface of Sainflou (1928), N/m ²
p_K	Pressure at the dam crest resulting from a tsunami and hydrostatic pressure with overtopping, N/m ²
p_{lin}	Linear dynamic wave pressure of Tadjbakhsh and Keller (1960), N/m ²
p_{nonlin}	Nonlinear dynamic wave pressure of Tadjbakhsh and Keller (1960), N/m ²
Q	Shear force, N
q	Discharge per unit dam width, m ² /s
R	Wave run-up height, m
R^2	Coefficient of determination
r_0	Elevation of the orbit centre, m
Re	Reynolds number

S	Cell area, m^2
s	Dam/plate thickness, m
T	Wave period, s
T_p	Peak wave period, s
T_s	Natural period of the plate, s
t	Time, s
t_0	Instant during the maximum run-up, s
t_{d0}	Instant during the maximum wave overtopping depth, s
$\bar{\mathbf{u}}$	Mean fluid velocity vector, m/s
$\overline{\mathbf{u}'\mathbf{u}'}$	Turbulent stress tensor, N/m^2
\mathbf{u}_r	Compression velocity vector, m/s
u	Fluid velocity, m/s
\bar{u}	Depth-averaged fluid velocity, m/s
$\bar{u}_x, \bar{u}_y, \bar{u}_z$	Mean fluid velocity component along x -, y -, z -axis, m/s
∇	Overtopping volume per unit dam width, m^3/m
We	Weber number
x, y, z	x -, y -, z -axis, m
x_{of}	Streamwise overland flow coordinate, m
Y	Observed values
\bar{Y}	Mean of the numerical values
z_f	Shore freeboard, m
z_H	Elevation of the resultant of F_H from the dam foundation, m
α	Fraction of volume
β	Dam/plate inclination, $^\circ$
γ	Wave propagation angle, $^\circ$
δ	Density diffusion coefficient
Δd_0	Deviation between the experimental and numerical maximum wave overtopping depth, %
Δd_x	Scale effects for the horizontal plate displacement, %
ΔF	Scale effects for the force on the plate, %
Δt	Time step, s

$\Delta\psi$	Deviation between the experimental and numerical overtopping volume per unit dam width, %
$\Delta x, \Delta y, \Delta z$	Cell sizes, m
$\Delta\lambda_p$	Deviation between the predicted and numerical pressure scale factor, %
ε	Turbulence energy dissipation rate, m^2/s^3
ε_p	Parameter of Tadjbakhsh and Keller (1960) model ($\varepsilon_p = kH$)
ε_{zz}	Strain component of the plate along z -axis
ζ	Damping ratio
η	Water surface elevation, m
θ	Inclination of the free water surface, $^\circ$
λ	Geometric scale factor
λ_E	Young's modulus scaling law
λ_p	Pressure scaling law
μ	Fluid dynamic viscosity, Ns/m^2
ν	Fluid kinematic viscosity ($\nu = \mu/\rho$), m^2/s
ν_t	Kinematic turbulent viscosity, m^2/s
Π_1 to Π_7	Dimensionless governing parameters for WFSI
π	Mathematical constant
ρ	Density, kg/m^3
σ	Surface tension, N/m
$\boldsymbol{\sigma}_s$	Stress tensor, N/m^2
σ_s	Stress, N/m^2
σ_{zz}	Normal plate stress component along z -axis, N/m^2
τ	Adjusted time, s
ϕ_m	Colour function
ω	Turbulence energy dissipation rate in the k - ω model, m^2/s^3
ω	Wave angular frequency, $1/\text{s}$
ω_0	Parameter of Tadjbakhsh and Keller (1960) model ($\omega_0 = \sqrt{\tanh kh}$)

This page was intentionally left blank.

Subscripts

<i>a</i>	Air
<i>b</i>	Block
<i>c</i>	Crest
<i>d</i>	Downwave
<i>exp</i>	Experimental
<i>H</i>	Horizontal
<i>M</i>	Model
<i>max</i>	Maximum
<i>min</i>	Minimum
<i>num</i>	Numerical
<i>P</i>	Prototype
<i>pred</i>	Predicted
<i>red</i>	Reduced
<i>ref</i>	Reference solution
<i>s</i>	Shore, solid, structure
<i>t</i>	Trough
<i>u</i>	Upwave
<i>w</i>	Wall, water

This page was intentionally left blank.

Abbreviations

APR	Adaptive Particle Refinement
CCP-WSI	Collaborative Computational Project in Wave-Structure Interaction
CFD	Computational Fluid Dynamics
CFL	Courant-Friedrichs-Lewy
CPU	Central Processing Unit
CSD	Computational Structural Dynamics
DfPM	Decoupled Finite Particle Method
EPSRC	Engineering and Physical Sciences Research Council
F	Flexible plate
FDM	Finite Difference Method
FE	Foam-Extend
FEM	Finite Element Method
FPSO	Floating Production Storage and Offloading
FVM	Finite Volume Method
GP	New scaling approach based on the WFSI Governing Parameters
HPC	High Performance Computing
IBM	Immersed Boundary Method
LC	Load Cell
LVDT	Linear Variable Differential Transformer
MEL	Mixed Eulerian Lagrangian
MPS	Moving Particle Semi-implicit
OF	OpenFOAM
PFr	Precise Froude scaling

PIMPLE	Combination of Pressure Implicit Splitting Operator (PISO) and Semi-Implicit Method for Pressure-Linked Equations (SIMPLE)
PPT	Precision Pressure Transducer
R	Rigid plate
RANS	Reynolds-Averaged Navier-Stokes
RS	Roller Support
S-FEM	Lagrangian Smoothed Finite Element Method
SG	Strain Gauge
SPH	Smoothed Particle Hydrodynamics
TF	Top Free
TFr	Traditional Froude scaling
TFr _E	Traditional Froude-Cauchy scaling
VOF	Volume Of Fluid
WEC	Wave Energy Converter
WFSI	Wave-Flexible Structure Interaction
WG	Wave Gauge
WSI	Wave-Structure Interaction
2D	Two-Dimensional (flume)
3D	Three-Dimensional (basin)

Appendix A

Supplementary laboratory data

Supplementary data for the laboratory experiments (Chapters 4 and 5) are provided in this appendix, including details about the instruments (Table A.1) and the full test programme (Table A.2), where h is the water depth, H the wave height, a the wave amplitude, T the wave period, β the plate inclination and $F_{3D,max}$ and $\varepsilon_{zz,max}$ are the maximum (subscript *max*) Three-Dimensional (3D) force and strain, respectively. In the present study, a positive value of ε_{zz} corresponds to a tensile strain. The largest deformations in the laboratory tests were due to positive F_{3D} , resulting in compressive strains at SGb, such that $\varepsilon_{zz,max} < 0$.

Table A.1. Accuracy and locations of the instruments used in the laboratory tests.

Instrument		Accuracy	Locations in function of the coordinates (x, y, z) (m) for a vertical plate (Fig. 4.3, with $z = 0$ m at the water surface and $\beta = 90^\circ$)
Resistance-type Wave Gauges	WG	± 1 mm	WG1 $(-1.25, 0.0, 0.0)$; WG2 $(-0.75, 0.0, 0.0)$; WG3 $(-0.25, 0.0, 0.0)$
MPXV5004GC7U Precision Pressure Transducers	PPT	± 10 Pa	PPT1 $(0.0, 0.0, -0.145)$; PPT2 $(0.0, 0.0, -0.09)$; PPT3 $(0.0, 0.0, -0.035)$; PPT4 $(0.0, 0.0, 0.02)$; PPT5 $(0.0, 0.03, -0.09)$; PPT6 $(0.0, 0.06, -0.09)$; PPT7 $(0.0, 0.09, -0.09)$
Load Cells (in-house)	LC	± 0.3 N	LC1 $(0.0, -0.12, -0.20)$; LC2 $(0.0, 0.12, -0.20)$; LC3 $(0.0, -0.12, 0.35)$; LC4 $(0.0, 0.12, 0.35)$
KFWB Strain Gauges	SG	$\pm 10^{-6}$	SGa $(0.0, 0.0, -0.123)$; SGb $(0.0, 0.0, -0.013)$; SGc $(0.0, 0.0, 0.103)$; SGd $(0.0, -0.06, -0.008)$; SGe $(0.004, 0.0, -0.123)$; SGf $(0.004, 0.0, -0.013)$; SGg $(0.004, 0.0, 0.103)$; SGh $(0.004, -0.06, -0.008)$

Fig. A.1 shows additional pictures of the laboratory wave flume, plates and the instrumentation. The time series of the water surface elevation η , pressure p , F_{3D} and ε_{zz} are then shown in Figs. A.2 to A.4 for 4 representative tests, with the time t , the gravitational acceleration g and the water density ρ_w .

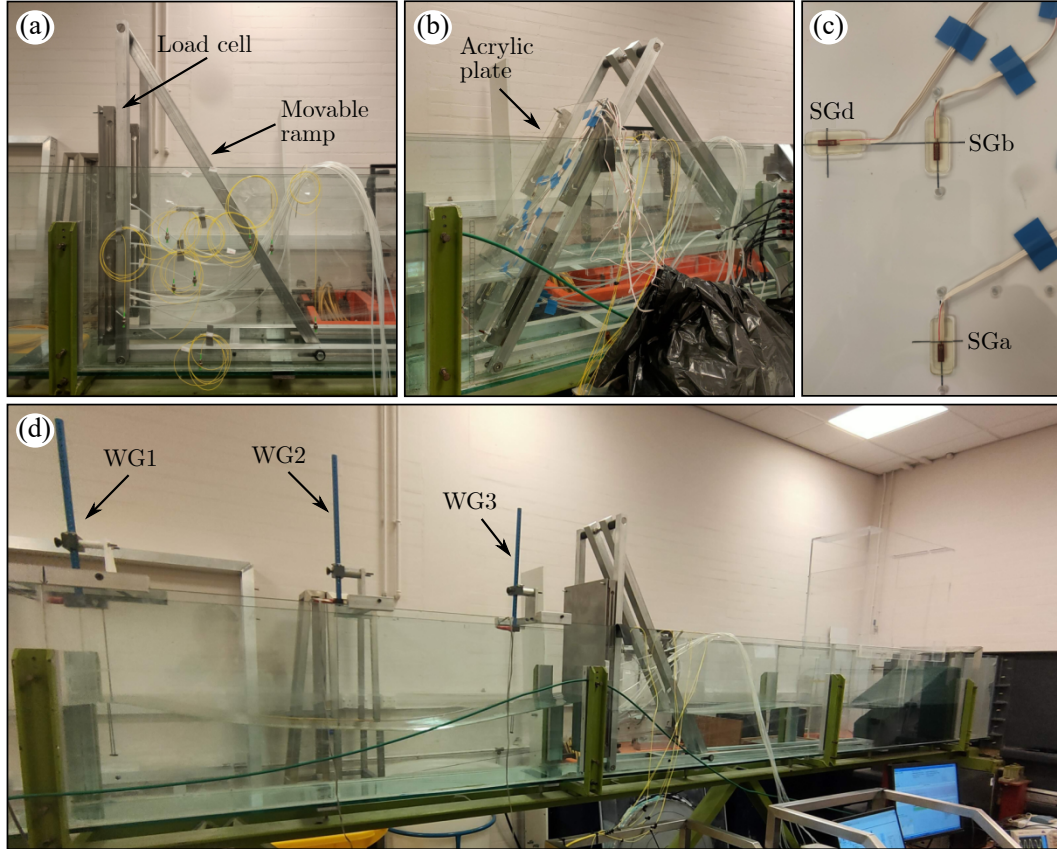


Figure A.1. Laboratory set-up: (a) movable angled ramp and stainless steel plate, (b) acrylic plate with $\beta = 60^\circ$, (c) detail view of the acrylic plate with SGa, b and d and (d) laboratory wave flume with the wave gauges and the stainless steel plate.

Table A.2. Overview of main investigated parameters for the 52 laboratory tests. R stands for a 3 mm thick stainless steel plate (Young's modulus $E = 200$ GPa) and F for a 4 mm thick acrylic plate ($E = 3.3$ GPa). Values marked with * were observed at WG1 in tests conducted without the plate.

Test	h (m)	Waves	H (m)*	a (m)*	T (s)	Plate	β ($^\circ$)	$F_{3D,max}$ (N)	$\varepsilon_{zz,max}$ ($\times 10^{-4}$)
1	0.25	Regular	0.014	-	0.7	R	60	2.35	-
2	0.25	Regular	0.016	-	1.0	R	60	3.55	-
3	0.25	Regular	0.014	-	1.3	R	60	3.98	-
4	0.25	Regular	0.026	-	0.7	R	60	4.39	-
5	0.25	Regular	0.028	-	1.0	R	60	6.83	-
6	0.25	Regular	0.026	-	1.3	R	60	6.68	-
7	0.25	Regular	0.036	-	0.7	R	60	5.47	-
8	0.25	Regular	0.041	-	1.0	R	60	9.36	-
9	0.25	Regular	0.038	-	1.3	R	60	9.93	-
10	0.25	Solitary	-	0.021	-	R	60	6.08	-
11	0.25	Solitary	-	0.042	-	R	60	17.95	-
12	0.25	Solitary	-	0.064	-	R	60	31.41	-
13	0.25	Solitary	-	0.085	-	R	60	56.14	-
14	0.25	Regular	0.014	-	0.7	R	90	2.63	-
15	0.25	Regular	0.016	-	1.0	R	90	4.59	-
16	0.25	Regular	0.014	-	1.3	R	90	3.85	-
17	0.25	Regular	0.026	-	0.7	R	90	5.40	-
18	0.25	Regular	0.028	-	1.0	R	90	6.97	-
19	0.25	Regular	0.026	-	1.3	R	90	6.68	-
20	0.25	Regular	0.036	-	0.7	R	90	7.22	-
21	0.25	Regular	0.041	-	1.0	R	90	10.07	-
22	0.25	Regular	0.038	-	1.3	R	90	10.67	-
23	0.25	Solitary	-	0.021	-	R	90	7.93	-
24	0.25	Solitary	-	0.042	-	R	90	20.97	-
25	0.25	Solitary	-	0.064	-	R	90	36.65	-
26	0.25	Solitary	-	0.085	-	R	90	56.09	-
27	0.25	Regular	0.014	-	0.7	F	60	2.23	-0.42
28	0.25	Regular	0.016	-	1.0	F	60	3.30	-0.59
29	0.25	Regular	0.014	-	1.3	F	60	3.28	-0.53
30	0.25	Regular	0.026	-	0.7	F	60	3.70	-0.76
31	0.25	Regular	0.028	-	1.0	F	60	5.91	-1.10
32	0.25	Regular	0.026	-	1.3	F	60	6.33	-1.08
33	0.25	Regular	0.036	-	0.7	F	60	4.99	-1.07
34	0.25	Regular	0.041	-	1.0	F	60	8.60	-1.63
35	0.25	Regular	0.038	-	1.3	F	60	9.46	-1.63
36	0.25	Solitary	-	0.021	-	F	60	5.88	-0.84
37	0.25	Solitary	-	0.042	-	F	60	17.56	-2.51
38	0.25	Solitary	-	0.064	-	F	60	30.95	-4.00
39	0.25	Solitary	-	0.085	-	F	60	46.19	-5.04
40	0.25	Regular	0.014	-	0.7	F	90	2.25	-0.40
41	0.25	Regular	0.016	-	1.0	F	90	3.28	-0.61
42	0.25	Regular	0.014	-	1.3	F	90	3.19	-0.52
43	0.25	Regular	0.026	-	0.7	F	90	3.89	-0.78
44	0.25	Regular	0.028	-	1.0	F	90	5.97	-1.11
45	0.25	Regular	0.026	-	1.3	F	90	5.87	-1.07
46	0.25	Regular	0.036	-	0.7	F	90	5.82	-1.17
47	0.25	Regular	0.041	-	1.0	F	90	8.81	-1.67
48	0.25	Regular	0.038	-	1.3	F	90	8.74	-1.62
49	0.25	Solitary	-	0.021	-	F	90	7.02	-1.12
50	0.25	Solitary	-	0.042	-	F	90	18.17	-2.96
51	0.25	Solitary	-	0.064	-	F	90	31.44	-4.58
52	0.25	Solitary	-	0.085	-	F	90	45.45	-5.73

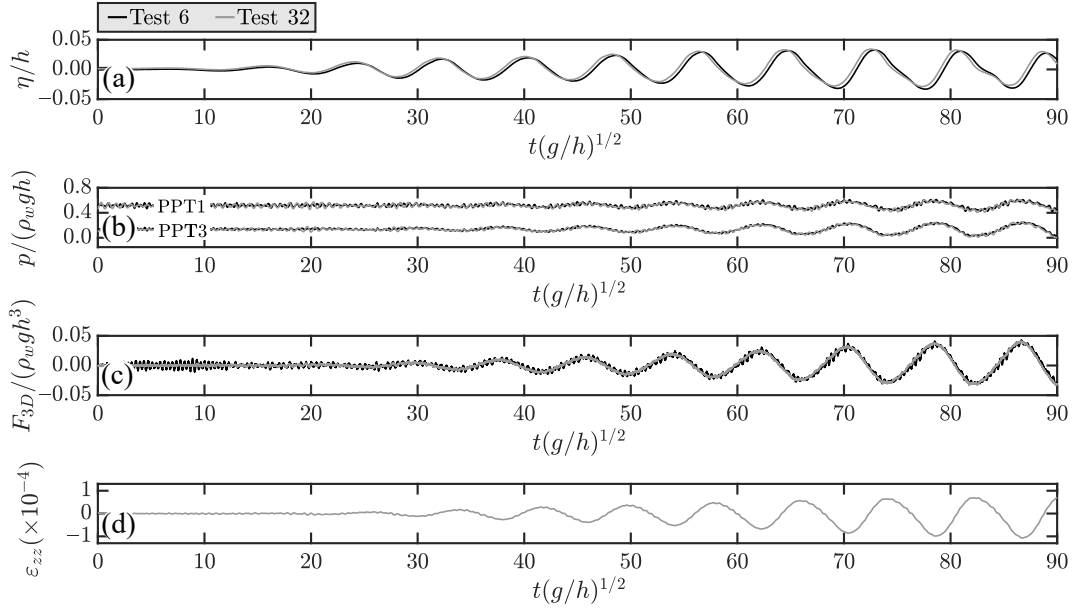


Figure A.2. Laboratory tests 6 and 32: dimensionless time series of (a) η/h at WG2, (b) $p/(\rho_wgh)$ at PPT1 and 3, (c) $F_{3D}/(\rho_wgh^3)$ and (d) ε_{zz} at SGb.

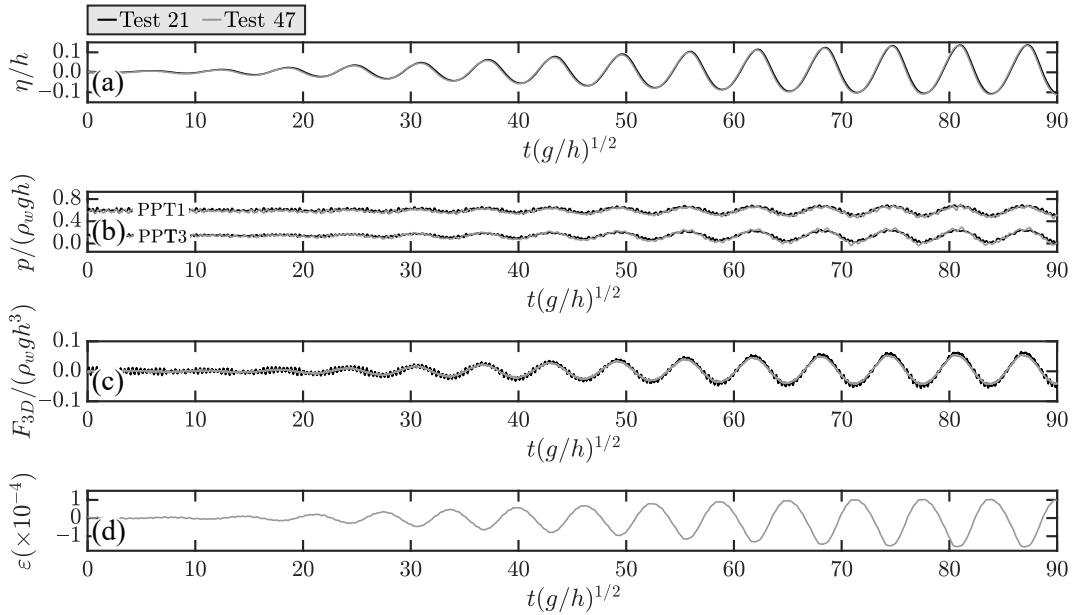


Figure A.3. Laboratory tests 21 and 47: dimensionless time series of (a) η/h at WG2, (b) $p/(\rho_wgh)$ at PPT1 and 3, (c) $F_{3D}/(\rho_wgh^3)$ and (d) ε_{zz} at SGb.

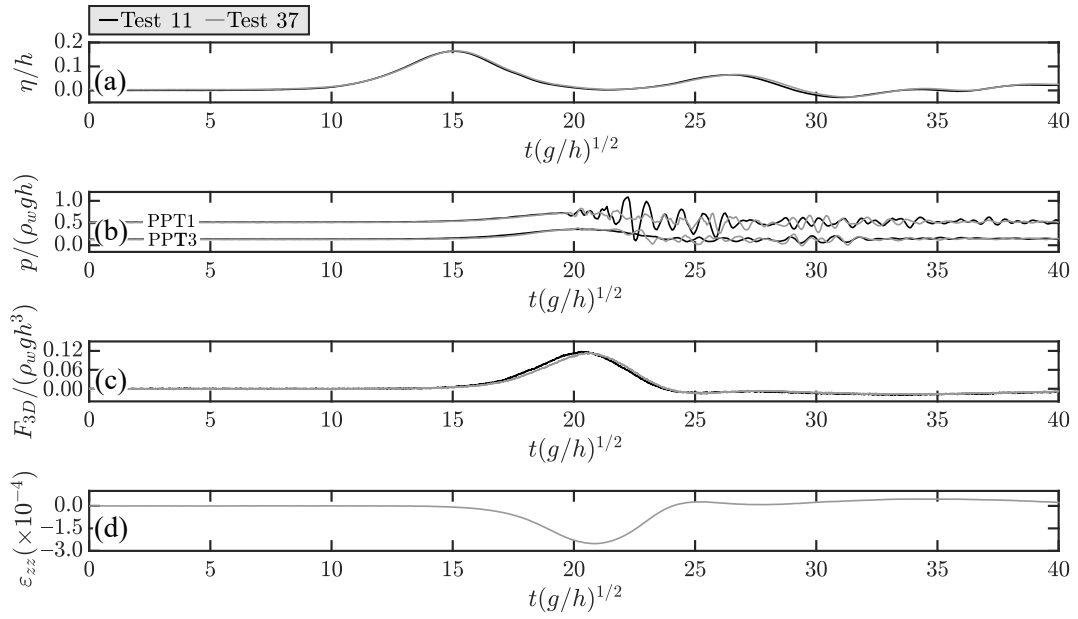


Figure A.4. Laboratory tests 11 and 37: dimensionless time series of (a) η/h at WG2, (b) $p/(\rho_wgh)$ at PPT1 and 3, (c) $F_{3D}/(\rho_wgh^3)$ and (d) ε_{zz} at SGb.

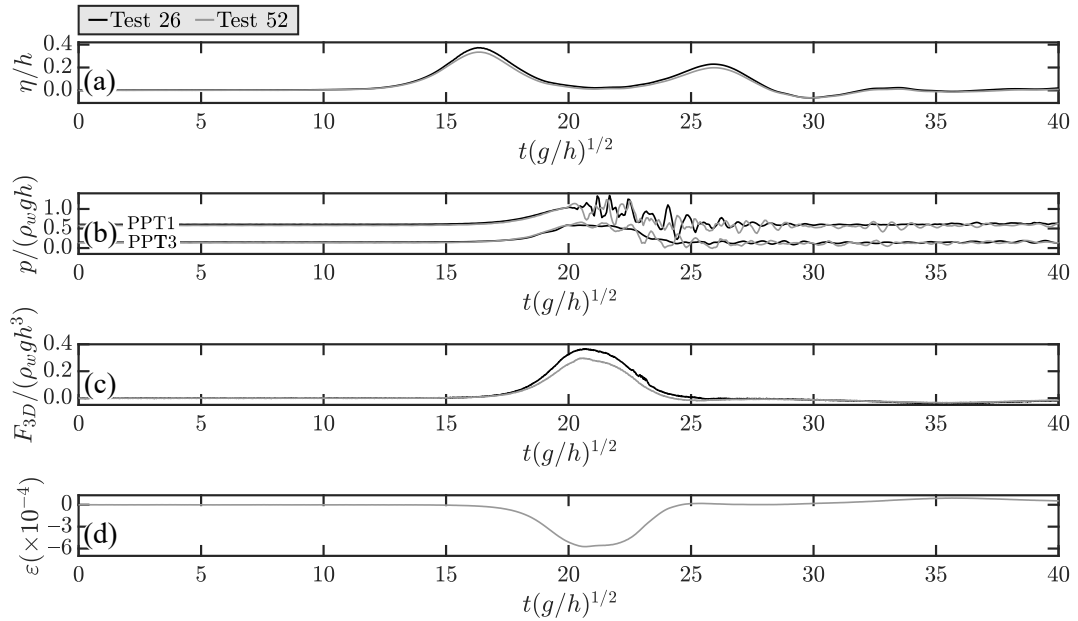


Figure A.5. Laboratory tests 26 and 52: dimensionless time series of (a) η/h at WG2, (b) $p/(\rho_wgh)$ at PPT1 and 3, (c) $F_{3D}/(\rho_wgh^3)$ and (d) ε_{zz} at SGb.

This page was intentionally left blank.

Appendix B

Breaking wave impact on a deformable truncated vertical wall (CCP-WSI comparative study 1)

The Collaborative Computational Project in Wave-Structure Interaction (CCP-WSI) was funded by the Engineering and Physical Sciences Research Council (EPSRC). CCP-WSI has been supporting a number of studies to understand the strengths of different WSI numerical models and provide directions for future developments (Ransley et al., 2019; 2020; 2021). The CCP-WSI comparative study 1 was proposed in October 2021, as a first step towards more complex WSI phenomena, including fully-coupled fluid and solid mechanics (CCP-WSI, 2021).

Participants have been invited to simulate offshore breaking wave impacts on a deformable truncated vertical wall with different numerical models. A total of 3 laboratory tests have been considered, including rigid and flexible walls. Initially, the time series of the laboratory water surface elevation were released along with a full description of the experimental tests (CCP-WSI, 2021). Participants were then asked to simulate the laboratory experiments and submit their numerical results, including

the water surface elevations η , water pressures p and Three-Dimensional (3D) force F_{3D} on the wall and the horizontal displacements d_x of the wall.

In the following sections, the laboratory set-up and the test programme of the CCP-WSI (2021) are addressed. A description of the current contribution of the author to the study, including the numerical set-up used and some of the results, are then presented.

B.1 Laboratory set-up and test programme

Laboratory experiments have been conducted in a 35.0 m long, 0.6 m wide and 1.2 m deep flume at the COAST laboratory of the University of Plymouth (Mai et al., 2020; CCP-WSI, 2021). These consisted in breaking waves impacting rigid and deformable walls. The flume was equipped with a piston-type wave maker and a water depth $h = 0.7$ m was used. The 0.560 m (width) \times 0.600 m (height) \times 0.012 m (thickness) truncated vertical wall was located 26.90 m downstream the wave maker (Fig. B.1a, b). The aluminium wall was connected to a rigid support frame by 4 springs and was free to move along the horizontal direction only.

A total of 3 laboratory tests were conducted by changing the spring configuration and/or stiffness k_s behind the wall. For test 1, the springs were locked, mimicking a rigid structure. For tests 2 and 3, 2 different spring systems have been used, with the main parameters summarised in Table B.1.

Table B.1. Test programme for the CCP-WSI (2021) laboratory tests.

Parameter	Symbol	Unit	Test 1	Test 2	Test 3
Water depth	h	m	0.70	0.70	0.70
Crest wave amplitude	a_c	m	0.1914	0.1914	0.1914
Significant wave height	H_s	m	0.163	0.163	0.163
Peak wave period	T_p	s	1.601	1.601	1.601
Spring stiffness	k_s	N/m	-	98493	37702

A single focused wave was used for all 3 tests. This was generated using 116 wave fronts with frequencies equally spaced between 0.2 and 2.0 Hz. The amplitudes of the frequency components were derived using the New Wave theory (Tromans et al.,

1991) based on the JONSWAP spectrum with a crest amplitude $a_c = 0.1914$ m, a significant wave height $H_s = 0.163$ m and a peak wave period $T_p = 1.601$ s (Table B.1).

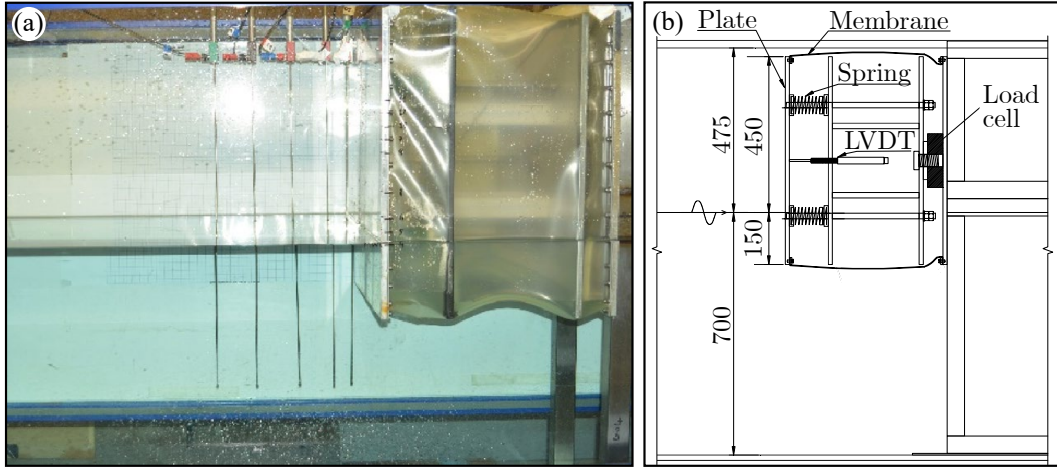


Figure B.1. Laboratory set-up of the CCP-WSI (2021) comparative study 1: (a) photograph of the experimental flume and wall and (b) sketch of the wall and spring system (all measurements are in mm).

The water surface elevations were sampled with 13 Wave Gauges (WGs, Table B.2) at 128 Hz. An array of FGP XPM10 pressure sensors was used to measure the pressure on the plate. The total force on the plate was measured with a low-profile load cell. In addition, the plate was equipped with a Linear Variable Differential Transformer (LVDT) to measure the horizontal displacement (Fig. B.1b).

Table B.2. Wave gauge locations along the flume: distance (m) from the wave maker.

WG1	WG2	WG3	WG4	WG5	WG6	WG7	WG8	WG9	WG10	WG11	WG12	WG13
1.00	6.00	11.00	16.00	21.15	22.11	22.90	26.05	26.57	26.66	26.75	26.84	26.89

B.2 Numerical simulations

The 3 CCP-WSI (2021) laboratory tests (Table B.1) were simulated with solids4foam (Cardiff et al., 2018) within the present work. The numerical set-up consisted of a Two-Dimensional (2D) wave flume with a rigid plate (Young's modulus $E = 80$ GPa, Fig. B.2), mimicking the truncated wall. This was anchored to 2 elastic blocks,

representing the spring system. These blocks were fixed at the downwave end and allowed horizontal displacements only. Each block (subscript b) modelled the 2 springs at the same coordinate z . Consequently, its Young's modulus was calculated as $E_b = 2k_s l_b / A_{\perp,b}$, where l_b and $A_{\perp,b}$ are the block length and cross-sectional area, respectively (Table B.3).

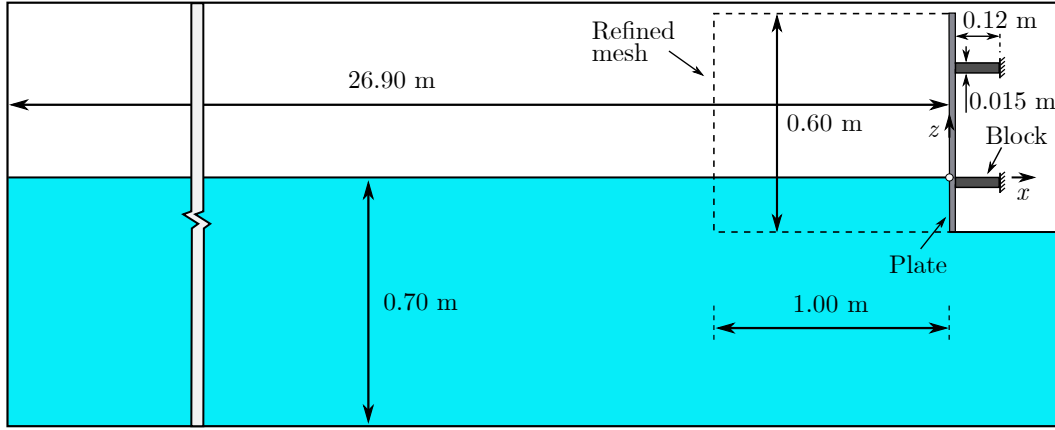


Figure B.2. Side view of the numerical set-up for the (CCP-WSI, 2021) comparative study 1.

Table B.3. Properties of the numerical block used to model the CCP-WSI (2021) laboratory tests.

	l_b (m)	$A_{\perp,b}$ (m ²)	ρ_b (kg/m ³)	E_b (MPa)
Test 2	0.120	0.0084	942.0	2.814
Test 3	0.120	0.0084	2282.0	1.077

Wave generation was performed with the toolbox waves2Foam (Jacobsen et al., 2012), where the new wave theory was implemented as shown in Katsidoniotaki (2019). The laminar flow model was used for these simulations, providing accurate results at reduced computational costs. Although simplifications had to be made due to the complexity of the laboratory tests, the simulations accurately capture the main aspects of the laboratory investigation.

A mesh resolution of $\Delta x = \Delta z = 0.0075$ m was employed in a 0.60 m \times 1.00 m refined area (Fig. B.2), with $\Delta x = \Delta z = 0.015$ m in the remainder of the fluid region. $\Delta x = \Delta z = 0.0075$ m was used for the wall. The simulations were conducted with an adaptive time step Δt , satisfying the Courant-Friedrichs-Lewy (CFL) convergence

condition, with a sampling frequency of 128 Hz for consistency with the laboratory measurements.

B.3 Numerical results

Comparisons between the laboratory and numerical η/h at several WGs are shown in Fig. B.3 for test 1. The numerical model captures the main physics of the laboratory waves. At WG1 and 4, a good agreement between laboratory and numerical results is observed, with relatively small deviations of less than 10% for the wave peaks of the main wave group ($65 \leq t(g/h)^{1/2} \leq 90$ at WG1 and $105 \leq t(g/h)^{1/2} \leq 130$ at WG4, where g is the gravitational acceleration). Some deviations can be observed at the WGs closer to the plate. These are partially due to the imprecise modelling of the wave breaking in the simulations, given the laminar flow assumption. However, the overall behaviour is captured well in the numerical simulation. At WG13, the largest wave amplitude observed in the laboratory tests is predicted by the numerical model, however, with a phase shift.

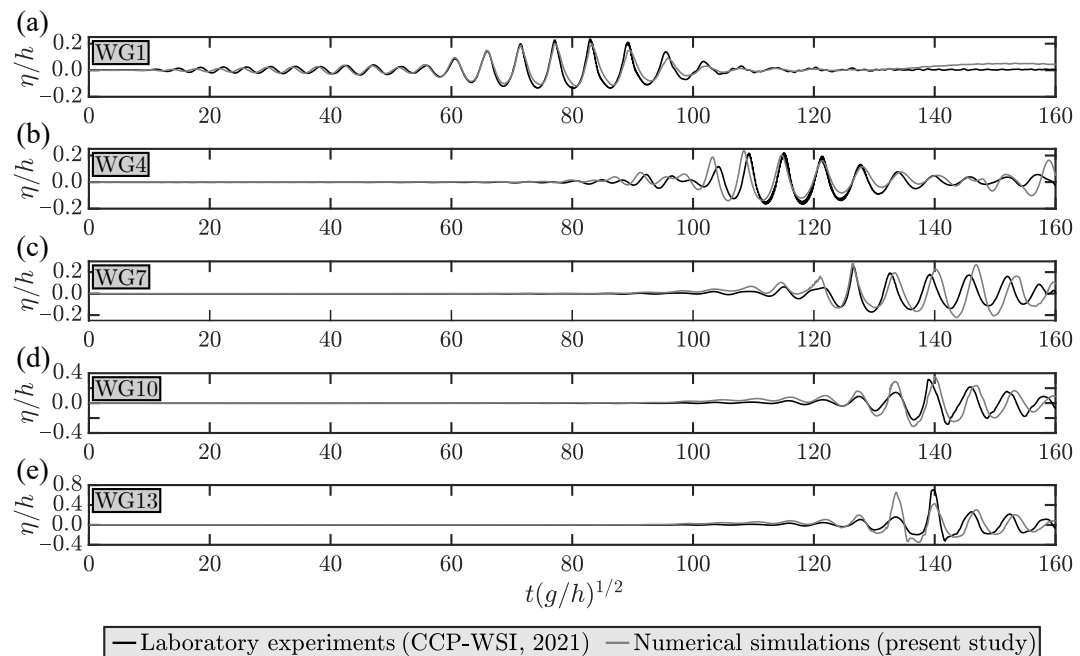


Figure B.3. Time series of the laboratory and numerical water surface elevations η/h at several wave gauges for test 1 of Table B.1.

The time series of the relative water surface elevations η/h at various WGs are shown in Fig. B.4 for the 3 numerical tests. No deviations of η/h are observed between the 3 tests at the WGs in proximity of the wave maker. However, some deviations can be observed near the plate due to different reflection processes. At WG13, the largest elevation is observed for test 1 ($\eta/h = 0.65$) followed by test 3 ($\eta/h = 0.60$) and 2 ($\eta/h = 0.58$).

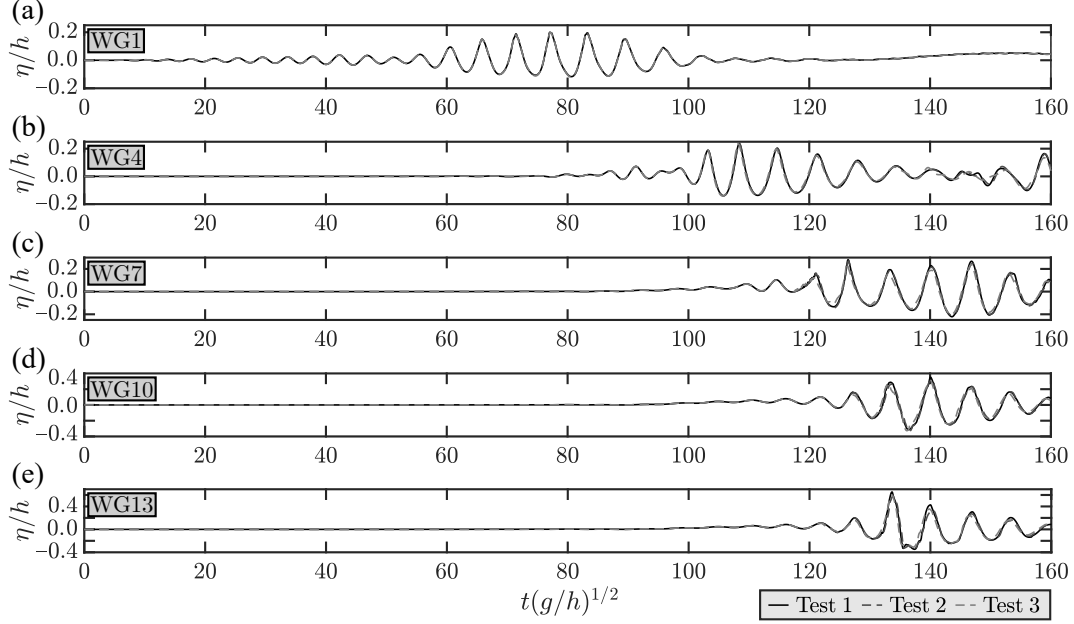


Figure B.4. Time series of the numerical water surface elevations η/h at several wave gauges for the 3 tests of Table B.1.

The numerical F_{3D} was calculated as $F_{3D} = Fb$, with the 2D force F and the wall width $b = 0.56$ m. For all 3 tests, the maximum numerical force $F_{3D}/(\rho_w gh)$ was observed at approximately $t(g/h)^{1/2} = 133$, as shown in Fig. B.5a, where ρ_w is the water density. Test 1 resulted in the largest $F_{3D}/(\rho_w gh)$, with deviations of 2.4 and 24.2% for test 2 and 3, respectively. Oscillations of the force are observed for the flexible configurations after the main peak.

Test 1 showed no displacements compared to tests 2 and 3 (Fig. B.5b). As expected, the largest displacements were observed for the most flexible configuration (test 3) with values from 2.0 to 2.6 times larger than in test 2. These deviations are reasonably consistent with the difference in the spring stiffnesses of these 2 tests. The

publication for this study, including the results of all contributors and comparison with the laboratory measurements, is still pending.

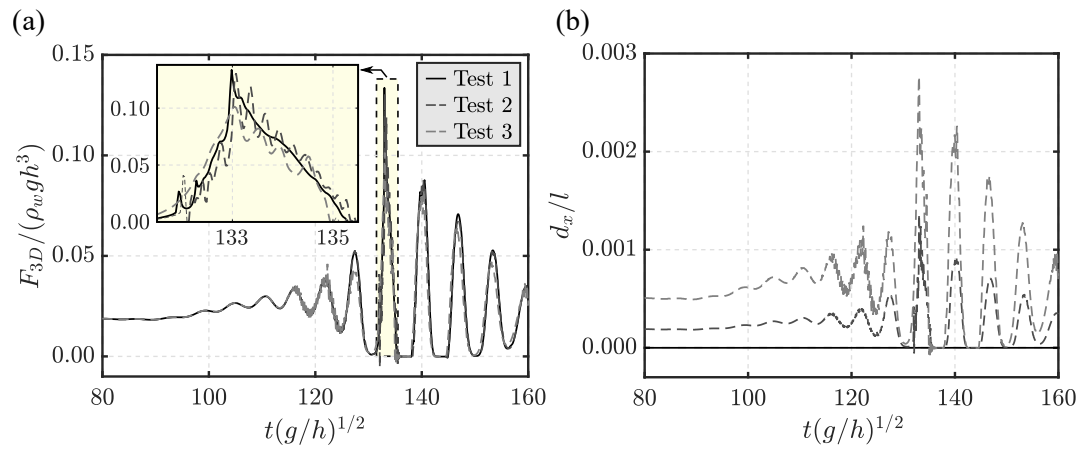


Figure B.5. Time series of the numerical results (a) $F_{3D}/(\rho_w g h^2)$ and (b) d_x/l for the 3 tests in Table B.1 of CCP-WSI (2021).

This page was intentionally left blank.

References

- Abrahamsen, B. C., Faltinsen, O. M., 2013. Scaling of entrapped gas pocket slamming events at dissimilar Euler number. *Journal of Fluids and Structures* 40, 246 – 256.
- Abrahamsen, B. C., Grytten, F., Hellan, Ø., Søreide, T. H., Faltinsen, O. M., 2023. Hydroelastic response of concrete shells during impact on calm water. *Journal of Fluids and Structures* 116, 103804.
- Aguerre, H. J., Damián, S. M., Gimenez, J. M., Nigro, N. M., 2013. Modeling of compressible fluid problems with OpenFOAM using dynamic mesh technology. *Mecánica Computacional* 32 (13), 995 – 1011.
- Airy, G., 1845. Tides and waves. Encyclopaedia Metropolitana.
- Allsop, N., Pullen, T., van der Meer, J., Bruce, T., Schuttrumpf, H., Kortenhaus, A., 2008. Improvements in wave overtopping analysis: The EurOtop overtopping manual and calculation tool. *In: Proceedings COPEDEC VII* 7, 1 – 14.
- Antoci, C., Gallati, M., Sibilla, S., 2007. Numerical simulation of fluid-structure interaction by SPH. *Computers & Structures* 85 (11), 879 – 890.
- ASCE/SEI 7-16, 2017. Minimum design loads and associated criteria for buildings and other structures. American Society of Civil Engineers, Standards.
- Attili, T., Heller, V., Triantafyllou, S., 2020. Numerical modelling of impulse wave forces on dams. *In: Proceedings of the 1st IAHR Young Professionals Congress online*, 186 – 187.

- Attili, T., Heller, V., Triantafyllou, S., 2021. A numerical investigation of tsunamis impacting dams. *Coastal Engineering* 169, 103942.
- Attili, T., Heller, V., Triantafyllou, S., 2022a. Numerical investigation of impulse waves impacting dams. *In: 39th International Association for Hydro-Environmental Engineering and Research World Congress*, 2222 – 2229.
- Attili, T., Heller, V., Triantafyllou, S., 2022b. Numerical investigation of waves interacting with rigid and flexible plates. *In: 39th International Association for Hydro-Environmental Engineering and Research World Congress*, 4438 – 4447.
- Attili, T., Heller, V., Triantafyllou, S., 2023a. Scaling approaches and scale effects in wave-flexible structure interaction. *Journal of Fluids and Structures* (in press).
- Attili, T., Heller, V., Triantafyllou, S., 2023b. Wave impact on rigid and flexible plates. *Coastal Engineering* 182, 104302.
- Bagnold, R., 1939. Interim report on wave-pressure research. *Journal of the Institution of Civil Engineers* 12 (7), 202 – 226.
- Baird, W. F., Caldwell, J. M., Edge, B. L., Magoon, O. T., Treadwell, D. D., 1980. Report on the damages to the Sines breakwater, Portugal. *Coastal Engineering*, 3063 – 3077.
- Blenkinsopp, C. E., Chaplin, J. R., 2011. Void fraction measurements and scale effects in breaking waves in freshwater and seawater. *Coastal Engineering* 58 (5), 417 – 428.
- Boussinesq, J., 1871. Théorie de l'intumescence liquide appelée onde solitaire ou de translation, se propageant dans un canal rectangulaire. *Comptes Rendus de l'Académie des Science* 72, 755 – 759.
- Brackbill, J. U., Kothe, D. B., Zemach, C., 1992. A continuum method for modeling surface tension. *Journal of Computational Physics* 100 (2), 335 – 354.

- Bredmose, H., Bullock, G., Hogg, A., 2015. Violent breaking wave impacts. Part 3. Effects of scale and aeration. *Journal of Fluid Mechanics* 765, 82 – 113.
- Buckingham, E., 1914. On physically similar systems - Illustrations of the use of dimensional equations. *Physical Review* 4 (4), 345 – 376.
- Bullard, G., Mulligan, R., Carreira, A., Take, W., 2019. Experimental analysis of tsunamis generated by the impact of landslides with high mobility. *Coastal Engineering* 152, 103538.
- Bureau of Reclamation, 2012. Embankment dams. URL: <https://www.usbr.gov/tsc/techreferences/designstandards-datacollectionguides/finals-pdfs/DS13-2.pdf>, accessed: 15 September 2023.
- Bureau of Reclamation, 2013. Design of double-curvature arch dams planning, appraisal, feasibility level. Technical Memorandum EM36-86-68110, Denver, Colorado.
- Cardiff, P., Karač, A., Jaeger, P. D., Jasak, H., Nagy, J., Ivanković, A., Tuković, Z., 2018. An open-source finite volume toolbox for solid mechanics and fluid-solid interaction simulations. *ArXiv Prepr ArXiv180810736*.
- Castellino, M., Romano, A., Lara, J. L., Losada, I. J., De Girolamo, P., 2021. Confined-crest impact: Forces dimensional analysis and extension of the Goda's formulae to recurved parapets. *Coastal Engineering* 163, 103814.
- Castellino, M., Sammarco, P., Romano, A., Martinelli, L., Ruol, P., Franco, L., De Girolamo, P., 2018. Large impulsive forces on recurved parapets under non-breaking waves. A numerical study. *Coastal Engineering* 136, 1 – 15.
- Catucci, D., Briganti, R., Heller, V., 2021. Numerical validation of novel scaling laws for air entrainment in water. *Proceedings of the Royal Society A: Mathematical, Physical and Engineering Sciences* 477 (2255), 20210339.

- Catucci, D., Briganti, R., Heller, V., 2023. Numerical validation of novel scaling laws for air-water flows including compressibility and heat transfer. *Journal of Hydraulic Research* (in press).
- CCP-WSI, 2021. Breaking wave impact on a ‘deformable’ truncated vertical wall (CCP-WSI Comparative Study 1). URL: https://www.ccp-wsi.ac.uk/data_repository/test_cases/test_case_013, accessed: 15 September 2023.
- Chakrabarti, S. K., 2005. Offshore structure modeling. Elsevier, London, UK.
- Chanson, H., Aoki, S., Hoque, A., 2004. Physical modelling and similitude of air bubble entrainment at vertical circular plunging jets. *Chemical Engineering Science* 59 (4), 747 – 758.
- Chaplin, J. R., Heller, V., Farley, F. J. M., Hearn, G. E., Rainey, R. C. T., 2012. Laboratory testing the Anaconda. *Proceedings of the Royal Society A: Mathematical, Physical and Engineering Sciences* 370 (1959), 403 – 424.
- Chen, F., Heller, V., Briganti, R., 2020. Numerical modelling of tsunamis generated by iceberg calving validated with large-scale laboratory experiments. *Advances in Water Resources* 142, 103647.
- Chen, L., Stagonas, D., Santo, H., Buldakov, E., Simons, R., Taylor, P., Zang, J., 2019. Numerical modelling of interactions of waves and sheared currents with a surface piercing vertical cylinder. *Coastal Engineering* 145, 65 – 83.
- Chen, L., Zang, J., Hillis, A., Morgan, G., Plummer, A., 2014. Numerical investigation of wave-structure interaction using OpenFOAM. *Ocean Engineering* 88, 91 – 109.
- Colagrossi, A., Landrini, M., 2003. Numerical simulation of interfacial flows by Smoothed Particle Hydrodynamics. *Journal of Computational Physics* 191 (2), 448 – 475.
- Collins, I., Hossain, M., Dettmer, W., Masters, I., 2021. Flexible membrane structures for wave energy harvesting: A review of the developments, materials and

- computational modelling approaches. *Renewable and Sustainable Energy Reviews* 151, 111478.
- Contestabile, P., Iuppa, C., Di Lauro, E., Cavallaro, L., Andersen, T. L., Vicinanza, D., 2017. Wave loadings acting on innovative rubble mound breakwater for overtopping wave energy conversion. *Coastal Engineering* 122, 60 – 74.
- Cooker, M. J., Weidman, P. D., Bale, D. S., 1997. Reflection of a high-amplitude solitary wave at a vertical wall. *Journal of Fluid Mechanics* 342, 141 – 158.
- Courant, R., Friedrichs, K., Lewy, H., 1928. Über die partiellen Differenzgleichungen der Mathematischen Physik. *Mathematische Annalen* 100, 32 – 74.
- Couston, L.-A., Mei, C., Alam, M.-R., 2015. Landslide tsunamis in lakes. *Journal of Fluid Mechanics* 772, 784 – 804.
- Cramer, O., 1993. The variation of the specific heat ratio and the speed of sound in air with temperature, pressure, humidity, and CO₂ concentration. *The Journal of the Acoustical Society of America* 93 (5), 2510 – 2516.
- Croquer, S., Díaz-Carrasco, P., Tamimi, V., Poncet, S., Lacey, J., Nistor, I., 2023. Modelling wave-structure interactions including air compressibility: A case study of breaking wave impacts on a vertical wall along the Saint-Lawrence Bay. *Ocean Engineering* 273, 113971.
- Cross, R., 1967. Tsunami surge forces. *Journal of the Waterways and Harbors Division* 93 (4), 201 – 234.
- Cuomo, G., Allsop, W., Bruce, T., Pearson, J., 2010a. Breaking wave loads at vertical seawalls and breakwaters. *Coastal Engineering* 57 (4), 424 – 439.
- Cuomo, G., Allsop, W., Takahashi, S., 2010b. Scaling wave impact pressures on vertical walls. *Coastal Engineering* 57 (6), 604 – 609.
- Dawson, D., Shaw, J., Gehrels, W. R., 2016. Sea-level rise impacts on transport

- infrastructure: The notorious case of the coastal railway line at Dawlish, England. *Journal of Transport Geography* 51, 97 – 109.
- Dean, R., Dalrymple, R., 1991. Water wave mechanics for engineers and scientists. Advanced series on ocean engineering 2. World Scientific, Singapore.
- Degroote, J., 2013. Partitioned simulation of fluid-structure interaction. *Archives of Computational Methods in Engineering* 20 (3), 185 – 238.
- Dermentzoglou, D., Castellino, M., De Girolamo, P., Partovi, M., Schreppers, G.-J., Antonini, A., 2021. Crownwall failure analysis through finite element method. *Journal of Marine Science and Engineering* 9 (1), 35.
- Di Paolo, B., Lara, J. L., Barajas, G., Losada, I. J., 2021. Wave and structure interaction using multi-domain couplings for Navier-Stokes solvers in OpenFOAM®. Part I: Implementation and validation. *Coastal Engineering* 164, 103799.
- Didier, E., Neves, D., Martins, R., Neves, M., 2014. Wave interaction with a vertical wall: SPH numerical and experimental modeling. *Ocean Engineering* 88, 330 – 341.
- Dingemans, M. W., 1997. Water wave propagation over uneven bottoms. Advanced Series on Ocean Engineering. World Scientific, Singapore.
- Erbisti, P., 2014. Design of hydraulic gates. Balkema, Netherlands.
- Evers, F. M., 2017. Spatial propagation of landslide generated impulse waves. Ph.D. thesis no. 24650, ETH Zurich, Zurich.
- Evers, F. M., Boes, R. M., 2019. Impulse wave runup on steep to vertical slopes. *Journal of Marine Science and Engineering* 7 (1), 8.
- Evers, F. M., Heller, V., Hager, W. H., Boes, R. M., 2019. Landslide-generated impulse waves in reservoirs: Basics and computation. 2nd edition. VAW-Mitteilung 254 (R. Boes, ed.), ETH Zurich, Zurich.

- Falcão, A. F., Henriques, J. C., 2014. Model-prototype similarity of oscillating-water-column wave energy converters. *International Journal of Marine Energy* 6, 18 – 34.
- Fenton, J. D., Rienecker, M. M., 1982. A Fourier method for solving nonlinear water-wave problems: Application to solitary-wave interactions. *Journal of Fluid Mechanics* 118, 411 – 443.
- Ferziger, J. H., 1987. Simulation of incompressible turbulent flows. *Journal of Computational Physics* 69 (1), 1 – 48.
- Franci, A., Cremonesi, M., Perego, U., Crosta, G., Oñate, E., 2020. 3D simulation of Vajont disaster. Part 1: Numerical formulation and validation. *Engineering Geology* 279, 105854.
- Fuchs, H., Hager, W. H., 2015. Solitary impulse wave transformation to overland flow. *Journal of Waterway, Port, Coastal, and Ocean Engineering* 141 (5), 04015004.
- Galvin, C. J., 1968. Breaker type classification on three laboratory beaches. *Journal of Geophysical Research* 73 (12), 3651 – 3659.
- Gerstner, F., 1802. Theorie der Wellen. *Annalen der Physik* 32 (8), 412 – 445.
- Gibson, R. F., 2007. Principles of composite material mechanics. CRC press, Florida.
- Girfoglio, M., Quaini, A., Rozza, G., 2021. Fluid-structure interaction simulations with a LES filtering approach in solids4foam. *ArXiv Preprint ArXiv210208011*.
- Goda, Y., 1967. The fourth order approximation to the pressure of standing waves. *Coastal Engineering in Japan* 10 (1), 1 – 11.
- Gomez-Gesteira, M., Rogers, B., Crespo, A., Dalrymple, R., Narayanaswamy, M., Dominguez, J., 2012. SPHysics - development of a free-surface fluid solver - Part 1: Theory and formulations. *Computer & Geoscience* 48, 289 – 299.

- Gylfadóttir, S. S., Kim, J., Helgason, J. K., Brynjólfsson, S., Höskuldsson, A., Jóhannesson, T., Harbitz, C. B., Løvholt, F., 2017. The 2014 lake Askja rockslide-induced tsunami: Optimization of numerical tsunami model using observed data. *Journal of Geophysical Research: Oceans* 122 (5), 4110 – 4122.
- Hall, J. V., Watts, G. M., 1953. Laboratory investigation of the vertical rise of solitary waves on impermeable slopes. Technical Memo Report No. 33. U.S. Army Corps of Engineers, Washington, USA.
- Hartmann, F., Katz, C., 2004. Structural analysis with finite elements. Springer, Germany.
- He, G., Kashiwagi, M., 2012. Numerical analysis of the hydroelastic behavior of a vertical plate due to solitary waves. *Journal of Marine Science and Technology* 17 (2), 154 – 167.
- Heller, V., 2011. Scale effects in physical hydraulic engineering models. *Journal of Hydraulic Research* 49 (3), 293 – 306.
- Heller, V., 2017. Self-similarity and Reynolds number invariance in Froude modelling. *Journal of Hydraulic Research* 55 (3), 293 – 309.
- Heller, V., Attili, T., Chen, F., Gabl, R., Wolters, G., 2021. Large-scale investigation into iceberg-tsunamis generated by various iceberg calving mechanisms. *Coastal Engineering* 163, 103745.
- Heller, V., Bruggemann, M., Spinneken, J., Rogers, B. D., 2016. Composite modelling of subaerial landslide-tsunamis in different water body geometries and novel insight into slide and wave kinematics. *Coastal Engineering* 109, 20 – 41.
- Heller, V., Hager, W. H., 2010. Impulse product parameter in landslide generated impulse waves. *Journal of Waterway, Port, Coastal, and Ocean Engineering* 136 (3), 145 – 155.

-
- Heller, V., Hager, W. H., 2011. Wave types of landslide generated impulse waves. *Ocean Engineering* 38 (4), 630 – 640.
- Heller, V., Hager, W. H., Minor, H.-E., 2008. Scale effects in subaerial landslide generated impulse waves. *Experiments in Fluids* 44 (5), 691 – 703.
- Heller, V., Hager, W. H., Minor, H.-E., 2009. Landslide-generated impulse waves in reservoirs: Basics and computation. VAW-Mitteilung 211 (R. Boes, ed.), ETH Zurich, Zurich.
- Heller, V., Spinneken, J., 2015. On the effect of the water body geometry on landslide-tsunamis: Physical insight from laboratory tests and 2D to 3D wave parameter transformation. *Coastal Engineering* 104, 113 – 134.
- Hess, F., Boes, R. M., Evers, F. M., 2023. Forces on a vertical dam due to solitary impulse wave run-up and overtopping. *Journal of Hydraulic Engineering* 149 (7), 04023020.
- Higuera, P., Lara, J. L., Losada, I. J., 2013. Realistic wave generation and active wave absorption for Navier-Stokes models: Application to OpenFOAM®. *Coastal Engineering* 71, 102 – 118.
- Higuera, P., Lara, J. L., Losada, I. J., 2014. Three-dimensional interaction of waves and porous coastal structures using OpenFOAM®. Part I: Formulation and validation. *Coastal Engineering* 83, 243 – 258.
- Hirt, C. W., Nichols, B. D., 1981. Volume of Fluid (VOF) method for the dynamics of free boundaries. *Journal of Computational Physics* 39, 201 – 225.
- Hu, Z., Huang, L., Li, Y., 2023. Fully-coupled hydroelastic modelling of a deformable wall in waves. *Coastal Engineering* 179, 104245.
- Hu, Z. Z., Greaves, D., Raby, A., 2016. Numerical wave tank study of extreme waves and wave-structure interaction using OpenFOAM. *Ocean Engineering* 126, 329 – 342.

- Huang, C., Zhang, D., Si, Y., Shi, Y., Lin, Y., 2018. Coupled finite particle method for simulations of wave and structure interaction. *Coastal Engineering* 140, 147 – 160.
- Huang, L., Li, Y., Benites, D., Windt, C., Feichtner, A., Tavakoli, S., Davidson, J., Paredes, R., Quintana, T., Ransley, E., Colombo, M., Li, M., Cardiff, P., Tabor, G., 2022. A review on the modelling of wave-structure interactions based on OpenFOAM. *OpenFOAM Journal* 2, 116 – 142.
- Hudson, R. Y., Herrmann, F. A., Sager, R. A., 1979. Coastal hydraulic models (technical report). US Army Engineer Waterways Experiment Station, Vicksburg, Mississippi.
- Hughes, S. A., 1993. Physical models and laboratory techniques in coastal engineering. World scientific, Singapore.
- Irvine, T., 2009. The Tacoma Narrows Bridge Failure. Vibrationdata. URL: <http://www.vibrationdata.com/Tacoma.pdf>.
- Jacobsen, N. G., Fuhrman, D. R., Fredsøe, J., 2012. A wave generation toolbox for the open-source CFD library: OpenFOAM. *International Journal for Numerical Methods in Fluids* 70 (9), 1073 – 1088.
- Jain, A., Jones, N. P., Scanlan, R. H., 1996. Coupled flutter and buffeting analysis of long-span bridges. *Journal of Structural Engineering* 122 (7), 716 – 725.
- Jasak, H., 1996. Error analysis and estimation for the finite volume method with applications to fluid flows. Ph.D. thesis, Imperial College of Science, Technology and Medicine, London.
- Katsidoniotaki, E., 2019. Focused wave generation based on linear new wave theory, using OpenFOAM and waves2Foam toolbox. In: *Proceedings of CFD with Open-Source Software, 2019, Edited by Nilsson. H.*

- Khayyer, A., Gotoh, H., Falahaty, H., Shimizu, Y., 2018. An enhanced ISPH-SPH coupled method for simulation of incompressible fluid-elastic structure interactions. *Computer Physics Communications* 232, 139 – 164.
- Khayyer, A., Tsuruta, N., Shimizu, Y., Gotoh, H., 2019. Multi-resolution MPS for incompressible fluid-elastic structure interactions in ocean engineering. *Applied Ocean Research* 82, 397 – 414.
- Kiger, K. T., Duncan, J. H., 2012. Air-entrainment mechanisms in plunging jets and breaking waves. *Annual Review of Fluid Mechanics* 44 (1), 563 – 596.
- Kimmoun, O., Malenica, s., Scolan, Y. M., 2009. Fluid structure interactions occurring at a flexible vertical wall impacted by a breaking wave. *In: The Nineteenth International Offshore and Polar Engineering Conference ISOPE-I-09-035*.
- Kobel, J., Evers, F. M., Hager, W. H., 2017. Impulse wave overtopping at rigid dam structures. *Journal of Hydraulic Engineering* 143 (6), 04017002.
- Kobus, H., 1980. Hydraulic modelling. German Association for Water Resources and Land Improvement (Bulletin 7), Hamburg, Germany.
- Krautwald, C., von Häfen, H., Niebuhr, P., Vögele, K., Stolle, J., Schimmels, S., Schürenkamp, D., Sieder, M., Goseberg, N., 2022. Collapse processes and associated loading of square light-frame timber structures due to bore-type waves. *Coastal Engineering* 177, 104178.
- Kumar, P., Yang, Q., Jones, V., McCue-Weil, L., 2015. Coupled SPH-FVM simulation within the OpenFOAM framework. *Procedia IUTAM* 18, 76 – 84.
- Lagoun, M. S., Benalia, A., Benbouzid, M. E. H., 2010. Ocean wave converters: State of the art and current status. *In: 2010 IEEE International Energy Conference*, 636 – 641.
- Laitone, E. V., 1960. The second approximation to cnoidal and solitary waves. *Journal of Fluid Mechanics* 9 (3), 430 – 444.

- Lambert, S., Bourrier, F., Ceron-Mayer, A. R., Dugelas, L., Dubois, F., Piton, G., 2023. Small-scale modeling of flexible barriers. I: Mechanical similitude of the structure. *Journal of Hydraulic Engineering* 149 (3), 04022043.
- Larsen, B. E., Fuhrman, D. R., 2019. Full-scale CFD simulation of tsunamis. Part 1: Model validation and run-up. *Coastal Engineering* 151, 22 – 41.
- Lauder, B., Spalding, D., 1974. The numerical computation of turbulent flows. *Computer Methods in Applied Mechanics and Engineering* 3 (2), 269 – 289.
- Laya, E. J., Connor, J. J., Sunder, S. S., 1984. Hydrodynamic forces on flexible offshore structures. *Journal of Engineering Mechanics* 110 (3), 433 – 448.
- Le Méhauté, B., 1965. On Froude-Cauchy similitude. In: *Proceedings Santa Barbara specialty conference*, 327 – 345.
- Le Méhauté, B., 1976. An introduction to hydrodynamics and water waves. Springer, New York.
- Le Méhauté, B., 1990. Similitude. In: B. Le Méhauté and D. M. Hanes (Eds.), *Ocean engineering science: The sea*. Wiley, New York.
- Li, Y., Raichlen, F., 2003. Energy balance model for breaking solitary wave runup. *Journal of Waterway, Port, Coastal, and Ocean Engineering* 129 (2), 47 – 59.
- Liao, K., Hu, C., Sueyoshi, M., 2015. Free surface flow impacting on an elastic structure: Experiment versus numerical simulation. *Applied Ocean Research* 50, 192 – 208.
- Linton, D., Gupta, R., Cox, D., van de Lindt, J., Oshnack, M. E., Clauson, M., 2013. Evaluation of tsunami loads on wood-frame walls at full scale. *Journal of Structural Engineering* 139 (8), 1318 – 1325.
- Liu, M., Zhang, Z., 2019. Smoothed Particle Hydrodynamics (SPH) for modeling fluid-structure interactions. *Science China Physics, Mechanics & Astronomy* 62 (8), 984701.

- Lo, H.-Y., Park, Y. S., Liu, P. L.-F., 2013. On the run-up and back-wash processes of single and double solitary waves - An experimental study. *Coastal Engineering* 80, 1 – 14.
- Mai, T., Mai, C., Raby, A., Greaves, D. M., 2020. Hydroelasticity effects on water-structure impacts. *Experiments in Fluids* 61 (9), 1 – 19.
- Mallayachari, V., Sundar, V., 1995. Standing wave pressures due to regular and random waves on a vertical wall. *Ocean Engineering* 22 (8), 859 – 879.
- Martinelli, L., Lamberti, A., Gaeta, M. G., Tirindelli, M., Alderson, J., Schimmels, S., 2011. Wave loads on exposed jetties: Description of large scale experiments and preliminary results. *Coastal Engineering Proceedings* 1 (32).
- Martinelli, L., Ruol, P., Volpato, M., Favaretto, C., Castellino, M., De Girolamo, P., Franco, L., Romano, A., Sammarco, P., 2018. Experimental investigation on non-breaking wave forces and overtopping at the recurved parapets of vertical breakwaters. *Coastal Engineering* 141, 52 – 67.
- Martínez-Ferrer, P. J., Qian, L., Ma, Z., Causon, D. M., Mingham, C. G., 2018. An efficient finite-volume method to study the interaction of two-phase fluid flows with elastic structures. *Journal of Fluids and Structures* 83, 54–71.
- Maxworthy, T., 1976. Experiments on collisions between solitary waves. *Journal of Fluid Mechanics* 76 (1), 177 – 186.
- Meng, Z., Hu, Y., Ancey, C., 2020. Using a data driven approach to predict waves generated by gravity driven mass flows. *Water* 12 (2), 600.
- Miche, M., 1951. Le pouvoir réfléchissant des ouvrages maritimes exposés à l'action de la houle. *Annales de Ponts et Chaussées* 121, 285 – 319.
- Moan, T., 2018. Life cycle structural integrity management of offshore structures. *Structure and Infrastructure Engineering* 14 (7), 911 – 927.

- Mohammadi, S., Nilsson, H., Cardiff, P., Rundström, D., 2021. Fluid-structure interaction on a fixed fan blade. *In: The 16th OpenFOAM Workshop*.
- Morison, J., Johnson, J., Schaaf, S., 1950. The force exerted by surface waves on piles. *Journal of Petroleum Technology* 2 (5), 149 – 154.
- Mose, 2023. URL: <https://www.mosevenezia.eu/mose/?lang=en>, accessed: 15 September 2023.
- Müller, D. R., 1995. Auflaufen und Überschwappen von Impulswellen an Talsperren. Ph.D. thesis no. 24650, ETH Zurich, Zurich.
- Mulligan, R. P., Franci, A., Celigueta, M. A., Take, W. A., 2020. Simulations of landslide wave generation and propagation using the particle finite element method. *Journal of Geophysical Research: Oceans* 125 (6), e2019JC015873.
- OpenFOAM documentation, 2020. User guide. URL: <https://openfoam.com/documentation/user-guide/>, accessed: 15 September 2023.
- OpenFOAM extension, 2016. URL: <https://sourceforge.net/u/hjasak/foam-extend-4.0/ci/master/tree/>, accessed: 15 September 2023.
- Oumeraci, H., 1984. Scale effects in coastal hydraulic models. *In: Symposium on Scale Effects in Modelling Hydraulic Structures*, 7 – 10.
- O’Connor, J., Rogers, B. D., 2021. A fluid-structure interaction model for free-surface flows and flexible structures using Smoothed Particle Hydrodynamics on a GPU. *Journal of Fluids and Structures* 104, 103312.
- Panizzo, A., De Girolamo, P., Di Risio, M., Maistri, A., Petaccia, A., 2005a. Great landslide events in Italian artificial reservoirs. *Natural Hazards and Earth System Science* 5 (5), 733 – 740.
- Panizzo, A., De Girolamo, P., Petaccia, A., 2005b. Forecasting impulse waves generated by subaerial landslides. *Journal of Geophysical Research: Oceans* 110 (C12), 1 – 23.

- Peregrine, D. H., 2003. Water-wave impact on walls. *Annual Review of Fluid Mechanics* 35 (1), 23 – 43.
- Ramsden, J. D., 1996. Forces on a vertical wall due to long waves, bores, and dry-bed surges. *Journal of Waterway, Port, Coastal, and Ocean Engineering* 122 (3), 134 – 141.
- Ransley, E., Brown, S. A., Hann, M., Greaves, D. M., Windt, C., Ringwood, J., Davidson, J., Schmitt, P., Yan, S., Wang, J. X., Wang, J. H., Ma, Q., Xie, Z., Giorgi, G., Hughes, J., Williams, A., Masters, I., Lin, Z., Chen, H., Qian, L., Ma, Z., Chen, Q., Ding, H., Zang, J., van Rij, J., Yu, Y.-H., Li, Z., Bouscasse, B., Ducrozet, G., Bingham, H., 2021. Focused wave interactions with floating structures: A blind comparative study. *Proceedings of the Institution of Civil Engineers - Engineering and Computational Mechanics* 174 (1), 46 – 61.
- Ransley, E., Yan, S., Brown, S. A., Hann, M., Graham, D., Windt, C., Schmitt, P., Davidson, J., Ringwood, J., Musiedlak, P.-H., Wang, J., Wang, J., Ma, Q., Xie, Z., Zhang, N., Zheng, X., Giorgi, G., Chen, H., Lin, Z., Qian, L., Ma, Z., Bai, W., Chen, Q., Zang, J., Ding, H., Cheng, L., Zheng, J., Gu, H., Gong, X., Liu, Z., Zhuang, Y., Wan, D., Bingham, H., Greaves, D., 2020. A blind comparative study of focused wave interactions with floating structures (CCP-WSI blind test series 3). *International Journal of Offshore and Polar Engineering* 30 (1), 1 – 10.
- Ransley, E., Yan, S., Brown, S. A., Mai, T., Graham, D., Ma, Q., Musiedlak, P.-H., Engsig-Karup, A. P., Eskilsson, C., Li, Q., Wang, J., Xie, Z., Venkatachalam, S., Stoesser, T., Zhuang, Y., Li, Q., Wan, D., Chen, G., Chen, H., Qian, L., Ma, Z., Mingham, C., Causon, D., Gatin, I., Jasak, H., Vukcevic, V., Downie, S., Higuera, P., Buldakov, E., Stagonas, D., Chen, Q., Zang, J., Greaves, D., 2019. A blind comparative study of focused wave interactions with a fixed FPSO-like structure (CCP-WSI blind test series 1). *International Journal of Offshore and Polar Engineering* 29 (2), 113 – 127.

- Rao, C., Zhang, Y., Wan, D., 2017. Numerical simulation of the solitary wave interacting with an elastic structure using MPS-FEM coupled method. *Journal of Marine Science and Application* 16 (4), 395 – 404.
- Rauter, M., Hoße, L., Mulligan, R., Take, W., Løvholt, F., 2021. Numerical simulation of impulse wave generation by idealized landslides with OpenFOAM. *Coastal Engineering* 165, 103815.
- Rege, K., Hjertager, B. H., 2017. Application of foam-extend on turbulent fluid-structure interaction. *IOP Conference Series: Materials Science and Engineering* 276, 012031.
- Romano, A., Lara, J. L., Barajas, G., Di Paolo, B., Bellotti, G., Di Risio, M., Losada, I. J., De Girolamo, P., 2020. Tsunamis generated by submerged landslides: Numerical analysis of the near-field wave characteristics. *Journal of Geophysical Research: Oceans* 125 (7), e2020JC016157.
- Ruffini, G., Heller, V., Briganti, R., 2019. Numerical modelling of landslide-tsunami propagation in a wide range of idealised water body geometries. *Coastal Engineering* 153, 103518.
- Ruffini, G., Heller, V., Briganti, R., 2021. Numerical characterisation and efficient prediction of landslide-tsunami propagation over a wide range of idealised bathymetries. *Coastal Engineering*, 103854.
- Sainflou, M., 1928. Essai sur les digues maritimes verticales (test on vertical sea dikes). *Annales des Ponts et Chaussées* 98, 5 – 48.
- Seiffert, B. R., Ertekin, R. C., Robertson, I. N., 2015. Wave loads on a coastal bridge deck and the role of entrapped air. *Applied Ocean Research* 53, 91 – 106.
- Shellard, H., 1967. Collapse of cooling towers in a gale, Ferrybridge, 1 November 1965. *Weather* 22 (6), 232 – 240.

- Sheng, W., Alcorn, R., Lewis, T., 2014. Physical modelling of wave energy converters. *Ocean Engineering* 84, 29 – 36.
- Sotiropoulos, F., Borazjani, I., 2009. A review of state-of-the-art numerical methods for simulating flow through mechanical heart valves. *Medical & Biological Engineering & Computing* 47 (3), 245 – 256.
- Sotiropoulos, F., Yang, X., 2014. Immersed boundary methods for simulating fluid-structure interaction. *Progress in Aerospace Sciences* 65, 1 – 21.
- Street, R. L., Camfield, F. E., 1967. Observations and experiments on solitary wave deformation. *Coastal Engineering* 1966.
- Streeter, V. L., Wylie, E. B., 1985. *Fluid Mechanics*. McGraw-Hill, New York.
- Sun, P., Touzé, D. L., Zhang, A.-M., 2019. Study of a complex fluid-structure dam-breaking benchmark problem using a multi-phase SPH method with APR. *Engineering Analysis with Boundary Elements* 104, 240 – 258.
- Swiss Federal Office of Energy, 2015. Directive on the Safety of Water Retaining Facilities. Swiss Federal Office of Energy, Supervision of Dams Section, Bern, Switzerland.
- Tadjbakhsh, I., Keller, J., 1960. Standing surface waves of finite amplitude. *Journal of Fluid Mechanics* 8 (3), 442 – 451.
- Takahashi, S., Tanimoto, K., Miyanaga, S., 1985. Uplift wave forces due to compression of enclosed air layer and their similitude law. *Coastal Engineering in Japan* 28 (1), 191 – 206.
- Teng, M. H., Feng, K., Liao, T. I., 2000. Experimental study on long wave run-up on plane beaches. *In: Proceedings of the 10th International Offshore and Polar Engineering Conference, Seattle, USA*, 660 – 664.
- Timoshenko, S., 1983. *History of strength of materials: With a brief account of the*

-
- history of theory of elasticity and theory of structures. Courier Corporation, New York.
- Tromans, P. S., Anaturk, A. R., Hagemeyer, P., 1991. A new model for the kinematics of large ocean waves-application as a design wave. *In: International Ocean and Polar Engineering Conference.*
- Tuković, Z., Karač, A., Cardiff, P., Jasak, H., Ivanković, A., 2018. OpenFOAM finite volume solver for fluid-solid interaction. *Transactions of FAMENA* 42, 1 – 31.
- Ursell, F., Dean, R. G., Yu, Y., 1960. Forced small-amplitude water waves: A comparison of theory and experiment. *Journal of Fluid Mechanics* 7 (1), 33 – 52.
- van Veelen, T. J., Karunarathna, H., Reeve, D. E., 2021. Modelling wave attenuation by quasi-flexible coastal vegetation. *Coastal Engineering* 164, 103820.
- von Häfen, H., Krautwald, C., Stolle, J., Bung, D. B., Goseberg, N., 2022. Overland flow of broken solitary waves over a two-dimensional coastal plane. *Coastal Engineering*, 104125.
- Wang, J., Ward, S. N., Xiao, L., 2015. Numerical simulation of the December 4, 2007 landslide-generated tsunami in Chehalis lake, Canada. *Geophysical Journal International* 201 (1), 372 – 376.
- Wang, K., Ma, X., Bai, W., Qian, L., Li, Z., Li, Y., 2023. Two-dimensional numerical simulation of water entry of a cylinder into waves using OpenFOAM. *Ocean Engineering* 269, 113516.
- Watt, S. F., Pyle, D. M., Naranjo, J. A., Mather, T. A., 2009. Landslide and tsunami hazard at Yate volcano, Chile as an example of edifice destruction on strike-slip fault zones. *Bulletin of Volcanology* 71 (5), 559.
- Weller, H., Tabor, G., Jasak, H., Fureby, C., 1998. A tensorial approach to computational continuum mechanics using object orientated techniques. *Computers in Physics* 12, 620 – 631.

- Wikipedia, 2023. URL: <https://en.wikipedia.org/wiki/Dam>, accessed: 15 September 2023.
- Windt, C., Davidson, J., Ringwood, J. V., 2021. Numerical analysis of the hydrodynamic scaling effects for the Wavestar wave energy converter. *Journal of Fluids and Structures* 105, 103328.
- Xie, P., Chu, V. H., 2019. The forces of tsunami waves on a vertical wall and on a structure of finite width. *Coastal Engineering* 149, 65 – 80.
- Xue, H., Ma, Q., Diao, M., Jiang, L., 2019. Propagation characteristics of subaerial landslide-generated impulse waves. *Environmental Fluid Mechanics* 19 (1), 203 – 230.
- Yang, J. N., Agrawal, A. K., Samali, B., Wu, J.-C., 2004. Benchmark problem for response control of wind-excited tall buildings. *Journal of Engineering Mechanics* 130 (4), 437 – 446.
- Yavari-Ramshe, S., Ataie-Ashtiani, B., 2016. Numerical modeling of subaerial and submarine landslide-generated tsunami waves - Recent advances and future challenges. *Landslides* 13 (6), 1325 – 1368.
- Yuan, Z., Huang, Z., 2015. Morison coefficients for a circular cylinder oscillating with dual frequency in still water: An analysis using independent-flow form of Morison's equation. *Journal of Ocean Engineering and Marine Energy* 1 (4), 435 – 444.
- Zhang, G., Chen, X., Wan, D., 2019a. MPS-FEM coupled method for study of wave-structure interaction. *Journal of Marine Science and Application* 18, 387 – 399.
- Zhang, Z., Long, T., Chang, J., Liu, M., 2019b. A smoothed particle element method (SPEM) for modeling fluid-structure interaction problems with large fluid deformations. *Computer Methods in Applied Mechanics and Engineering* 356, 261 – 293.